DOE-ER-0313/64
Distribution
Categories
UC-423, -424

FUSION MATERIALS
SEMIANNUAL PROGRESS REPORT
FOR THE PERIOD ENDING

June 30, 2018

Prepared for
DOE Office of Fusion Energy Sciences
(AT 60 20 10 0)

DATE PUBLISHED: September 2018

Prepared by
OAK RIDGE NATIONAL LABORATORY
Oak Ridge, Tennessee 37831
Managed by
UT-Battelle, LLC
For the
U.S. DEPARTMENT OF ENERGY

FOREWORD

This is the sixty-fourth in a series of semiannual technical progress reports on fusion materials science activity supported by the Fusion Energy Sciences Program of the U.S. Department of Energy. It covers the period ending June 30, 2018. This report focuses on research addressing the effects on materials properties and performance of exposure to the neutronic, thermal and chemical environments anticipated in the chambers of fusion experiments and energy systems. This research is a major element of the national effort to establish the materials knowledge base for an economically and environmentally attractive fusion energy source. Research activities on issues related to the interaction of materials with plasmas are reported separately.

The results reported are the products of a national effort involving a number of national laboratories and universities. A large fraction of this work, particularly in relation to fission reactor irradiations, is carried out collaboratively with partners in Japan, Russia, and the European Union. The purpose of this series of reports is to provide a working technical record for the use of program participants, and to provide a means of communicating the efforts of fusion materials scientists to the broader fusion community, both nationally and worldwide.

This report has been compiled under the guidance of F. W. (Bill) Wiffen and Stephanie Melton, Oak Ridge National Laboratory. Their efforts, and the efforts of the many persons who made technical contributions, are gratefully acknowledged.

Daniel Clark
Research Division
Office of Fusion Energy Sciences

TABLE OF CONTENTS

TABLE OF CONTENTS

TABLE OF CONTENTS

TABLE OF CONTENTS

1. FERRITIC/MARTENSITIC STEEL DEVELOPMENT

1.1 MICROSTRUCTURE AND PROPERTY TAILORING OF CASTABLE NANOSTRUCTURED ALLOYS THROUGH THERMOMECHANICAL TREATMENTS—L. Tan, C.M. Parish and X. Hu (Oak Ridge National Laboratory)

OBJECTIVE

Castable nanostructured alloys (CNAs) are being developed to favor the formation of a larger amount of ultrafine stable precipitates in reduced-activation ferritic-martensitic (RAFM) steels using conventional, affordable steelmaking methods. However, the microstructure of CNAs is dependent on the thermomechanical treatment. This work correlates the mechanical properties and thermal helium desorption behavior with microstructures that were developed under different thermomechanical treatments.

SUMMARY

One CNA composition, designated CNA5, was developed into three types of microstructures—fully tempered martensite (TM), fully ferrite (F), and dual-phase (TM+F), termed R900, FC, and R700, respectively, according to their different processing and heat treatment conditions. The backscattered electron images in Figure 1 exhibit the typical microstructures of the three material conditions. The R900 and R700 refer to rolling at 900 and 700°C, respectively, after normalization at 1130°C, followed by water quenching and then tempering at 750°C with air cooling. In contrast, FC refers to furnace cooling to room temperature after a secondary normalization at 980°C. Microstructure and its effects on tensile properties, Charpy impact toughness, and thermal helium desorption behavior were systematically investigated in this work.

Other than the differences in grain size and dislocation density, the three material conditions primarily differed in the sizes and densities of MX and $M_{23}C_6$ precipitates. The R700 possessed ~32% ferrite grains with an average size of ~2 μm and had a significantly higher density of ultrafine (Ti,Ta)C and more $M_{23}C_6$ in finer sizes in the TM domain compared with R900. The F domain had a higher density of $M_{23}C_6$ in generally small sizes and slightly less MX than the TM domain of R700. In contrast, the FC exhibited new, fine (Ti,Ta)C, together with a higher density of ultrafine (Ti,Ta)C and less $M_{23}C_6$ in coarser sizes than R900. Additionally, the lath structure in the TM domains of R700 was not as well developed as that in R900, which is attributable to the rolling temperature at 700°C closer to the martensite start temperature of the CNA. Figure 1 shows the basic microstructural distinctions between the three material conditions of the CNA5.

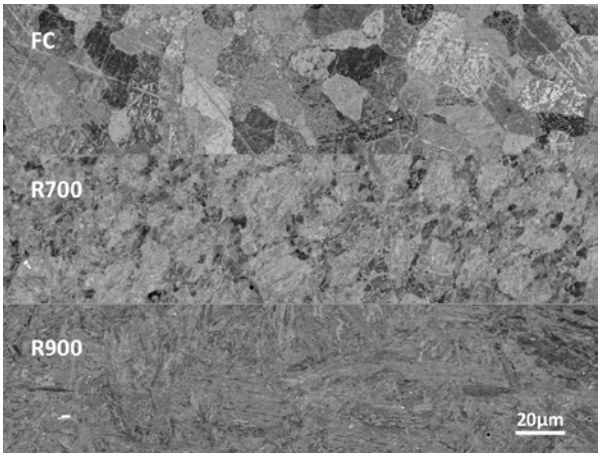

Figure 1. Backscattered electron images of the CNA5 in the three material conditions FC, R700 and R900.

With R900 as a reference, R700 showed slightly lower yield and tensile strengths with slightly lower or comparable uniform and total elongations. The F domain governed the strength of R700, as suggested by

microstructural strengthening calculations, which also slightly impaired the impact toughness of R700. In contrast, FC exhibited significantly higher yield and tensile strengths with higher uniform and total elongations at temperatures below ~600°C, but noticeably reduced impact toughness. The observed microstructures could not describe the significantly higher strength but could explain the poor impact toughness of FC.

Thermal helium desorption behavior differed for the different microstructures as shown in Figure 2. In addition to the classic primary desorption peaks at ~800–830°C (peak-I) for the ferrite-to-austenite phase transformation and at ~1070–1100°C (peak-II) for desorption by helium bubble migration, as in R900, the higher density of MX in R700 and FC amplified a desorption peak at ~960–980°C (peak-III). Additionally, the complex boundaries and dislocations in R700 extended the shoulder peak at ~580°C (peak-IV), in contrast to the insignificant shoulder peak at ~725°C (peak-IV) in FC induced by the low dislocation density and simple grain structure. The distinct properties of the varied microstructures could be exploited to engineer advanced RAFM steel components with functionally graded microstructures for demanding application requirements.

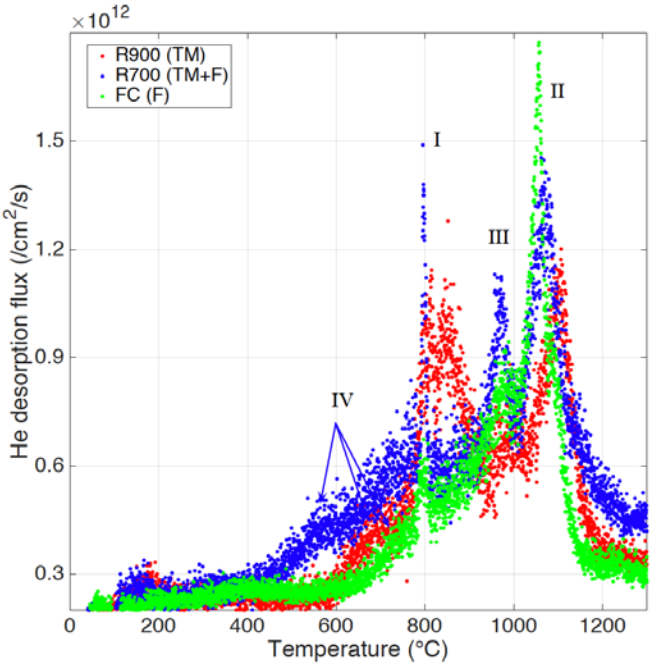

Figure 2. Temperature-dependent helium desorption flux of the CNA5 in three conditions of R900, R700 and FC.

For the detailed microstructure and property results and relevant discussions, see — L. Tan, C.M. Parish, X. Hu, "Microstructure and property tailoring of castable nanostructured alloys through thermomechanical treatments," *J. Nucl. Mater.* 509 (2018) 267–275 (https://doi.org/10.1016/j.jnucmat.2018.07.012).

1.2 CHARACTERIZATION OF NANOMETER SCALE Mn-Ni-Si PRECIPITATES USING THE TEM NANO-DIFFRACTION TECHNIQUE—S. Pal, P. Wells, N. Almirall, G.R. Odette (University of California, Santa Barbara)

OBJECTIVE

The objective of this study is to explore the use of the Transmission electron microscopy (TEM) nano-beam diffraction (NBD) technique to characterize the structure of nm-scale Mn-Ni-Si precipitates (MNSP) in irradiated steels.

SUMMARY

There is increasing evidence that nm-scale solute clusters and precipitates play a critical, if not dominant role in irradiation hardening in a wide range of materials and over a wide range of irradiation conditions. The cluster-precipitate number densities are typically in the range of ≈ 10^{23} to more than 10^{24} /m^3, with average sizes from ≈ 1.5 to 4 nm. While these clusters-precipitates have a wide range of compositions, depending on the alloy composition, they are often rich in Mn, Ni and Si and often classified as G-phase precipitates or their precursors. More generally we will refer to them as MNSPs. The atom probe tomography (APT) can characterize the solute content of MNSPs and estimate their true composition if the excess Fe APT artifact is accounted for. However APT cannot determine structure of MNSPs, to provide phase identification, or pertinent details, such as the MNSP interface orientation relationship (OR) with the Fe(-Cr) matrix that they are embedded in. The nm-scale size and small mole fractions (typically < 1%) of the embedded MNSPs, makes phase identification by most TEM and X-Ray Diffraction (XRD) methods extremely difficult; and to date carbon replica extraction methods have not been successful. Here, we report a successful characterization of nanometer-scale MNSP formed in an ion-irradiated and thermally annealed low alloy steel by combining NBD and scanning transmission electron microscopy (STEM) imaging techniques, with electron diffraction pattern simulations for various zone axis and MNSP-Fe ORs. High-resolution STEM imaging, on a Titan aberration-corrected microscope, finds well-developed polyhedral ≈ 3-10 nm MNSPs. The APT shows that the MNSPs have average compositions near either the stoichiometric $Mn_6Ni_{16}Si_7$ (G-phase) or the Mn_2Ni_3Si (Γ_2-phase). The NBD zone axis diffraction patterns correspond to the bcc Fe matrix but contain extra diffraction spots from the precipitates. The NBD diffraction patterns, for the <100>, <110> and <111> zone axis probes, show that the extra spots are consistent with a G-phase precipitate structure, with a coherent cube-on-cube OR.

PROGRESS AND STATUS

Introduction

Determination of the crystal structure of a small volume fraction of nm-scale precipitates embedded in matrix is extremely difficult using the conventional structural characterization techniques. Conventional XRD can probe the structure of precipitates if their volume fraction is sufficient, but their nm-scale sizes cause severe line broadening and decreased intensity of the diffraction peaks, that are hard to deconvolute from the background. The TEM selected area diffraction (SAD) is capable of characterizing precipitates low volume fraction; however, for precipitate less than ≈ 5-10 nm extra diffraction spots become invisible. Convergent beam electron diffraction (CBED) can easily probe precipitate in the ≈ 5-10 nm size range, but produce diffraction disks, rather than diffraction spots; analyzing the disk patterns, especially for small precipitates embedded Fe matrix, is very difficult. Even the Fast Fourier Power Spectra analysis of the high-resolution transmission electron microscopy (HRTEM) images containing nano-precipitates is difficult to analyze at small precipitate sizes.

The NBD technique has an advantage in that it can produce nm size parallel beams that can focus on the small precipitates to generate extra diffractions spots like site-selective diffraction (SAD), which are more easily indexed [1–3]. Here, we focus on characterizing the structure of ≈ 5-10 nm MNSPs in an ion irradiated and annealed low alloy steel.

Figure 1 shows schematics of the electron-optics ray diagram for three different diffraction techniques.

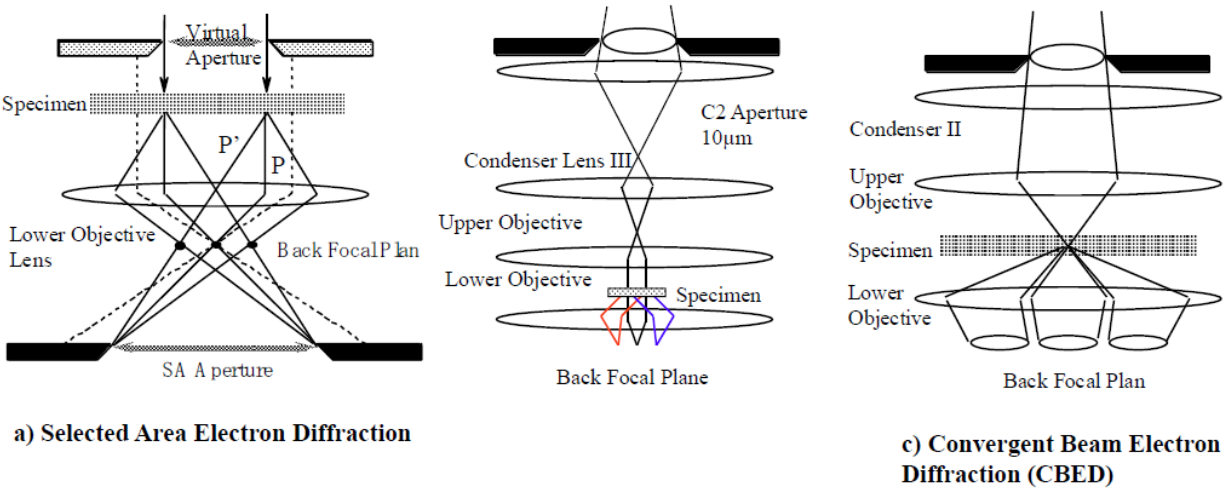

a) Selected Area Electron Diffraction

b) Nanobeam electron diffraction

c) Convergent Beam Electron Diffraction (CBED)

Figure 1. TEM beam configurations for: a) SAD; b) NBD and, c) CBED.

In case of SAD, parallel electron beam falls on the specimen and forms diffraction pattern on the back focal plane (see Figure 1a). For the CBED technique see Figure 1c), strengthening the condenser 2 (C2) and upper objective lenses, produce a very sharp probe focus on the specimen, producing disk pattern on the back focal plane. The presence of an extra mini condenser lens below the C2 lens and above the upper objective lens is produces a small parallel beam probe, in a region as small as ≈ 10 nm.

Experimental Procedure

The nominal low alloy steel composition in this study was a model reactor pressure vessel (RPV) steel with 0.02Cu-1.68Ni-1.50Mn-0.54Mo-0.007P-0.15C-0.17Si and balanced Fe, formally known as CM6. While the Mn, Ni and Si contents of this alloy are much larger than in 9-14Cr steels, the MNSPs that form in both cases are qualitatively similar. The higher solute in this case allows the use of ion irradiations to generate large volume fractions of MNSPs in the size range from ≈ 2 to 4 nm. In the 9-14Cr steels the clusters, or precipitates, form as a result of irradiation induced and thermal segregation of solutes to dislocations and dislocation loops [4]. The CM6 alloy was irradiated by 2.4 MeV Fe^{+3} ions at the University of Tokyo High Fluence Irradiation (HIT) facility to 1.25 displacements per atom (dpa) at 330°C to nucleate MNSPs. The 330°C ion irradiated alloy was then re-irradiated with another 1.25 dpa increment at 400°C to grow the MNSP so they are represntative of the higher temperature. Further a 330°C irradiation was carried out to a total of 2.5 dpa for comparison. The APT and energy-dispersive spectroscopy (EDS) TEM showed that the 330°C 2.5 dpa irradiation contained a higher density of smaller MNSPs compared to the final 400°C irradiation condition, as expected. Following the ion irradiations this alloy was annealed at 425°C for 52 weeks to assess the thermal stability of the MNSPs.

The APT study on the irradiated and irradiated and annealed was carried on a Local Electrode Atom Probe (LEAP)3000HRX (Cameca Instruments Inc.) to determine the composition, diameter, number density and volume fraction of the MNSPs. The crystal structure and OR of the MNSPs was characterized by the NBD technique. The morphology of the MNSPs was characterized by high-resolution STEM imaging. NBD, bright field (BF)-TEM and HRTEM imaging were performed on a 300 KV TEM/STEM instrument (Titan, FEI). The HR-STEM imaging was performed at the Lawrence Berkeley National Laboratory (LBNL) National Center for Electron Microscopy using the probe corrected TEAM-1 microscope [Transmission Electron Aberration-Corrected Microscope]. The TEM foils and APT tips were fabricated by the lift out method on a Helios 600 focused dual ion beam (FIB) SEM. The NBD patterns

were compared to simulations of the diffraction pattern for the most plausible Mn-Ni-Si precipitate phases system embedded in the Fe matrix, using Crystalkit software, developed by Total Resolution LLC.

Results

The APT solute maps of the as-irradiated and 425°C/52-week annealed specimen are shown in Figure 2 and the corresponding average precipitates sizes, volume fractions, number densities and compositions are summarized in Table 1.

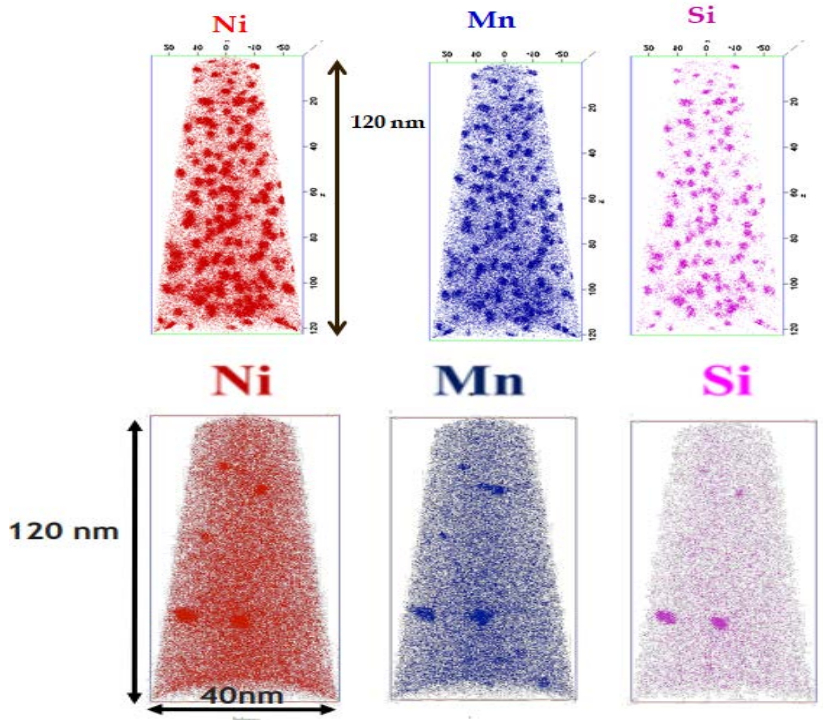

Figure 2. APT solutes maps of the: a) as irradiated; and, b) 52-week 425C annealed conditions.

Table 1. The average diameter (d), number density (N), volume fraction (f) and composition (Ni/Mn/Si) of the MNSP in the as irradiated (AI) and post irradiation annealed (PIA)

Condition	d (nm)	N (10^{23}/m^3)	f (%)	Ni/Mn/Si (%)
As irradiated	3.48	9.59	1.97	58/28/14
425°C/52 w PIA	4.79	3.95	0.12	51/23/16

The APT shows that most of the smaller precipitates below the critical size in the solute depleted matrix dissolve during annealing. However, precipitates above the critical size remain in the matrix after long-term thermal annealing and after dissolved solutes are replenished in the matrix. The average Ni/Mn/Si composition in the AI condition at 58/28/14 is reasonably close to that for the G2 phase at 50/33/17. The PIA increases the Si and decreases the Mn moving the Ni/Mn/Si composition at 51/23/16 closer to G-phase at 55/24/21. However, neither case is stoichiometric, which is not surprising since both are expected to have a finite phase field. Clearly, however, a diffraction-based technique is needed to determine on structure of the MNSP. Table 2 shows the crystal structures, lattice parameters of possible phases in the Mn-Ni-Si ternary phase system.

Table 2. Compositions, crystal structures and lattice parameters of phases in the ternary Mn-Ni-Si system [5].

Phase	Composition	Person Symbol	Space Group	Type	a (nm)	b (nm)	c (nm)
E	MnNiSi	oP12	Pnma	$PbCl_2$	0.58967	0.36124	0.69162
Γ1	$Mn_3Ni_3Si_2$	hP12	P63/mmc	$MgZn_2$	0.4762		0.7507
$Γ_2$ (T_6)	Mn_2Ni_3Si	cF24	Fd-3m	Cu_2Mg	0.6687		
G (T_3)	$Mn_6Ni_{11}Si_7$	cF116	Fm3-m	$Mg_6Cu_{16}Si_7$	1.1158		

Figure 3a shows a lower magnification view of high-angle annular dark-field (HAADF)-HRSTEM image of the as-irradiated specimen for the <111>-zone axis of Fe, where some of the MNSPs are outlined, although this is not meant to be an indication of their true shape. Since the MNSP is an intermetallic Mn-Ni-Si and having only a slightly lower electron density than the bcc-Fe matrix, they appear as the dark regions. Only very faint extra spots from the MNSPs are observed in the corresponding fast Fourier transform (FFT) HRTEM power spectrum in Figure 3b. A higher magnification view of one (or two closely spaced in the projection) MNSP in Figure 4 shows a polyhedral shape, with what appears to be a coherent or semi coherent interface with the matrix

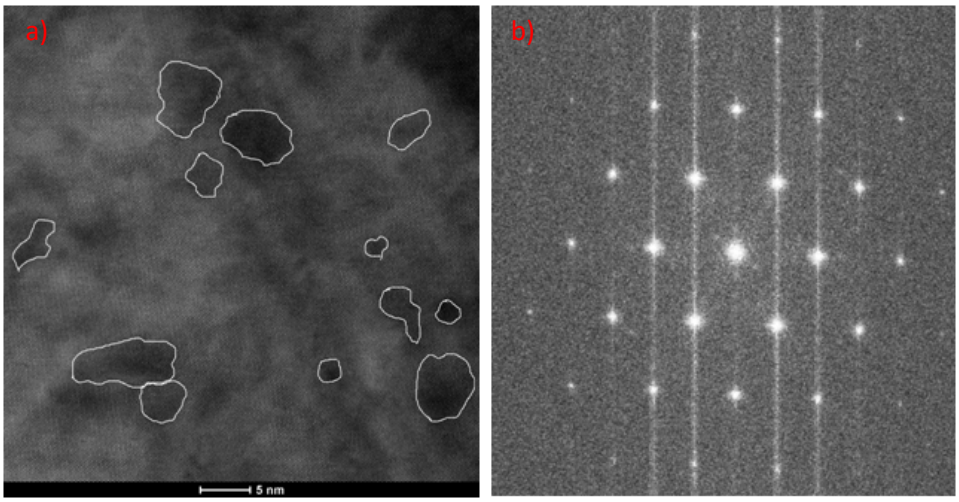

Figure 3. a) A HAADF-STEM image of the as-irradiated condition; and, b) an FFT power spectrum pattern of the image in Figure 2a.

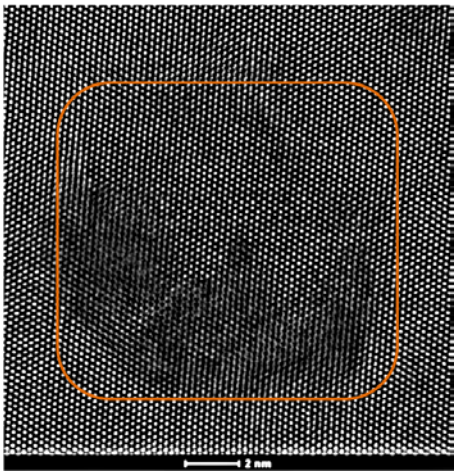

Figure 4. A high magnification atomic resolution STEM image of an MNSP.

While HRSTEM images can help characterize the morphology and suggest a coherent (or semi coherent) character of the MNSP, as indicated by the alignment of atomic columns inside and outside the precipitate region. However, the FFT power spectrum in the Figure 3b is not an accurate representation of the diffraction pattern. The absence of extra spots from the FFT pattern is likely due to the extremely small size of the coherent embedded MNSP.

Figure 5 shows an NBD pattern for a Fe <110> zone axis from a ≈10 nm probe near the peak damage depth. The high-intensity bright spots of the NBD pattern, marked in red, represent bcc matrix low index Fe planes. The white arrows indicate the extra spots from the nanometer scale precipitates.

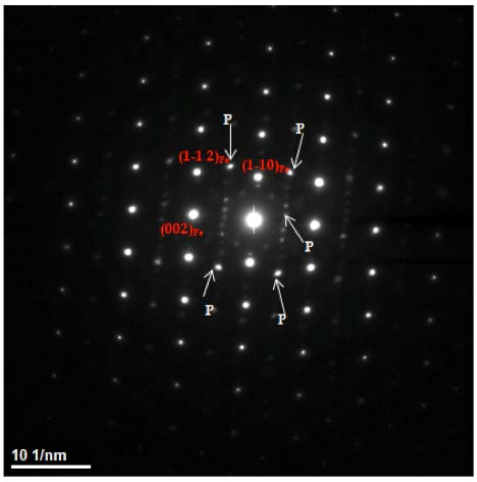

Figure 5. The NBD for the MNSP in Figure 4, with the extra spots indicated by the white arrows.

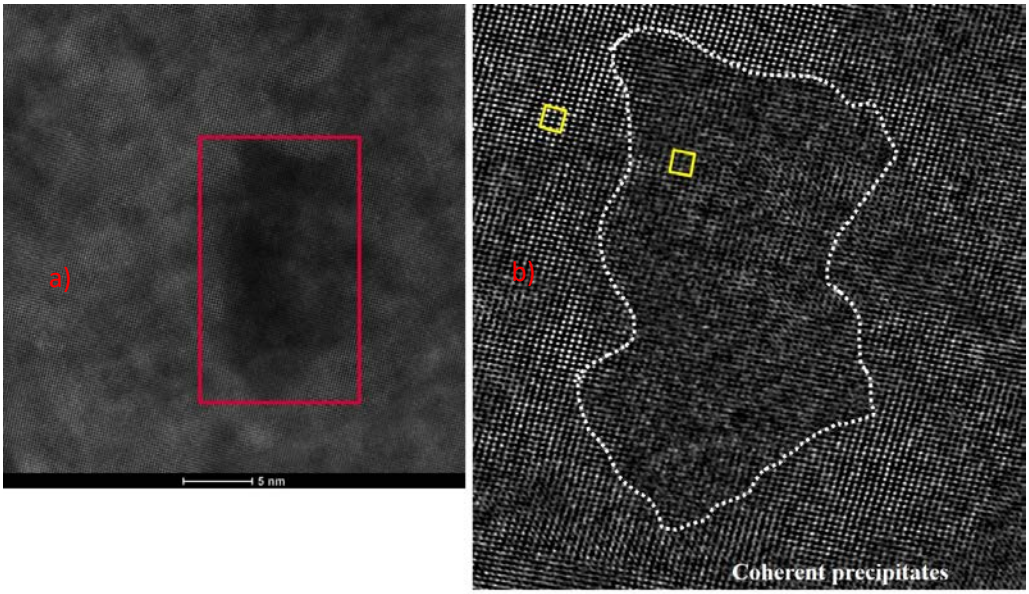

Figure 6. a) A BF-TEM image showing a large highlighted MNSP; and, b) a corresponding HRTEM image of the MNSP.

Figure 7 shows the NBD patterns for the 52 weeks annealed condition, with extra spots from MNSPs, for the extra spots are indicated using numbers in Figure 7a.

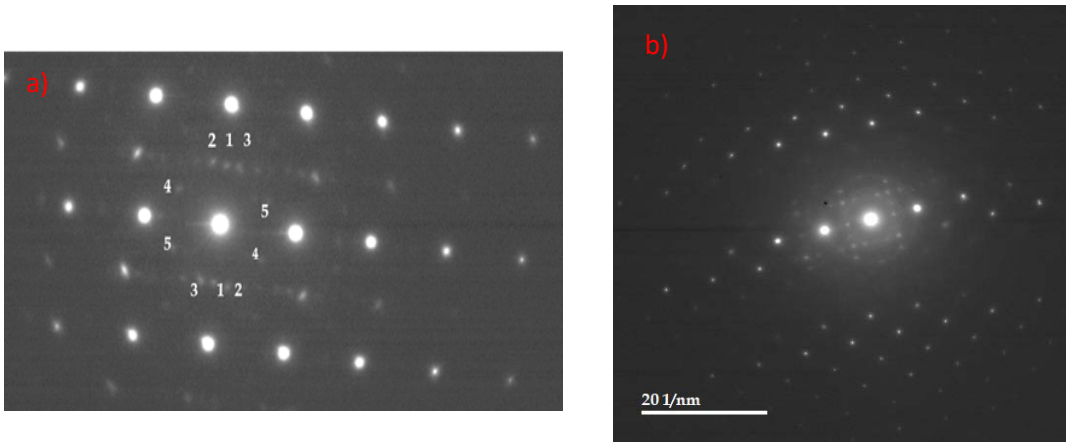

Figure 7. The 52 weeks annealed condition NBD patterns for the zone axis: a) <110>; and, b) <100>.

A BF-HRTEM image from the damaged region of the annealed specimen is shown in Figure 8a. Due to their weak phase contrast and coherent character, the MNSPs are difficult to image in a BF-HRTEM image. However, the corresponding FFT pattern of the Figure 8b shows the extra spots from for the <111> Fe axis. Figure 8c and d are the inverse FFT images of the Figure 8b after masking the extra spots from the MNSP and matrix spots, respectively. After masking of the matrix spot, the continuous lattice fringes corresponding to MNSP seen in Figure 7d and are marked by the orange boxes.

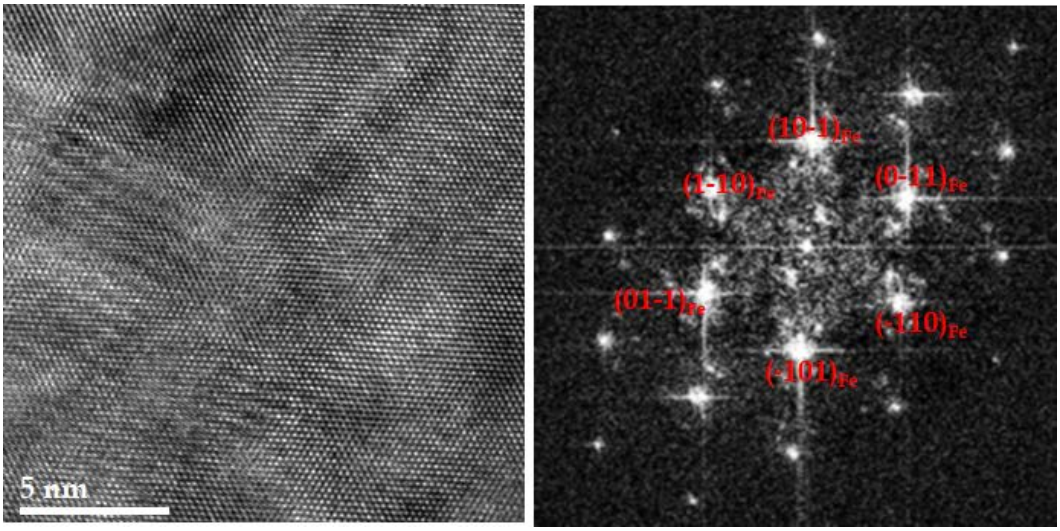

(a) (b)

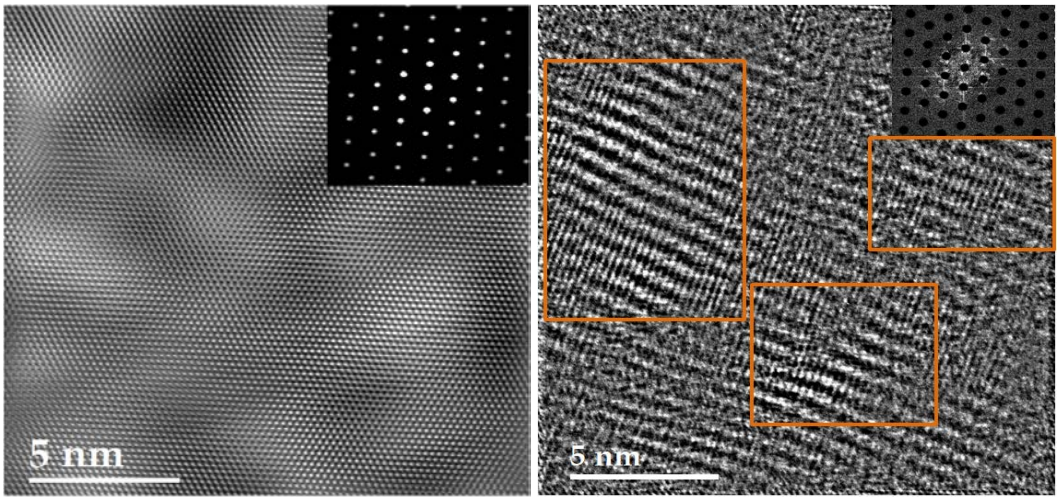

(c) (d)

Figure 8. a) A BF-HRTEM image for the 52 weeks annealed condition; b) the FFT spectra of the Figure 8a; c) an inverse FFT image of Figure b after masking the extra spots from the MNSP, matrix spots FFT inserted; and, d) an inverse FFT image of the Figure 8b after masking the spots from the bcc-Fe matrix, FFT pattern of the image inserted.

Analysis of the NBD Patterns

We simulated the diffraction pattern of both the G-phase and Γ_2 embedded in a bcc-Fe matrix considering different OR with the matrix. The closest match between the simulated and experimental <110> NBD pattern are shown Figures 9a and b G-phase precipitate embedded in a Fe matrix with a cube-on-cube OR, where <100> type of direction and {001} type of bcc-Fe matrix is parallel to the <100> type of direction and {001} types of planes of cubic G-phase.

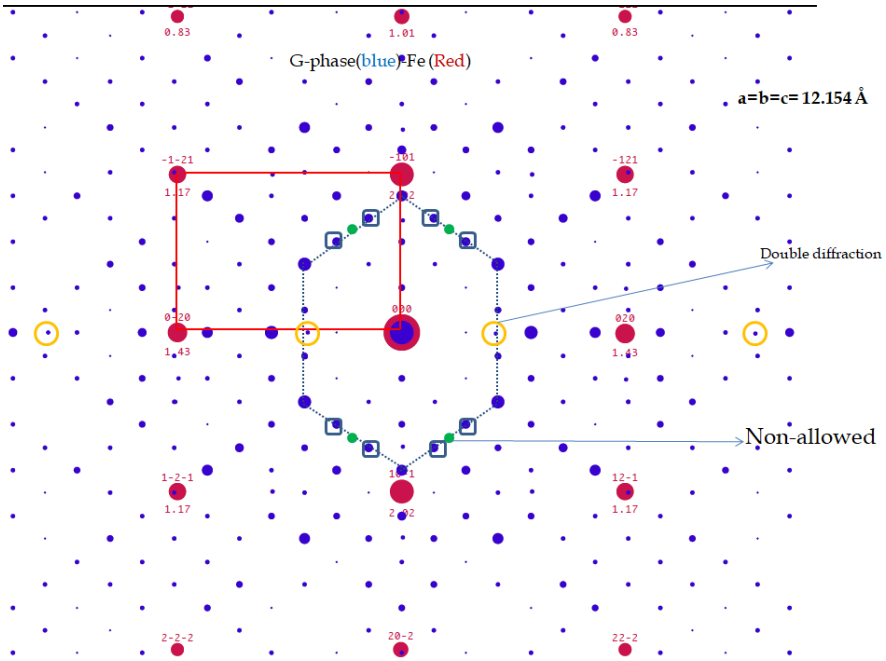

(a)

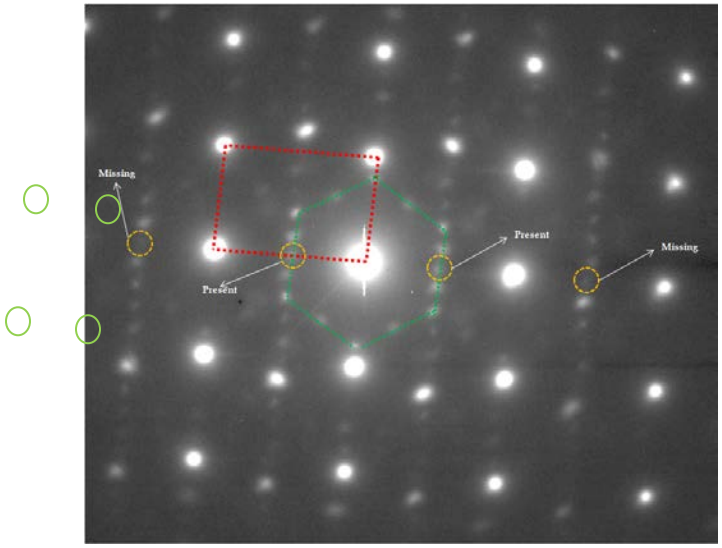

(b)

Figure 9. a) Simulated DP along the <110> of bcc Fe; and, b) experimental DP.

The Fe lattice is marked using the red dotted line in both Figures 9a and b, while in the simulated pattern G-phase pattern (Figure 9a) is marked using dotted blue line and in the experimental pattern it is marked using green dotted line. In Figure 9b, the spots arise from double diffraction are marked using yellow circle which is clearly seen in our simulated pattern. Similarly, forbidden reflections which are labeled as green circle in Figure 9a, are marked in Figure 9b. On another note, due to smaller crystal thickness of G-

phase and cube-on-cube OR, some of the allowed reflections (marked using blue box in Figure 9a) are missing in the experimentally DP, as they are not parallel to any {hkl} planes of bcc-Fe matrix. The DP simulation of Γ_2 phase embedded in Fe matrix was also carried following the same methodology and shown in Figure 10. From Figure10 it is very much evident that the crystal structure of the MNSP does not match with the Γ_2 phase of Mn-Ni-Si system.

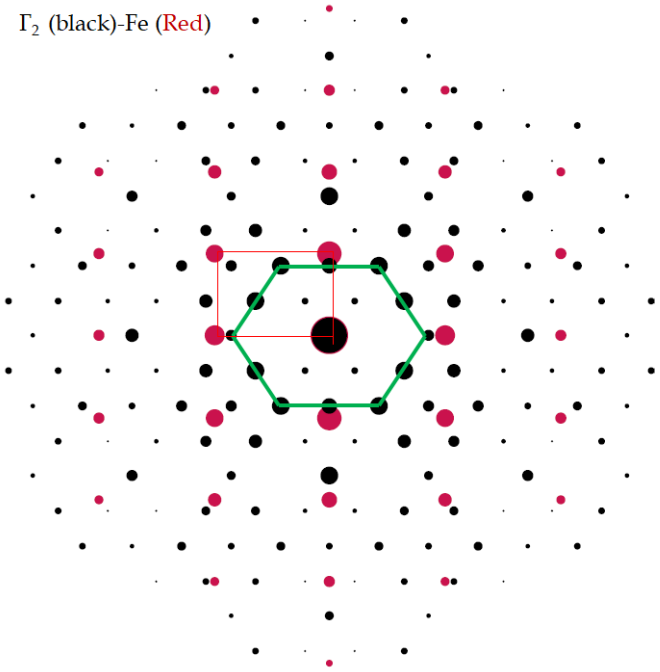

Figure 10. Simulated pattern of Γ_2 phase.

Similar pattern matching is observed for other zone axes but is not reported here.

Conclusions

- The 3-10 nm MNSPs in the irradiated and aged CM6 alloys highly coherent G-phase precipitate forming a cube-on-cube OR with the bcc-Fe matrix.
- The NBD technique coupled with DP simulation a promising technique for characterizing nm scale precipitates embedded matrix.

Future work

- We are working on creating a structure file to include the size, shape, and thickness of the diffracting crystals in order to match the intensity of the spots from the precipitates.
- These structure files will also be used to simulate HRTEM and HR-STEM images.
- We are also planning complete collecting NBD patterns from other low-index –zone axis.

References

[1] M. Herbig, P. Choi, D. Raabe, Combining structural and chemical information at the nanometer scale by correlative transmission electron microscopy and atom probe tomography, Ultramicroscopy. 153 (2015) 32–39. doi:https://doi.org/10.1016/j.ultramic.2015.02.003.

[2] R. Holmestad, R. Bjørge, F.J.H. Ehlers, M. Torsæter, C.D. Marioara, S.J. Andersen, Characterization and structure of precipitates in 6xxx Aluminium Alloys, J. Phys. Conf. Ser. 371

(2012). doi:10.1088/1742-6596/371/1/012082.
[3] M.R. Ward, E.D. Boyes, P.L. Gai, Aberration corrected (S)TEM and nano beam diffraction (NBD) of Pt and Pd on Al2O3catalysts, J. Phys. Conf. Ser. 522 (2014) 8–12. doi:10.1088/1742-6596/522/1/012068.
[4] M. Bachhav, G. Robert Odette, E.A. Marquis, α′ precipitation in neutron-irradiated Fe–Cr alloys, Scr. Mater. 74 (2014) 48–51. doi:https://doi.org/10.1016/j.scriptamat.2013.10.001.
[5] K.P. Gupta, The Mn-Ni-Si (Manganese-Nickel-Silicon) system, J. Phase Equilibria Diffus. 27 (2006) 529–534. doi:10.1007/BF02736466.

1.3 MICROSTRUCTURE BASED PREDICTIONS OF HARDENING IN IRRADIATED TEMPERED MARTENSITIC STEELS—T. Yamamoto, G.R. Odette (University of California Santa Barbara), T. Saleh, S. Maloy (Los Alamos National Laboratory)

OBJECTIVE:

The objective of the research is to develop well calibrated physically based models to predict changes in mechanical properties of irradiated alloys based on microstructural observations, here specifically to predict yield stress changes ($\Delta\sigma_y$) that occur under irradiation applied to a tempered martensitic steel (TMS).

SUMMARY

A new microstructure-based irradiation hardening ($\Delta\sigma_y$) prediction model is described for tempered martensitic steels utilizing corresponding sets of microstructure and mechanical properties characterized after neutron irradiations. The individual hardening feature contributions (σ_j) to the change in the net yield stress, ($\Delta\sigma_y$), based on a dispersed-barrier hardening model, were appropriately super-positioned, including the effect of strong pre-existing obstacles (σ_u), to evaluate $\Delta\sigma_y$. The obstacle strength factors (α_j) include those for dislocation loops (α_l), α' precipitates ($\alpha_{\alpha'}$) and solute clusters (α_c), that were previously fitted to ATR-1 irradiated Fe-3 t0 18Cr alloy series. A G-phase type precipitates α_p was fitted to irradiated reactor pressure vessel (RPV) steels database. The obstacle strength factors for voids (α_v) and helium (He) bubbles (α_b) were taken from the literature. The fitted hardening model for a 9Cr TMS (T91) was calibrated using BOR-60 data to account for an optimized pre-existing hardening, $\sigma_u \approx 168$ MPa, that is typical of this type of steel.

PROGRESS AND STATUS

Introduction

The broad objective of this research is to use physically based, well-calibrated models to predict changes in mechanical properties of neutron alloys based on microstructural observations and models. The first objective is to predict changes in the ≈ 23°C yield stress ($\Delta\sigma_y$) that occur under irradiation. The $\Delta\sigma_y$ can, in turn, be related to changes in other mechanical properties, such as temperature shifts (ΔT_o) in the master fracture toughness $K_{Jc}(T)$ curve. Other long-term objectives include predicting post-yield changes in flow stress and ductility as well as properties related to creep and fatigue behavior.

Previously we derived a dispersed barrier model for irradiation hardening by α' precipitates (α'), solute clusters (sc), and dislocation loops (l) using a database of Fe-3 to 18%Cr model alloys, where the loops were characterized by transmission electron microscopy (TEM), while the α' and sc were characterized by atom probe tomography [1]. Then, the feature's diameters (d) and number densities (N) were used to determine the corresponding spacing on a slip plane $L_j \approx 1/\sqrt{(N_j d_j)}$. The analyses showed that the loops and solute clusters are moderately strong obstacles, while the α' is a weak dislocation barrier. Thus, the loop and solute cluster hardening was treated with a root sum square superposition rule, while the hardening contribution of α' was simply added following a linear sum superposition rule. The key model parameters – the individual obstacle strength parameters, α_j (j = α', sc, l) were least square fitted to yield $\alpha_{\alpha'} = 0.031$, $\alpha_l = 0.2$ and $\alpha_{sc} = 0.17$, with a predicted to measured standard deviation of 39 MPa.

Now in this report, we focus on predicting ambient temperature $\Delta\sigma_y$ in a TMS T91 heat of 9Cr irradiated in BOR-60 reactor.

The hardening model

Hardening Contributions of Individual Features: As has been reported previously simple dispersed obstacle individual hardenings were super-positioned appropriately considering the dislocation bowing on

multiple features. The individual models for isolated hardening, based on single dislocation obstacle interactions, can be expressed in various ways but the most frequent and simplest formulation is [2.3]

$$\sigma_j = M\alpha_j(r_j)Gb/(L - 2r_j) \quad (1a)$$

Here, the spacing between the centers of the obstacles is

$$L \approx 1/\sqrt{}(2N_j r_j) \quad (1b)$$

Here N_j and r_j are the feature number density and radius, respectively. The α_j is the obstacle-dislocation interaction strength parameter, M ≈ 3.06 term is the polycrystalline Taylor factor for bcc lattices, G is the shear modulus (≈ 82000 MPa at 25°C) and b = 0.248 nm is the dislocation Burgers vector.

Strength Superposition Models: Earlier computer simulations showed that the net $\Delta\sigma_y$ based on the individual yield stress contributions from combinations of weak ($\alpha_w < 0.05$, σ_w), medium ($0.05 < \alpha_m < 0.6$, σ_{ym}) and high ($\alpha_s > 0.6$, σ_{ys}) strength obstacles can be described by a simple fitted analytical model [3]:

$$\Delta\sigma_y = \sigma_{yw} + (1\text{-}S)(\sigma_{ym}^2 + \sigma_{ys}^2)^{1/2} + S(\sigma_{ym} + \sigma_{ys}) - \sigma_{ys} \quad (4)$$

Here the superposition factor S was previously given by [2,3]

$$S \approx \alpha_{so} - \alpha_{mo}(5.0 - 3.3\alpha_{so}) \quad (5)$$

where the α_{io} are for an isolate single obstacle based on the critical angle when dislocations bypass the obstacle. The strength factors α_i used in Equation 1 are for randomly distributed obstacles, which is related to α_{io} by [4,5],

$$\alpha_i = \alpha_{io}^{3/2} (\alpha_{io} < 0.64) \text{ or } 0.8\,\alpha_{io} (\alpha_{io} \geq 0.64) \quad (6)$$

Thus, obstacles with similar strengths can approximately be described by a residual sum of squares (RSS) superposition model, while those with very different strengths (very low and high) come closer to a LS law. The superposition of the strengthening contributions of medium strength and strong obstacles falls in between.

Experimental Procedure

A brief and incomplete literature survey was carried out for neutron and ion irradiated ferritic alloys including Fe-Cr alloys and TMS that are one of the following types:

1) Proposed obstacle hardening models based on fitted irradiated microstructural and hardening data.

2) Irradiation microstructure-based hardening predictions compared to measured values based on literature hardening and strength factors models.

3) Computational models of dislocation-obstacle interactions that are, or can be, represented by obstacle strength factors α_j.

A web of science search identified 80 candidate publications, that were screened to 40 papers published in the last five years, as well as key references therein. These papers were carefully examined to extract information on obstacle hardening strength factors, α_j. The results are summarized in Tables 1a to c [6-22]. Table 1a summarizes α_j values obtained from type-1 papers, on Fe-Cr and Fe-Cr-Al alloys, where both irradiation hardening and observed microstructures, that included dislocation loops, α' precipitates, solute clusters and network dislocations were analyzed to determine the α_j that gave the best fit $\Delta\sigma_y$ from the microstructure-based hardening models. Table 1b summarizes the type-2 papers that did not carry

out least squares fitting, but where measured $\Delta\sigma_y$ (or equivalent) were compared to predicted hardening based on the observed microstructure using a dispersed-barrier hardening model with the α_j taken from earlier experimental or modeling studies. Table 1c summarizes the α_j found in modeling studies, including molecular dynamics (MD) and discrete dislocation dynamics (DDD) computer simulations as well as dislocation theory based analytical models.

Table 1a. Obstacle strength factors, α_j, based on microstructure fits to hardening data [6-9]

Alloy	Model	Super-position	Dislo-cation	Loop			α'		Precipitate		Irrad. facility	Test type	Ref.
			α	α_l	d (nm)	b	$\alpha_{\alpha'}$	d (nm)	α_p	d (nm)			
Fe 2.5-9Cr	DBH	LS	0.1	0.187	7-13		0.148		0.148	3.2-4.4	BR2	tens	[6.7]
Fe 10-18Cr 3Al	DBH	RSS	0.56	0.33	30-50	<1 0 0>	0.06	2.5-4.4			HFIR	tens	[8]
				0.17	20-32	1/2<1 1 1>							
		LS	0.68	0.31	30-50	<1 0 0>	0.038	2.5- 4.4					
				0.05	20-32	1/2<1 1 1>							
Fe 2.5-12Cr	BKS	LS		0.403	7-13		0.048	2	0.274	3.2 - 4.4	BR2	tens	[9]
	BKS mod.	LS		0.503	7-13		0.08	2	0.397	3.2- 4.4			
	BKS	RSS		0.661	7-13		0.087	2	0.34	3.2 -4.4			
	BKS mod.	RSS		0.833	7-13		0.142	2	0.49	3.2- 4.4			
	DBH	LS		0.296	7-13		0.015	2	0.1	3.2- 4.4			
	DBH	RSS		0.44	7-13		0.03	2	0.134	3.2- 4.4			

Table 1b. Microstructure based hardening prediction based on literature models compared to measured $\Delta\sigma_y$ [9-17]

Alloy	Model	Super-position	Dislo-cation	Loop		Cavity		α'		$M_{23}C_6$		MX		Irrad. facility	Test type	Ref.
			α	α	d (nm)	α	d (nm)	α	d (nm)	α	d (nm)	α	d (nm)			
Fe	DBH	LS	0.64	0.4	6-9									ATR	NI	[10,11]
					8.5									ATR	H_v	
Fe-(10,14)Cr	DBH	LS						0.048	2.4					ATR	NI	[9-.12]
Fe -10-16Cr (Single Crystal)	DBH	LS	0.64	0.4	2.6-5.2			0.048	2.5					ATR	H_v	
CLAM	loop: DBH bubble: FKH	LS		0.3-0.45	16-52	1	6-10 (voids)							Fe^{3+}	NI	[13,14]
Eurofer 97	DBH	RSS		0.6	3-14	1	1.6-2.6 (voids)			1	74-106	1	19-32	BOR60	tens	[15,16]
F82H (bubbles)	DBH	N/A				0.1	1-1.5 (bubbles)							STIP	H_v	[17]

Table 1c. Obstacles strength factors, α_j, determined from various computational studies [18-22]

Alloy	Model	Super-position	Loop			Void		Bubble		Precipitate (spherical)		Cu rich ppt		Rigid particle		Method	Ref.
			α	d (nm)	b	α	d (nm)	α	d	α	d	α	d	α	d		
Fe	DBH (l')	N/A	0.35 ±0.16	2.3-7.4	<1 0 0>											MD	[18]
Fe	DBH (l')	N/A	0.50	1.6-4.4	1/2[1 -1 1]											MD	[18]
Fe	DBH	N/A	0.435	1.1-5.6		0.09-0.58	0.6 - 4.6									DDD	[19]
Fe	FKH	N/A	25.12													DDD	[19]
Fe	BKS	N/A	1.209			1.0	0.6-2.9									DDD	[19
Fe	DBH	RSS	0.1-0.9	2-5		0.3-0.75	2-5									Rate theory	[20]
Fe	DBH	N/A				0.58	2	0.65	2			0.3	2	0.75	2	MD	[21]
AuSS	DBH	N/A	0.39-0.52	5-10		0.05-1	1.2-10			0.25-0.58	1.5 -10					Analytical models	[22]

Analysis of the BOR60 irradiated T91

Table 2 summarizes the α_j used in the T91 hardening models, which are based on the hardening models for Fe-Cr alloys and RPV steels reported previously [1] as well as the literature survey in the previous section. Table 3 summarizes microstructure of T91 irradiated in BOR-60 to up to 35 dpa at the temperatures from 376 to 524°C reported by Jiao et al. [23] The table also shows yield and ultimate shear stress, τ_y and τ_u, from shear punch tests (SPT) carried out at Los Alamos National Laboratory (LANL) for selected conditions. Irradiation hardening, $\Delta\sigma_y$, are evaluated based on previously obtained correlation, $\sigma_y/\tau_y = 1.77$ [24], using the baseline $\tau_y = 350$ MPa. The hardening models potentially involve three groups of obstacles: 1) very weak α' precipitate; 2) medium strength dislocation loops, bubbles and G-phase precipitates; and 3) very strong voids and pre-existing (e,g. Mo_2C) obstacles. Thus, the individual hardenings σ_j given by Equation 1 (USE THIS FORMAT) were super-positioned using the following formula based on Equation 4, where S is given by Equation 5.

$$\Delta\sigma_y = \sigma_{\alpha'} + (1-S)(\sigma_{ym}^2 + \sigma_v^2 + \sigma_u^2)^{1/2} + S(\sigma_{ym} + \sigma_v + \sigma_u) - \sigma_u \quad (6a)$$

$$\sigma_{ym} = [\sigma_l^2 + \sigma_b^2 + \sigma_p^2]^{1/2} \quad (6b)$$

Here, σ_u is the only unknown parameter, thus the final hardening model calibration was based on least squares fitting σ_u to the corresponding experimental T91 BOR 60 $\Delta\sigma_y$ data for irradiations at 385 and 412°C.

The orange diamonds in Figure 1a are the predicted values for the best fit $\sigma_u = 168$ MPa, while the blue squares are corresponding measured $\Delta\sigma_y$ at 376 and 415°C in BOR-60 as well as at 300°C in University of California Santa Barbara (UCSB) ATR1 experiment. Figure 1a also shows a previously derived hardening $\Delta\sigma_y(T)$ temperature dependent fit to a variety of 9Cr TMS [25]. The $\Delta\sigma_y$ is for an estimated saturated condition and tensile testing at room temperature. The red circle symbols are the average data used to establish the $\Delta\sigma_y(T)$ red solid trend curve. Both the predicted and measured $\Delta\sigma_y$ are in good agreement with the general 9Cr TMS $\Delta\sigma_y(T)$ trend, except that the prediction at 524°C. At the high temperature no significant hardening features have been observed, consistent with the $\Delta\sigma_y(T)$ trend that shows softening at $T > \approx 430$°C.

Figure 1b shows the contributions of various features to the total predicted hardening. Note: these are not isolated hardening of the features but were prorated so that the linear sum corresponds to the final $\Delta\sigma_y$ prediction. Major contributions are from dislocation loops, voids and solute rich (G-phase) precipitates after neutron irradiation with limited contribution of He bubbles

Table 3. The α_j values used in the analysis of the IRP T91 data

Obstacle	Strength, α_j	Value
Dislocation loop	α_l	0.2
Void	α_v	0.75
Bubble	α_b	0.1
α' precipitate	$\alpha_{\alpha'}$	0.031
G-phase precipitate	α_p	≈ 0.2
Pre-existing (MoC)	α_u	0.8

Table 4. Summary of microstructures and hardening observed in T91 irradiated in BOR-60 [23]

Capsule #	Temperature(°C) : dose(dpa)	G phase and NiSi cluster		Cavity				Loop		SPT
		<d > (nm)	N (m^{-3})	<d>> (> 2nm) (nm)	N (>2nm) (m^{-3})	N (< 2nm) (m^{-3})	Swelling (%)	<d > (nm)	N (m^{-3})	1% / UTS (MPa)
P027	376:17.1	5.8	3.6E+21	6.9	7.3E+20	12E+22	1.6E-02	21.8	2.9E+21	420/548 445/583
P028	378:35.1	7.0	2.4E+21	6.5	14.7E+20	2.2E+22	3.3E-02	22.9	1.9E+21	
P033	415:18.6	6.7	3.0E+21	5.6	4.8E+20	7.3E+20	5.8E-03	25.8	2.0E+21	372/540 390/556
P035	426:19.5	5.9	8.2E+21	7.2	6.2E+20	5.7E+21	1.9E-02	22.4	2.8E+21	
P037	460:18.8	N.O.	N.O.	N.O.	N.O.	3.2E+21	Negl.	Negl.	Negl.	
P042	524:15.4	N.O.	N.O.	N.O.	N.O.	3.3E+21	Negl.	N.O.	N.O.	

N.M = not measure; N.O. = not observed;

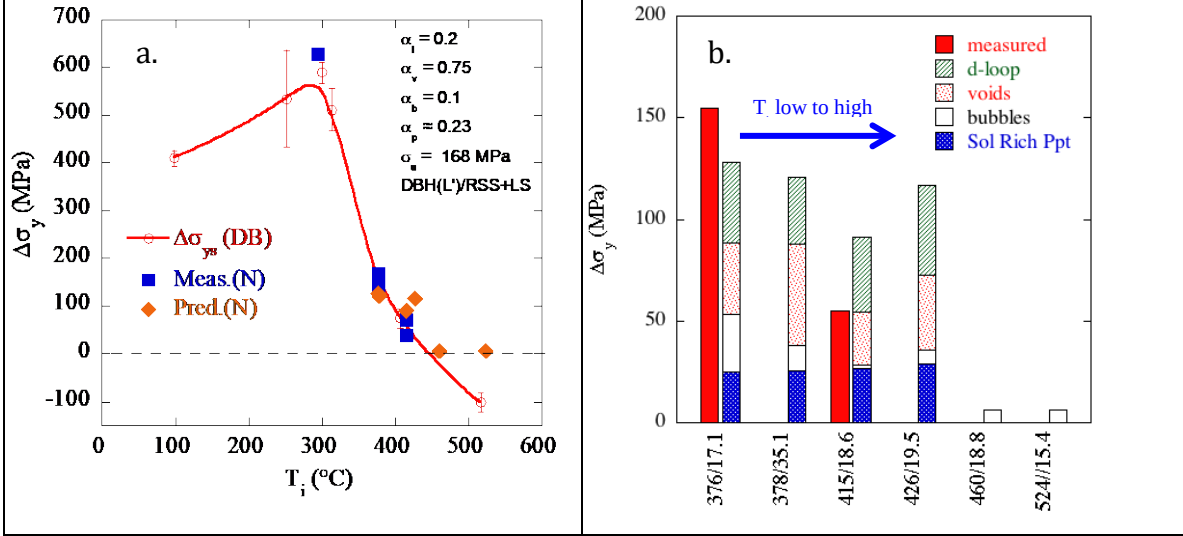

Figure 1. a) Predicted and measured $\Delta\sigma_y$ versus irradiation temperature Ti including predictions (orange diamonds) for neutron irradiated microstructures for a best fit σ_u = 168 MPa, comparing to the corresponding measured $\Delta\sigma_y$ (blue squares) as well as database derived $\Delta\sigma_y$(T) temperature dependent fit to a variety of 9Cr TMS [25] (red circles with solid curve); b) hardening component break-down for $\Delta\sigma_y$ predictions for neutron (labeled by temperature/dpa) irradiations.

Future Work

We will refine the hardening models while extending them to other irradiation conditions and ferritic materials as we acquire the corresponding sets of microstructure and mechanical data.

Acknowledgements

The work is supported by Department of Energy (DOE) OFS as well as Nuclear Energy (NE) through the Integrated Research Projects (IRP) program. Authors also thank the contributions of our many collaborators and especially acknowledge the excellent leadership and feedback provided by the IRP Principal Investigator (PI) Professor Gary Was.

References

[1.] T. Yamamoto, P. Wells, G. R. Odette, D. Bhattacharyya, “Microstructure Based Predictions of Hardening in Fe-3- to 18%Cr Binary Model Alloys Irradiated in the ATR Reactor,” Fusion Materials Semiannual Report 7/1 to 12/31/2017 DOE/ER-313/63.

[2.] J. W. Martin, Micromechanisms in Particle-Hardened Alloys, Cambridge University Press (1980).

[3.] G. R. Odette, Chapter 2 - Embrittlement Mechanisms and Physical Models Underpinning the TTS Model, in the report E. E. Eason, G. R. Odette, R. K. Nanstad and T. Yamamoto, A Physically Based Correlation of Irradiation-Induced Transition Temperature Shifts for RPV Steels, Oak Ridge National Laboratory ORNL/TM-2006/530 (2007).

[4.] G.R. Odette, G.E. Lucas, G. Tedeski, B.D. Wirth, Development of superposition rules for hardening in alloys containing multiple defect populations, in: F.W. Wiffen (Ed.), Fusion Materials, U.S. DOE Office of Fusion Energy Sciences, Oak Ridge National Laboratory, 1998, 221**.**

[5.] Foreman AJE and Makin MJ. "Dislocation Movement Through Random Arrays of Obstacles", Can. J. Phys. 1967;45(2):511–517.

[6.] X. Xiao, D. Terentyev, L. Yu, A. Nakaev, Z. Jin, H. Juan, “Investigation of the thermo-mechanical behavior of neutronirradiated Fe-Cr alloys by self-consistent plasticity theory,” J. Nucl. Mater, 477 (2016) 123.

[7.] X. Xiao, D. Terentyev, L. Yu, D. Song, A. Bakaev, H. Duan, "Modelling irradiationinduced softening in BCC iron by crystal plasticity approach," J. Nucl. Mater. 466 (2015) 312-315.
[8.] K.G. Field, X. Hu, K.C. Littrell, Y. Yamamoto, L.L. Snead, "Radiation tolerance of neutron-irradiated model Fe-Cr-Al alloys," J. Nucl. Mater. 465 (2015) 746-765.
[9.] F. Bergner, C. Pareige, M. Hernandez-Mayoral, L. Malerba, C. Heintze, "Application of a three-feature dispersed-barrier hardening model to neutron-irradiated Fe–Cr model alloys," J. Nucl. Mater. 448 (2014) 96 – 102.
[10.] S. Porollo, A. Dvoriashin, A. Vorobyev, Y.V. Konobeev, "The microstructure and tensile properties of Fe-Cr alloys after neutron irradiation at 400 C to 5.5-7.1 dpa," J. Nucl. Mater. 256 (1998) 247-253.
[11.] Wei-Ying Chen, Yinbin Miao, Jian Gan, Maria A. Okuniewski, Stuart A. Maloy, James F. Stubbins. "Neutron irradiation effects in Fe and Fe-Cr at 300°C," Acta Materiallia 111 (2016) 407-416.
[12.] Wei-Ying Chen, Yinbin Miao, Yaqiao Wu, Carolyn A. Tomchik, Kun Mo, Jian Gan, Maria A. Okuniewski, Stuart A. Maloy, James F. Stubbins, "Atom probe study of irradiation-enhance.
[13.] Y.P. Wei, P.P. Liu, Y.M. Zhu, Z.Q. Wang, F.R. Wan, Q.Zhan, "Evaluation of irradiation hardening and microstructure evolution under the synergistic interaction of He an subsequent Fe ion irradiation in CLAM steel," J. Alloys and Compds. 676 (2016) 481-488.
[14.] Ohr SM, Wechsler MS, Chen CW, Hinkle NE, Radiation hardening and radiation-anneal hardening in body-centered cubic metals, pp 742**e**6 of Second International Conference on the Strength of Metals and Alloys, Pacific Grove, California, 30 August**e**4 September 1970 Vol. II Metals Park, Ohio American Society for Metals.
[15.] Christian Dethloff, Ermile Gaganidze, Jarir Aktaa, "Quantitative TEM analysis of precipitation and grain boundary segregation in neutron irradiated EUROFER97," J. Nucl. Mater. 454 (2014) 323-331.
[16.] O.J. Weiß, E. Gaganidze, J. Aktaa, "Quantitative characterization of microstructural defects in up to 32 dpa neutron irradiated Eurofer 97," J. Nucl. Mater. 426 (2012) 52–58.
[17.] L. Peng, Y. Dai, "Helium-induced hardening effect in ferritic/martensitic steels F82H and Optimax-A irradiated in a mixed spectrum of high energy protons and spallation neutrons," J. Nucl. Mater. 417 (2011) 996.
[18.] G. Bonny D. Terentyev, J. Elena, A. Zinovev, B. Minov, E.E. Zhurkin "Assessment of hardening due to dislocation loops in bcc iron: Overview and analysis of atomistic simulations for edge dislocations," J. Nucl. Mater. 473 (2016) 283-289.
[19.] C. Sobie, N. Bertin, L. Capolungo "Analysis of Obstacle Hardening Models Using Dislocation Dynamics: Application to Irradiation-Induced Defects," Metall Mater Trans A 46A (2015) 3761-3772.
[20.] Xunxiang Hu, Donghua Xu, Thak Sang Byun and Brian D Wirth "Modeling of irradiation hardening of iron after low-dose and low-temperature neutron irradiation," Modelling Simul. Mater. Sci. Eng. 22 (2014) 065002 (27pp).
[21.] Y.N. Osetsky and D.J. Bacon, "Atomic-Level Level Dislocation Dynamics in Irradiated Metals," Reference Module in Materials Science and Materials Engineering (2016) Elsevier.
[22.] L. Tan and J.T. Busby "Formulating the strength factor a for improved predictability of radiation hardening".
[23.] Z. Jiao, S. Taller, K. Field, G. Yeli, M.P. Moody, G.S. Was, J. Nucl. Mater. 504 (2018) 122**.**
[24.] T.S. Milot, "Establishing Correlations for Predicting Tensile Properties Based on the Shear Punch Test and Vickers Microhardness Data" (Mater Thesis). University of California, Santa Barbara, 2013.
[25.] T. Yamamoto, G. R. Odette, H. Kishimoto, J-W. Rensman and P. Miao, "On the effects of irradiation and helium on the yield stress changes and hardening and non-hardening embrittlement of ≈8Cr tempered martensitic steels: Compilation and analysis of existing data", *J. Nucl. Mater.* 356 (2006) 27-49.

1.4 FRACTURE TOUGHNESS CHARACTERIZATION OF EUROFER97 STEELS FOR EUROFUSION COLLABORATION—X. Chen, M.A. Sokolov, L.N. Clowers, Y. Yamamoto, R.L. Swain, E.T. Manneschmidt, K.D. Linton, Y. Katoh (Oak Ridge National Laboratory)

OBJECTIVE

The aim of this task is to characterize pre-irradiation fracture toughness of ten Eurofer97 steels for the EUROfusion project. The testing was performed on multi-notch bend type specimens (referred to as M4CVN specimens) based on the American Society for Testing and Materials (ASTM) E1921 Master Curve method.

SUMMARY

We have completed pre-irradiation fracture toughness testing of 10 Eurofer97 steels for the EUROfusion project. The Master Curve transition temperatures (T_{0q}) have been calculated for these materials, which will serve as the baseline data to determine the extent of irradiation embrittlement after irradiating the same materials in High Flux Isotope Reactor (HFIR).

PROGRESS AND STATUS

Introduction

Eurofer97 is one of leading candidates of reduced activation ferritic martensitic (RAFM) steels for first wall structural materials of early demonstration fusion power plants. During fusion plant operation, high neutron irradiation damage on first wall materials can cause irradiation embrittlement and reduce the fracture toughness of RAFM steels. Therefore, in the EUROfusion project, the irradiation effects on the fracture toughness of Eurofer97 is one of the core required properties. In this study, we characterized the pre-irradiation fracture toughness of ten Eurofer97 steels for the EUROfusion project. The Master Curve transition temperatures (T_{0q}) have been calculated for these materials, which will serve as the baseline data to determine the extent of irradiation embrittlement after irradiating the same materials in HFIR.

Experimental Procedure

The test matrix, summarized in Table 1, includes ten variants of Eurofer97 materials with one material, Group E, tested for two different heat treatment conditions.

Table 1. Eurofer97 fracture toughness test matrix

Materials	Heat treatment condition	Specimen orientation
Group H	As received	L-T
Group I	As received	L-T
Group J	As received	L-T
Group K	As received	L-T
Group L	As received	L-T
Group M	As received	L-T
Group N	As received	L-T
Group O	As received	L-T
Group P	As received	L-T
Group E	As received	L-S
	1. Homogenization at 1050°C/30min/air cool 2. Normalization at 980°C/30min/air cool 3. Tempering at 760°C/90min/air cool	L-S

Figure 1 shows the M4CVN specimen with dimensions 45 mm (length) x 3.3 mm (width) x 1.65 mm (thickness) to characterize the fracture toughness of Eurofer97 steel based on the ASTM E1921 Master Curve method [1].

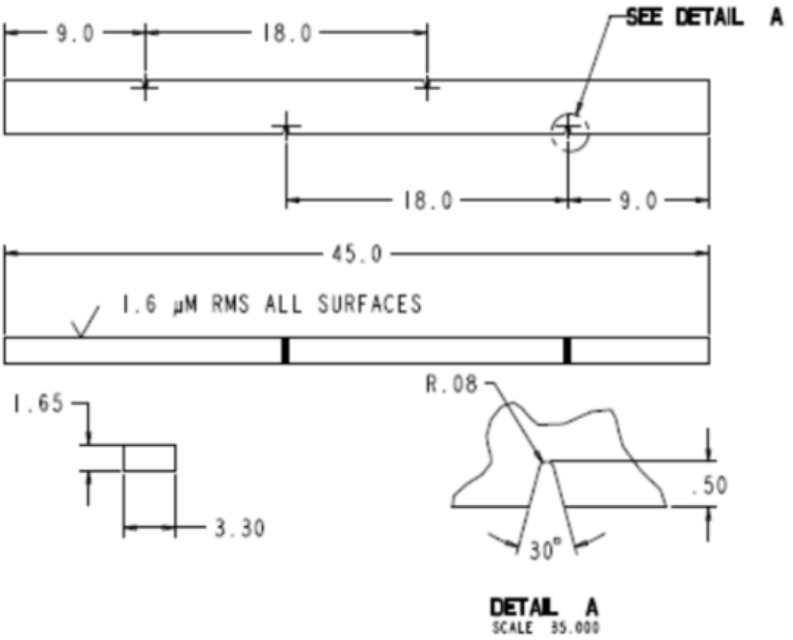

Figure 1. M4CVN specimen drawing. Units in millimeters.

The prerequisite of transition fracture toughness testing is having a sharp starting crack in the specimen which is realized by high frequency fatigue precracking in this study. We performed fatigue precracking on M4CVN specimens using a three-point bend type test fixture mounted on a 44.5 kN capacity servo-hydraulic frame as shown in Figure 2. The span to width ratio of the specimen was kept constant at four. During the fatigue precracking process, the load-line compliance at the machined notch of the specimen was measured by a deflection gauge which yields the real-time crack length using the following equation from Ref. [2]:

$$a/W = 1.0005 - 4.1527U + 9.7477U^2 - 214.2U^3 + 1604.3U^4 - 4633.4U^5$$
$$U = 1/\{[dE(BB_n)^{1/2}/P]^{1/2} + 1\} \quad (1)$$

where:
a = crack length,
d/P = measured load-line compliance,
E = material Young's modulus,
B_n = specimen net thickness (equals B for non-side grooved specimen),
B = specimen thickness.

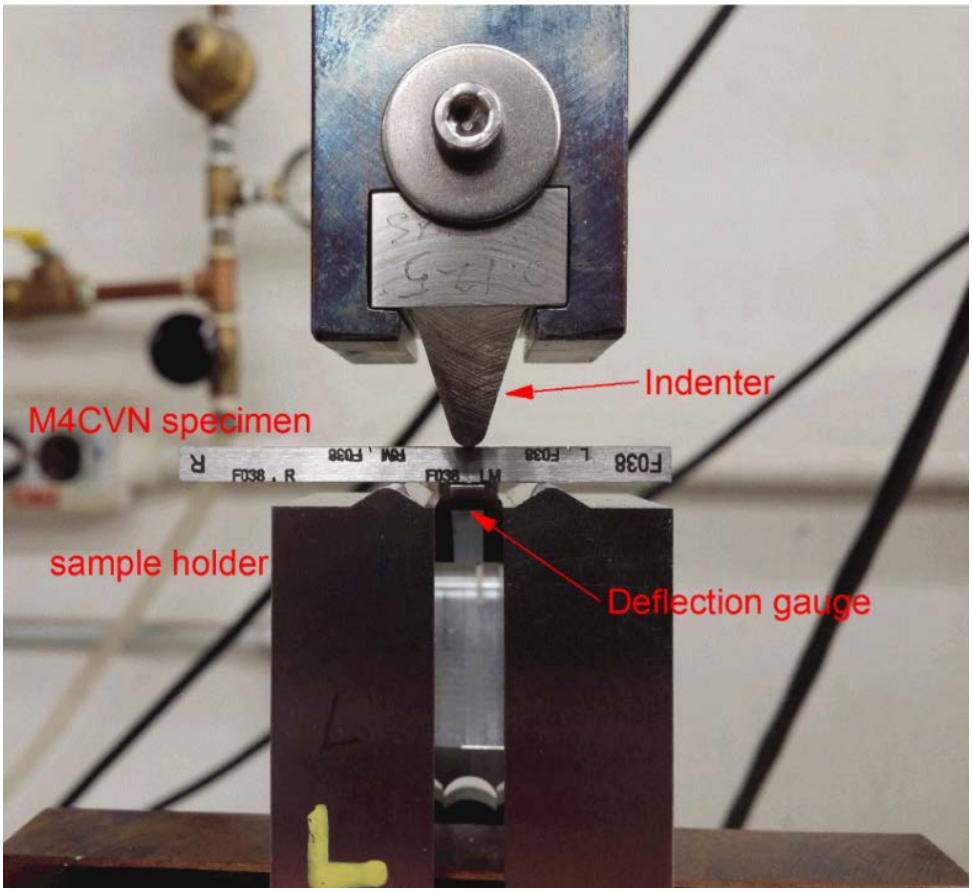

Figure 2. Fatigue precracking test fixture for a M4CVN specimen.

We applied the fatigue precracking procedure in accordance with the ASTM E1921 Standard. The standard sets limitations on both the maximum fatigue force (P_m) as well as the allowable maximum stress intensity factor (K_{max}) during the fatigue precracking process. P_m for the M4CVN specimen used in this study is defined per ASTM E1921:

$$P_m = \frac{0.5 B b_0^{\,2} \sigma_Y}{S} \qquad (2)$$

where:
B = specimen thickness,
b_0 = length for the initial uncracked ligament,
σ_Y = average of material yield and tensile strengths,
S = span distance.

After substituting the specimen dimensions and typical Eurofer97 yield strength (560 MPa) and tensile strength (670 MPa) into Equation (2), P_m for the M4CVN specimen is approximately 302.5 N (68 lbs). During fatigue precracking, we applied a constant stress intensity in the range of 11.3-12.3 MPa$\sqrt{m}$ which was well below the allowable K_{max} per ASTM E1921. In addition, the maximum fatigue force was also less than P_m. The fatigue precracking frequency was 45-50 Hz and the minimum to maximum fatigue force ratio, R-ratio, was kept constant at 0.1. In general, it took approximately 200-400 thousand cycles for completing fatigue precracking of one notch to a crack size to width (a/W) ratio of 0.44-0.5.

The test frame used for fracture toughness testing was a 222.4 kN capacity servo-hydraulic frame with a calibrated 4.45 kN capacity load cell. Figure 3 illustrates the general layout of the experimental setup. We used liquid nitrogen to control testing temperatures which were measured directly from type-T thermocouple wires spot welded to specimens. The environment chamber enclosed specimens and the test setup was used to maintain a relatively stable temperature during testing. As shown in Figure 4, the M4CVN specimen test setup consists of a specimen indenter and a specimen fixture. The deflection gauge attached to the specimen fixture was used to measure the load-line displacement of the specimen. The push bar can slide left and right and is used to push the specimen against the positioning block such that the specimen notch is aligned with the specimen indenter and the deflection gauge.

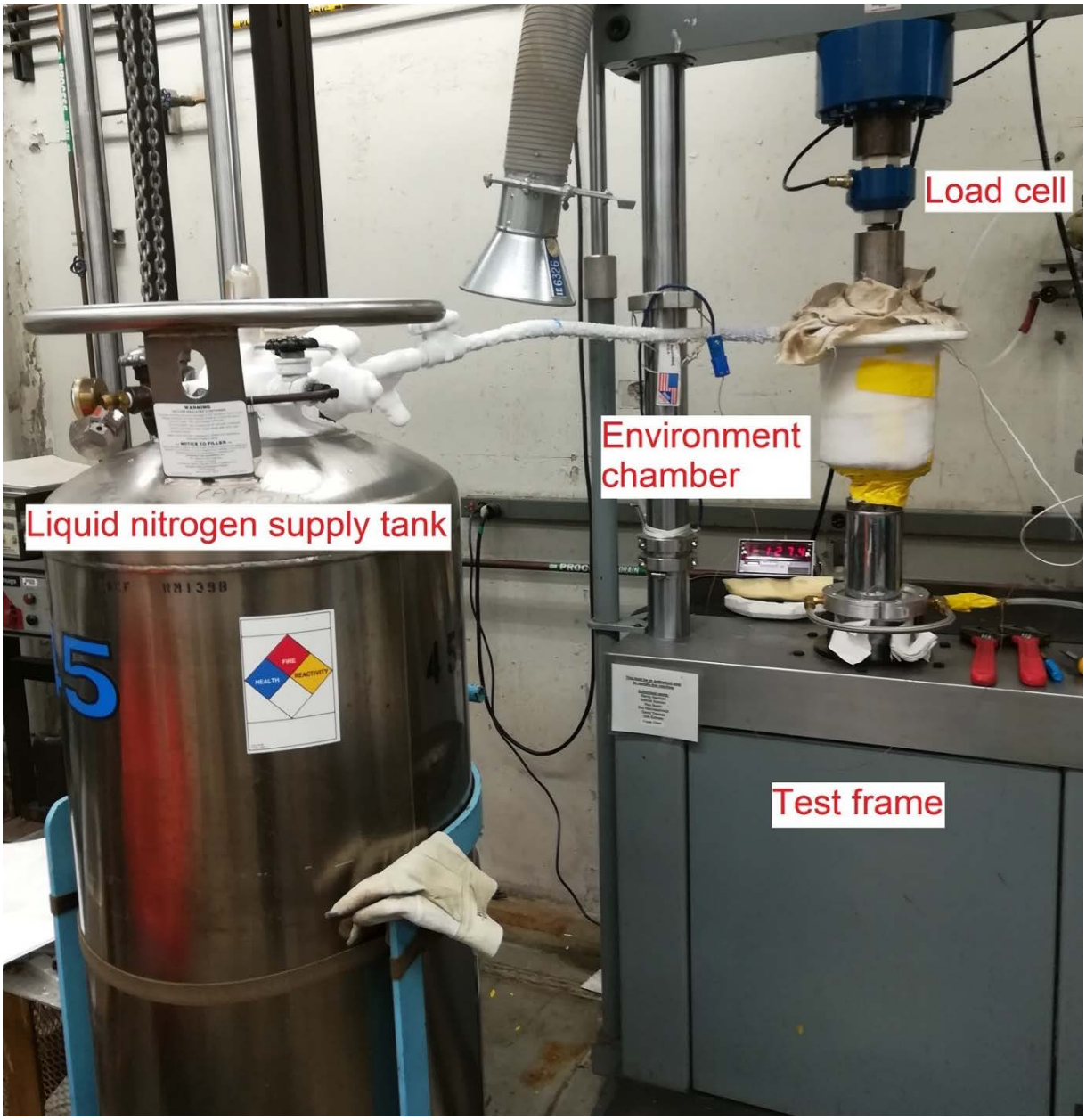

Figure 3. General layout of the fracture toughness test setup.

(a)

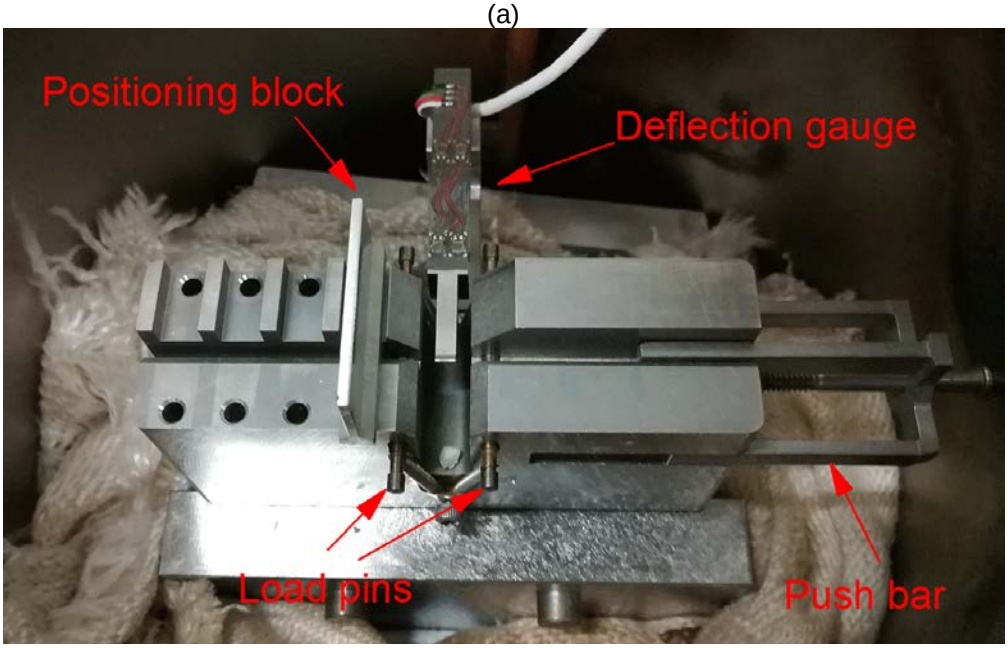

(b)

Figure 4. M4CVN specimen test setup: specimen indenter in (a) and specimen fixture in (b).

We performed fracture toughness testing according to the ASTM E1921 Master Curve method. The test temperatures were selected by balancing between obtaining as high fracture toughness results as possible and still within the fracture toughness capacity limit $K_{Jclimit}$ given in Equation (3):

$$K_{Jc\lim it} = \sqrt{\frac{Eb_o\sigma_{YS}}{30(1-\nu^2)}} \quad (3)$$

where:
E = material Young's modulus at the test temperature,

b_0 = length for the initial uncracked ligament,
σ_{YS} = material yield strength at the test temperature,
v = Poisson's ratio.

Each specimen notch was tested until cleavage and then the crack length was measured from the fracture surface. The elastic-plastic equivalent stress intensity factor, K_{Jc}, was derived from the J-integral at the onset of cleavage fracture and size-adjusted to 1T value based on the statistical weakest-link theory:

$$K_{Jc(1T)} = 20 + [K_{JC(o)} - 20](\frac{B_0}{B_{1T}})^{1/4} \quad (4)$$

where:
$K_{Jc(1T)}$ = K_{Jc} for a specimen thickness of one inch (B_{1T}=25.4 mm),
$K_{Jc(o)}$ = K_{Jc} for a specimen thickness of B_o (B_o=1.641 mm for M4CVN specimens).

We then calculated the Master Curve provisional reference temperature T_{oQ} using multi-temperature analysis method in Equation (5) and K_{Jc} data were censored against both the fracture toughness capacity limit $K_{Jclimit}$ and the slow stable crack growth limit $K_{Jc\Delta a}$.

$$\sum_{i=1}^{N} \delta_i \frac{\exp[0.019(T_i - T_{oQ})]}{11.0 + 76.7\exp[0.019(T_i - T_{oQ})]} - \sum_{i=1}^{N} \frac{(K_{Jc(i)} - 20)^4 \exp[0.019(T_i - T_{oQ})]}{\{11.0 + 76.7\exp[0.019(T_i - T_{oQ})]\}^5} = 0 \quad (5)$$

where:
N = number of specimens tested,
T_i = test temperature corresponding to $K_{Jc(i)}$,
$K_{Jc(i)}$ = either a valid K_{Jc} datum or a datum replaced with a censoring value,
δ_i = 1.0 if the datum is valid or zero if the datum is a censored value,
T_{oQ} = Master Curve provisional reference temperature solved by iteration.

Results

The fracture toughness results of ten variants of Eurofer97 materials are summarized in Tables 2 to 12. Figures 5 to 15 show the test data along with the derived Maser Curve. The equation for the Master Curve is:

$$K_{Jc(med)} = 30 + 70\exp[0.019(T - T_{oQ})] \quad (6)$$

where:
$K_{Jc(med)}$ = median fracture toughness for a multi-temperature data set from 1T size specimen,
T = test temperature,
T_{oQ} = Master Curve provisional reference temperature.

The tolerance bounds were calculated using the equation below:

$$K_{Jc(0.xx)} = 20 + [\ln(\frac{1}{1-0.xx})]^{1/4}\{11 + 77\exp[0.019(T - T_{oQ})]\} \quad (7)$$

where:
0.xx = selected cumulative probability level, e.g., for the 2% tolerance bound, 0.xx=0.02.

Table 2. Fracture toughness of Eurofer97 Group H in the as-received condition

Specimen ID	Test temperature (°C)	K_{Jc} (MPa√m)	1T-K_{Jc} (MPa√m)	Censored (Y/N)	Censored 1T value (MPa√m)	T_{oQ} (°C)
H006L	-165	40.5	30.3	N	NA	-89
H006LM	-154	204.8	113.2	Y	56.6	
H006RM	-165	63.1	41.7	N	NA	
H006R	-165	71.8	46.1	N	NA	
H002L	-159	68.0	44.2	N	NA	
H002RM	-154	179.7	100.5	Y	56.6	
H002R	-158	51.1	35.7	N	NA	
H003L	-154	89.9	55.2	N	NA	
H003LM	-154	33.0	26.6	N	NA	
H003RM	-154	64.2	42.3	N	NA	
H003R	-152	89.4	55.0	N	NA	
H004L	-154	92.6	56.6	N	NA	
H004LM	-155	53.2	36.7	N	NA	
H004RM	-155	237.5	129.7	Y	56.6	
H004R	-148	301.3	161.8	Y	56.6	

Table 3. Fracture toughness of Eurofer97 Group I in the as-received condition

Specimen ID	Test temperature (°C)	K_{Jc} (MPa√m)	1T-K_{Jc} (MPa√m)	Censored (Y/N)	Censored 1T value (MPa√m)	T_{oQ} (°C)
I006L	-165	54.7	37.5	N	NA	-78
I006LM	-165	33.9	27.0	N	NA	
I006RM	-165	39.5	29.8	N	NA	
I006R	-157	52.4	36.3	N	NA	
I005L	-124	280.5	151.3	Y	56.5	
I005LM	-126	292.5	157.4	Y	56.8	
I005RM	-126	76.0	48.2	N	NA	
I002L	-146	144.8	82.9	Y	58.8	
I002LM	-146	114.5	67.6	Y	58.1	
I002RM	-146	36.4	28.3	N	NA	
I002R	-146	93.8	57.2	N	NA	
I003L	-148	15.0	17.5	N	NA	
I003LM	-151	55.1	37.7	N	NA	
I003RM	-152	50.3	35.3	N	NA	
I003R	-146	254.9	138.4	Y	57.2	

Table 4. Fracture toughness of Eurofer97 Group J in the as-received condition

Specimen ID	Test temperature (°C)	K_{Jc} (MPa√m)	1T-K_{Jc} (MPa√m)	Censored (Y/N)	Censored 1T value (MPa√m)	T_{oQ} (°C)
J001L	-168	59.0	39.7	N	NA	-99
J001LM	-165	55.8	38.0	N	NA	
J001RM	-165	59.0	39.7	N	NA	
J001R	-165	65.2	42.8	N	NA	
J002L	-161	56.6	38.5	N	NA	
J002LM	-159	86.4	53.5	N	NA	
J002RM	-159	45.7	33.0	N	NA	
J002R	-156	244.2	133.0	Y	53.5	
J005L	-149	201.3	111.4	Y	53.5	
J005RM	-136	231.2	126.5	Y	53.5	
J005R	-130	233.2	127.5	Y	53.5	
J003L	-155	166.1	93.7	Y	53.5	
J003LM	-156	162.6	91.9	Y	53.5	
J003RM	-151	254.4	138.2	Y	53.5	
J003R	-154	81.0	50.8	N	NA	
J006L	-154	120.0	70.4	Y	60.1	
J006LM	-153	102.4	61.5	Y	60.5	
J006RM	-153	71.3	45.9	N	NA	
J006R	-154	179.3	100.3	Y	53.5	

Table 5. Fracture toughness of Eurofer97 Group K in the as-received condition

Specimen ID	Test temperature (°C)	K_{Jc} (MPa√m)	1T-K_{Jc} (MPa√m)	Censored (Y/N)	Censored 1T value (MPa√m)	T_{oQ} (°C)
K007L*	-147	23.2	21.6	N	NA	-12
K007LM*	-161	14.1	17.0	N	NA	
K007RM*	-165	23.1	21.6	N	NA	
K002L	-97	31.2	25.6	N	NA	
K002LM	-96	83.8	52.2	N	NA	
K002RM	-109	34.3	27.2	N	NA	
K005L	-84	42.3	31.2	N	NA	
K005LM	-84	106.5	63.6	Y	63.4	
K005RM	-84	44.4	32.3	N	NA	
K005R	-89	289.4	155.8	Y	52.2	
K006L	-90	61.5	40.9	N	NA	
K006LM	-90	56.3	38.3	N	NA	
K006RM	-90	56.0	38.1	N	NA	
K006R	-90	64.5	42.4	N	NA	

*Fracture toughness results for information only, not used for Master Curve calculation

Table 6. Fracture toughness of Eurofer97 Group L in the as-received condition

Specimen ID	Test temperature (°C)	K_{Jc} (MPa√m)	1T-K_{Jc} (MPa√m)	Censored (Y/N)	Censored 1T value (MPa√m)	T_{oQ} (°C)
L006L*	-137	21.8	20.9	N	NA	-53
L006LM*	-149	21.9	20.9	N	NA	
L006RM*	-153	25.2	22.6	N	NA	
L006R*	-171	16.8	18.4	N	NA	
L007L	-96	114.0	67.4	Y	67.3	
L007LM	-94	93.3	57.0	N	NA	
L007RM	-94	73.3	46.9	N	NA	
L007R	-95	89.7	55.1	N	NA	
L002L	-90	149.7	85.4	Y	65.7	
L002LM	-90	110.6	65.7	N	NA	
L002RM	-91	109.6	65.2	N	NA	
L002R	-90	144.8	82.9	Y	67.2	
L004L	-89	145.7	83.4	Y	64.6	
L004LM	-92	50.1	35.1	N	NA	
L004RM	-91	68.9	44.6	N	NA	
L004R	-91	137.3	79.1	Y	67.3	

*Fracture toughness results for information only, not used for Master Curve calculation

Table 7. Fracture toughness of Eurofer97 Group M in the as-received condition

Specimen ID	Test temperature (°C)	K_{Jc} (MPa√m)	1T-K_{Jc} (MPa√m)	Censored (Y/N)	Censored 1T value (MPa√m)	T_{oQ} (°C)
M003L	-165	25.2	22.6	N	NA	-75
M003LM	-165	83.8	52.2	N	NA	
M003RM	-165	52.9	36.6	N	NA	
M003R	-165	39.7	29.9	N	NA	
M002L	-150	220.8	121.2	Y	53.7	
M002LM	-150	58.7	39.5	N	NA	
M002R	-142	194.6	108.0	Y	53.7	
M004L	-154	80.5	50.5	N	NA	
M004LM	-154	40.3	30.2	N	NA	
M004RM	-154	86.9	53.7	N	NA	
M004R	-154	37.0	28.6	N	NA	
M007L	-142	232.1	126.9	Y	53.7	
M007LM	-142	78.0	49.2	N	NA	
M007RM	-148	35.8	28.0	N	NA	
M007R	-148	67.9	44.1	N	NA	
M003L	-165	25.2	22.6	N	NA	

Table 8. Fracture toughness of Eurofer97 Group N in the as-received condition

Specimen ID	Test temperature (°C)	K_{Jc} (MPa√m)	1T-K_{Jc} (MPa√m)	Censored (Y/N)	Censored 1T value (MPa√m)	T_{oQ} (°C)
N003L	-170	45.4	32.8	N	NA	-92
N003LM	-170	32.9	26.5	N	NA	
N003RM	-165	108.3	64.5	Y	61.1	
N003R	-171	35.0	27.6	N	NA	
N006L	-152	43.7	31.9	N	NA	
N006LM	-151	67.7	44.0	N	NA	
N006RM	-154	117.0	68.9	Y	60.5	
N006R	-151	80.4	50.5	N	NA	
N002L	-149	168.7	95.0	Y	58.6	
N002LM	-150	96.6	58.6	N	NA	
N002RM	-151	64.7	42.5	N	NA	
N002R	-151	54.2	37.2	N	NA	
N005L	-152	87.7	54.1	N	NA	
N005LM	-153	85.8	53.2	N	NA	
N005RM	-153	226.0	123.9	Y	58.6	
N005R	-151	65.9	43.1	N	NA	

Table 9. Fracture toughness of Eurofer97 Group O in the as-received condition

Specimen ID	Test temperature (°C)	K_{Jc} (MPa√m)	1T-K_{Jc} (MPa√m)	Censored (Y/N)	Censored 1T value (MPa√m)	T_{oQ} (°C)
O002L*	-167	25.0	22.5	N	NA	-79
O002LM*	-165	21.6	20.8	N	NA	
O002RM*	-165	37.2	28.7	N	NA	
O002R*	-169	32.8	26.5	N	NA	
O005L	-132	62.5	41.4	N	NA	
O005LM	-126	243.3	132.6	Y	61.9	
O005RM	-130	42.0	31.1	N	NA	
O003L	-129	104.9	62.8	Y	59.7	
O003LM	-129	169.3	95.3	Y	59.7	
O003RM	-129	70.2	45.3	N	NA	
O003R	-128	98.8	59.7	Y	59.5	
O004L	-132	98.7	59.7	N	NA	
O004LM	-130	35.6	27.9	N	NA	
O004RM	-131	46.2	33.2	N	NA	
O004R	-127	161.2	91.2	Y	60.5	

*Fracture toughness results for information only, not used for Master Curve calculation

Table 10. Fracture toughness of Eurofer97 Group P in the as-received condition

Specimen ID	Test temperature (°C)	K_{Jc} (MPa√m)	1T-K_{Jc} (MPa√m)	Censored (Y/N)	Censored 1T value (MPa√m)	T_{oQ} (°C)
P002L*	-165	34.7	27.4	N	NA	-87
P002LM*	-165	31.9	26.0	N	NA	
P002RM*	-165	39.1	29.6	N	NA	
P002R*	-165	34.5	27.3	N	NA	
P003L	-132	239.3	130.6	Y	53.2	
P003LM	-131	298.9	160.6	Y	53.2	
P003RM	-131	312.4	167.4	Y	53.2	
P003R	-131	66.4	43.4	N	NA	
P004L	-146	106.1	63.4	Y	58.7	
P004LM	-146	133.6	77.3	Y	58.6	
P004RM	-145	76.1	48.3	N	NA	
P004R	-147	69.9	45.2	N	NA	
P005L	-146	85.9	53.2	N	NA	
P005LM	-146	266.9	144.5	Y	53.2	
P005RM	-146	44.8	32.5	N	NA	
P005R	-146	74.4	47.4	N	NA	

*Fracture toughness results for information only, not used for Master Curve calculation

Table 11. Fracture toughness of Eurofer97 Group E in the as-received condition

Specimen ID	Test temperature (°C)	K_{Jc} (MPa√m)	1T-K_{Jc} (MPa√m)	Censored (Y/N)	Censored 1T value (MPa√m)	T_{oQ} (°C)
E032L*	-112	39.7	29.9	N	NA	-29
E032LM*	-112	52.5	36.4	N	NA	
E032RM*	-169	20.2	20.1	N	NA	
E032R*	-169	18.1	19.0	N	NA	
E035L*	-112	50.7	35.5	N	NA	
E035LM*	-112	33.1	26.6	N	NA	
E035RM*	-166	19.7	19.8	N	NA	
E035R*	-169	23.3	21.7	N	NA	
E031RM	-90	73.9	47.2	N	NA	
E031R	-90	82.4	51.5	N	NA	
E034L	-90	132.0	76.5	Y	53.5	
E034LM	-90	72.3	46.4	N	NA	
E034RM	-90	87.3	53.9	Y	52.8	
E034R	-90	71.1	45.8	N	NA	
E033L	-90	100.0	60.3	Y	53.2	
E033LM	-90	104.1	62.4	Y	52.8	
E033R	-90	90.77	55.7	Y	53.2	
E025L	-89	68.1	44.2	N	NA	
E025LM	-92	51.8	36.0	N	NA	
E025RM	-91	68.3	44.4	N	NA	
E025R	-90	102.1	61.4	Y	53.2	

*Fracture toughness results for information only, not used for Master Curve calculation

Table 12. Fracture toughness of Eurofer97 Group E in the heat-treated condition

Specimen ID	Test temperature (°C)	K_{Jc} (MPa√m)	1T-K_{Jc} (MPa√m)	Censored (Y/N)	Censored 1T value (MPa√m)	T_{oQ} (°C)
1L	-159	76.6	48.5	N	NA	
1LM	-159	90.8	55.7	N	NA	
1RM	-159	78.3	49.4	N	NA	
1R	-159	53.1	36.7	N	NA	
2L	-153	256.2	139.1	Y	55.7	
2LM	-156	63.1	41.7	N	NA	
2RM	-151	326.0	174.3	Y	55.7	
2R	-153	77.6	49.0	N	NA	-92
3L	-158	82.0	51.3	N	NA	
3LM	-157	108.0	64.4	Y	63.0	
3RM	-159	32.5	26.3	N	NA	
4L	-152	288.5	155.4	Y	55.7	
4LM	-152	86.1	53.3	N	NA	
4RM	-157	48.4	34.3	N	NA	
4R	-157	39.8	30.0	N	NA	

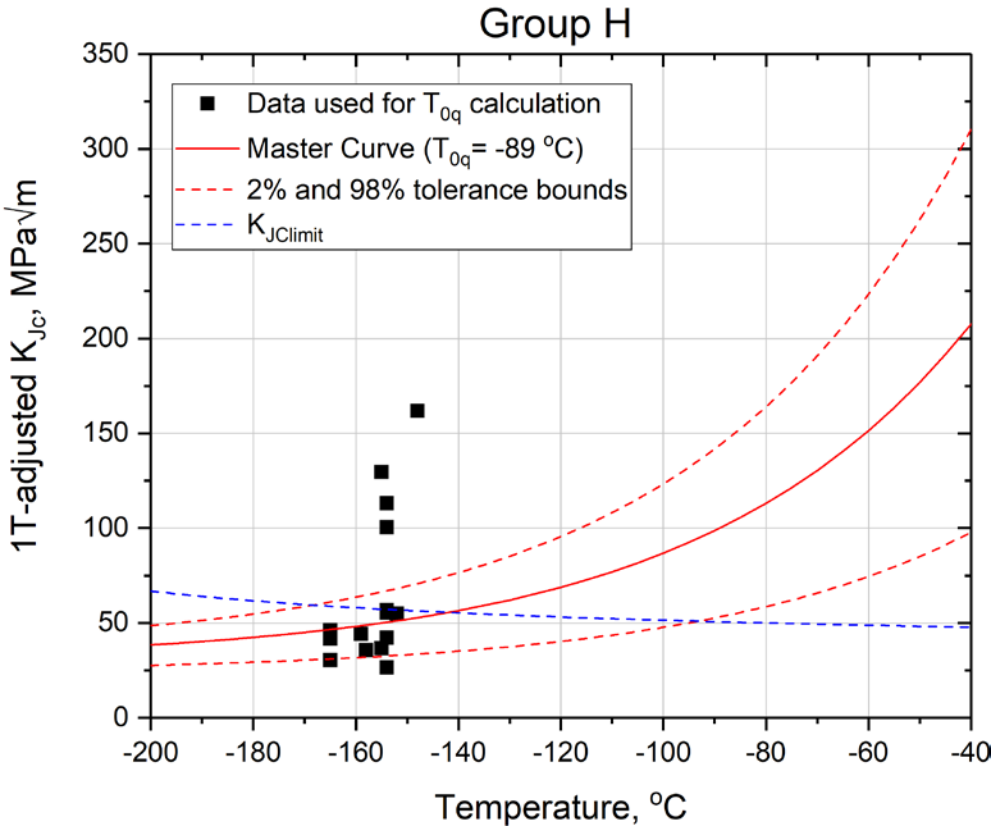

Figure 5. Master Curve results of Eurofer97 Group H in the as-received condition.

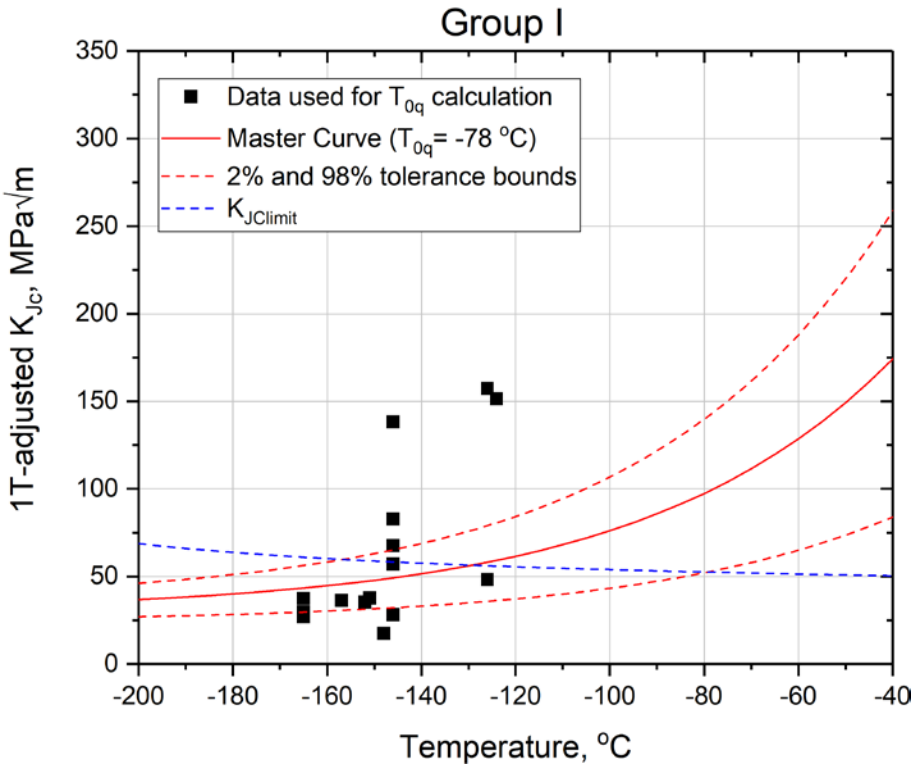

Figure 6. Master Curve results of Eurofer97 Group I in the as-received condition.

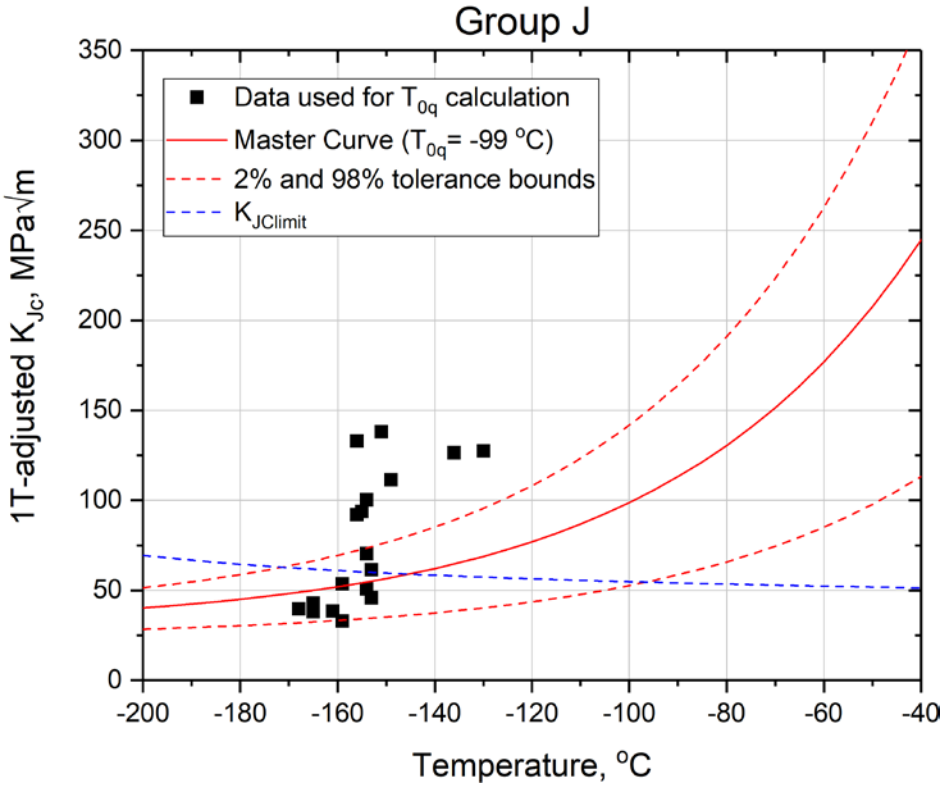

Figure 7. Master Curve results of Eurofer97 Group J in the as-received condition.

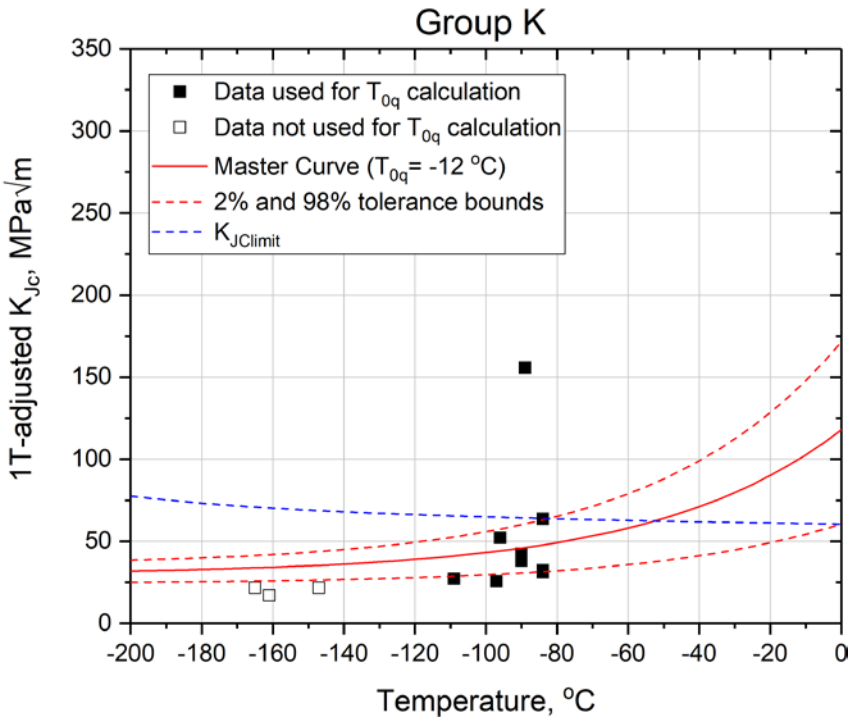

Figure 8. Master Curve results of Eurofer97 Group K in the as-received condition.

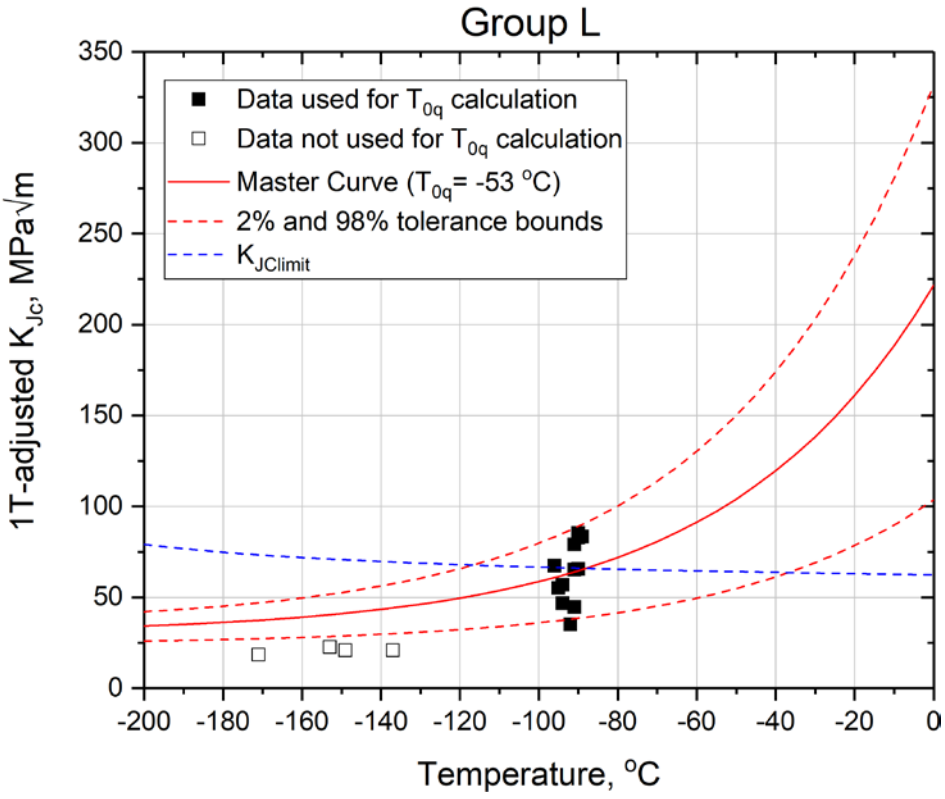

Figure 9. Master Curve results of Eurofer97 Group L in the as-received condition.

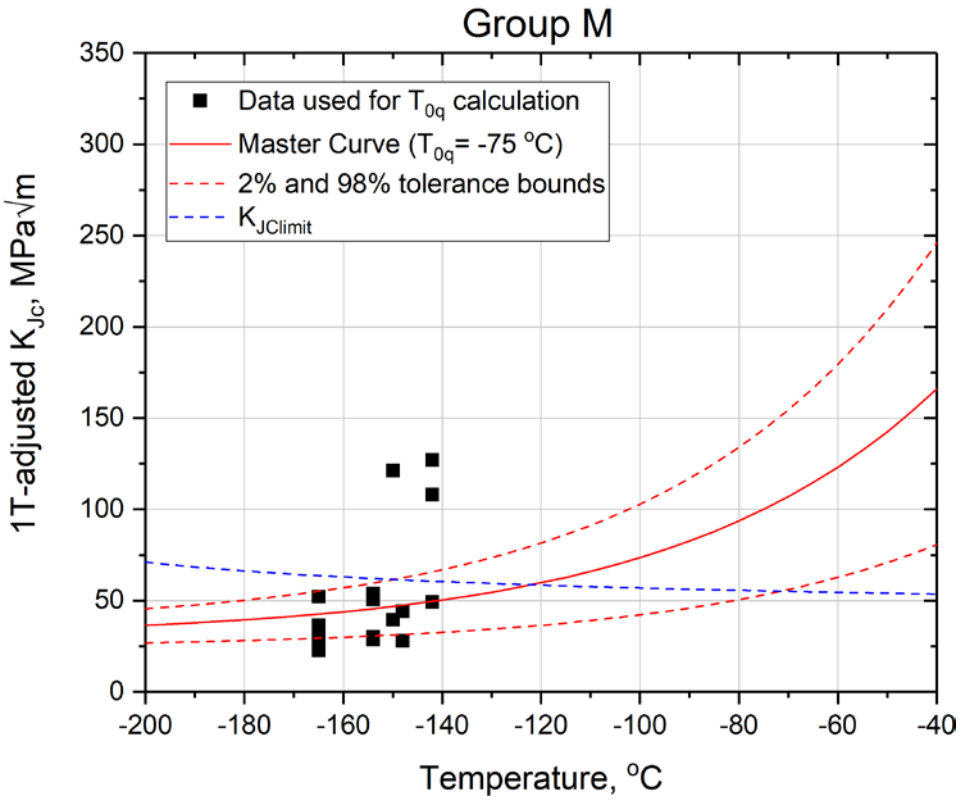

Figure 10. Master Curve results of Eurofer97 Group M in the as-received condition.

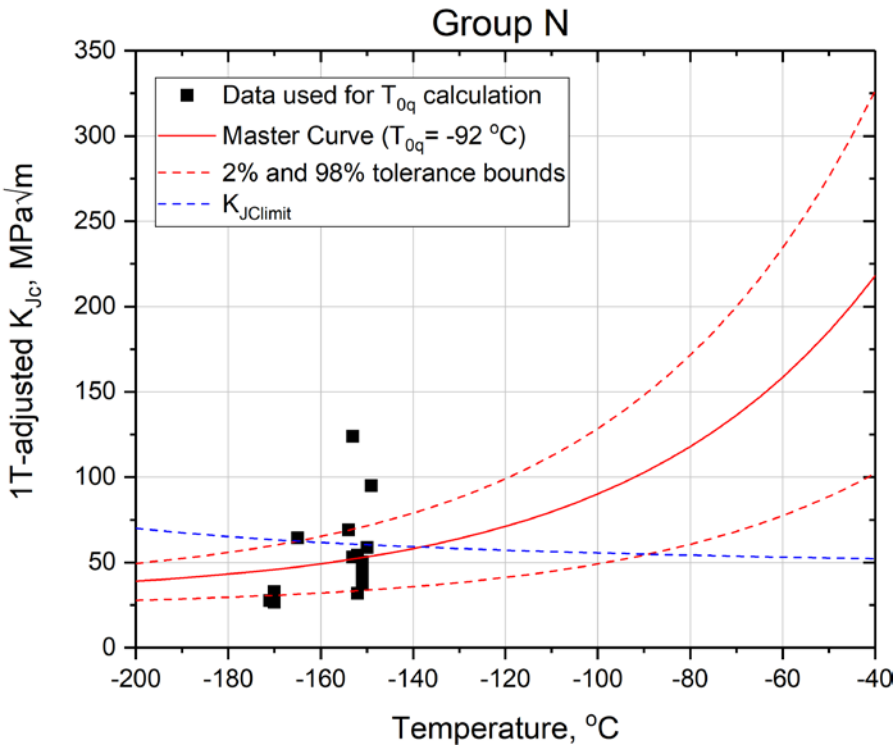

Figure 11. Master Curve results of Eurofer97 Group N in the as-received condition.

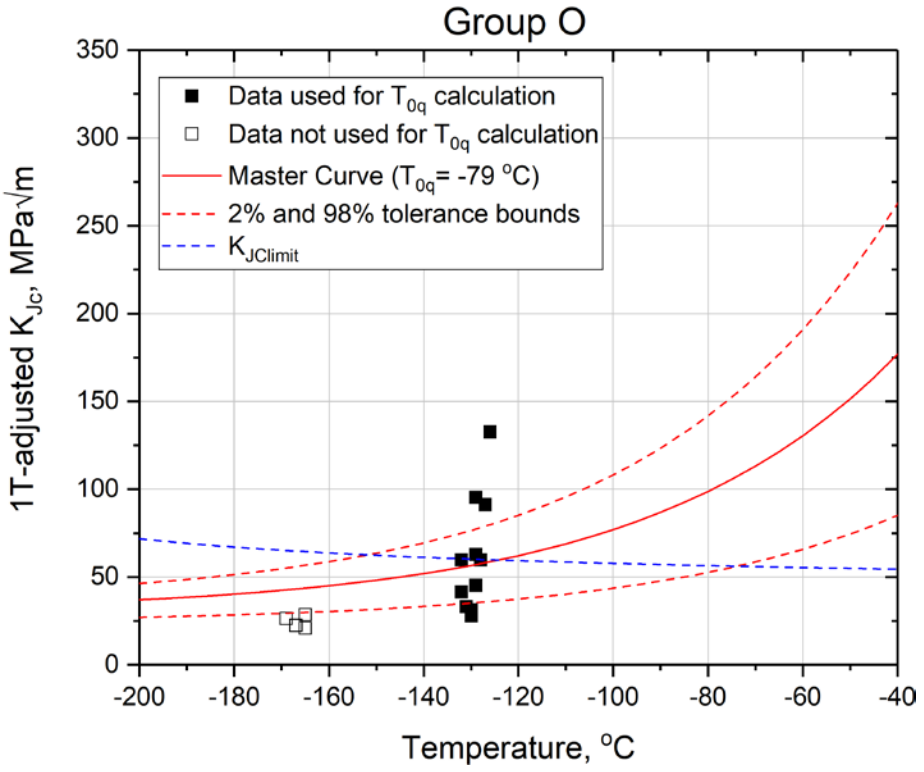

Figure 12. Master Curve results of Eurofer97 Group O in the as-received condition.

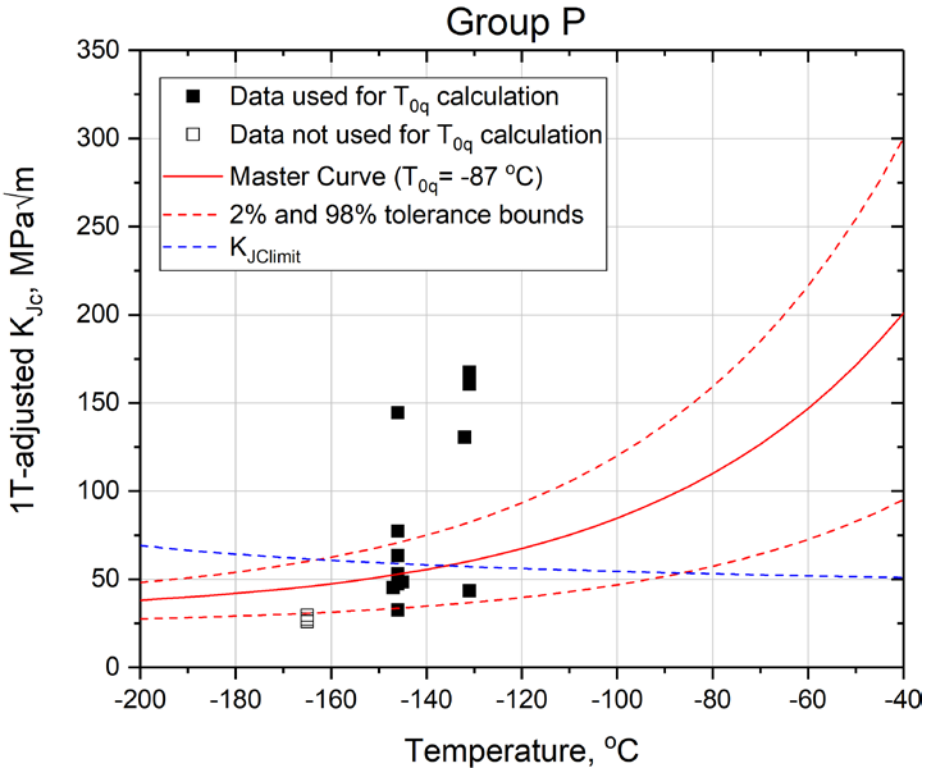

Figure 13. Master Curve results of Eurofer97 Group P in the as-received condition.

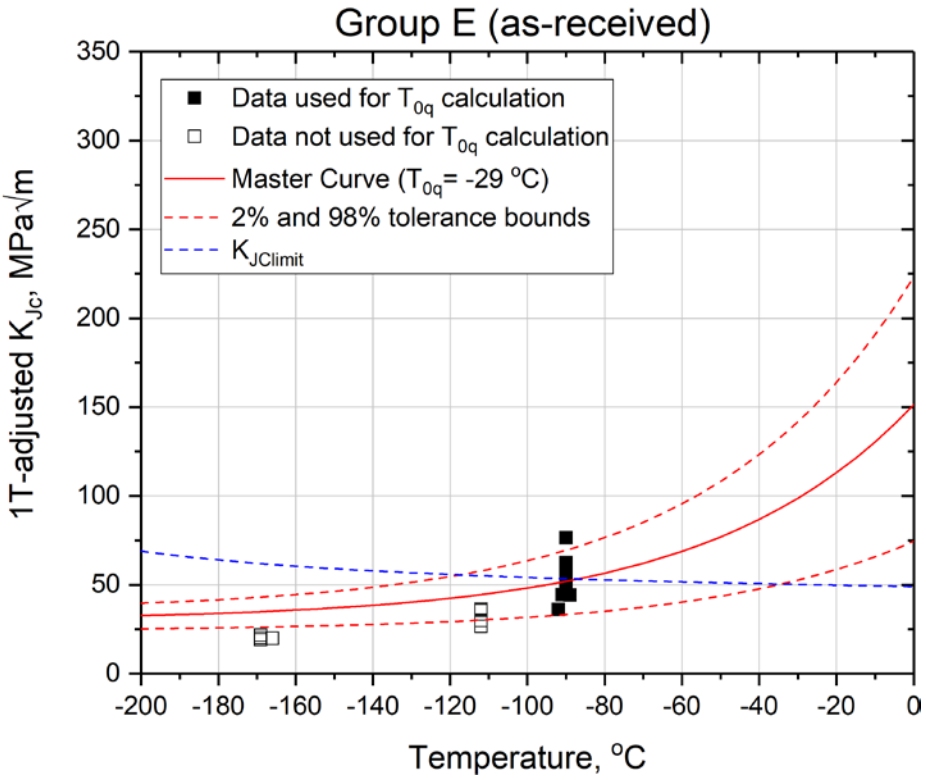

Figure 14. Master Curve results of Eurofer97 Group E in the as-received condition.

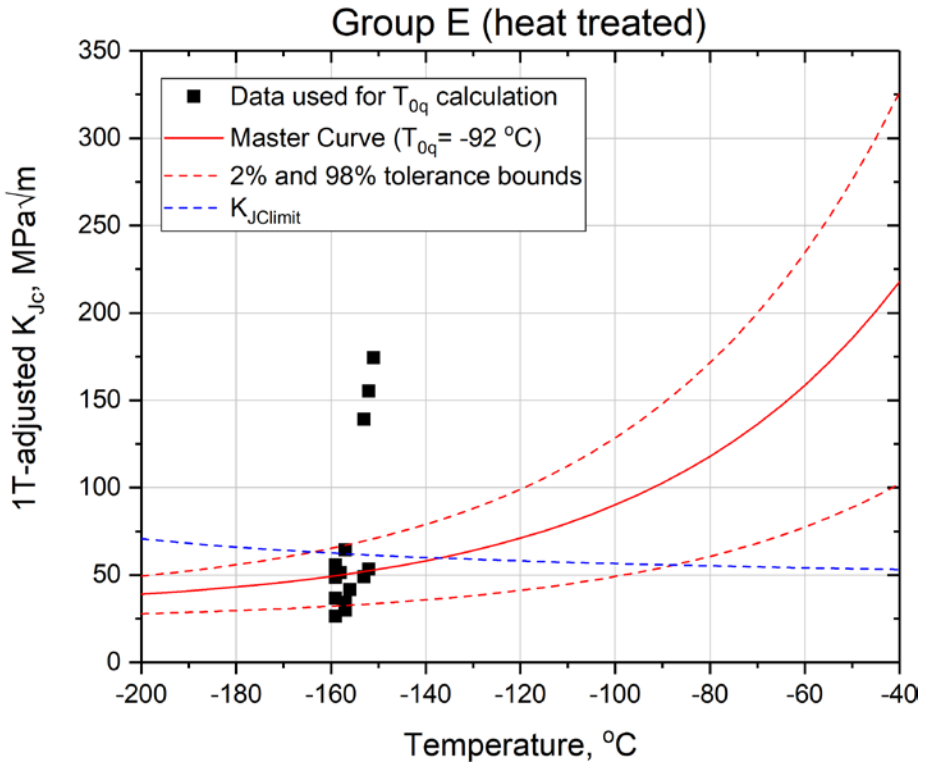

Figure 15. Master Curve results of Eurofer97 Group E in in the heat-treated condition.

References

[1] ASTM E1921-17a: Standard Test Method for Determination of Reference Temperature, T0, for Ferritic Steels in the Transition Range, ASTM International, West Conshohocken, PA, 2017.
[2] J. Underwood et al., ASTM STP 1114 (1991) p197.

1.5 WELD PROPERTY EVALUATION OF MODIFIED 3Cr-3WV(Ta) BAINITIC STEEL—Y. Yamamoto (Oak Ridge National Laboratory)

OBJECTIVE

This work aims to develop new bainitic steels, based on 3Cr-3WV(Ta) steels originally developed at Oak Ridge National Laboratory (ORNL). The goal is mechanical properties of both base metal and weldments superior to those of existing commercial bainitic steels or ferritic martensitic (FM) steels, together with no requirement for post-weld heat treatment (PWHT). The target applications are high temperature structural components in fusion reactors such as vacuum vessel, structural ring which supports the blanket modules, and magnet shields, to be used at or above the 400-500ºC range. Improvement of long-term creep properties by introducing additional fine, stable second-phase dispersions, as well as maintaining good weldability, is targeted via optimization of alloy composition and thermo-mechanical heat treatment.

SUMMARY

Property evaluation of newly proposed 3Cr-3WVTa base bainitic steel with high Mn + Si and low C (ID: MSLC2) with a design strategy for PWHT-free was completed. A gas tungsten arc weld (GTAW) was applied to both “as-normalized (N)” and “normalized-and-tempered (NT)” plates of the new steel with compositionally matched weld filler metal. The creep properties of the base metal and the cross-weld specimen were comparable to those of the original 3Cr-3WVTa steel, with the weld strengthening factor of ~ 0.8 at 550°C in the case of the NT sample. No significant difference in the cross-weld creep-rupture life was observed between the N and NT base metals. However, the creep rupture occurred at the weld metal (WM) for N and the heat affected zone (HAZ) for NT, which corresponded to unintentionally over-tempered regions, such as temper-beads inside WM and inter-critical HAZ, respectively. In addition, temper-embrittlement was also observed at the HAZ for N, indicating that the proposed MSLC2 alloy requires further modification to improve the stability of microstructure against tempering. New alloy compositions were proposed to potentially improve the microstructural stability, and the property evaluation was initiated.

PROGRESS AND STATUS

Introduction

Development of new bainitic steels was initiated under the Fusion Energy Materials Program in FY2014, as a modification of the original 3Cr-3WV(Ta) steels developed at ORNL [1, 2, 3]. The target applications include vacuum vessels or structural rings supporting the blanket modules in fusion reactor applications such as the conceptual United States (US) Fusion Neutron Sciences Facility (FNSF) [4]. The current alloy design strategy is to produce materials usable without PWHT-free to lower the capital cost of large volume components described above. Potential concern in the characteristics of the PWHT-free components would be the property inhomogeneity of the as-welded material across the weldment. Such inhomogeneity needs to be minimized to avoid any premature failure attributed to itself (e.g. stress concentration). To solve the potential issue, an alloy design was proposed which focused on decreasing the hardness in the normalized condition without losing the high “hardenability” to promote the carbide-free acicular bainite ferrite formation. Based on the design strategy, a steel with 2 wt.% Mn combined with 0.05% C (ID: MSLC2, shown in Table 1) was suggested, and the lab-scale heat of the steel prepared at ORNL successfully showed less hardness in the normalized condition compared to that of the original steel, whereas the hardness after tempering remained comparable to the original. The cross-weld hardness distribution of the steels also indicated a successful reduction of the hardness inhomogeneity across the weld, suggesting that the new design strategy would potentially be suitable for PWHT-free behavior.

A vacuum induction melted ingot (~30 kg) was commercially procured in early 2017, and then thermo-mechanically processed at ORNL to prepare a hot-rolled plate with 0.5-inch-thickness. As reported previously [5], creep-rupture properties of MSLC2 base metal, NT, at 550°C and 400-480 MPa exhibited similar creep properties to the original steel, suggesting that the high Mn addition successfully compensated

the potential creep degradation due to low carbon content. A GTAW was also applied to the NT plate with compositionally matched weld filler wire for evaluation of the cross-weld properties such as creep and Charpy impact toughness. The weld strength reduction factor (WSRF) of the MSLC2-NT plate was ~0.8 at 550°C in the as-welded condition, which was comparable to the low Cr steel weldments reported in American Society of Mechanical Engineers (ASME) B31.3 [6]. Although the WSRF was decent, the cross-weld creep strength of the MSLC2 steel at 550°C still exceeded Mod. 9Cr-1Mo steel by a factor of ~1.5, which promises the advantage of the newly proposed steel. However, it was also found that the new steel suffered from a significant drop of room-temperature toughness after tempering, which is so-called "temper-embrittlement". This gives potential issues of unexpected material failure during installation in the field or increased crack susceptibility during long-term service.

In this report, the updated creep test results of the original 3Cr-3WVTa steel and MSLC2, together with Charpy impact test results, are summarized, and the potential issues in the current alloy design are discussed. In the latter part of the report, a new alloy design strategy is proposed and the evaluation efforts on newly proposed alloys is introduced.

Table 1. Nominal compositions of original 3Cr-3WVTa steel and MSLC2

Name	Composition, wt.% (balanced Fe)							Remarks
	C	Mn	Si	Cr	V	W	Ta	
Original 3Cr-3WVTa	0.10	0.40	0.16	3.0	0.2	3	0.1	Heat #2751
MSLC2	0.05	2.00	0.5	3.0	0.2	3	0.1	Low C + 2Mn

Results

Figure 1 summarizes the creep-rupture test results of original 3Cr-3WVTa and MSLC2 at 550°C. The base metal creep data of original 3Cr-3WVTa steel was reported by Klueh [2], and the others were produced in the current effort. The base metal creep performance of MSLC2 was comparable to original 3Cr-3WVTa in the current test condition range, for both N and NT specimens. The cross-weld creep properties of as-welded specimens did not show significant differences among three different specimens; original 3Cr-3WVTa-NT, MSLC2-N, and MSLC2-NT. After applying PWHT, the creep strength decreased drastically for both original 3Cr-3WVTa-NT and MSLC2-NT (not shown in the plotted range) with ~40% strength reduction compared to the base metal, although the cross-weld creep strength were superior to that of the welded Mod. 9Cr-1Mo steels at the temperature.

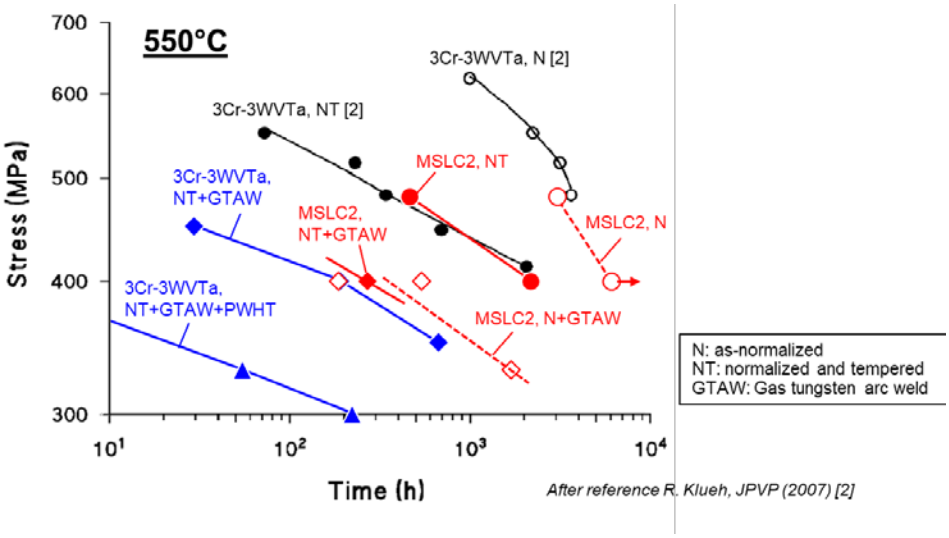

Figure 1. Creep-rupture test results at 550°C of the original 3Cr-3WVTa steel (black symbols: base metal [2]; blue symbols: cross-weld) and the MSLC2 (open red symbols: as-normalized, base metal and cross-weld; filled red symbols: normalized-and-tempered, base metal and cross-weld).

Despite the comparable creep-rupture strengths between the as-welded MSLC2 steel weldments with and without tempering, the rupture mode was quite different, as shown in Figure 2. The NT sample ruptured at the HAZ as previously reported, whereas the N sample broke inside the weld metal. The HAZ region in the NT sample was over-tempered during the welding process, which weakened the material along the HAZ and led to the premature failure. On the other hand, the weld metal in the N sample exhibited unexpectedly over-tempered weld beads (so-called “temper beads”) which formed due to the repeated weld deposition process and created the weakened region inside the weld metal. Both results clearly indicated that an improvement of bainitic microstructure stability against “over” tempering is necessary to improve the cross-weld creep properties.

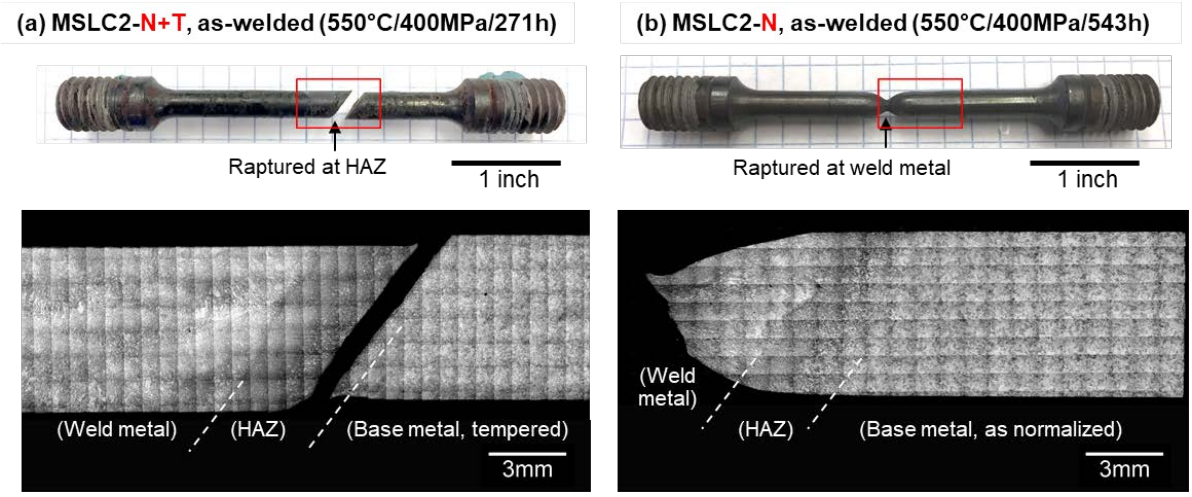

Figure 2. Cross-weld creep tested specimens of as-welded MSLC2 steel and cross-sectional optical micrographs near fracture surface; (a) NT base metal and (b) N base metal.

Charpy impact testing revealed a disadvantage of applying tempering or PWHT in the MSLC2 steel due to temper embrittlement. Figure 3 shows a machining plan of Charpy impact specimens to evaluate the impact toughness of the base metal, weld metal, and HAZ. As summarized in Table 2, the room-temperature room

toughness of MSLC2 base/weld metals decreased after applying tempering/PWHT, respectively, as reported previously. It was also found that the HAZ also showed very low absorbed energy, indicating that the susceptibility of temper embrittlement of the newly proposed steel is relatively high. Based on the results of creep and impact toughness, it was concluded that newly proposed MSLC2 steel would require further modification to meet the design strategy of "PWHT-free" materials.

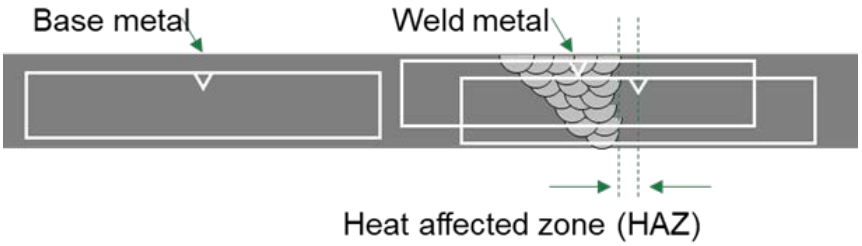

Figure 3. Machining plan of Charpy impact test specimens.

Table 2. Summary of Charpy impact test results at room temperature

Material	Location	Absorbed energy at 23°C, J	
		As-normalized (or As-welded)	N+T (or PWHT)
MSLC2	Base metal	69.5	4.4
	Weld metal	276.6	59.7
	HAZ	20.3	-
Original 3Cr-3WVTa	Base metal	-	177.3
Original 3Cr-3WV*	Weld metal	39.3	249.5
			*Ref: ORNL/TM-2005/82 [3]

Based on the findings described above, a new alloy design has been proposed to satisfy the following targets; (1) high Mn + low C to provide less hardness in the N (as-welded) condition without losing high hardenability, and (2) less Si to avoid the temper embrittlement [7]. To expect the microstructure stability at the HAZ, the addition of 100 wppm B is also attempted this time [8]. In addition to these considerations, the target has also been changed to Ta-free steel (3Cr-3WV) because of a concern about the producibility. The control of Ta content in the steel would not be easy in the large-scale production, since the melt process may need to be conducted in air (or only cover gas) and prohibit the precise control of Ta content in the steel due to high reactivity of Ta with oxygen in the environment. The nominal compositions of the new steels are summarized in Table 3. Lab-scale heats were prepared by arc-melting and drop casting to make 25 x 25 x 100 mm size ingots. They were homogenized at 1200°C in Ar gas for 2 h, followed air-cooling to room temperature (RT). They were forged and normalized at 1100°C, followed by air cooling to RT, to prepare N plates with ~7 mm thickness. A section of the plates was tempered at 700°C for 1h, followed by air-cooling to RT.

Table 3. Nominal composition of original 3Cr-3WV steel and newly proposed steels

Name	Composition, wt.% (balanced Fe)								Remarks
	C	Mn	Si	Cr	V	W	Ta	B	
Original 3Cr-3WV	0.08	0.4	0.16	3	0.2	3	-		Ref. 2
MLC02	0.05	2	0.16	3	0.2	3	-		high Mn, low C
MLC03	0.08	2	0.16	3	0.2	3	-		high Mn
MLC03B	0.08	2	0.16	3	0.2	3	-	0.01	high Mn + B addition

The Vickers hardness of the new steels are summarized and compared with the reference materials in Table 4. The new alloys showed relatively low hardness in the as-normalized conditions and relatively high hardness in the tempered conditions, compared to original 3Cr-3WV steel. Charpy impact test of the new steels was also conducted by using half-size Charpy test specimens (Figure 4). The absorbed energy at room temperature of the steels were compared with the Ta containing steels, as summarized in Figure 5. The impact toughness of the new steels increased after tempering, indicating that low Si content (0.16 wt.%) was effective to avoid the temper embrittlement. On the other hand, the N toughness is not so high for any steels, especially for relatively high C content (0.08 wt.%) and with B addition, so that the toughness of the as-welded samples may have some issues. Preparation of the welded samples is currently in progress, and the evaluation of RT impact toughness and the creep-rupture properties of the base metals and the cross-weld specimens are planned.

Table 4. Vickers hardness of newly proposed steels and other reference materials

Name	Vickers hardness (HV0.5)		Remarks
	As-normalized	Normalized and tempered	
MLC02	310 ± 7	258 ± 6	High Mn, low C
MLC03	337 ± 6	264 ± 5	High Mn
MLC03B	330 ± 6	243 ± 4	High Mn + 0.01B
Original 3Cr-3WV	338 ± 7	226 ± 7	Heat #2750 (HV1.0), Ta free
MSLC2	350 ± 9	290 ± 7	High Mn and Si, low C
Original 3Cr-3WVTa	349 ± 10	293 ± 3	Heat #2751 (HV1.0), w/0.1Ta

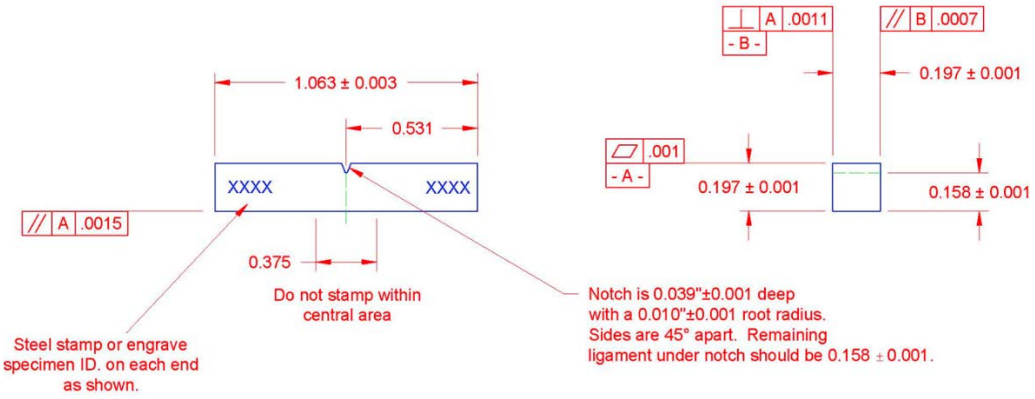

Figure 4. Drawing of half-size Charpy test specimen (unit: inch).

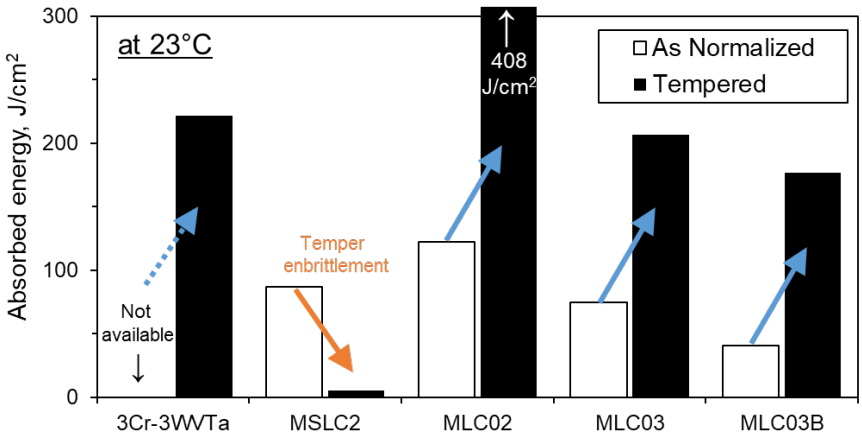

Figure 5. Schematic illustrations of two different welded plates with machining plans of cross-weld creep specimens and Charpy impact test specimens.

References

[1] R.L. Klueh, Elevated-Temperature Ferritic and Martensitic Steels and Their Application to Future Nuclear Reactors, ORNL/TM-2004/176, November 2004.

[2] R.L. Klueh, N.D. Evans, P.J. Maziasz, V.K. Sikka, Creep-rupture behavior of 3Cr-3W-V bainitic steels, International Journal of Pressure Vessels and Piping, 84 (2007) 29-36.

[3] M. Jawad, V.K. Sikka, Development of a New Class of Fe-3Cr-W(V) Ferritic Steels for Industrial Process Applications, ORNL/TM-2005/82, 2005, Oak Ridge National Laboratory.

[4] L. El-Guebaly, et al., Design Challenges and Activation Concerns for Aries Vacuum Vessel, Fusion Science and Technology, 64 (2013) 449-454.

[5] F.W. Wiffen and Y. Katoh, ORNL Fusion Materials Program – Annual Report for FY-2017, ORNL/TM-2017?32.

[6] ASME B31.3, ASME Code for Pressure Piping, the American Society of Mechanical Engineering (2008) p.18-19.

[7] J. Yu and C.J. McMahon, Jr., The Effects of Composition and Carbide Precipitation on Temper Embrittlement of 2.25Cr-1 Mo Steel- Part I1. Effects of Mn and Si, Metallurgical Transactions A, 11, (1980) 291-300.

[8] F. Abe, Science and Technology of Advanced Materials, 9 (2008) pp. 1-15.

2. ODS AND NANOCOMPOSITED ALLOY DEVELOPMENT

2.1 STEM CHARACTERIZATION OF UNIRRADIATED 14YW—Danny Edwards, Karen Kruska, Richard J. Kurtz (Pacific Northwest National Laboratory), G.R. Odette and Takuya Yamamoto (University of California-Santa Barbara)

OBJECTIVE

The objective is to establish the baseline microstructure of the oxide dispersion strengthened ferritic 14YW alloy for comparison with samples irradiated in the High Flux Isotope Reactor (HFIR) JP27 In-situ Helium Injection (ISHI) experiment.

SUMMARY

Scanning Transmission Electron Microscopy (STEM) dislocation contrast imaging and elemental mapping were used to characterize the microstructure of unirradiated 14YW. This work provides the baseline for comparison with specimens irradiated in the HFIR JP27 ISHI experiment [1-3]. The STEM analysis was performed on an aberration corrected Japan Electron Optics Laboratory (JEOL) ARM200CF equipped with a large collection angle Silicon drift detector (SDD). No evidence of α'-phase formation was found, as expected for unirradiated material. The oxide dispersion is rather course compared to the Y-Ti-O nano-oxides in its nanostructured ferritic counterpart, 14YWT. Large intragranular Cr-W oxy-carbo-nitrides, were mapped using Energy Dispersive Spectroscopy (EDS) elemental mapping. All particles were visible in annular dark field and STEM bright field images, particularly if collection angles less than <60 mR were used.

PROGRESS AND STATUS

Introduction

The effects of high helium production during neutron irradiation are expected to lead to detrimental changes in the mechanical properties of ferritic alloys for fusion first-wall structural components. An ISHI experiment was conceived and implemented to investigate the effects of prototypical helium generation rates on the microstructure of various ferritic and ferritic/martensitic alloys [1-3]. In the JP-27 experiment, samples of the various alloys were irradiated at irradiation temperatures from 300 to 500ºC to doses of 21 dpa. The helium created by transmutation of the NiAl coating applied to the samples reached a peak level of 1230 appm helium distributed uniformly over a range of 6 μm. Work is underway at University of California Santa Barbara (UCSB) and Pacific Northwest National Laboratory (PNNL) to document the effects of this high helium on microstructure evolution. The results of these have been reported in several prior semiannual reports by staff at both UCSB and PNNL.

Here we describe recent STEM work on unirradiated 14YW, a variant of the yittria dispersion strengthened ferritic oxide dispersion strengthened (ODS) alloys that include 14YWT and 12YWT. The latter two alloys contain roughly 0.4 wt% Ti that refines the yittria dispersion to a much finer, sub-nanometer oxide phase identified to be $Y_2Ti_2O_7$, present in densities over 10^{23} per m^3. The characterization of this unirradiated material was conducted on an aberration corrected JEOL ARM200CF, which permits acquisition of high resolution elemental information. This information is obtained by coupling the intense, sub-nanometer electron probes formed in the cold field emission gun, probe corrected STEM with the higher detection efficiency of large area energy dispersive SDDs.

Experimental Procedure

The 14YW alloy, the composition of which is listed in Table 1, is a powder metallurgy product hot isostatically pressed at 1150°C. Transmission electron microscope (TEM) discs of this material were provided by UCSB. Focused Ion Beam (FIB) liftouts were prepared for STEM analysis using a Field Electron and Ion Company (FEI) Quanta 3D FIB; atom probe tomography (APT) samples were also prepared and analyzed, but the oxide distribution is too coarse to capture sufficient oxide particles in a small

set of APT needles to yield reliable results on particle size distribution and density. Only the results of the STEM analysis are presented in this semiannual report. One TEM sample was prepared from the region shown in Figure 1. The liftout was thinned by ion milling at 30 keV, followed by 5 keV, and a final low-energy surface cleaning (2 keV Ga^+ ion) at ±2° tilt angles.

Table 1. Composition in wt% of Unirradiated 14YW

Alloy	Cr	Fe	Y	W
14YW	14.26	82.46	0.25	3.03

The analytical TEM characterization was performed using a Cs-corrected JEOL ARM 200CF microscope equipped with a Centurio SDD for EDS, a Gatan Quantum 965 Dual electron energy loss spectroscopy (EELS) system, and high angle annular dark field (HAADF) and bright field (BF) STEM detectors. For elemental mapping in STEM mode, a sub-nanometer probe of 0.18 nm with a probe current of ~2 nA was used with a convergence angle of 48 mrad.

Results

SEM analysis

Electropolishing of the specimen surface revealed the grain structure as shown below in Figure 1. The SEM imaging was performed to select suitable regions for STEM and APT sample preparation. The grain structure is bimodal with large grains of ~5-10 μm diameter surrounded by small grains (<1 μm). Large intragranular particles are visible throughout the SEM image and the FIB liftout, and are usually associated with grain or subgrain boundaries.

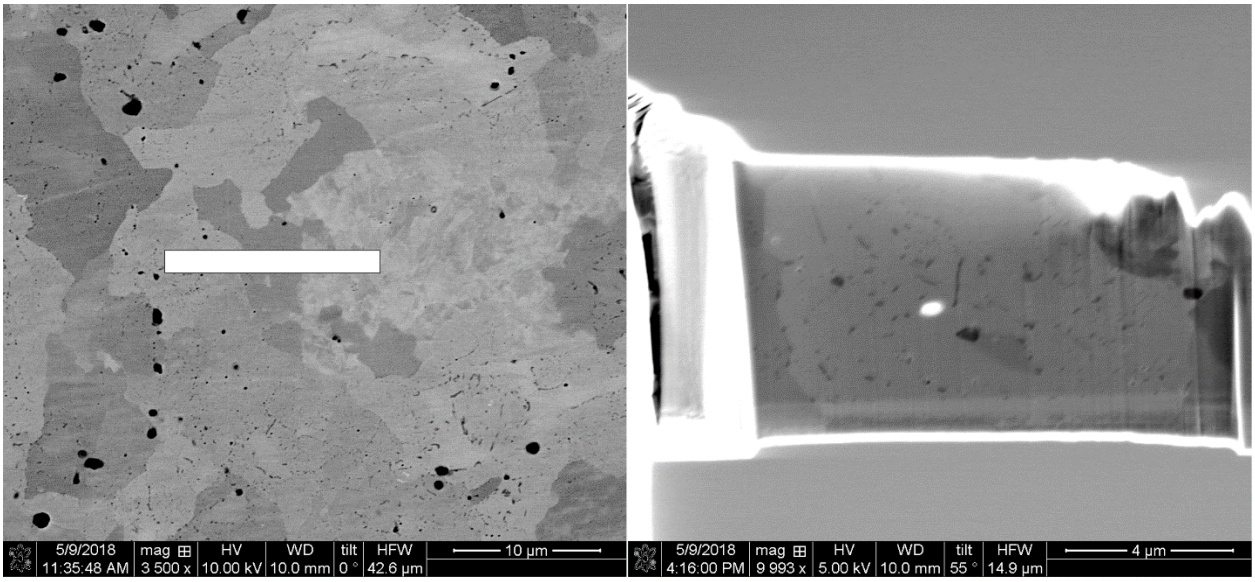

Figure 1. An SEM image is shown of the region from which a liftout was extracted for the STEM analysis. The area chosen encompasses both fine grained and coarse grain regions to sample the range of microstructures. The extracted liftout, shown on the right, turned out to be mostly a large grained region.

STEM analysis

Dislocation contrast STEM imaging (see Zhu et al [4] for a description of this technique) was used to document the microstructure before elemental mapping was performed. Figure 2 presents an overview of the FIB liftout using high angle annular dark field and the corresponding STEM BF at a semi-collection angle of 90-218 mrads. The HAADF image in Figure 2a does not reveal the particle distribution very clearly, which was somewhat surprising given differences in average atomic weight between the various particles and the Fe-Cr matrix. The corresponding STEM BF image in Figure 2b clearly shows more of the particles present in this material. The images in Figure 2c and 2d show a close-up of the highlighted area in Figure 2a, but taken at a camera length that lowers the semi-collection angle to 14-55 mrad. Under these conditions, dislocations, large intragranular particles, and much smaller particles are clearly visible. Note, the diffraction contrast imaging (DCI)-STEM conditions also negates the bend contour contrast in the annular dark-field (ADF) image, which can be seen by observing that the upper left corner of the STEM BF in Figure 2d (indicated by the arrow) is obscured by the bend contour from the bent foil, but this entire region is visible with uniform contrast in the ADF image in Figure 2c.

Figure 3 shows higher magnification DCI-STEM views of the yittria oxide distribution, mostly composed of spherical particles along with some of the larger particles determined to be Cr-W oxy-carbo-nitrides (see arrow in Figure 3a). The yittria particles occasionally were observed to have moiré fringes, but this was rare, indicating the particles do not necessarily share a common orientation with the matrix. The average size of the yittria particles is ~8 nm, with a density of ~1 x 10^{23} per m^{-3}.

Figure 4 presents a set of elemental maps taken under the HAADF conditions used in Figure 2a. Two phases are evident from these maps, large intragranular particles that are often enriched in Cr, minor levels of W, and N, O. Some carbon is present in these particles also, but in this thick region the low energy carbon is absorbed by the foil. The other phase captured is the yittria particles, seen in the Y L map. The full size distribution cannot be captured at this magnification in a relatively thick area (150 nm). The map shown in Figure 5 was taken in a thinner region at higher magnification. The small yittria particles were better captured, however, even in this area the particles are fairly blurry and indistinct compared to the accompanying ADF image, indicating the need to move to even thinner areas. Prior experience with mapping α' particles in irradiated 14YW revealed a lower limit of ~3 nm diameter, below which α' could not be detected from elemental maps even though APT analysis of the same material definitely showed smaller particles were present. It is likely similar limitations exist even with the enhanced EDS systems available on these instruments, and may require use of high resolution electron energy loss spectral imaging to pull out small particles.

Summary

The STEM analysis of unirradiated 14YW shows that a fine distribution of yittria particles can be seen in both ADF and STEM bright field images, with smaller semi-collection angles yielding better images of the particles. This imaging mode also revealed both the dislocation structure and the larger intragranular oxy-carbo-nitride particles, with the added benefit of reducing the bend contour contrast in the ADF images. The oxide distribution in unirradiated 14YW alloy is noticeably coarser compared to the 14YWT alloy (3 x 10^{23} m^{-3}, diameter = ~2.5 nm), which has been attributed to the lack of Ti in this material [5].

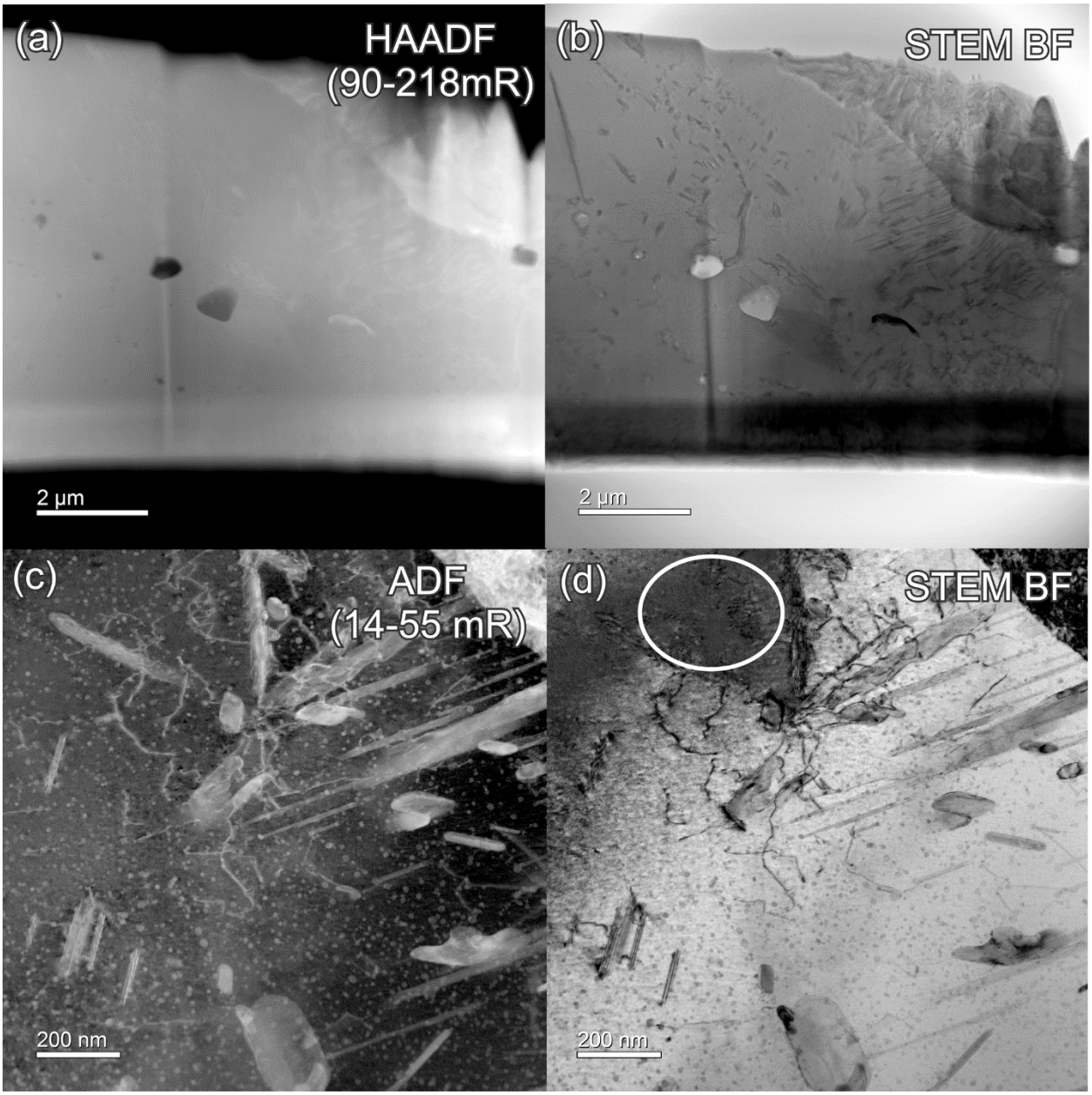

Figure 2. The STEM images in (a) and (b) were taken with a camera length that yields a semi-collection angle that corresponds to HAADF conditions. Numerous intergranular particles can be seen in the STEM BF image in (b), but they are faint in the HAADF image. Changing the camera length to ADF conditions of 14-55 mrads reveals each discrete particle from all of the phases as well as the dislocations. Note the absence of bend contours in the ADF image (see circled area in (d)).

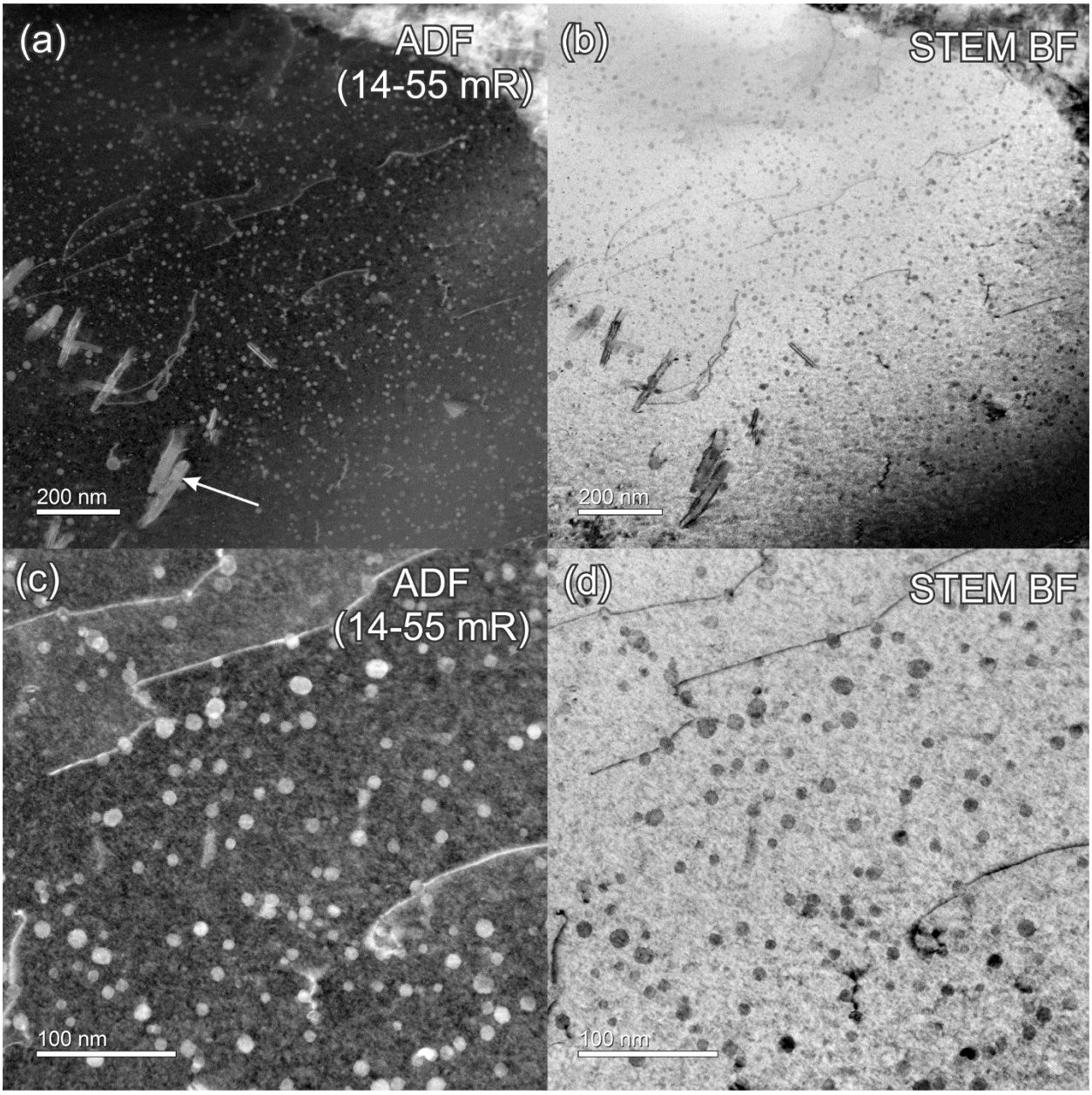

Figure 3. The STEM ADF/BF pairs showing the uniform distribution of small spherical yittria particles with isolated dislocations. Larger oxy-carbo-nitrides are shown in (a), indicated by the arrow. Note again the lack of bend contours in the ADF image in (a) compared to its BF counterpart in (b).

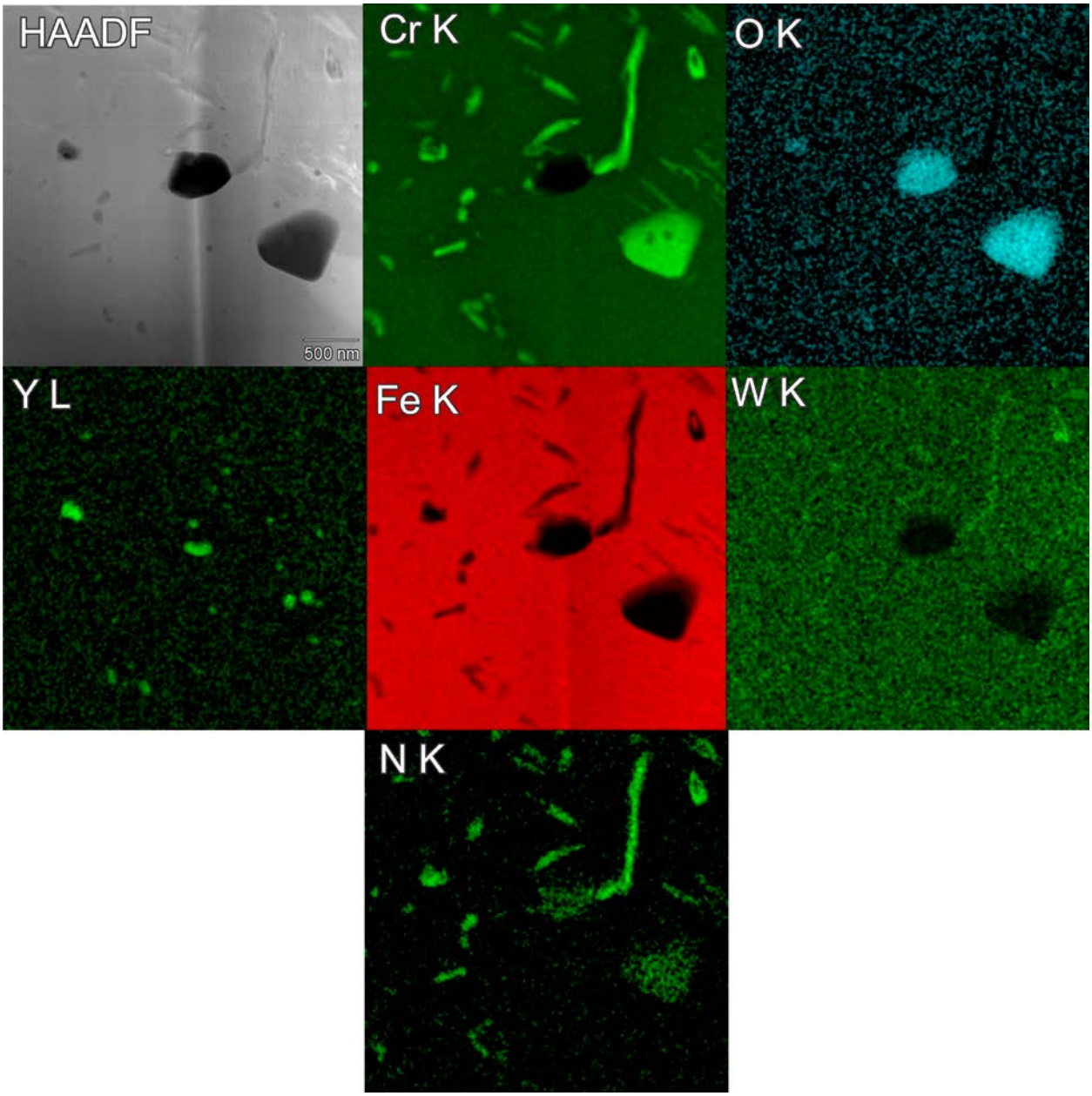

Figure 4. Elemental maps taken under HAADF conditions reveal the presence of large intragranular particles that are rich in Cr, with some W present. Most of these larger particles contain both oxygen and nitrogen to varying levels. The carbon maps (not shown) were fairly uniform, but this section of the foil was around 150 nm thick and it was likely that the carbon x-rays were absorbed too much to effectively map the C distribution. The Y L map captures some of the larger yittria particles, but higher magnifications are need to see the entire size range properly.

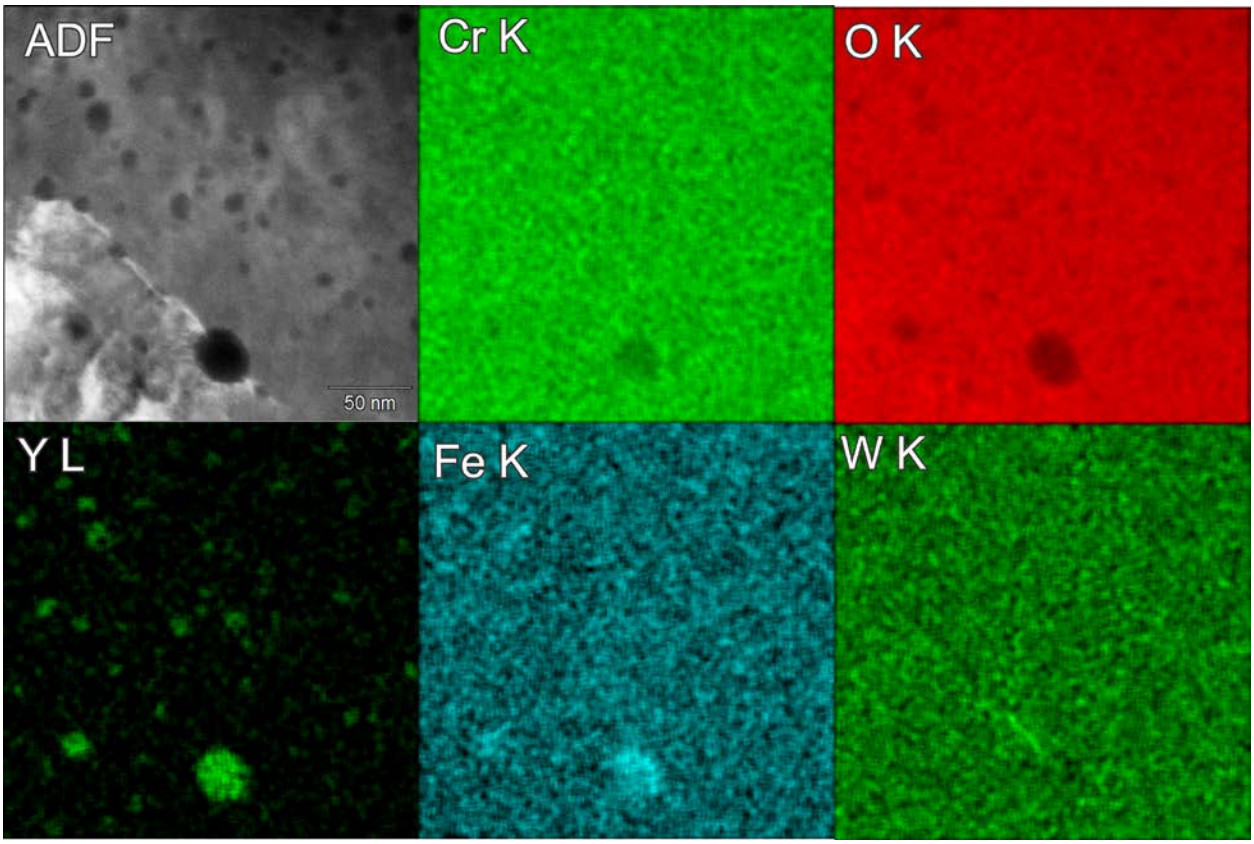

Figure 5. In this area, which was ~100 nm thick, very few intragranular particles are present. However, the yittria particles clearly show up in the Y L map. The smallest particles may not be fully captured, and may require acquiring elemental maps in thinner regions near the foil edge.

Future Work

A journal paper is in preparation summarizing APT and STEM analyses of 14YW compared to 14YWT, both before and after irradiation. These results will be submitted to a relevant journal this fiscal year.

Acknowledgements

This research was supported by Office of Fusion Energy Sciences, U.S. Department of Energy (DOE) under Contract DE-AC05-76RL01830. A portion of the research was performed using Environmental Molecular Science Laboratory (EMSL), a national scientific user facility sponsored by the DOE's Office of Biological and Environmental Research and located at PNNL.

References

[1] T. Yamamoto, G.R. Odette, L.R. Greenwood, Fusion Materials Semiannual Report 1/1 to 6/30/2005 DOE/ER-313/38, 2005, p. 95.

[2] T. Yamamoto, G.R. Odette, P. Miao, D.T. Hoelzer, J. Bentley, N. Hashimoto, H. Tanigawa, R. J. Kurtz, J. Nucl. Mater, **367-370** (2007) 399.

[3] R.J. Kurtz, G.R. Odette, T. Yamamoto, D.S. Gelles, P. Miao, B.M. Oliver, J. Nucl. Mater. **367-370** (2007) 417.

[4] Yuanyuan Zhu, Colin Ophus, Mychailo B. Toloczko, Danny J. Edwards, Ultramicroscopy **193** (2018) 12-23.
[5] M.J. Alinger, G.R. Odette, D.T. Hoelzer, Acta Mater. **57** (2009) 392-406.

3. CERAMIC COMPOSITE STRUCTURAL MATERIAL DEVELOPMENT

3.1 RECENT PROGRESS IN THE DEVELOPMENT OF SiC COMPOSITES FOR NUCLEAR FUSION APPLICATIONS—T. Koyanagi, Y. Katoh (Oak Ridge National Laboratory), T. Nozawa (National Institutes for Quantum and Radiological Science and Technology), L.L. Snead (Stony Brook University), S. Kondo (Institute for Materials Research, Tohoku University), C.H. Henager Jr (Pacific Northwest National Laboratory), M. Ferraris (Politecnico di Torino), T. Hinoki (Institute of Advanced Energy, Kyoto University), Q. Huang (Ningbo Institute of Industrial Technology, Chinese Academy of Sciences)

Abstract of a manuscript in press for Journal of the Nuclear Materials

Silicon carbide (SiC) fiber reinforced SiC matrix composites continue to undergo development for fusion applications worldwide because of inherent advantages of the material including low activation, high temperature capability, relatively low neutron absorption, and radiation resistance. This paper presents an international overview of recent achievements in SiC-based composites for fusion applications. Key subjects include applications in fusion reactors, high-dose radiation effects, transmutation effects, material lifetime assessment, and development of joining technology (processing, test method development, irradiation resistance, and modeling capability). This paper also discusses synergy among research for fusion materials and non-fusion materials (for fission and aerospace applications). Finally, future research directions and opportunities are proposed.

3.2 MICROSTRUCTURAL EVOLUTION OF 3C-SiC EXPOSED TO SIMULTANEOUS NEUTRON IRRADIATION AND HELIUM IMPLANTATION—X. Hu, T. Koyanagi, Y. Katoh (Oak Ridge National Laboratory), T. Yamamoto (University of California, Santa Barbara)

OBJECTIVE

The objective of this project is to investigate the synergism of transmutant helium (He) and irradiation effects in Silicon Carbide (SiC). The impact of He on the microstructural evolution in neutron-irradiated SiC was captured by comparing the microstructures of SiC following neutron irradiation with and without in-situ He implantation.

SUMMARY

We exposed 3C-SiC in contact with a 2μm Ni foil to neutron irradiation at 500°C to 29 dpa in High Flux Isotope Reactor (HFIR). Transmission electron microscopy (TEM) observations and thermal desorption measurements helped elucidate the impact of He on the microstructural evolution in 3C-SiC. Thermal He desorption spectra from ion-implanted and neutron-irradiated SiC showed a completely different desorption behavior. The identification of possible He trapping sites was attempted by applying the first order dissociation model to the measured thermal helium desorption spectra. The TEM showed He stabilized the defect clusters and promoted the formation of visible He bubbles in SiC subject to simultaneous neutron irradiation and in-situ He implantation. Following thermal desorption large faceted He bubbles were found along grain boundaries in the neutron-irradiated SiC with in-situ He implantation, while the He bubbles in the grain interior were relatively smaller than in the neutron-irradiated sample without in-situ He implantation. The He content in the neutron-irradiated samples was quantified based on the experimental data from TEM and thermal desorption measurements.

PROGRESS AND STATUS

Introduction

The SiC has been widely applied or considered in nuclear systems as a fuel and structural material since 1960s [1],. The extremely hostile service environment in nuclear systems imposes significant challenges to SiC. Of interest is the neutron irradiation, altering the microstructure and the consequential thermo-mechanical properties of SiC. In addition, the presence of gaseous species (e.g., He, hydrogen isotopes, and fission gases) together with irradiation-induced defects complicates the microstructural evolution of SiC in the real service environments. One of the primary concerns is He effects in SiC. The He can be introduced into SiC through two major pathways, i.e., (n, α) nuclear reactions and implantation of energetic He produced elsewhere. For example, the 14 MeV-peaked fusion neutron spectrum induces a high He generation rate in SiC, up to 150 atomic parts per million (appm) He/dpa [2], due to the large reaction cross section between high energy neutron and Si and C (0.18 and 0.07 barns for reactions between 14.1MeV neutrons, respectively). In fission reactors, about 90% of the light nuclei that arise from ternary fission are He. The He has negligible solubility in SiC and correspondingly has a strong tendency to bind with vacancy and other radiation-induced defects, resulting in the accumulation of He and the subsequent nucleation and growth of He bubbles. The presence of abundant He bubbles leads to changes in mechanical properties and dimensional stability of SiC [3]. Therefore, it is critically important to understand the interactions of He and irradiation-induced defects in SiC in order to predict the He behavior in SiC, to assess performance and to enable optimized design of SiC devices subject to a high flux of fast neutrons.

Experimental Procedure

High purity polycrystalline chemical vapor deposition (CVD) 3C-SiC specimens (Rohm & Haas Co., Woburn, USA) were used in this study. A 2 μm thick Ni foil worked as implanter to inject high energy α particles from (n, α) reactions into an adjacent sample during neutron irradiation. The sample assemblies, SiC stacked with Ni foil, were exposed to neutron irradiation in HFIR. Irradiation dose and temperature were

30 dpa and 500°C. The 4.76 MeV α particles from the ^{59}Ni (n, α) reaction has a range of 14.8 μm in SiC with a theoretical density of 3.21 g/cm^3. The He implantation profiles in SiC are determined in terms of the He/dpa ratio as a function of depth in SiC covered with Ni foil implanters of various thicknesses, as shown in Figure 1.

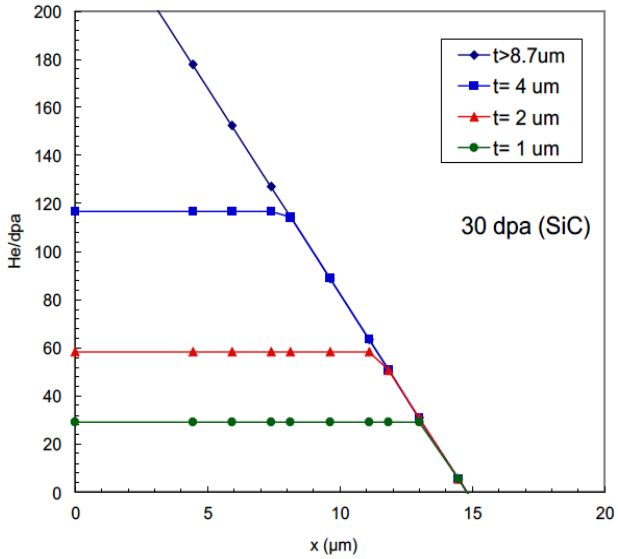

Figure 1. He/dpa ratio as a function of depth in SiC wrapped with Ni foils of various thickness (1, 2, 4, >8.7μm) irradiated in HFIR.

Thermal Desorption Spectroscopy (TDS) measurements were performed by using the gas implantation and thermal desorption system (GITDS) [4] at Oak Ridge National Laboratory (ORNL). During the TDS run, temperature of the sample was increased to 1600°C with a ramping rate of 0.5°C/s. Microstructure characterization was performed on the neutron irradiated samples before and after TDS measurements with a Japan Electron Optics Laboratory (JEOL) JEM 2100F field emission gun TEM operating at 200 kV. Electron transparent TEM foils were prepared using a focused ion beam system.

Microstructure of 3C-SiC following Neutron Irradiation and in-situ He Implantation

Figure 2 shows a set of TEM bright field images of the observed area (~10 μm) below the free surface together with the under- and over-focused cavity images of two selected areas, locations D (2 μm below surface) and A (7.5 μm below surface), respectively. It is evident that cavities with a diameter of ~ 2.5 nm were observed, which most likely are He bubbles due to the homogenous distribution of implanted He within this area. The observation of cavities is surprising since both type vacancies in SiC are considered immobile at this low irradiation temperature. Katoh et al. [5] identified the low temperature limit for the formation of visible voids in neutron irradiated SiC may be as high as 1100°C without He. In a different study, no voids were observed in 3C-SiC sample neutron irradiated at 440°C to 31 dpa in the same reactor [6]. Therefore, the introduction of He promoted the nucleation and growth of cavities in 3C-SiC.

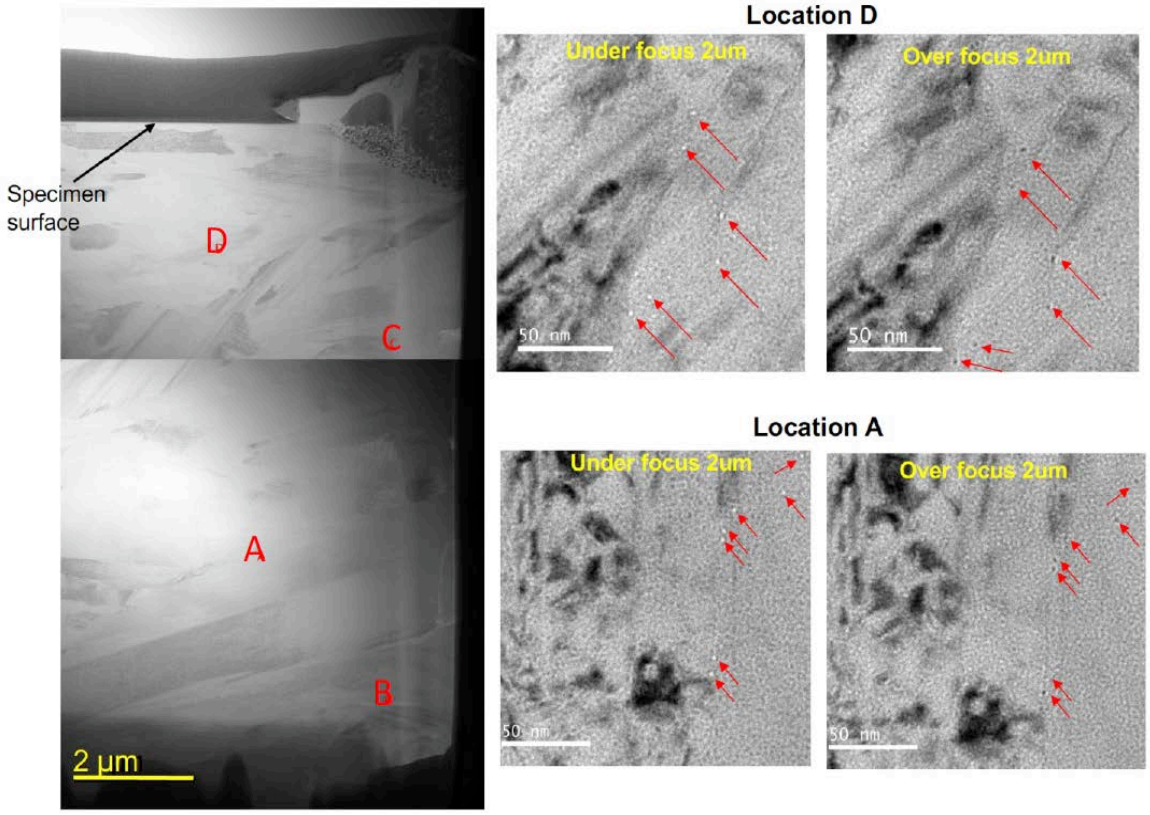

Figure 2. Micrographs of TEM-imaged cavities in neutron irradiated 3C-SiC with in-situ He implantation.

Thermal He Desorption Behavior of Neutron-Irradiated and He-Implanted SiC

Thermal He desorption spectra of both neutron-irradiated with in-situ He implantation and He-implanted samples are shown in Figure 3. The He desorption spectra from the 3C-SiC samples implanted with 10 keV He ions to a fluence of $1\times10^{15}/cm^2$ showed good repeatability in these two measurements. The measured spectra had a major He desorption group around 800°C in the studied temperature regime. It is noted that the maximum temperature in the current TDS measurement is 1600°C, 60% of the dissociation point of SiC. Therefore, the contained He will not be completely released until the sample is melted. It is expected that higher temperature beyond 1600°C will continue to enhance the evolution of He-defect clusters and promote the dissociation of He from unstable He-defect clusters. More significant He desorption groups could be observed in the higher temperature regime (>1600°C).

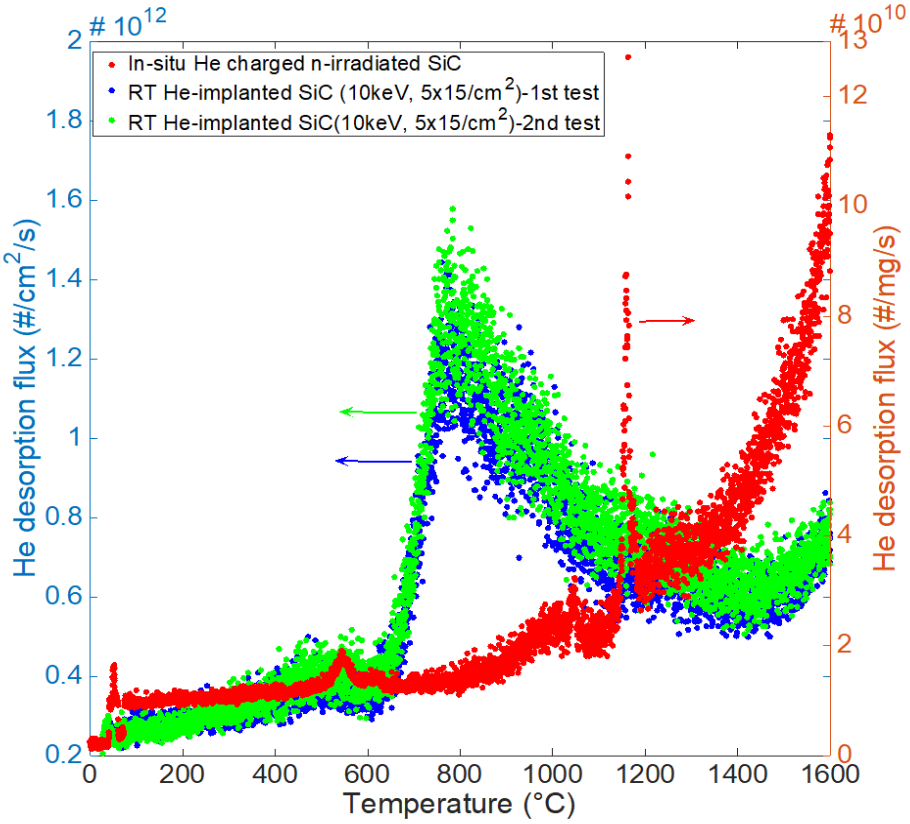

Figure 3. Thermal He desorption spectra from He implanted 3C-SiC (10 keV to a fluence of 5×10^{15}/cm^2 at room temperature) and neutron-irradiated 3C-SiC with in-situ He implantation (500°C, 30 dpa, 58 appm He/dpa).

The He desorption spectrum from the neutron irradiated sample with in-situ He implantation is also shown in Figure 3. Generally, the desorption spectra showed a continuously increasing He release flux up to the maximum temperature during the TDS measurement, leaving an incompletely developed desorption peak at the upper temperature limit. The other noticeable feature is that a sharp peak occurred at 1163°C, and this excessive sharpness is inconsistent with a first order dissociation model as generally adopted in classical rate-theory. Such a sharp peak has also been observed for high purity iron under other implantation conditions [7, 8], which is primarily due to the alpha-gamma phase transformation. However, 3C-SiC is relatively stable below 2100°C without showing any phase transformation [1]. It is unclear what mechanism is responsible for this sharp He release. A possible explanation could be that a specific He-defect cluster with significant concentration was fully dissociated in a narrow temperature region around 1163°C while a quick pathway for He diffusion is present to enable the fast release of He (most likely grain boundaries present within the SiC).

Microstructure of Neutron-Irradiated Samples following TDS Measurements

The TEM observations were performed on the neutron-irradiated 3C-SiC samples with and without in-situ He implantation to capture the impact of in-situ He implantation on the microstructural evolution following the heat treatment during TDS measurements. The TEM bright field images are shown in Figure 4. As shown in Figure 4 (a), it is apparent that a great number density of cavities is distributed homogeneously throughout the grain interior in the neutron irradiated 3C-SiC without in-situ He implantation following the TDS heat treatment. No cavities were observed along the grain boundaries, implying these cavities are actually voids. It is noted that most of the large visible voids are faceted. The maximum annealing

temperature used in the current study is 1600°C. Therefore, it is not surprising that abundant visible voids were observed within the samples, owing to the enhanced mobility of vacancies when temperature was greater than 1100°C.

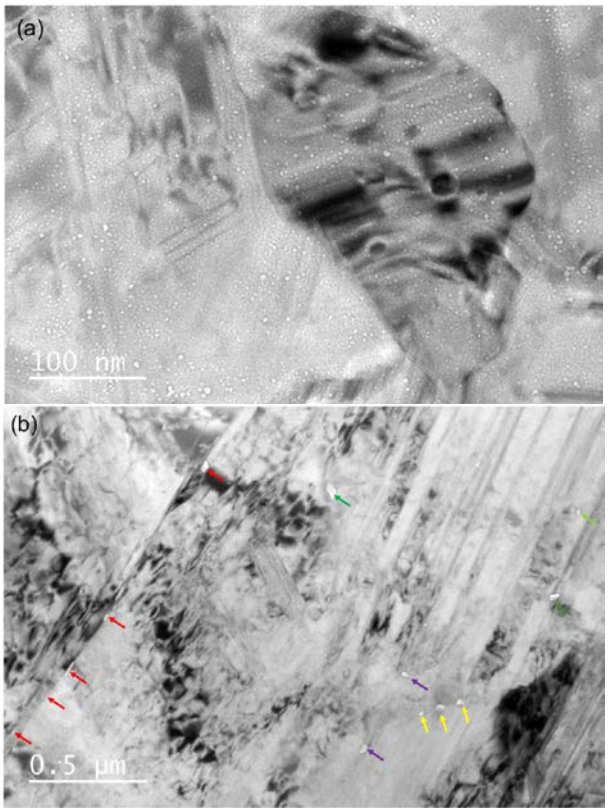

Figure 4. The TEM bright field images of neutron irradiated 3C-SiC (a) without and (b) with in-situ He implantation following the heat treatment in TDS measurements. The large He bubbles along grain boundaries are labeled with arrows.

The SiC samples after simultaneous neutron irradiation and He implantation displayed certain similarities and distinctions in comparison with the non-He neutron irradiated samples. The similarity involves the presence of abundant cavities in the grain interior, as shown in Figure 4 (b). These observed cavities are more likely He bubbles, considering the intensive He implantation within this damaged area. A significant difference in the microstructure observed in this sample was that large He bubbles exist along the grain boundaries or stacking faults, which are all faceted. Grain boundaries serve as strong sinks for mobile species (i.e., He, vacancy, etc.) in the studied materials.

Results

The microstructural evolution in 3C-SiC subject to simultaneous He implantation and neutron irradiation at 500°C to 30 dpa was examined before and after TDS measurements using TEM. The TDS measurements on both neutron-irradiated and ion-implanted samples were performed to capture the fundamentals of He-defect interactions in 3C-SiC. The results indicate that the presence of implanted He promoted the formation of He bubbles in SiC at such low irradiation temperature to 30dpa, implying He stabilized the defect clusters. Thermal He desorption spectra of ion-implanted and neutron-irradiated 3C-SiC display completely different features, which strongly depend on the initial microstructures of samples. The microstructure of neutron-irradiated 3C-SiC with in-situ He implantation following TDS measurements showed the existence of large faceted He bubbles along grain boundaries.

References

[1.] 1. Snead, L.L., et al., *Handbook of SiC properties for fuel performance modeling.* Journal of Nuclear Materials, 2007. **371**(1-3): p. 329-377.
[2.] 2. Snead, L.L., et al., *Status of silicon carbide composites for fusion.* Journal of Nuclear Materials, 1996. **233-237**: p. 26-36.
[3.] 3. Katoh, Y., H. Kishimoto, and A. Kohyama, *The influences of irradiation temperature and helium production on the dimensional stability of silicon carbide.* Journal of Nuclear Materials, 2002. **307-311**: p. 1221-1226.
[4.] 4. Hu, X., et al., *Impact of neutron irradiation on thermal helium desorption from iron.* Journal of Nuclear Materials, 2017. **489**: p. 109-117.
[5.] 5. Katoh, Y., et al., *Microstructural development in cubic silicon carbide during irradiation at elevated temperatures.* Journal of Nuclear Materials, 2006. **351**(1-3): p. 228-240.
[6.] 6. Koyanagi, T., et al., *Neutron-irradiation creep of silicon carbide materials beyond the initial transient.* Journal of Nuclear Materials, 2016. **478**: p. 97-111.
[7.] 7. Xu, D. and B.D. Wirth, *Post-implantation thermal desorption of helium from poly- and single-crystalline iron.* Journal of Nuclear Materials, 2009. **386-388**: p. 395-399.
[8.] 8. Hu, X., D. Xu, and B.D. Wirth, *Quantifying He-point defect interactions in Fe through coordinated experimental and modeling studies of He-ion implanted single-crystal Fe.* Journal of Nuclear Materials, 2013. **442**(1-3): p. S649-S654.

3.3 GRAIN SIZE VARIATION IN NANOCRYSTALLINE SILICON CARBIDE IRRADIATED AT ELEVATED TEMPERATURES—Limin Zhang, Wensi Ai, Liang Chen, Chenlong Pan, Tieshan Wang (Lanzhou University), Weilin Jiang (Pacific Northwest National Laboratory)

Extended abstract of a paper recently published in the Journal of the American Ceramic Society [1]

ABSTRACT

Nanocrystalline materials possess a large volume fraction of grain boundaries that could be a sink for mobile point defects. However, the material may become less stable and more susceptible to irradiation at decreasing grain size. This study reports on ion irradiation-induced grain size variations in nanocrystalline SiC. The SiC grains embedded in amorphous SiC matrices had average sizes ranging from 2 to 20 nm, estimated by Grazing Incidence X-ray Diffraction (GIXRD) along the (111) orientation. Irradiation was performed using 5 MeV Xe^{23+} ions to 1.15×10^{16} ions/cm^2 at 700 K. Significant growth is observed for smaller grains that saturated at ~8 nm, while larger grains (~20 nm in size) decreased in size. Homonuclear C-C bonds in the irradiated amorphous SiC matrix were graphitized, which could contribute to the observed size saturation. Grain size saturation may reflect the resistance of nanocrystalline SiC to irradiation, a desirable property for potential applications in nuclear environments.

HIGHLIGHTS

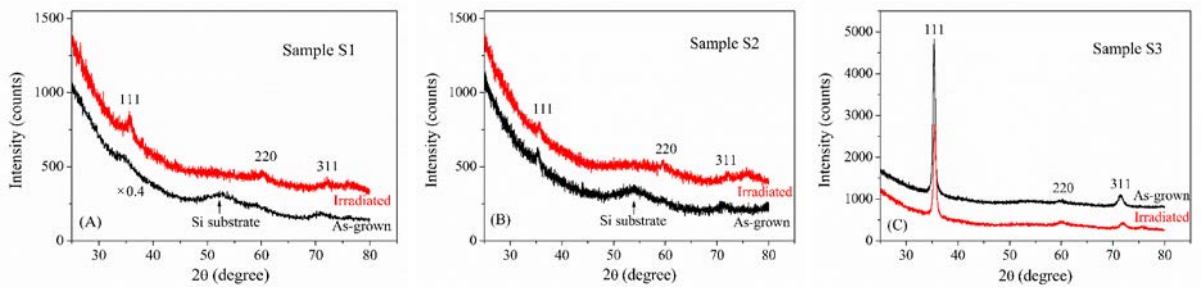

Figure 1. GIXRD patterns for nanocrystalline SiC before and after irradiation with 5 MeV Xe ions to 1.15×10^{16} Xe/cm^2 at 700 K.

Table 1. Average grain size of nanocrystalline SiC before and after irradiation at 700 K

Sample ID	Thickness (nm)	Dose (dpa)	As-grown Size (nm)	Irradiated Size (nm)
S1	~210	8.8	2.7 ± 0.5	5.6 ± 0.8
S2	~120	8.1	7.5 ± 1.1	8.3 ± 1.5
S3	~480	10.2	19.7 ± 0.3	16.8 ± 0.4

Figure 1 shows the GIXRD patterns of the as-grown and irradiated nanocrystalline SiC films on Si substrates. The film thickness and average dose for each film are listed in Table 1. The samples exhibit three diffraction peaks from 3C-SiC (111), (220) and (311). The strongest (111) peak was employed to estimate the average grain size using the Scherrer formula. After irradiation, the grain size of sample S1 significantly increases from 2.7 to 5.6 nm, as given in Table 1. In comparison, the grain size of sample S2 only slightly increases from 7.5 to 8.3 nm. The average grain size is determined by the competition of epitaxial growth of existing grains, nucleation and growth in the amorphous matrix and coalescence of neighboring grains. For the larger grains in sample S3, the grain size shows a decrease from 19.7 to 16.8 nm, which is attributed to the production of damage that perturbs the lattice periodicity in the grain. The data suggest that when the grain size exceeds a certain threshold, grain shrinkage occurs during irradiation at 700 K.

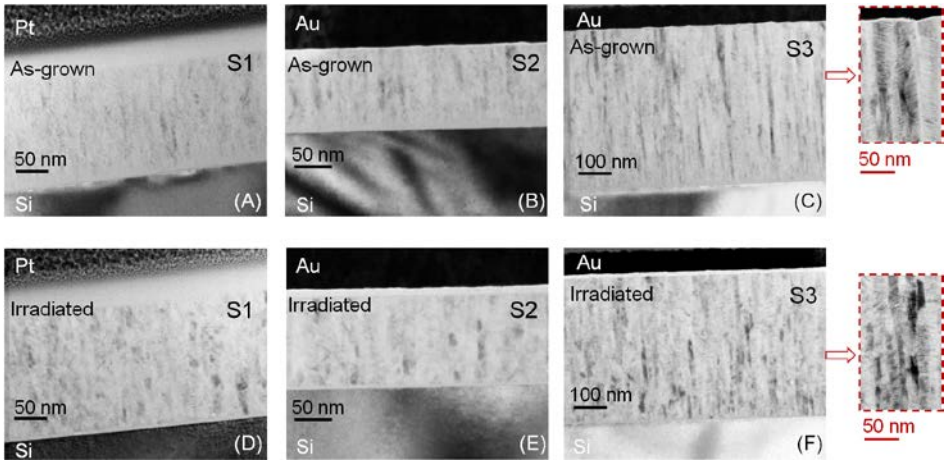

Figure 2. TEM images for nanocrystalline SiC before and after irradiation.

Figure 2 shows the transmission electron microscopy (TEM) images of the as-grown and irradiated nanocrystalline SiC samples. The SiC grains exhibit a distinct columnar structure that may contain a high density of planar defects (see the enlarged images for sample S3). The columnar growth of the SiC grains is along the preferred <111> direction, as suggested by the GIXRD data. Larger grains are observed in the thicker film, which could be a result of thermal growth during longer film deposition at 973 K. After irradiation, grain growth in sample S1 is apparent, as shown by the larger dark areas in Figure 2D. No significant changes in the grain size are observed in samples S2 and S3. However, the number of the smaller grains (dark dots) in sample S3 appears to increase with irradiation (Figure 2F), which could be attributed to irradiation-induced grain nucleation and growth in the amorphous matrix. Creation of the smaller grains leads to a reduction in the average grain size.

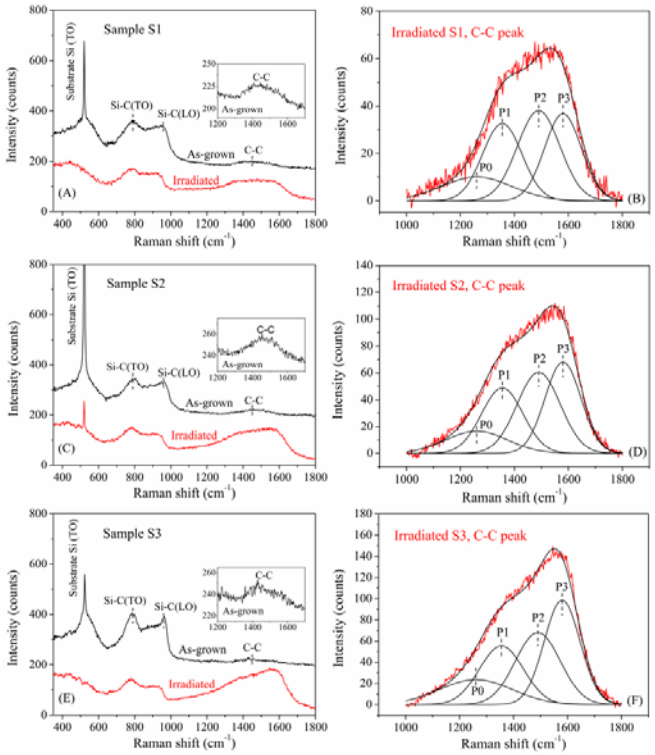

Figure 3. Raman spectra for nanocrystalline SiC before and after irradiation. Peak P0 and peaks P1, P2 and P3 in (B), (D) and (F) are associated with sp^3 bonding and various types of sp^2 bonding, respectively.

After irradiation, a significant change in the chemical bonding occurs in the three samples, as shown in Figure 3. The homonuclear C-C bonds in the amorphous SiC matrix are found to transform from a diamond-like sp^3 bond to a more stable graphite-like sp^2 bond during irradiation. As a result, further grain nucleation and growth in the irradiated films may be limited or inhibited, which could contribute to the observed size saturation.

References

[1] Limin Zhang, Weilin Jiang, Wensi Ai, Liang Chen, Chenlong Pan, and Tieshan Wang, Journal of the American Ceramic Society 2018; https://doi.org/10.1111/jace.15895.

3.4 RAMAN SPECTROSCOPY OF NEUTRON IRRADIATED SILICON CARBIDE: CORRELATION AMONG RAMAN SPECTRA, SWELLING AND IRRADIATION TEMPERATURE—T. Koyanagi, Y. Katoh, M.J. Lance (Oak Ridge National Laboratory)

Abstract of a manuscript accepted by Journal of Raman Spectroscopy

The effects of neutron irradiation on microstructural evolution and the resultant changes in physical and mechanical properties are of critical importance for the development of silicon carbide (SiC) materials for nuclear applications. This study of neutron-irradiated β-SiC under a wide range of conditions at temperatures between 235 and 750°C and neutron doses of 0.01–11.8 displacements per atom evaluated the effects on the SiC structure using Raman spectroscopy. The SiC optical phonon lines were shifted to lower wavenumbers by irradiation. Correlations were found among the wavenumber of the longitudinal optical phonon line, irradiation-induced swelling, and irradiation temperature. The peak shift also correlated indirectly with decreasing thermal conductivity of irradiated SiC. The irradiation-induced peak shift is explained by combinations of lattice strain, reduction of the elastic modulus, and other factors including decreasing coherent domain size. These findings bridge irradiation-induced microstructural changes and property changes and illustrate how Raman spectroscopy is a useful tool for nondestructively assessing irradiated SiC materials for nuclear applications.

4. HIGH HEAT FLUX MATERIALS AND COMPONENT TESTING

4.1 PROPERTIES AND CHARACTERIZATION OF NOVEL COPPER ALLOYS FOR FUSION ENERGY APPLICATIONS—Ying Yang (Oak Ridge National Laboratory), Ling Wang (University of Tennessee), Steven J. Zinkle (University of Tennessee and Oak Ridge National Lab), Lance Snead (Stony Brook University)

OBJECTIVE

This study aims at developing high strength, high conductivity Cu alloys with improved thermal creep strength for long pulse fusion high heat flux structures, through an accelerated approach of computational thermodynamics guided alloy design.

SUMMARY

Work performed during this reporting period was to reduce/eliminate Sn and Fe contamination found in previous batches of CuCrNbZr alloys and evaluate physical and mechanical properties of newly fabricated higher-purity CuCrNbZr alloys.

PROGRESS AND STATUS

Sn and Fe contamination identified in the previous CuCrNbZr alloy

The transmission electron microscopy (TEM) analysis found trace Sn and Fe elements in previously fabricated CuCrNbZr alloys. Subsequent chemical analysis indicated about 0.1% Fe and 0.5%Sn in the alloys. The presence of Sn and Fe was speculated as the leading cause of the lower electrical conductivity (56~58% IACs) in the initial heat of CuCrNbZr alloys, compared to 76~90% IACs of typical CuCrZr alloys. To reduce or eliminate the contamination of Sn and Fe, high purity elements (Cu, 99.996%, Cr, 99.995%, Nb, 99.97% and Zr 99.94%) from Alfa Aesar were used in fabricating a new high-purity CrCrNbZr alloy heat. In addition to using higher-purity elements, the arc-melting and cast process was refined to reduce oxygen partial pressure so that the Nb and Zr chemistry can be better controlled in the alloy. The high-purity alloy follows the same designed chemistry as the previous 1CCNZ alloys. The as-cast ingot was then given the same thermal mechanical treatment and heat-treatment scheme as before. Chemical analysis showed significantly reduced Fe (<0.004%) and Sn (<0.002%) in the new high-purity heat.

Electrical resistance screening

Electrical resistivity was measured on the new CCNZ_HP alloys and compared with that of the CCNZ1 alloy. The conductivity of the high purity CCNZ_HP heat is significantly higher than the (Fe + Sn)-contaminated CCNZ1 heat (76% IACS vs. 58% IACS), as shown in Figures 1 (a) and (b).

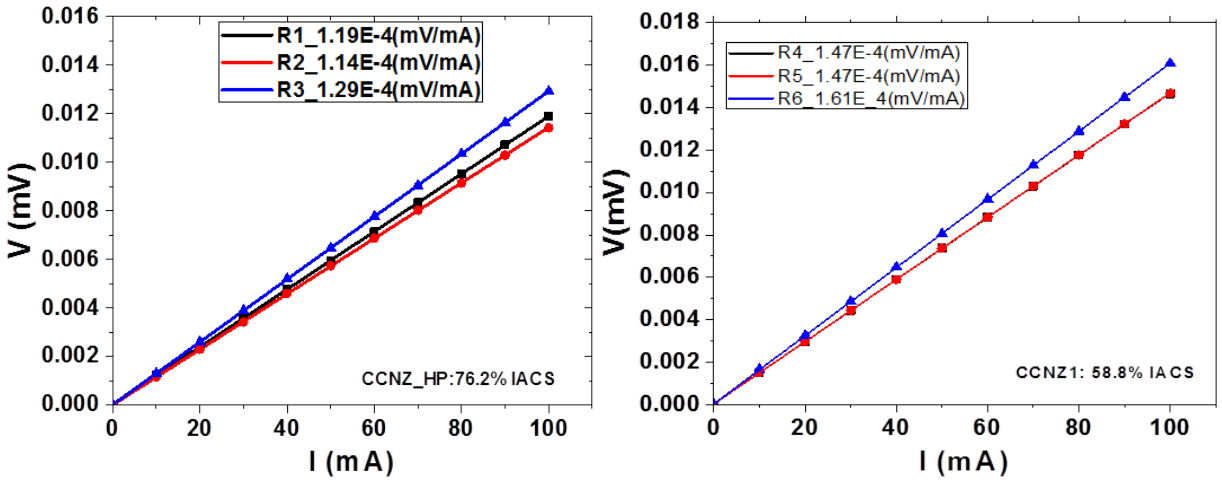

Figure 1. Electrical resistance measurements on (a) the high-purity CCNZ_HP heat and (b) the (Fe+Sn) contaminated CCNZ1 heat.

Mechanical properties

Tensile and creep properties were measured on the high-purity heat and compared to the contaminated heat. The initial screening results are shown in Figure 2 (a)~(d). The yield and ultimate tensile strengths of CCNZ_HP are comparable to CCNZ1 at 24 and 300°C, and slightly higher at 500°C. Uniform and total elongation of both heats are comparable at 300 and 500°C. The contaminated heat has higher uniform and total elongation than the HP heat, which is probably due to lower Nb and Zr contents in the contaminated heat. The yield strength of the HP heat is comparable to the upper limit of CuCrZr alloys available from literature [1]. The creep test was done at 500°C under 90 MPa in air. The contaminated CCNZ1 alloy experienced catastrophic failure shortly after loading, while the creep life of CCNZ HP heat is about 110 h, which is about a one third increase over that of the reference Kabelmetal-produced CuCrZr (CCZ) alloy. Significant oxidation occurred in all three alloys during the creep test.

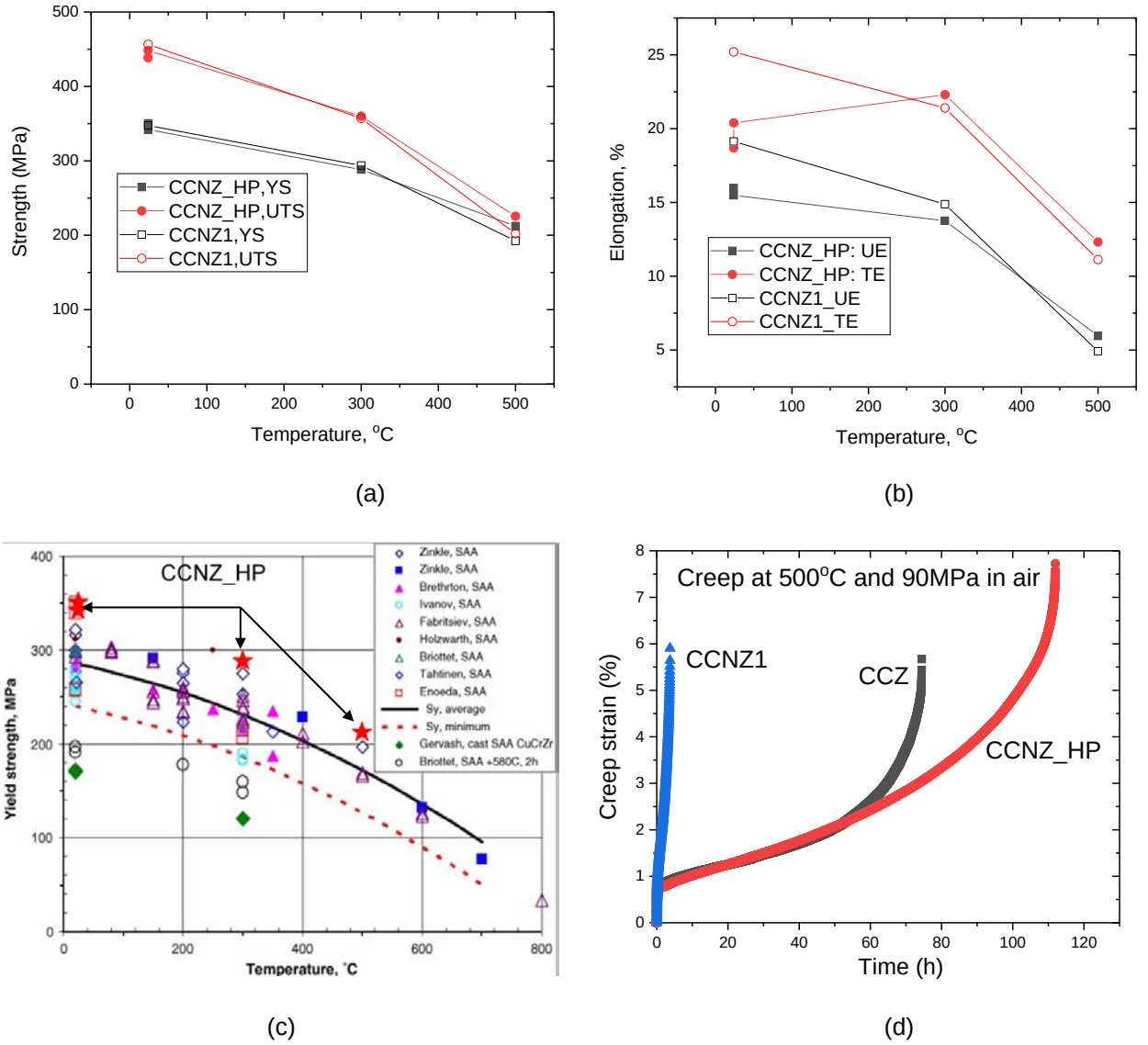

Figure 2. Mechanical screening test results for the high-purity heat CCNZ_HP alloy and comparison with the contaminated heat CCNZ1 alloys and the reference Kabelmetal-produced CuCrZr alloy (CCZ).

Microstructure characterization

Preliminary characterization of the microstructure of the CCNZ_HP and the reference CCZ alloys used optical, scanning electron and transmission electron microscopy. The optical micrographs of the as-aged CCZ and CCNZ_HP alloys are in Figure 3. In the optical images, the CCNZ_HP alloy has slightly smaller grain size (~50±2 μm) compared to that of CCZ (~55 -8/+5 μm). The CCNZ_HP alloy has large facet precipitates range from ~2 μm to ~11 μm, while the CCZ alloy has small spherical precipitates ranging from ~1 to 2.5 μm. Detailed scanning electron microscopy (SEM) and TEM analysis is currently ongoing to determine the crystal structure and chemical composition of matrix and precipitates phases. The Vickers hardness of CCNZ_HP was 137.9, comparable to that of CCZ at 135.8, for both samples in the as-aged condition.

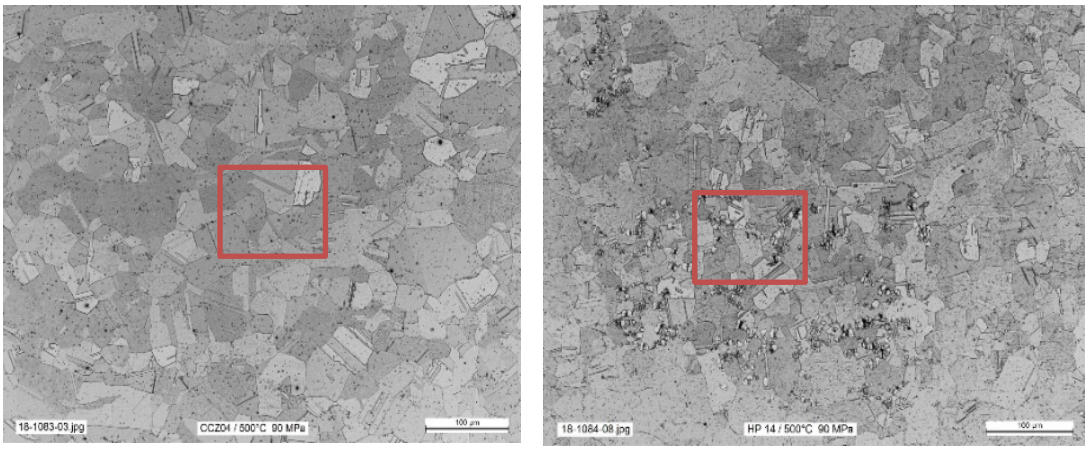

Figure 3. The optical images of CCZ (left) and CCNZ_HP (right) alloys in the as-aged condition.

Future work

1) Prepare CCNZ_HP specimen for neutron irradiation experiments.
2) Characterize the microstructure of the CCNZ_HP alloy before and after deformation and compare with the CCZ alloy.
3) Perform systematic creep tests under vacuum or inert gas protection.

References

[1] Barabash, V., A. Peacock, S. Fabritsiev, G. Kalinin, S. Zinkle, A. Rowcliffe, J-W. Rensman et al. "Materials challenges for ITER–Current status and future activities." *Journal of Nuclear Materials* 367 (2007): 21-32.

4.2 SOLUTE STABILIZATION OF NANOCRYSTALLINE TUNGSTEN ALLOYS—Jason R. Trelewicz (Stony Brook University)

OBJECTIVE

Tungsten has emerged as a promising candidate material for the high heat flux divertor region of future fusion reactors due to its high melting point, good thermal conductivity, creep resistance, high temperature strength, sputtering resistance, and chemical compatibility with tritium. However, the potential for transient events in International Thermonuclear Experimental Reactor (ITER) and an eye toward demonstration reactor (DEMO) raises concerns about tungsten's recrystallization temperature, oxidation resistance, long-term radiation tolerance, and mechanical performance. The technical aim of this research is to address these limitations in tandem by precisely tailoring the volume fraction, chemistry, and structural state of grain boundaries in nanostructured tungsten alloys.

SUMMARY

Binary nanocrystalline tungsten alloys were synthesized using solute additions selected based on their propensity to produce stable nanocrystalline states from a subset of reduced activation elements. The elements Cr and Ti were identified as stabilizers and used in the production of nanocrystalline W-Cr and W-Ti alloys. In situ electron microscopy experiments leveraging thin film geometries were used to probe thermal stability of the alloys, which was correlated to the underlying solute distributions through analytical microscopy techniques. The results show exceptional microstructural stability up to 1000 ºC, which is attributed to heterogeneous solute distributions reducing the fundamental driving force for grain coarsening in the nanostructured alloys relative to pure nanocrystalline tungsten.

PROGRESS AND STATUS

Microstructure and phase evolution in magnetron sputtered nanocrystalline W-20 at.% Ti, and W-15 at.% Cr were explored through in situ transmission electron microscopy (TEM) annealing experiments at temperatures up to 1000 °C. Alloy compositions were selected to achieve thermodynamically preferred nanocrystalline states as guided by lattice Monte Carlo modeling in these binary systems. Thermal stability was compared with unalloyed nanocrystalline W, selected as a baseline to eliminate artifacts associated with thin film geometries (i.e. as compared to bulk materials). Shown in Figure 1(a-c), grain growth in unalloyed nanocrystalline tungsten transpired through a discontinuous process at temperatures up to 550 °C, which was coupled to an allotropic phase transformation of metastable β-tungsten with the A-15 cubic structure (common in thin film W) to stable body-centred cubic (BCC) α-tungsten. Complete transformation to the α-phase was accompanied by the convergence to a unimodal nanocrystalline structure at 650 °C, signaling a transition to continuous grain growth.

Sputter deposition of W-20 at%. Ti produced the nanocrystalline grain structure shown in Figure 2a with a mean grain size of 14 +/- 4 nm from the histogram in Figure 2e for the as-deposited condition. This structure remained stable through in situ TEM annealing of the film at 1000 °C as evident in Figure 2b and was reflected in the mean grain size exhibiting only a subtle increase to 18 +/- 4 nm in the histogram. Indexing of the selected area diffraction patterns demonstrated the as-deposited films were solely BCC α-tungsten, indicating the addition of solute stabilized the films against the formation of metastable β-tungsten and grain growth. The W-15 at.% Cr film also exhibited a nanocrystalline grain structure in the as-deposited state as shown in Figure 2c, but with a larger initial grain size of 55 nm +/- 17 nm from the histogram in Figure 2e. It was difficult to ascertain qualitative changes to the grain structure in Figure 2d upon annealing of the W-Cr film; however, the mean grain size in the histogram evolved to 86 nm +/- 31, corresponding to a 56% increase from the as-deposited grain size.

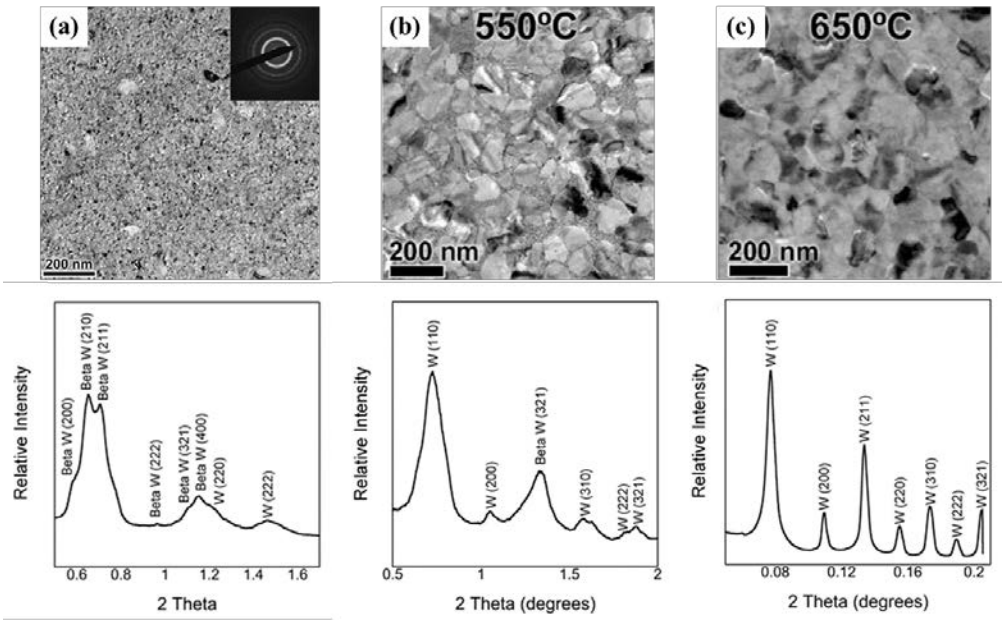

Figure 1. Nanocrystalline tungsten microstructures and radial intensity profiles from the electron diffraction patterns in (a) the as-deposited state and after annealing to (b) 550 °C and (c) 650 °C.

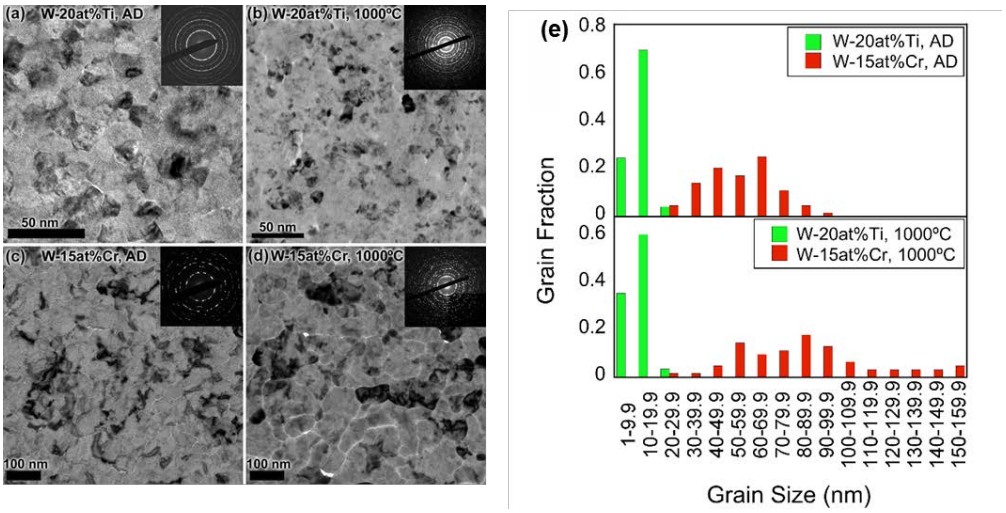

Figure 2. Bright-field images for (a) as-deposited W-20 at.% Ti, (b) 1000 °C annealed W-20 at.% Ti, (c) as-deposited W-15 at. % Cr, and (d) 1000 °C annealed W-15 at.% Cr. (e) Grain size distributions for both alloys in the as-deposited state (upper) and annealed at 1000 °C (lower).

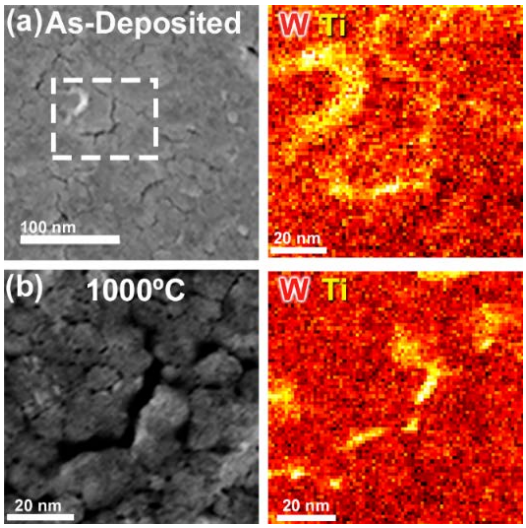

Figure 3. HAADF images and EELS maps from the denoted regions for the W-20 at.% Ti film in the (a) as-deposited and (b) 1000 °C annealed conditions.

The scanning transmission electron microscope (STEM) measurements were employed to map the distribution of solute in the alloy films and correlate compositional heterogeneities with underlying microstructural features. An example is shown in Figure 3a with the High-Angle Annular Dark Field (HAADF) image of the as-deposited film accompanied by the corresponding elemental map produced from the electron energy loss spectroscopy (EELS) scan. The Z-contrast in the HAADF image indicated that compositional heterogeneities were present in the as-deposited W-Ti film, which was confirmed in the EELS map from the selected region of the HAADF image. Annealing of the W-Ti film amplified this solute partitioning in Figure 3b with the spatial distribution of Ti commensurate with the grain size, thus suggesting Ti was segregated to grain boundaries. A heterogeneous solute distribution was also detected in the as-deposited W-Cr film (not shown here); however, it was difficult to ascertain whether the Cr-rich regions aligned with the grain boundary network. A noticeable change in this solute distribution was uncovered upon annealing of the W-Cr film at 1000 °C, where the EELS map demonstrated extended Cr-rich regions that coincided with the finest grain sizes in the tail of the distributions of the annealed film, i.e. grain sizes < 40 nm. The contrasting thermal stability between W-Ti and W-Cr was thus attributed to different grain boundary segregation states and underscores the critical role of grain boundary chemistry in alloy stabilization.

Future Work

Future work will explore thermodynamically preferred states in ternary tungsten alloys using lattice Monte Carlo simulations initially focused on the W-Cr-Ti system. Alloy compositions that produce predictively stable nanocrystalline states will be identified and bulk materials synthesized through high energy ball milling and spark plasma sintering. Microstructural evolution in both the powders and sintered compacts will be quantified with specific focus on stability against grain growth and recrystallization.

4.3 ON NEW AND REMARKABLY POWERFUL TOUGHENING MECHANISMS IN W-NiFe HEAVY ALLOYS—M.E. Alam and G. R. Odette (University of California Santa Barbara)

OBJECTIVE

The objective of this report is to describe newly identified, powerful toughening mechanisms in tungsten heavy alloys, as a possible candidate as divertor material.

SUMMARY

The strength, microhardness and fracture toughness properties of four ductile phase toughened (DPT) commercially available tungsten (W)-based heavy metal alloys (W-NiFe), reinforced with 3 to 10 (wt.%) of a NiFe phase, were previously characterized from room to liquid nitrogen (LN_2) temperatures. All the alloys manifested a sub-zero brittle-to-ductile transition temperature (BDTT) ranging from -25ºC to -150ºC, depending on the amount of the ductile NiFe phase. Here, we report a new toughening mechanism that contributes ≈ 10 to 20 times higher room temperature toughness values of a tungsten heavy alloy (WHA) than for unalloyed W, while containing only 3 wt.% of a NiWFe ductile phase. In contrast to the classical ductile phase toughening, which is primarily due to macrocrack bridging and deflection, WHA toughening mainly involves new mechanisms associated with arrest, blunting and bridging of numerous process zone microcracks.

PROGRESS AND STATUS

Introduction

The WHA are currently considered the most promising candidates for plasma facing component for future fusion reactor divertor applications due to its high melting temperature, good conductivity, low sputtering rates and high-temperature strength, [1-3]. This application requires that structural W-based alloys and structures have sufficient fracture toughness to withstand the severe thermal-mechanical environment of a divertor [3-5]. It is likely that monolithic W is intrinsically too brittle for this task. A promising approach to toughening is to composite W with a ductile phase. Previously a series of DPT W-NiFe (90, 92.5, 95 and 97 wt.% W with 7:3 = Ni:Fe) heavy metal alloys were characterized that shown to have much higher room temperature toughness (> 10x) and much lower BDTT temperatures (-150 to -25 ºC) than monolithic W (several hundred °C), depending on their ductile phase NiFe content [6]. In the work reported here, we describe and analyze new toughening mechanisms that are responsible for their remarkably high WHA toughness.

The W-NiFe WHA microstructure is composed of a 3-dimensional, NiWFe ductile phase honeycomb web surrounding unalloyed W powders. Our study revealed that the toughening in the W-NiFe WHA is dominated by new mechanisms associated with this microstructure. In most classical ductile phase toughening systems, the matrix phase remains brittle, and ductile phase toughening is due to bridging of the *macrocrack* wake, as well as crack arrest-renucleation-deflection mechanisms [7,8]. However, in the case of the W-NiFe WHA, toughening is dominated by *microcrack* arrest, blunting and bridging in a fully ductilized crack tip plastic zone. Plastic zone deformation, including in the embedded W particles, and dilatational microcrack blunting effects, dissipate a large amounts of energy. Further, the process-zone dilatation, extensively shields the crack tip stress fields, including wake effects. Microcrack blunting shielding is far more effective than that provided by elastic microcracks in brittle matrix systems [9]. To the best of our knowledge, these *ductile* process zone microcrack toughening mechanisms have not previously been identified and explored in metallic alloys. However, similar toughening effects have been observed in some polymer-rubber composites [10].

Experimental Procedure

The four commercial (Mi-Tech Metals, Indianapolis, IN, USA) liquid-phase sintered (LPS) were received in the form of 100mm x100mm x14mm plates. The WHAs contained 90, 92.5, 95 and 97 wt. % W with a balance of an initially 70% Ni and 30 %Fe phase. Details of the materials and sample preparation can be found elsewhere [6, 11].

The W particle size distribution was determined by sampling ~500 individual grains using 'ImageJ64' software. The particle aspect ratio (PAR) was defined by dividing the longest dimension (l) to the shortest dimension (s) of a particle. The cleavage crack length and the mid-crack opening displacement were defined by measuring the length and the maximum width of a crack, respectively. Contiguity (C_w) defines the amount of W-W contact, and expressed as $C_w = (S_{w-w})/S_w$ where S_w is the surface area of the W grains, and S_{w-w} is the surface area of W-W contacts [12]. The area fraction of the NiWFe was measured by converting scanning electron microscopy (SEM) electron backscattered channelling contrast (EBSC) micrographs into binary black-white images and measuring the fraction of the white area (see Figure 1). The NiWFe DP honeycomb structure thickness (t) was measured using a line-intercept method (LIM), as the average width of the NiWFe phase measured on lines drawn on the binary image [13]. The NiWFe DP thickness/W length ratio was also calculated by the same LIM, by dividing the total intersected DP length by the total intersected W length. The percentages of the various local fracture modes were also determined by the LIM.

Results

Microstructure

The SEM micrographs of the polished and etched W-NiFe plates shown in Figure 1 reveal roughly spheroidal W particles (PAR: 1.1 ± 0.2) surrounded by an interconnected honeycomb web structure of the ductile NiWFe phase. Multiple energy dispersive X-ray spectroscopy (EDS) scans show that the particles are close to 100% W, while the NiWFe ductile phase is approximately 50%Ni, 30%W and 20%Fe (wt.%). Figure 1 and Table 1 also show the W–particle size increases from ≈ 17 μm for 90W alloy to ≈ 38 μm for 97W alloy.

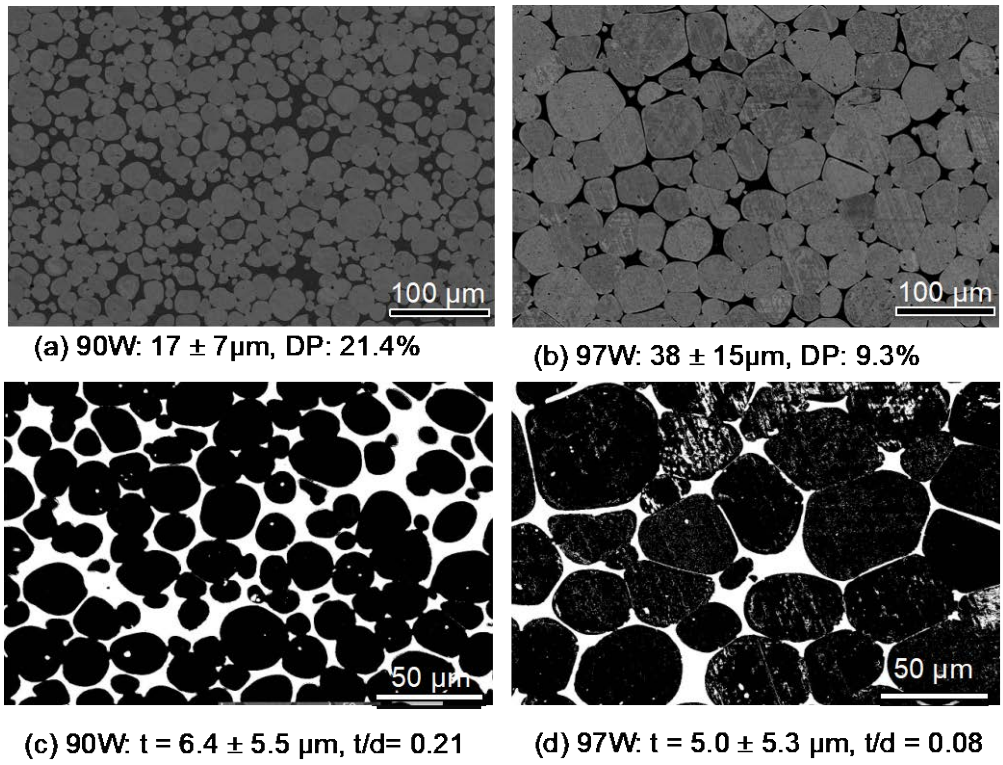

Figure 1. The SEM images of the W particles (gray) and the ductile NiWFe phase (dark) for: (a) 90W, and (b) 97W WHA, respectively. The binary black (W) and white (NiWFe) images of: (c) 90W, and (d) 97W highlight the NiWFe honeycomb web characterized by the web thickness (t), and the t to W particle diameter (d) ratio.

Table 1. The size and contiguity of W-particles, and the composition and morphology of the NiWFe honeycomb web structure

WHA	W particle size (µm)	W-W contiguity, C_w	Ni/W/Fe (wt.%)	NiWFe Area fraction (%)	Thickness, t (µm)	t/d (µm/µm)
90W	17 ± 7	14.2	51.2/28.5/20.3	21.4	6.4 ± 5.5	0.21
92.5W	18 ± 7	20.0	49.1/31.3/19.6	14.9	5.7 ± 4.3	0.15
95W	27 ± 11	23.3	49.1/32.2/18.7	12.3	5.2 ± 4.3	0.14
97W	38 ± 15	29.1	48.3/34.3/17.4	9.3	5.0 ± 5.3	0.08

t = NiWFe thickness, d = W diameter.

The average NiWFe web thickness is similar in all the W-NiFe WHAs at ≈ 5.6 ± 0.6 µm. As expected, the area fraction of the NiWFe phase decreases from ~24% for 90W to ~9% for 97W. A higher W fraction lowers the NiWFe phase continuity and increases both the W-W contiguity and the frequency of particle bonded W-W interface, while reducing the NiWFe/W t/d ratio (Figures 1c-d and Table 1).

Fracture Toughness

As reported previously, fracture toughness tests on 90-97W-NiFe alloys were conducted from room temperature (RT) down to liquid nitrogen (LN_2) temperature (Table 2) [6]. In summary, all alloys tested at

RT show continuous load drop after the maximum load (P_m) with increasing load point displacement (d), indicating stable crack growth. The RT K_{Jm} are essentially the same up to 95W, averaging 102 ± 7 MPa√m, in spite of the contiguity increase (see Tables 1 and 2). The K_{Jm} decreases to between 95W and 97W, where K_{Jm} = 73 ± 13 MPa√m. In this case, the K_{Jm} toughness is still ≈ 10x higher than that for typical unalloyed W with K_{Ic} ≈ 8 ± 4 MPa√m; the corresponding $K_{J0.8}$ = 142 ± 8 MPa√m is ≈ 18x higher. The massive toughening provided by a relatively small addition of ductile phase of ≈ 5 vol.% is remarkable. From a practical engineering perspective, crack initiation followed by extremely stable crack growth, provides very high effective cracked body ductility in all cases.

Table 2. The K_{Jm} and $K_{J0.8}$ for the W-NiFe WHAs

Temp	K_{Jm} (MPa√m)			
(ºC)	90W	92.5W	95W	97W
23	100 ± 20	96 ± 9	110 ± 17	73 ± 13
-50	-	59 ± 9	65 ± 4	40 ± 2
-100	73 ± 4	48 ± 5	35 ± 4	32 ± 0.1
-150	50 ± 1	-	-	-
-196	36 ± 3	30 ± 3	27 ± 5	25 ± 2
23ºC ($K_{J0.8}$)	176 ± 25	152 ± 22	204 ± 20	142 ± 8

The 3PB tests were stopped at a P/P_{max} from ≈ 0.77 to 0.92, since the lateral contraction and surface dimpling, indicated by the dark areas in Figure 2, prevented imaging the crack tip. Having said that, we have developed an quasi-J-da type blunting line toughness curve for the 97W after extensively analyzing pre-, in-situ, and post test optical and SEM images for crack extension, which is ≈ 130μm at P/P_m ≈ 0.88 that corresponds to a K_J ≈ 139 MPa√m from its maximum load K_{Jm} ≈ 90 MPa√m (see insert of Figure 2). However, pre-and post-test SEM micrographs analysis for all RT 3PB tested specimens show very little crack growth (da < 200 μm) at these P/P_m loads. Thus, the initial post P_m crack blunting, and the corresponding increase in the crack tip opening displacement (CTOD), are used to estimate an initiation toughness, rather than a classical J-da R-curve tests. Specifically, the K_J at P/P_m ≈ 0.8 ($K_{J0.8}$) was estimated to be ≈ K_{Jc} and is summarized in Table 2. These results show that the $K_{J0.8}$ is ≈ 60-85% higher than K_{Jm} for the 90W to 95W alloys and ≈ 95% higher at 97W.

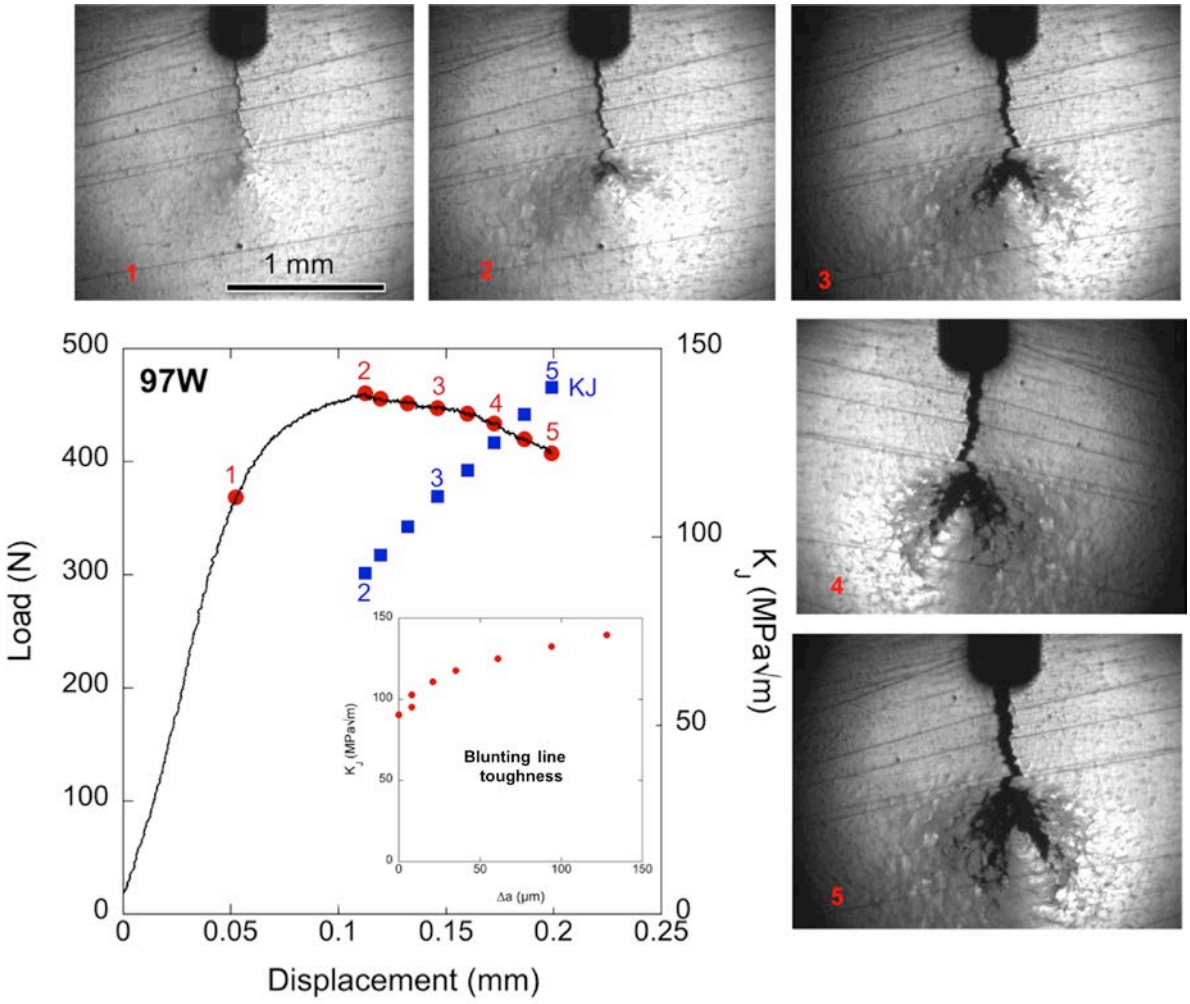

Figure 2. The RT 97W WHA P-d curve with *in-situ* optical images showing the formation of a plastic zone indicated by the dark area, in front of the crack tip, that is out of focus due to lateral contraction. The red circles are P-d points and blue squares are their corresponding K_J values. Insert showing J-Δa blunting line curve based on optical and SEM image analysis. Note that the total crack extension is ≈ 130μ, corresponding to a blunting line toughness of ≈ 139 MPa√m.

The objective of low temperature toughness tests was to probe the effects of lower W toughness, associated with a higher $\sigma_y(T)$, to at least partly emulate the effects of irradiation hardening. Stable ductile tearing is still observed in the 90W alloy at -100ºC, while somewhat mixed (stable + unstable) crack growth occurs at -150ºC [6]. Brittle fracture is observed at -196ºC in all cases. The corresponding BDTT for the other alloys were ≈ -100 ºC, -75 ºC, and -25 ºC for the 92.5, 95 and 97.5W, respectively.

Fracture toughness mechanisms and damage

Post-test SEM studies of the sides of the 3PB bars, shown in Figure 3, demonstrate some of the multiple interacting toughening mechanisms: (a) crack wake bridging; (b) process zone microcrack and microcrack bridging; and, (c) as indicated by slip lines (and the grain shape changes, white dashed circles), plastic deformation of otherwise brittle W particles encapsulated by the DP. These mechanisms lead to the ductilization of the entire W-NiFe dual phase microstructure resulting in large crack tip CTOD ductility and the corresponding development of large semi-classical plasticity zones. That is, on a macro scale, the fracture of the W-NiFe WHA is entirely ductile.

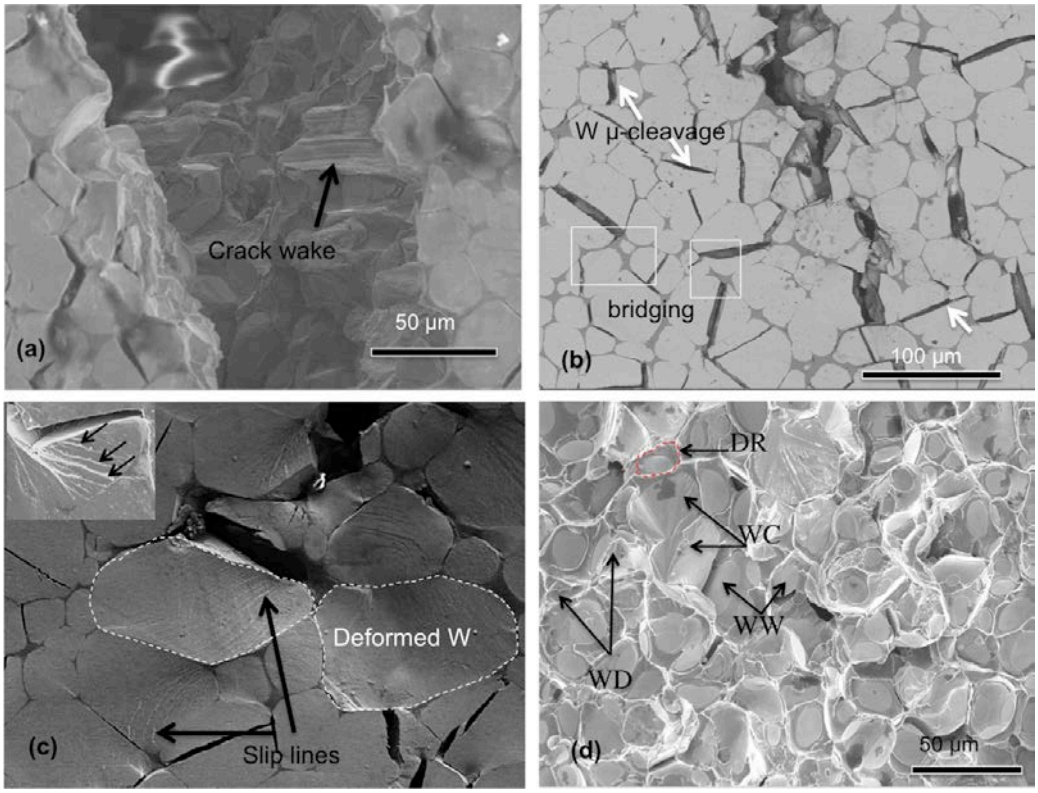

Figure 3. The SEM images illustrating: (a) crack wake bridging; (b) crack tip plasticity, crack bridging, and stable WC microcracks; (c) slip lines in the deformed W-particles; and, (d) various local fracture modes.

As reported previously by many for tensile tests, [14, 15], all four types of local fracture modes, (WC-W cleavage, WD-W ductile phase debonding, WW-W to W particle boundary separation, and DR-NiWFe DP rupture) are also observed on the fracture surfaces of the bend bars as seen in Figure 3d. The fraction of WW increases and WD decreases systematically with increasing W%, and accounts for ≈ 80% of the local fracture mode (see Table 3). However, side surface observations (Figures 3b and 4) clearly show that there are large numbers of WC in the process zone that blunt and open under increasing load, thus producing large dilatational shielding effects.

Table 3. The percentage of local fracture modes from toughness fractographs

T (ºC)	Alloy	WW	WC	WD	DR
23	90W	31.7	12.6	43.7	12.0
	92.5W	42.4	6.9	39.8	10.9
	95W	50.6	6.6	33.7	9.1
	97W	63.2	6.1	24.9	5.8
-100	90W	35.6	12.5	42.4	9.5
	92.5W	15.3	68.2	13.9	2.6
	95W	2.5	91.5	5.1	0.8
	97W	4	96	0	0
-196	90W	2.6	95.6	0	1.8
	92.5W	3.7	96.3	0	0
	95W	2.7	97.3	0	0
	97W	3.5	96.5	0	0

The density of the particle-sized WC blunted microcracks in the process-zone is ≈ 556 (90W) to 231 (97W) per mm^2 (see Table 4 and Figure 4). Some WW interface fracture and W-NiWFe interfacial debonding (WD) are also observed. The WC microcracks might have initiated at small pores in the as-received WHA. The microcracks are arrested by the NiWFe DP and blunt under increased loading. The mid-crack opening displacements range from 0.3μ to 15μ, averaging from 1.7μ to 3.3μ (see Table 4). However, a few microcracks are linked up to 2 to 3 particle diameters, especially in the 97W WHA due to lack of DP. Both the cleaved and unbroken W particles also deform along the principal stress direction. The strain in W particles normal to the loading direction, including the blunted microcracks, is again higher in the 90W WHA (≈ 0.18) compared to that in 97W WHA (≈ 0.11) (see Table 4). The small boxed area in Figures 5 a and b shows the undeformed and deformed regions at the crack tip (arrow), respectively, for the same location in a 95W WHA. The NiWFe honeycomb web is also strained normal to the loading direction (≈ 0.18 - 0.27) in all cases. The WHA crack tip region also undergoes lateral contraction in the thickness (Z) direction. The $\Delta Z/Z$ was measured on the broken specimens, also verified by the 3D tomography, using Keyence VHX-5000 Microscope as shown in the insert in Figure 5c; $\Delta Z/Z \approx 0.044 \pm 0.004$ for 90-95W and ≈ 0.023 for 97W (Table 4). Figure 5d schematically illustrates the deformation and dilatational damage mechanisms in the crack tip process zone. In summary, the WC and WW microcracks are arrested by DP and blunt with increasing loading. The blunting dilatation decreases with increasing W and decreasing temperature.

Unlike room temperature cracks that are more frequently aligned ~ 45º to the loading direction, the lower temperature cracks are narrow and sharp and primarily aligned perpendicular to the loading direction. In this case, once initiated, adjacent microcracks link and propagate at a much lower toughness (see Table 2 and Figures 4 c, d).

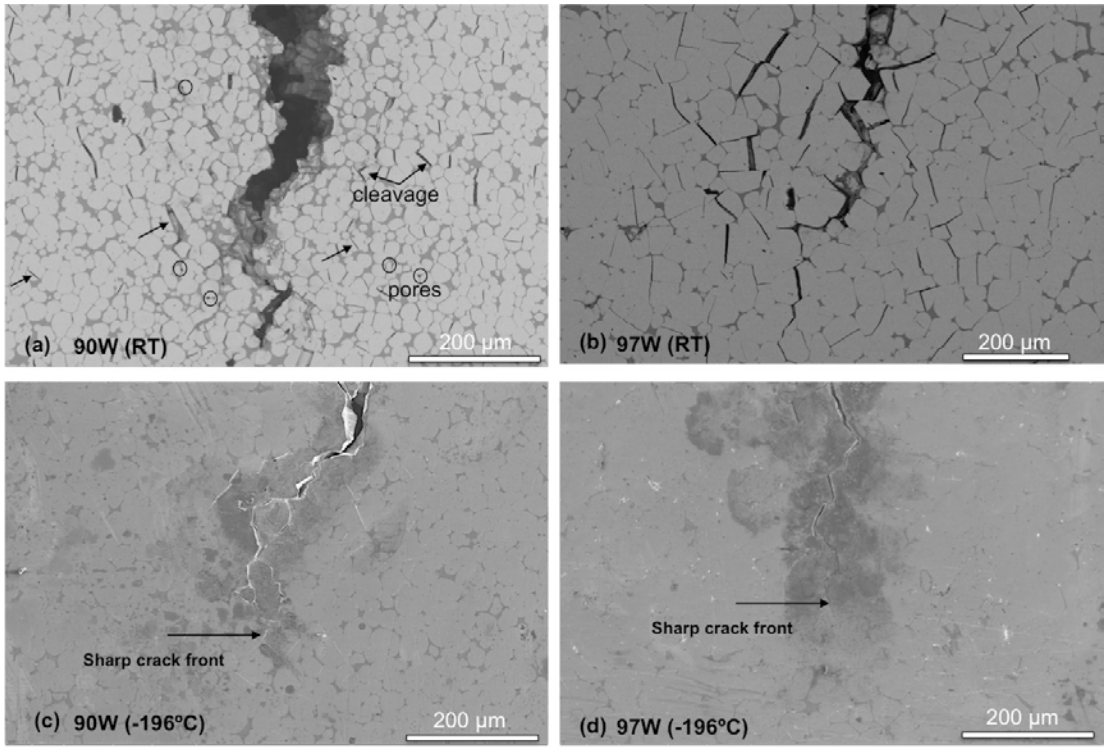

Figure 4. The SEM side surface views for the: (a) 90, and (b) 97W at room temperature; and, (c) 90W, and (d) 97W at -196ºC. RT test showing numerous amount of micro-cleavage and pores, whereas -196ºC test showing only the propagation of the macrocrack (note, the dark region around the propagating cracks are alcohol stains).

Table 4. Process zone damage statistics of WHAs

WHA	Crack mouth opening (µm), Range (µm)	Crack length (µm)	Crack density (mm^{-2})	Process zone W strain (µm/µm)	DP strain (µm/µm)	ΔZ/Z	ΔV/V
90W (RT)	2.53 ± 1.82 (0.415 – 12.12)	15 ± 8	556	0.18	0.20	0.048	0.10
92.5W (RT)	1.66 ± 1.29 (0.270-7.431)	14 ± 6	387	0.17	0.23	0.044	0.09
95W (RT)	3.26 ± 2.63 (0.401 – 14.66)	33 ± 15	339	0.13	0.27	0.041	0.13
97W (RT)	2.28 ± 1.96 (3.47 – 11.69)	45 ± 19	231	0.11	0.18	0.023	0.05
90W (-100C)	1.42 ± 0.86 (0.270-5.763)	16 ± 9	376	0.09	0.17	0.039	0.07
97W (-100C)	0.27	49	4	0.00	0.01	0.00	0.00

ΔZ/Z = change in thickness/initial thickness, ΔV/V = change in volume/initial volume.

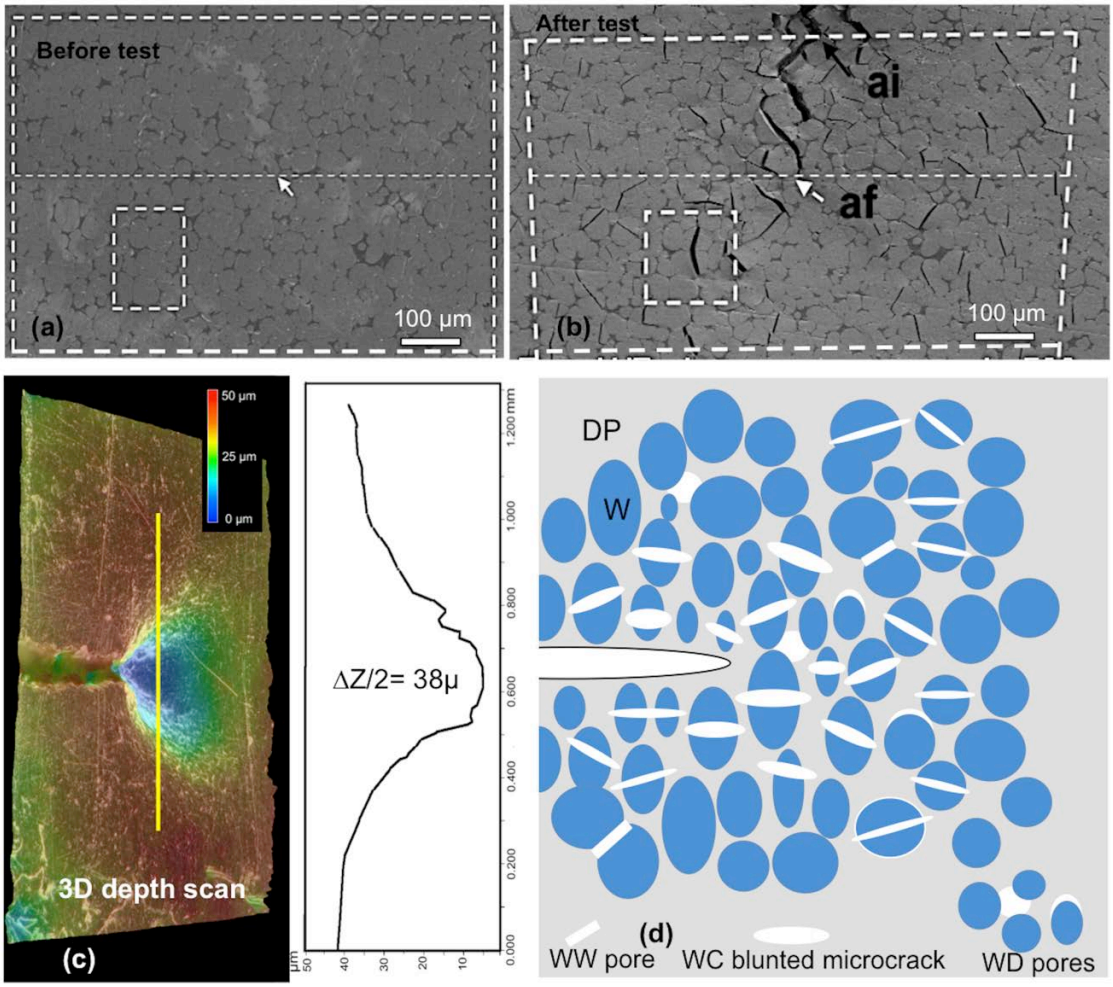

Figure 5. (a and b): the identical location of a 95W alloy before and after deformation, respectively; (c) a 3D depth scan showing the lateral contraction in a 90W alloy near the crack tip; and (d) schematic illustrating the toughening mechanisms.

Discussion

The microcrack arrest and blunting mechanisms, that derive from only small amounts of the ductile NiWFe phase, lead to a remarkable W-NiFe WHA ductilization and toughening. The multi-mechanism toughening will be modelled in future, but this topic is beyond the scope of the current report. Briefly, however, as a result of the requisite 3-dimensional flow geometry of the NiWFe honeycomb web surrounding a large volume fraction of harder W particles, deformation results in a highly triaxial stress state in the DP and large W-NiWFe interface stresses. However, the NiWFe interface is strong, and WD local fracture modes are rare. The predominant local fracture modes are WC and WW, that produce small, particle-sized, microcracks. The small microcracks are arrested and subsequently blunted by the NiWFe DP honeycomb web (Figures 3b, 4 and 5). The web also bridges multiple coplanar microcracks that ultimately form. Thus the key DPT mechanism is shifted from the classical macrocrack bridging and deflection, to process zone microcrack arrest, blunting and bridging. Under these conditions large scale bridging effects and arrest mechanisms stabilize the microcracks against propagation (see Figure 3), in part due to the small dimensions of the W-particles and the corresponding initial microcracks (15 to 45 µ, averaging ≈ 27 ± 15 µm, see Table 4). Further, while the W particles remain encased in the DP, they can plastically deform under high stresses. However, there are limits to toughening by microcrack bridging

that emerge in tests below RT. The primary effect of lower temperature appears to be the increase in WC, leading to decreasing K_{Jm} or K_{Ic} with decreasing temperature, as illustrated in Figure 6a (see Table 3). Here the average of the local fracture mode percentages for all 4 W-NiFe WHAs are plotted as a function of temperature, along with the corresponding average K_{Jm} (Figure 6a).

It appears that the decrease in toughness and transition to elastic fracture is associated with the increased brittleness of W at lower temperature leading to more initial WC microcracks, which are not isolated to fewer and more widely-spaced W particles. The larger number of proximate microcracks link to form larger mesocracks that, in the limit, unstably propagate as an elastic fracture event. However, plastic rupture of the linked microcrack bridging ligaments still contributes to a higher WHA toughness compared to monolithic W.

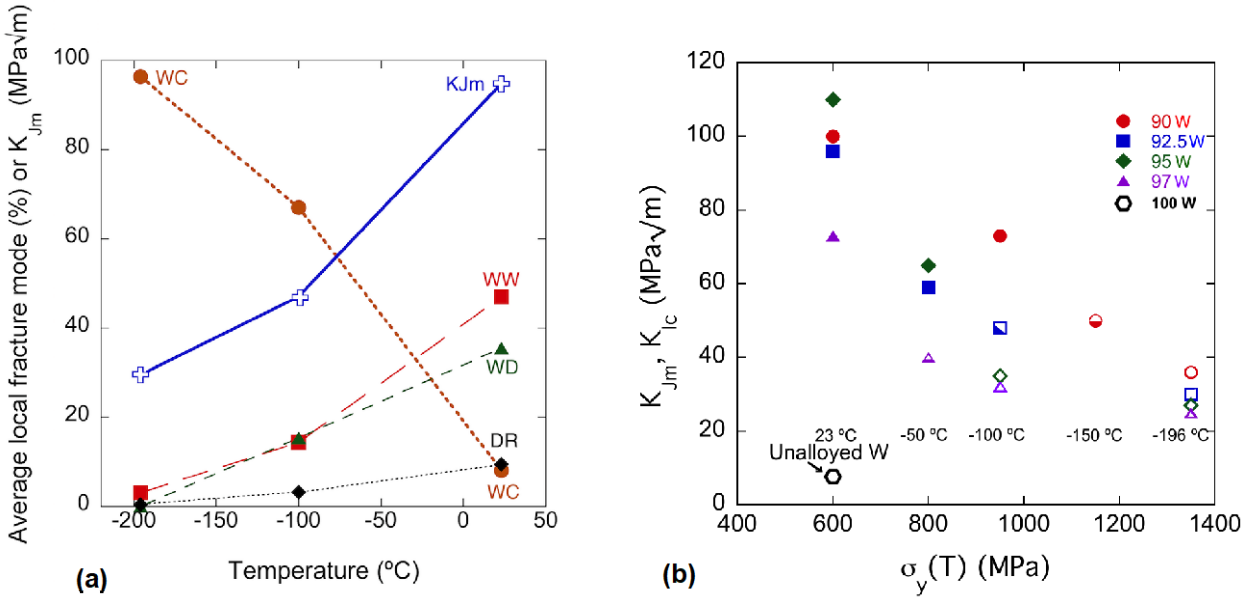

Figure 6. (a) The average local fracture mode percentages as a function of temperature along with the corresponding average K_{Jm} or K_{Ic} for all the 4 WHAs, and (b) toughness (K_{Jm}) versus the estimated W yield strength (σ_y) for the various WNiFe WHAs. The filled and unfilled symbols represent stable crack growth and elastic (unstable) fracture, respectively, while the half-filled symbols represent mixed stable and unstable crack growth. The K_{Ic} for monolithic (unalloyed) W is also shown.

The most important consequence of this combination of micromechanisms is the large dissipation of plastic energy, partly due to the dilatational strains, from the blunting microcracks, that also shield the crack tip fields, greatly reducing the local stress concentrations. Thus, the process zone deformation leading to crack growth in some ways resembles classical microvoid nucleation (initial microcracking), growth (microcrack blunting and opening) and coalesce (microcrack linking and unstable growth), typical of highly ductile metals and alloys, such as low alloy reactor pressure vessel (RPV) steel.

A simple dimensional ductile fracture cohesive zone plain strain model rationalizes the observed RT WHA toughness in terms of the tensile flow stress ($\sigma_{fl} \approx 750$ MPa), elastic modulus and Poisson's ratio ($E \approx 400$ GPa and $\nu \approx 0.28$) and the typical critical CTOD ($\delta_c \approx 35$ μm) observed at crack growth initiation as:

$$K_{Jc} \approx \sqrt{[2\sigma_{fl}E\delta_c /(1-\nu^2)]} \approx 151 \text{ MPa}\sqrt{\text{m}}$$

Note K_{Jc} has a contribution from the process zone dilatation.

The tests at low temperature were aimed at assessing the effects of decreases in the W-particle K_{Ic}, associated with a corresponding increased σ_y. While not fully representative, the low temperature tests may partially emulate irradiation hardening at higher service temperatures. Figure 6b shows the K_{Jm} or K_{Ic} versus σ_y (T) for the 4 WHAs. K_{Jm} systematically decreases in toughness with increasing σ_y. Again, however, the WHAs are much tougher than monolithic W at RT. Assuming lower temperature is an approximate surrogate for neutron irradiation hardening, $\Delta\sigma_y$ up to 750 MPa may be tolerable in WHA plasma facing components. However, only the 90W WHA is able to avoid elastic fracture with $\Delta\sigma_y \approx 550$ MPa. At higher W, the corresponding hardening limit to avoid elastic fracture is $\Delta\sigma_y < \approx 200$ MPa.

There are numerous open questions regarding the use of W-NiFe WHA for fusion divertor applications. First and perhaps foremost, Ni is not a low activation element allowed in the class of normal reduced activation ferritic-martensitic steels. Thus the system level tolerance for limited amounts of Ni should be assessed. Further, these alloys will almost certainly be part of hybrid materials components, perhaps serving an intermediate crack arrest function like in a monolithic W:W-NiFe:ODS steel:Cu multilayer. The opportunities for using graded systems and additive manufacturing techniques for component fabrication are obvious. Other issues include temperature limits, phase stability, irradiation effects, DP and interface strength at higher temperature including in the creep regime, and integrated thermal-mechanical durability in the presence of high temperatures and time-varying very intense heat fluxes.

Ongoing and Future Work

- Pre-cracking the 90 to 97WNiFe 3PB bars has been completed, and they will be tested to evaluate high-temperature (600 and 800ºC) toughness and crack growth.
- The 50Ni-30W-20Fe (wt.%) will be further exploring to assess its contribution in toughness.
- The multi-mechanism toughening model will be developed.
- Special fracture specimens will be tested measure interface toughness and strength.
- Thermal shock tests will be performed on these WNiFe alloy and hybrids.

Acknowledgement

We like to acknowledge the support provided by U.S. Department of Energy (DOE) through the Office of Fusion Energy Sciences (DOE Pacific Northwest National Laboratory (PNNL) Tungsten: 8-442520-22403-3 ROF02), and DOE-Fusion (8-442520-22419-3). The U.S. National Science Foundation supported California Nanoscience Institute provided facilities critical the success of this research.

References

[1] M. Rieth, S.L. Dudarev, S.M. Gonzalez De Vicente et al, Recent progress in research on tungsten materials for nuclear fusion applications in Europe, J. Nucl. Mater. 432 (2013) 482–500.

[2] P. Norajitra, R. Giniyatulin, W. Krauss, V. Kuznetsov, I. Mazul, I. Ovchinnikov, J. Reiser, M. Rieth, V. Widak, Current status of He-cooled divertor development for DEMO, Fusion Eng. Des. 84 (2009) 1429–1433.

[3] V. Philipps, Tungsten as material for plasma-facing components in fusion devices, J. Nucl. Mater. 415 (2011) S2–S9.

[4] J. Reiser, J. Hoffmann, U. Jäntsch, M. Klimenkov, S. Bonk, C. Bonnekoh, M. Rieth, A. Hoffmann, T. Mrotzek, Ductilisation of tungsten (W): On the shift of the brittle-to-ductile transition (BDT) to lower temperatures through cold rolling, Int. J. Refract. Met. Hard Mater. 54 (2016) 351–369.

[5] B. Gludovatz, S. Wurster, A. Hoffmann, R. Pippan, Fracture toughness of polycrystalline tungsten alloys, Int. J. Refract. Met. Hard Mater. 28 (2010) 674–678.

[6] M.E. Alam, S. Pal, K. Fields, G.R. Odette, Mechanical properties characterization of 90-97wt% WNiFe heavy alloys, 2016. DOE/ER-0313/61 (2016), DOE Fusion Reactor Materials Program Semiannual Progress Report, 61.

[7] K.T. Venkateswara Rao, G.R. Odette, R.O. Ritchie, Ductile-reinforcement toughening in γ-TiAl intermetallic-matrix composites: Effects on fracture toughness and fatigue-crack propagation resistance, Acta Metall. Mater. 42 (1994) 893–911.

[8] M.G. Mendiratta, J.J. Lewandowski, D.M. Dimiduk, Strength and ductile-phase toughening in the two-phase Nb/Nb5Si3 alloys, Metall. Trans. A. 22 (1991) 1573–1583.
[9] A.G. Evans, R.M. Cannon, Toughening of brittle solids by martensitic transformations, Acta Metall. 34 (1986) 761–800.
[10] A.G. Evans, Z.B. Ahmad, D.G. Gilbert, P.W.R. Beaumont, Mechanisms of toughening in rubber toughened polymers, Acta Metall. 34 (1986) 79–87.
[11] M.E. Alam, S. Pal, K. Fields and G.R. Odette, "Ductile Phase Toughening of 90-97wt.% W-NiFe Heavy Metal Alloys", in DOE/ER-0313/60 - Volume 60, Semiannual Progress Report, June 30 (2016) 93-102.
[12] K.S. Churn, R.M. German, Fracture behavior of W-Ni-Fe heavy alloys, Metall. Trans. A, Phys. Metall. Mater. Sci. 15 A (1984) 331–338.
[13] K. Hu, X. Li, X. Ai, S. Qu, Y. Li, Fabrication, characterization, and mechanical properties of 93W-4.9Ni-2.1Fe/95W-2.8Ni-1.2Fe/95W-2.8Ni-1.2Fe-1Al_2O_3 heavy alloy composites, Mater. Sci. Eng. A. 636 (2015) 452–458.
[14] X. Gong, J. Fan, F. Ding, Tensile mechanical properties and fracture behavior of tungsten heavy alloys at 25-1100 °C, Mater. Sci. Eng. A. 646 (2015) 315–321.
[15] Z.H. Zhang, F.C. Wang, S.K. Li, L. Wang, Deformation characteristics of the 93W-4.9Ni-2.1Fe tungsten heavy alloy deformed by hydrostatic extrusion, Mater. Sci. Eng. A. 435–436 (2006) 632–637.

4.4 SIMULATION OF MECHANICAL PROPERTIES OF TUNGSTEN COMPOSITES—L. M. Garrison, A. Hayes (Oak Ridge National Laboratory)

OBJECTIVE

The objective of this project is to perform a finite element analysis of a tensile test simulation of tungsten composites to understand and optimize their properties for use as plasma facing components in fusion reactors.

SUMMARY

As a first step toward modeling tungsten composites, simplified tensile tests of individual tungsten foils were simulated. To realistically define the material properties required for modelling with Analysis System (ANSYS), experimentally measured stress-strain data from uniaxial tensile tests was imported. These tests were completed at room temperature for unirradiated tensile bars machined from 250 µm thick tungsten foil. Strength, elasticity, and other relevant material properties were manually defined for tungsten foil as well. A mesh consisting of 4806 elements was generated by ANSYS across a solid body geometry and a fixed support was applied to one end face and a force of 550 N was applied to the other. A finite element analysis of the uniaxial tensile test simulation over 1 second solved for the stress, strain, and deformation in ANSYS. This project considers errors relating to the inclusion of relevant input parameters, geometry, mesh fineness, and force application location and rate.

PROGRESS AND STATUS

Introduction

Since tungsten is brittle and has low fracture toughness, tungsten composites and joints between tungsten and other materials are required. There is general promise for tungsten composites, but their behavior under relevant fusion conditions is not yet predictable. For instance, initial tests of tungsten copper laminate composite had good unirradiated tensile ductility, but little to no ductility after neutron irradiation.

There are several types of tungsten composites being considered in the fusion community, including sintered, laminate, and tungsten-fibre reinforced materials. Many of these options have been successfully fabricated on a trial basis, but they have not been optimized. However, simulation of tungsten composites facilitates easier parameter modification, anticipates material properties and behavior, and identifies trends while avoiding the costs of time and resource intensive fabrication.

Of the tungsten composites considered in the fusion community, the laminate composite was chosen to model first. To properly model a laminate with such complex interface properties, individual tungsten, steel, and copper foils must be accurately simulated to reduce error in modeling the composite material. Foils of varying thicknesses can then be combined using the ANSYS Composite PrepPost (ACP) software to model laminates. Individual foils and a variety of laminates will be tensile tested to compare material and mechanical properties.

Results

<u>Input Parameters and Geometry</u>

In this first round of testing, only the minimum material properties required to simulate a tensile test were defined for a sample tungsten material in Table 1. The simulated tungsten is meant to imitate the properties of a tungsten foil originally 250 µm thick. It was assumed that density would be unchanged during fabrication, so the value for tungsten metal was used. Isotropic elasticity was defined using Poisson's ratio and Young's modulus. In several previous studies, elasticity properties were found to be similar when tested for both tungsten metal and tungsten foil [1], [2], [3]. Values for the yield strength and ultimate tensile

strength were taken from tensile tests of 250 µm thick tungsten foil. Stress-strain data from uniaxial tensile tests performed at room temperature was imported to improve the material definition. These values defined the material “Tungsten Foil” in the Engineering Data for the project in ANSYS.

Table 1. Material property input parameters to ANSYS model for 250 µm thick tungsten foil

Property	Value	Unit	Citation	Form
Density	19250	kg m^-3	[1]	Metal
Tensile YS	1994.2	MPa	Tungsten Foil Tensile Data W10a-1	Foil
Tensile US	2023.2	MPa	Tungsten Foil Tensile Data W10a-1	Foil
Poisson's Ratio	0.28	-	[1], [2]	Foil
Young's Modulus	4.05E+11	Pa	[1], [2], [3]	Foil

The SSJ2 geometry was used for both the experimental and simulated tensile tests . This is a tensile bar with dimensions 16 x 4 x 0.5 mm. The specimen design is shown in Figure 2. The complimentary experimental data applies for a 250 µm thick foil, but its properties were extrapolated to a 500 µm dummy thickness as the ACP composite module has not yet been integrated into the model.

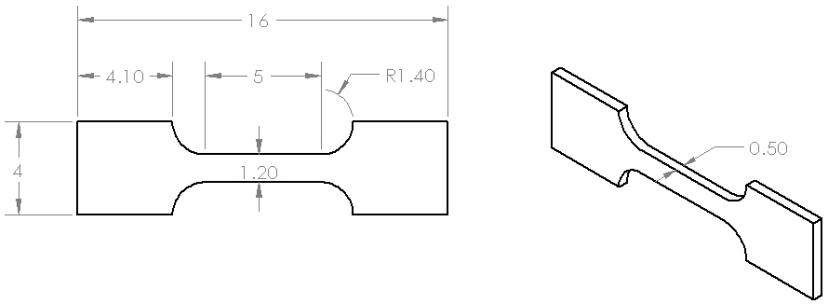

Figure 1. The SSJ2 specimen geometry, with dimensions in mm.

Mesh and Model Setup

The mesh generated with ANSYS is shown in Figure 2. The size function used was “Proximity and Curvature”. The mesh had a fine relevance center with 4806 elements, medium smoothing with 5 iterations, fast transition between element types, and a coarse (91° to 60°) span angle center. These settings allowed for an adequately fine mesh and precise enough solution for the general scope of this project without taking too much solving time or processing power.

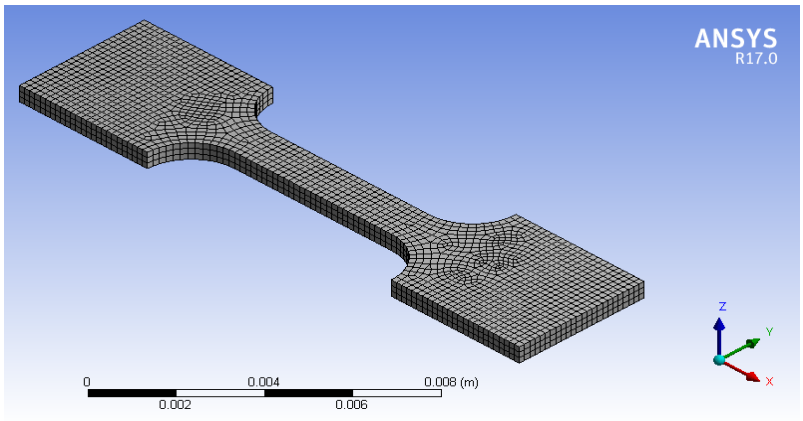

Figure 2. Visual representation of geometry division into mesh elements.

The conditions for this first simulated tensile test were simplified and differed from the real experiment in several ways. There was only a fixed support (Figure 3 mark A) and one uniform force of 550 N (Figure 3 mark B), each applied at opposing ends of the tensile bar. Each was applied uniformly across an entire face in the YZ plane, which is not realistic. The position of the grips during an experiment changes the locations of the support and the forces, and therefore the breaking points and deformation of the bar. Additionally, the simulated force was applied over 1 second, but the experimental force was applied over the course of at least 2 minutes. This does somewhat influence the results, but compounded with several other sources of error, the drastic decrease in solving time outweighed the benefit of increased accuracy.

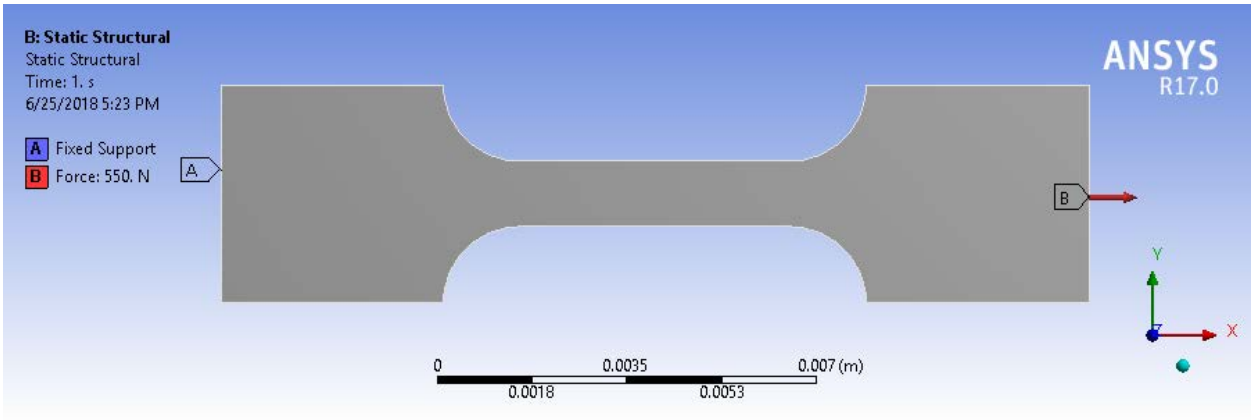

Figure 3. A fixed support was applied across the end in the YZ plane marked with “A” and a 550 N force was uniformly applied over 1 second in the positive x direction across the end in the YZ plane marked with “B”.

Results

Figures 4 through 8 show the results at the end of the 1 second test when the full 550 N has been applied and the material has stretched to reach equilibrium. The undeformed ghost is only shown in Figure 4 and it is excluded in Figures 5 through 8 to display the mesh elements instead. The simple, symmetric geometry allowed a coarse mesh to give a general idea of the results in a short solve time of about 1 minute. The points carrying the greatest load are in the four inversely filleted faces of the specimen and are the most likely locations for failure to occur. However, the grip location was inaccurately defined, so this prediction is not reliable.

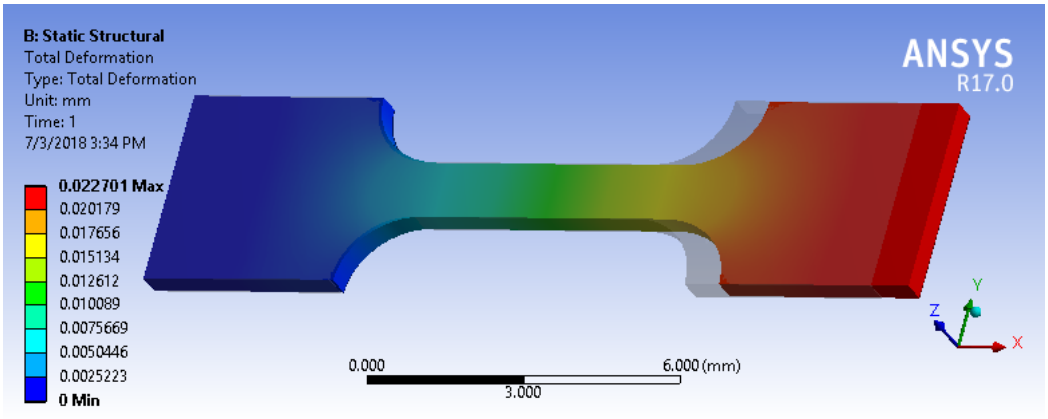

Figure 4. Total deformation, including undeformed model.

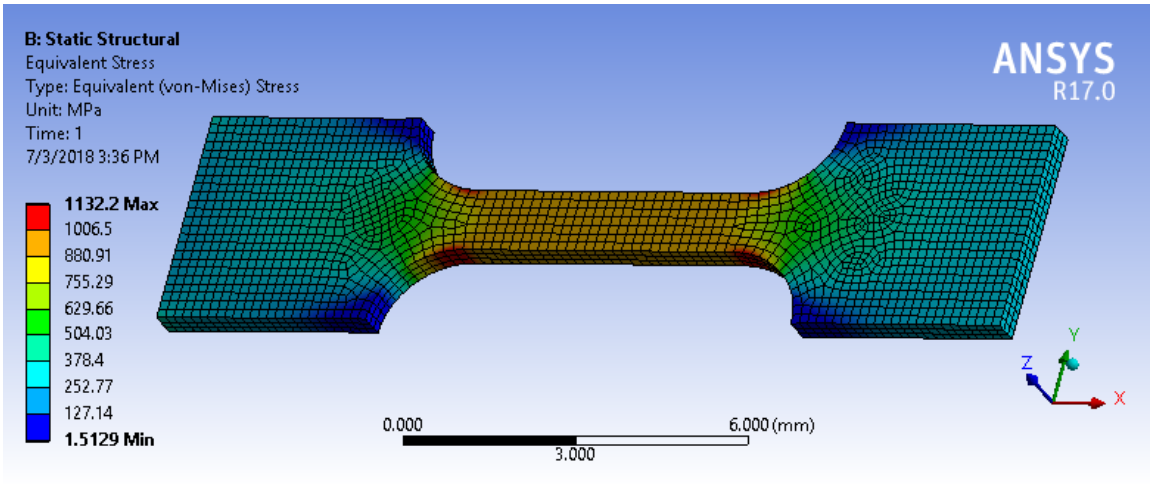

Figure 5. Equivalent (von-Mises) stress.

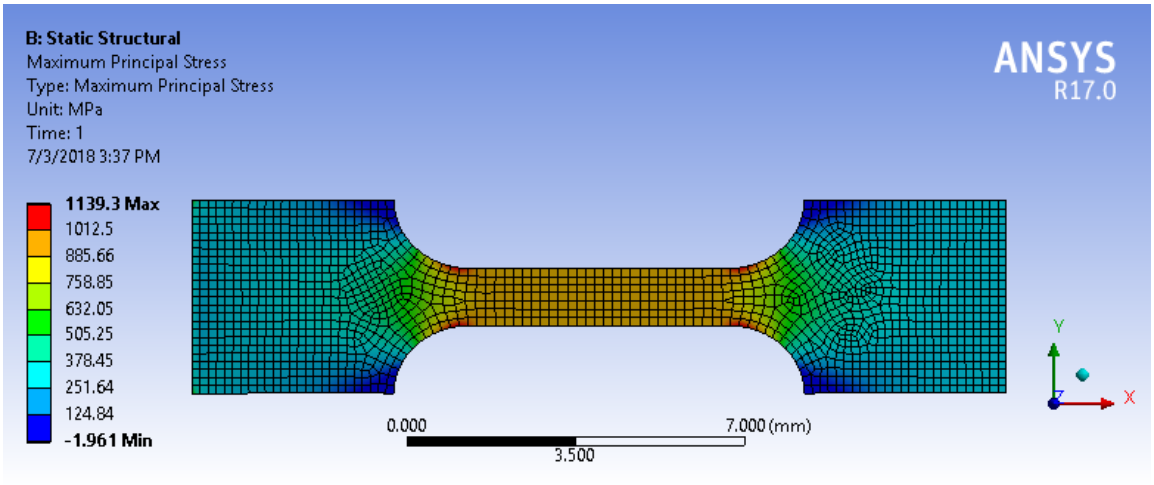

Figure 6. Maximum principal stress.

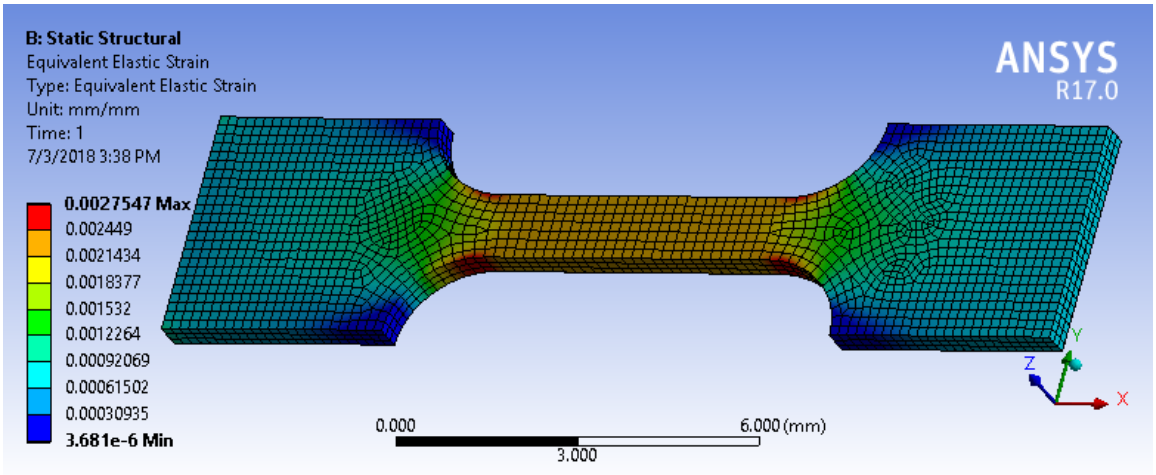

Figure 7. Equivalent elastic strain.

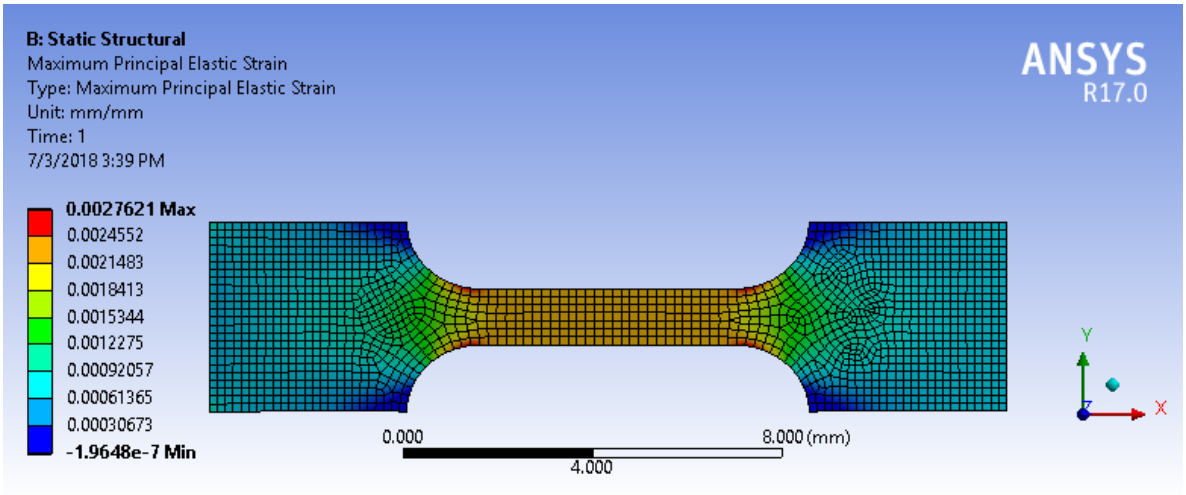

Figure 8. Maximum principal elastic strain.

Future Work

A basic understanding of a tensile test simulation was obtained and several routes for improving this model were identified. The fixed support and applied forces need to be updated to match the experimental setup. This adjustment has the highest priority, as the simulated failure points do not match the expected failure location, which is along the 5 mm gauge segment of the specimen. The simulated tungsten material retains the same geometry as the tested SSJ2 tensile bars, but a singular tungsten foil will have different properties depending on its thickness. The simulated tensile bar needs to match the geometry of the material in question. Results from an updated model also must be validated with experimental data. Additional foil properties may need to be measured to be included in the model.

Once the model sufficiently reflects experimental results, mesh optimization should be explored, using relevant finite element analysis literature. The force also needs to be applied over the same amount of time as the corresponding experimental tensile test.

Once the single foil tensile test is modeled satisfactorily, the modeling process described here will be applied to composite applications. The ANSYS ACP has laminate design capabilities that can be integrated to simulate tungsten-steel and tungsten-copper composites with various foil thicknesses.

References

[1] E. Lassner, W. -D. Schubert, Tungsten: Properties, Chemistry, Technology of the Element, Alloys, and Chemical Compounds, Kluwer Academic / Plenum Publishers, New York, 1999.

[2] E. Grünwald, R. Nuster, R. Treml, D. Kiener, G. Paltauf, R. Brunner, Young's Modulus and Poisson's Ratio Characterization of Tungsten Thin Films via Laser Ultrasound, Materials Today: Proceedings 2 (2015) 4289-4294.

[3] J. Reiser, M. Rieth, A. Moslang, B. Dafferner, A. Hoffmann, X. Yi, D.E.J. Armstrong, Tungsten foil laminate for structural divertor applications – Tensile test properties of tungsten foil, Journal of Nuclear Materials 434 (2013) 357-366.

4.5 MECHANICAL PROPERTIES OF TUNGSTEN IN THE PHENIX COLLABORATION IRRADIATION—L.M. Garrison, N. Reid, B. Gregory, T. Ray, Y. Katoh (Oak Ridge National Laboratory)

OBJECTIVE

The photon electron new heavy ion experiment (PHENIX) collaboration tungsten irradiation aims to expand the database on neutron irradiation data for tungsten materials.

SUMMARY

Hardness tests and equibiaxial flexure disc tests have been completed on the unirradiated control materials from the PHENIX high flux isotope reactor (HFIR) RB*19J irradiation experiment. The RB*19J capsule included over 20 varieties of tungsten and had three temperature zones, nominally 500, 800, and 1200°C. Hardness tests on the unirradiated materials were completed. Hardness tests have also been completed on the irradiated samples from the 800°C sub-capsule and are planned to continue for the other materials. Equibiaxial flexure tests were done on selected unirradiated samples. Multiple other mechanical tests will follow including tensile tests and fracture toughness tests.

PROGRESS AND STATUS

The PHENIX United States (US)-Japan collaboration has a goal of investigating tungsten for use in future fusion reactors. For this potential use, more information is needed about tungsten's response to neutron irradiation at fusion relevant conditions. To investigate this, the PHENIX collaboration prepared over 1500 tungsten samples for the HFIR RB*19J irradiation capsule, including several varieties of single and polycrystalline tungsten and tungsten alloys. The materials are identified by a unique two symbol code for the RB*19J irradiation, which is also used here for tracking the many material varieties.

Hardness

A full range of microhardness indent loads were tested on select materials from the PHENIX campaign using a Future-Tech FM-7 microhardness tester to determine the hardness dependence on indent load for these materials. The expected trend is a slightly exponential decay that levels out to the true hardness value as the load increases. This true hardness for tungsten is typically found between 200-500 g, varying based on the surface condition of the samples.

The data in Figure 1 shows a clear trend as expected, but for samples RW-D6T1 (material code RW) and WPIM (material code ZE) the curve appears to level off at higher loads or not at all. One possibility for why the leveling off is not seen until later for sample RW-D6T1 is that the surface structure is rough with many cracks or gaps. The WPIM sample levels off within one standard deviation at approximately 500 g. There are also large deviations of hardness values taken at loads of 10, 25, and 50 g, simply due to the equipment and human error of measuring. The expected trend is displayed for International Thermonuclear Experimental Reactor (ITER)-B (material code BT), which had a smooth surface structure.

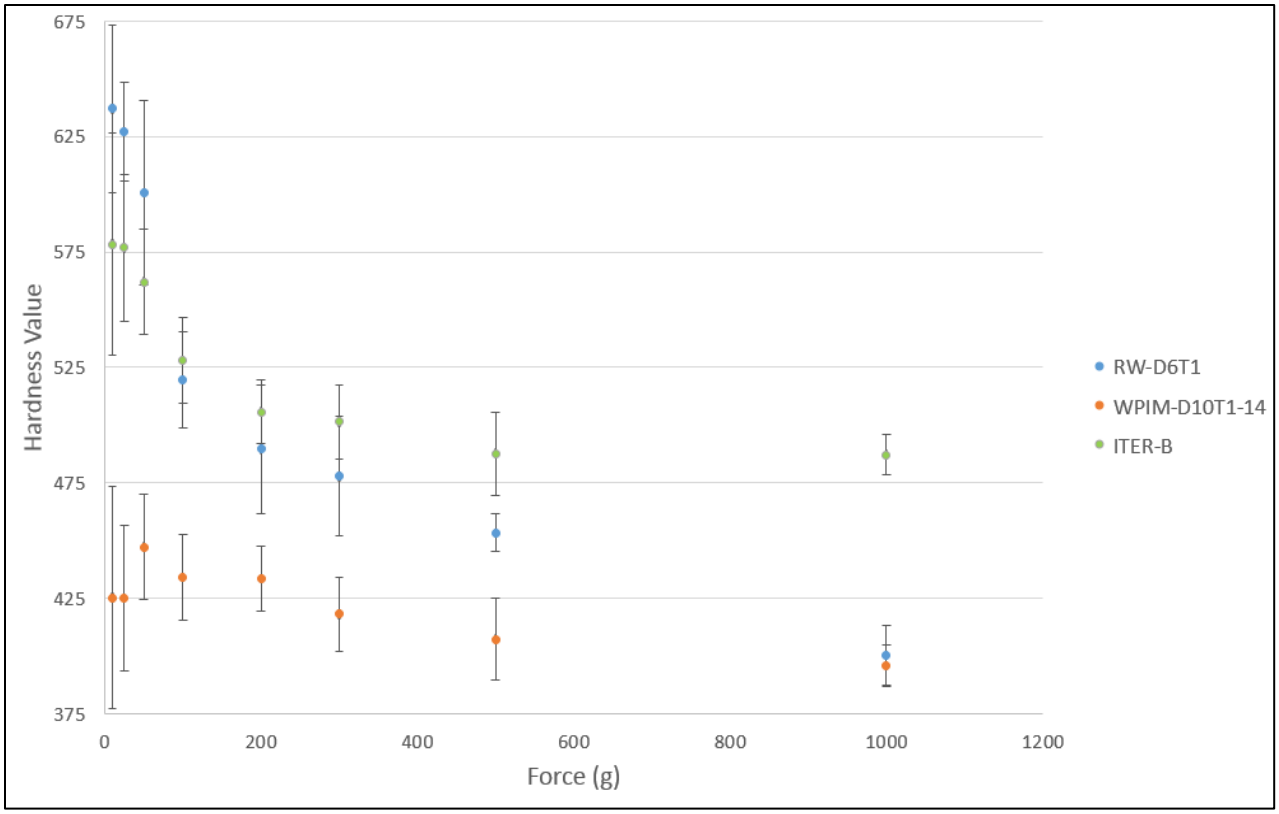

Figure 1. Vickers microhardness values on three tungsten types with a range of indent loads. Error bars represent the standard deviation in the five measurements averaged for each hardness value.

The hardness of 10 tungsten-based samples from the Japan side of the PHENIX collaboration was determined with Vickers microhardness testing. Table 1 displays the composition, size, and processing of each of the 10 samples prior to hardness testing. These samples include pure tungsten and tungsten alloys, and several samples were cold-rolled and heat-treated. Each sample was tested with loads of 200 g and 1000 g with a ten second dwell time. The 200 g load was chosen to align with past experiments conducted with 200 g loads. Five measurements were averaged at each load to determine the hardness of each sample at that particular load.

Figure 2 displays the results of Vickers microhardness testing on the tungsten-based samples at 200 g and 1000 g loads. The hardness values for induvial samples at 200 g and 1000 g loads were similar, so the 200 g measurements were likely accurate. The samples that were cold-rolled then heat-treated were the softest of all samples, and the samples that were only cold-rolled were still softer than the unprocessed samples except for Allied W. The samples alloyed with rhenium were softer than samples of similar processing without rhenium, and the alloys including potassium were equal to or slightly harder than samples of similar processing without potassium. Thus, it appears that cold-rolling and heat-treating a tungsten-rhenium alloy will result in the softest sample.

Sample KY01, not displayed on Figure 2, had a hardness of 1014±180 HV at a load of 1000 g. No clear indent was present at 200 g, and even at 1000 g the indents had varying shapes and no clear boundary. Thus, the measured hardness of this sample may not be an accurate representation of its true hardness value. This material was determined to be incredibly brittle in the past, so the load was not increased beyond 1000 g to avoid the possibility of fracture.

Table 1: Composition, processing, and size of ten tungsten-based samples analyzed by Vickers microhardness testing

Sample	Material	Processing	Disk diameter (mm)	Disk thickness (mm)
KY01	SiC_f(40%)/W(60%)	Tungsten with SiC fibers	6	0.25
00K05	Allied W	Commercial polycrystalline tungsten	6	0.25
Y00K	UFG-W	Ultra-fine grain tungsten	6	0.50
7128	W-5Re	Tungsten with 5% Re	6	0.50
P006	Pure W	Rolled, 80%, X-direction	3	0.25
6005	K-doped W	Rolled, 80%, X-direction	3	0.25
4107	W-3%Re	Rolled, 80%, X-direction	3	0.25
8006	K-doped W-3%Re	Rolled, 80%, X-direction	3	0.25
X007	Pure W	Rolled, 80%, X-direction, heat treated at 1500°C	3	0.25
7006	K-doped W-3%Re	Rolled, 80%, X-direction, heat treated at 1500°C	3	0.25

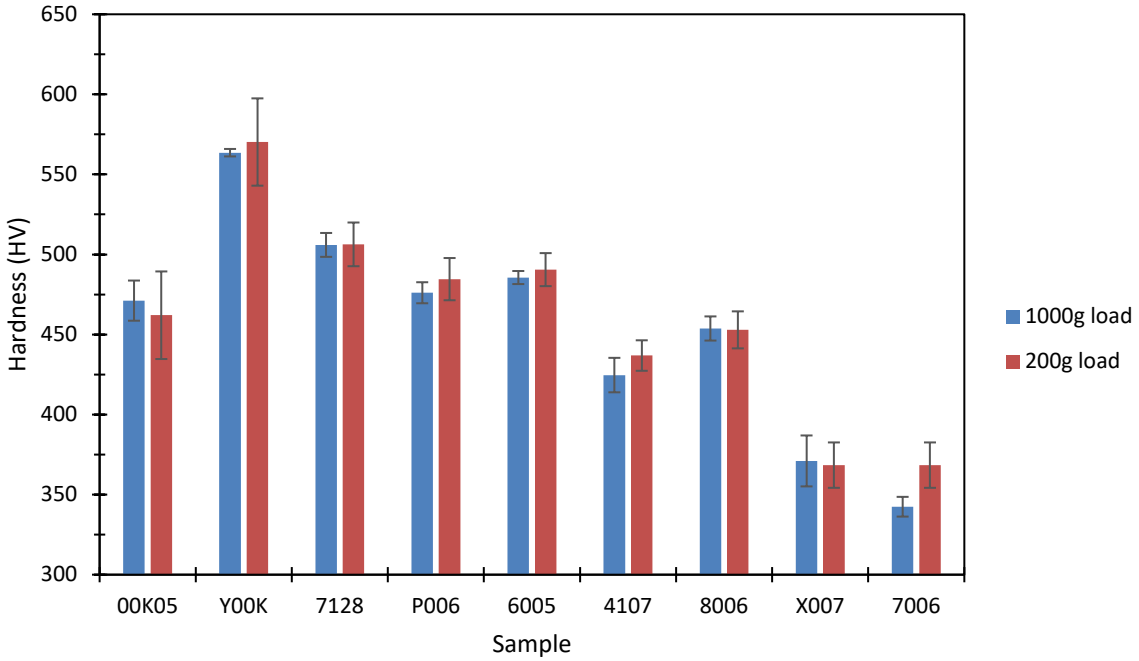

Figure 2: Microhardness results on nine of the tungsten-based samples. Error bars represent the standard deviation in the five measurements.

Vickers microhardness tests have been completed on many of the materials irradiated in the ~800°C sub-capsule of the PHENIX RB*19J capsule. The results are being analyzed and the hardness test of the other temperature zone materials is ongoing.

Equibiaxial Flexure Tests

Tungsten materials exhibit brittle fracture behavior at room temperature. The strength of brittle materials is not a deterministic property; however, it is adequately described by the equibiaxial flexural (EBF) test. This is because multi-axial stress states are necessary to evaluate not only the weakest-link failure state (the so-called *characteristic strength* of the bulk material), but the entire distribution of flaws (size and

orientation) that exist in the sample. This type of test provides a much deeper understanding of the scatter of failure strength in brittle, ceramic-like refractory metals. It becomes an even more valuable tool in the case of neutron irradiation-induced embrittlement. This test has several benefits compared to a simple uniaxial tensile test. The EBF results are derived from multiple tensile stresses, and it reflects the intrinsic fracture toughness of the material. It gives additional information in the crack pattern fractography and probabilistic Weibull flaw distributions. Additionally, the generated stresses are lowest at the specimen edges – where sample edge preparation is a pitfall of uniaxial tensile testing.

Preliminary EBF tests were done on selected unirradiated PHENIX 6 mm disk specimens. A single test was performed on orientations A, B, and C of a polycrystalline W block (irradiation material codes AT, BT, CT respectively), and a rolled W foil (irradiation material code RE). The accuracy of the estimate of the characteristic strength, $\hat{\sigma}_\theta$, of the bulk material W with the 6 mm disk size and geometry that is standard for specimens from the RB-19J capsule dramatically increases with number of EBF test specimens, *N*. For that reason, 10 AA 2 mm foil (irradiation material code EE) disk samples were tested to develop a flaw distribution for this tungsten material. One of these 10 disks was previously used for hardness tests, shown in Figures 3-5.

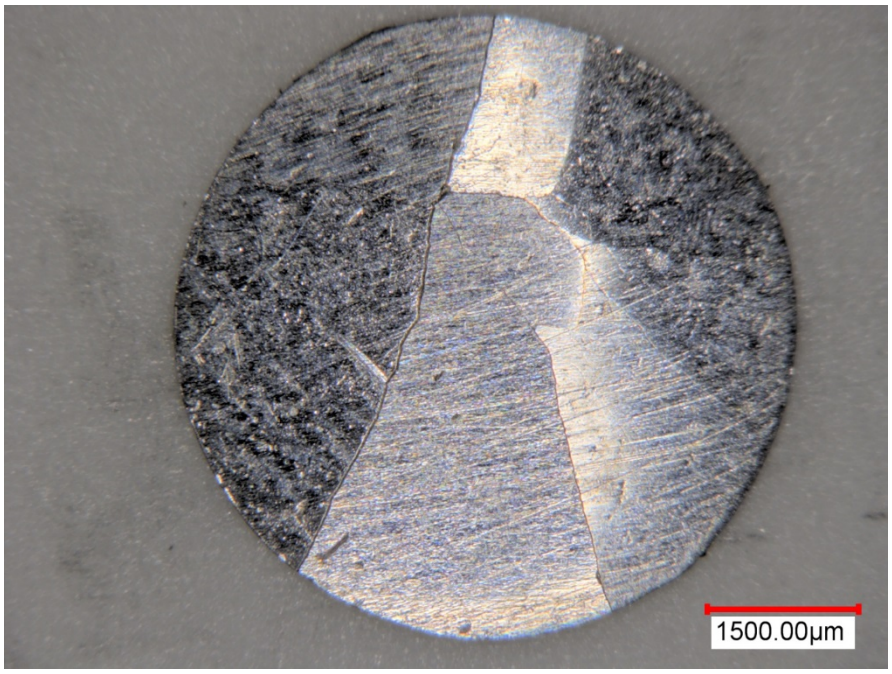

Figure 3. Tension side of hardness-tested AA 2 mm foil (facing the support ring during test).

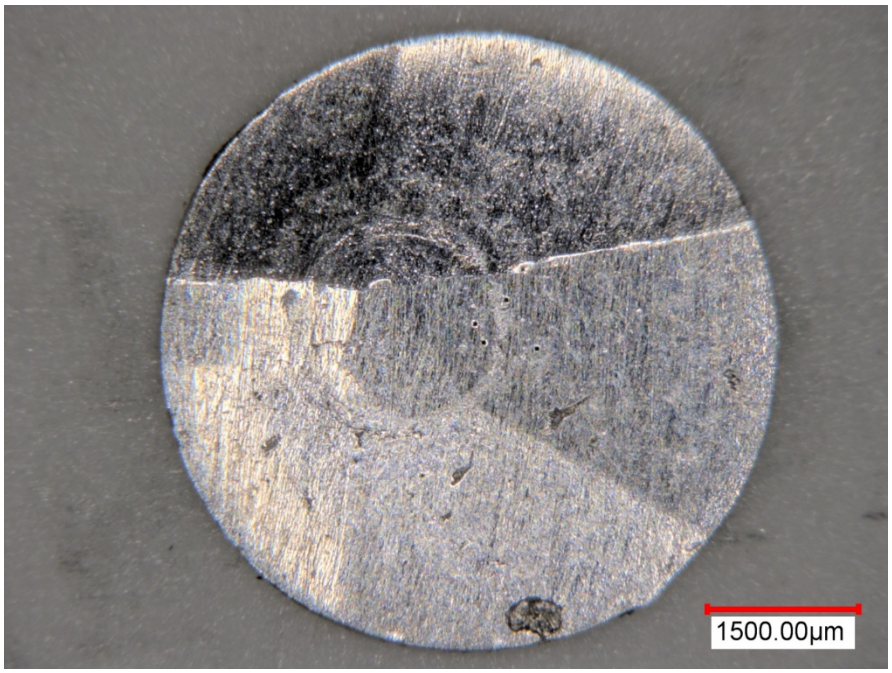

Figure 4. Compression side of hardness-tested AA 2mm foil (facing the load ring during the test, tape side).

Following the procedure of American Society for Testing and Materials (ASTM) C1239-13, the calculated equibiaxial strength, σ_f, was fitted with the probability of fracture, P_f. The resulting fit gave an R-squared value of 0.983 and an estimated Weibull modulus, $\hat{m}$, of 5.28. However, since there is statistical bias in the sample size, this value should be reduced by an unbiasing factor to 4.54. Since the value of $\hat{m}$ is greater than unity, this points to only minor variation in fracture behavior and suggests that flaws are quite evenly distributed in the sample. This slight variation allows us to use a characteristic strength of $\hat{\sigma}_\theta = 2{,}880\ MPa$ as a good descriptor of sample-to-sample equibiaxial strength, where 63.2% of specimens will fail below this value of stress. The 90% confidence interval gives a reliable range for expected sample breaking strength, and where we see the Weibull modulus for the AA 2mm foil falls within. For the Weibull modulus, the interval is $2.92 < m < 7.16$. The 90% confidence interval for characteristic equibiaxial strength is $2{,}550\ \text{MPa} < \sigma_\theta < 3{,}270\ \text{MPa}$.

The hardness-tested sample did not have the smallest breaking load, *F*, but its σ_f is below the lower-limit estimate for the characteristic strength, $\hat{\sigma}_{\theta,lower} = 2{,}550\ MPa$. However, due to the linearity of the plotted σ_f values, we can assume unimodal failure of the AA 2 mm foil specimens due to a single fracture origin type. Fractography analysis of the surface under tension can determine the mode of failure (pore, machine damage, large grain). For example, Figure 3 shows the tension side of the specimen, which does not look dissimilar from any of the other fracture patterns of AA foils. Figure 4 shows the compression side, where we can see five black dots near the center of the disc that are the hardness indentations.

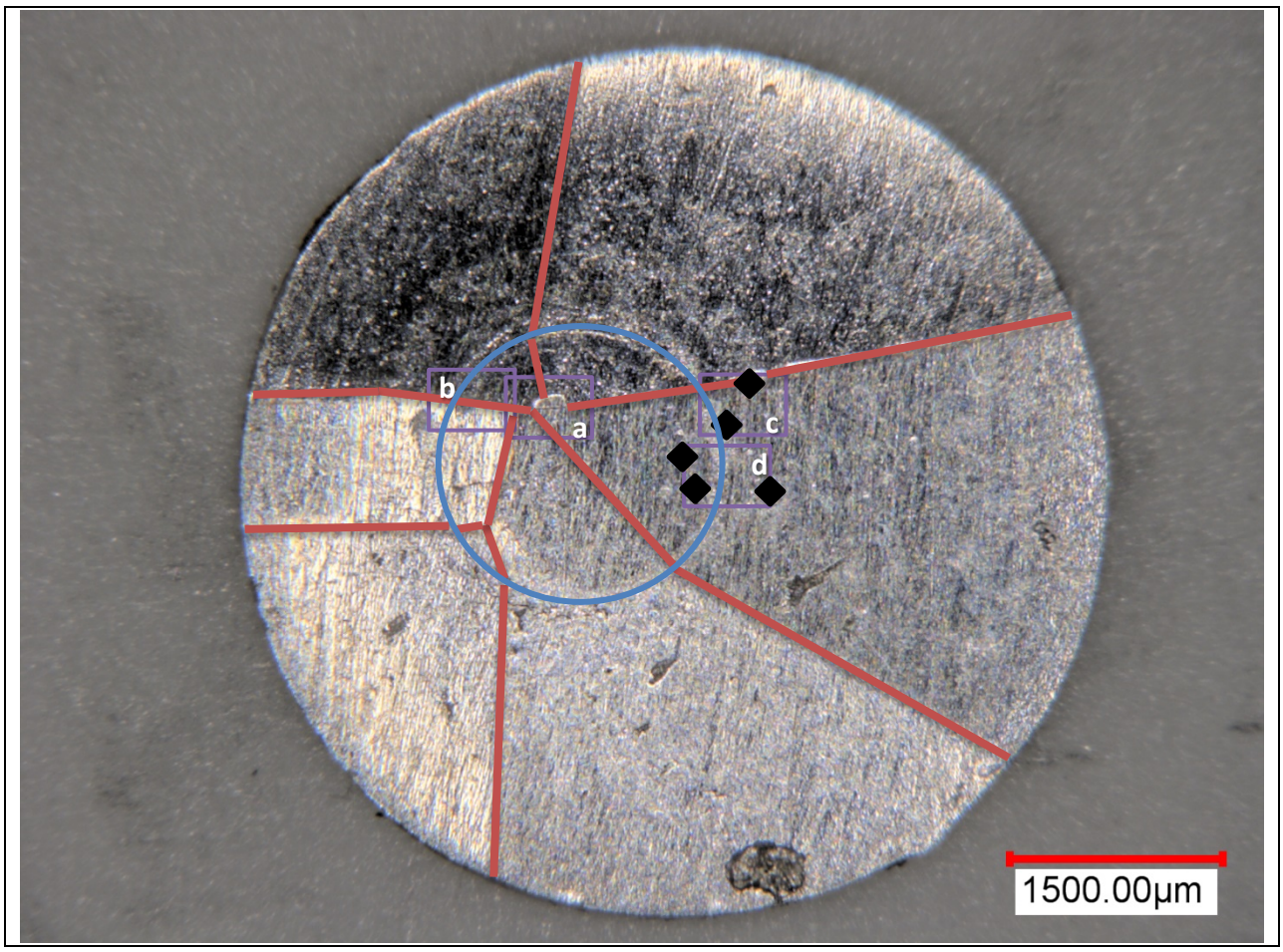

Figure 5. A map of the compression side of specimen AA, as in Figure 4. The black diamonds are the hardness indentations. The blue circle shows location of the load ring during test. The orange lines are bends or cracks. The lavender boxes identify areas shown in Figure 6.

A map of the hardness-tested disk is given in Figure 5. The crack likely initiated from near the dimple shown in the box “a”. The primary crack plane extends from the left of box b to the right of box c, where we can clearly see this plane in Figure 3 going from north to southwest. Given that some of the hardness test indents (box d) are located within the load ring area of the sample (blue ring), the cracks do not appear at all close to the activation volume of the hardness test. Other hardness tests are outside the load ring, but inside the support ring of the flexural test. These also do not appear to be crack initiation points.

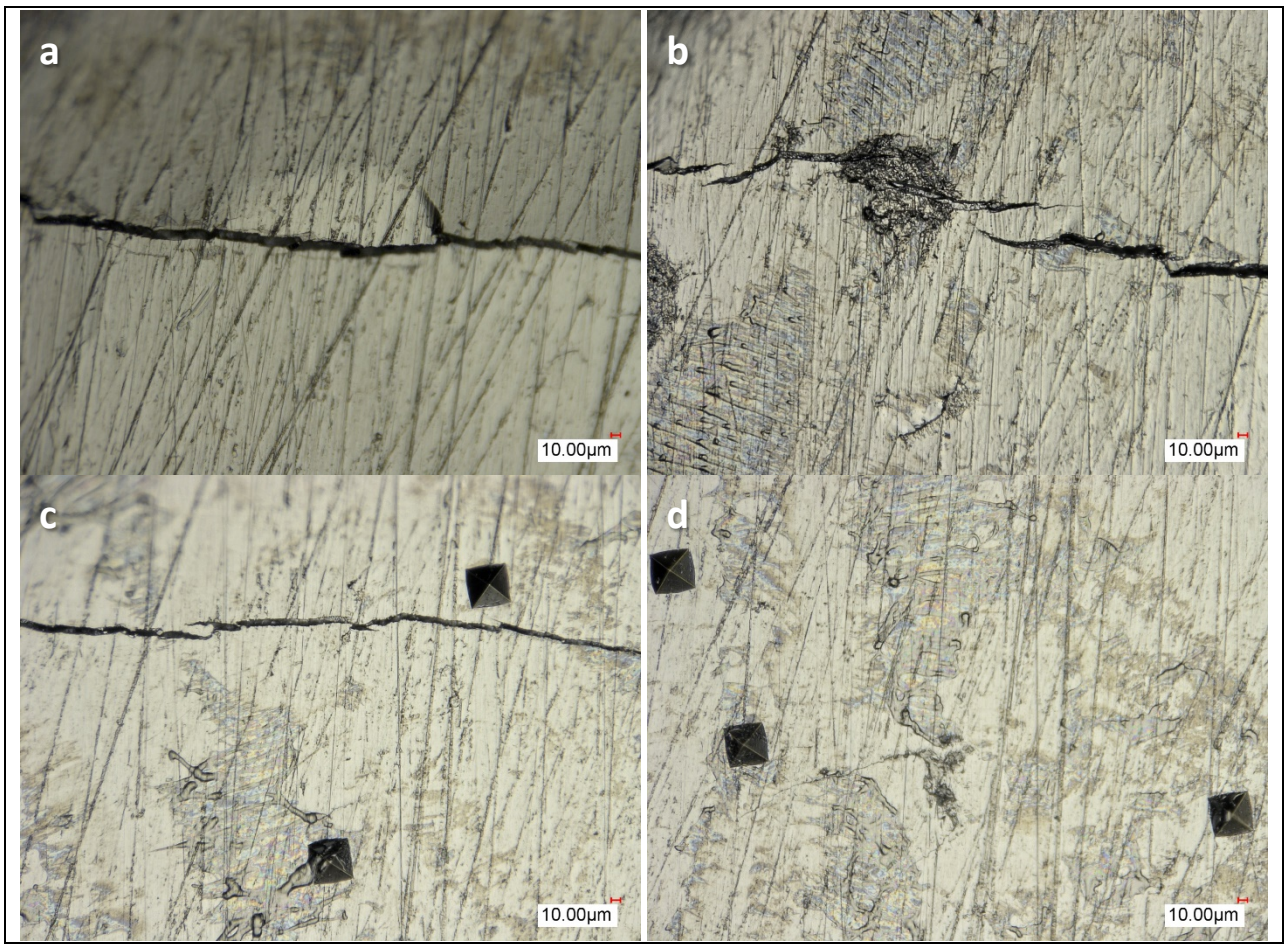

Figure 6. a) Possible origin of the fracture, compression side, areas identified in Figure 5. b) Crack propagation to the left. c) Crack propagation to the right, seemingly unperturbed by but within the activation volume of the micro-hardness indent. d) Other indents, which had no effect on the fracture of the specimen.

Higher magnification micrographs of the primary crack plane are shown from the compression side of the sample in Figure 6. Box b shows two indents where the crack runs near the hardness test-activated volume. The other three hardness indents are shown in box d, two of which were within the load ring (the textured blueish-band imprints in the image). None of these hardness indents showed any influence on the fracture behavior.

This study provides evidence that minor surface architecture on the compression side of the sample has little impact on the outcome of the EBF test. To make the best use of the limited samples available, it is proposed to perform elemental depth profiles of several 10s of microns depth on the compression-side of the sample before EBF testing using the glow-discharge optical emission spectroscopy (GD-OES) , which erodes a crater by physical sputtering with an inert gas plasma. The effect of the GD-OES eroded crater on EBF results will be tested directly.

4.6 CHARACTERIZATION OF ION IRRADIATED TUNGSTEN MICROSTRUCTURES—Weilin Jiang, Yuanyuan Zhu, Giridhar Nandipati, Wahyu Setyawan, Danny Edwards, Charles H. Henager Jr., Richard J. Kurtz (Pacific Northwest National Laboratory), Aaron French, Xuemei Wang, and Lin Shao (Texas A&M University)

OBJECTIVE

The aim of this experimental work is to study void lattice formation in tungsten as a function of irradiation parameters, especially dose and dose rate, and compare the results to predictions by Object Kinetic Monte Carlo (OKMC) simulations.

SUMMARY

This progress report presents our recent data from transmission electron microscopy (TEM) characterization of single-crystal tungsten irradiated with self-ions at 900 K. The TEM results suggest that the focused ion beam (FIB) process for TEM sample preparation produces a high concentration of black-spot defects and dislocation loops in tungsten. Flash electrochemical polishing under various conditions has been attempted to remove the FIB damage, but the polishing parameters still need to be optimized. A high concentration of voids is observed in single-crystal tungsten irradiated with self-ions to 1 dpa at 10^{-3} dpa/s and 900 K. Under these conditions, only randomly distributed, nanometer-sized voids appear. However, there is no evidence of void formation in the FIB lamella of pristine tungsten. Further efforts are being made to characterize irradiated polycrystalline tungsten.

PROGRESS AND STATUS

Introduction

Void lattice formation was observed in neutron-irradiated materials, including tungsten, at temperatures between $0.25T_m$ and $0.5T_m$ (T_m: melting point). It is attributed to the fast one-dimensional (1D) diffusion of self-interstitial clusters along close-packed directions [1,2], which are ⟨111⟩ directions in body-centered cubic (bcc) tungsten. In this temperature range, mono-vacancies are mobile and vacancy clusters larger than a critical size (depending on dose rate and temperature) are stable against dissolution. At low doses, a large fraction of self-interstitial atom (SIA) clusters are absorbed by grain boundaries due to their fast 1D diffusion, leading to a sharp increase in the void concentration. With increasing dose, SIA clusters start to interact with voids, resulting in an increased recombination that lowers the void accumulation rate. A recombination event can result in either a partial or complete annihilation of voids. Some of the partially annihilated voids decay via thermal emission. The resulting mono-vacancies are subsequently captured by stable voids. Due to 1D diffusion of SIA clusters, most of these recombination events occur along the ⟨111⟩ directions in tungsten, leading to the formation of void-free and void-rich regions along those directions. The void-rich regions become the lattice points, while the void-free regions form perfect crystal.

The OKMC simulations [3,4] predict void lattice formation in pure, polycrystalline tungsten, irradiated with neutrons up to 1 dpa at 1025 K. The simulations show that at low doses, voids are randomly distributed; with increasing dose, voids appear to order into a regular lattice. Void formation also depends on the dose rate. In the simulations, only grain boundary effects are considered; intragranular sinks such as dislocation loops and precipitates from transmutation elements (e.g. osmium and rhenium) in neutron-irradiated tungsten are not yet considered. In order to validate the simulation results in pure tungsten without transmutation elements, a self-ion irradiation study of high-purity monocrystalline and polycrystalline tungsten at different dose rates is being performed. The TEM is employed to investigate microstructural features.

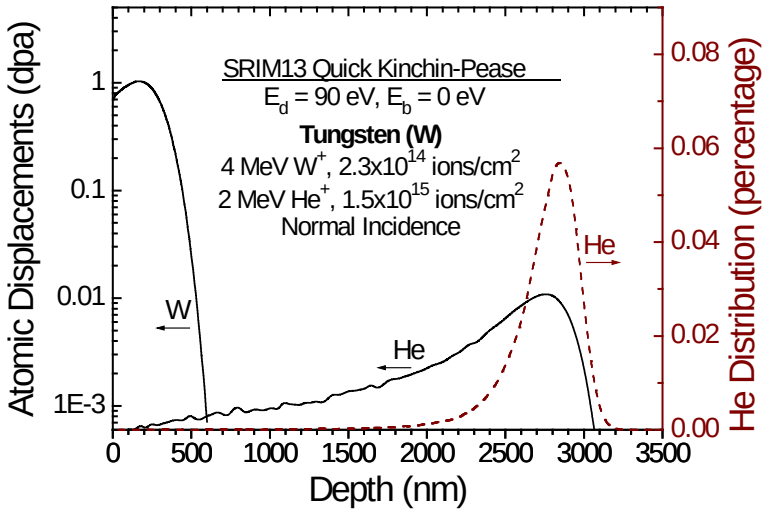

Figure 1. SRIM quick Kinchin-Pease simulations of 4 MeV W ions to 2.3×10^{14} ions/cm^2 and 2 MeV He ions to 1.5×10^{15} ions/cm^2 in tungsten.

Experimental Procedure

As previously reported [5,6], both monocrystalline and polycrystalline tungsten samples were irradiated 7° off the surface normal in different areas, with 4 MeV W^{2+} ions to peak doses of 0.01, 0.1 and 1 dpa at peak dose rates of 10^{-3} and 10^{-4} dpa/s at 900 K. A dose of 1 dpa at the damage peak corresponds to an ion fluence of 2.3×10^{14} W^{2+}/cm^2. *In situ* 2 MeV Helium $(He)^+$ ion-channeling analysis based on Rutherford backscattering spectrometry (RBS/C) along the ⟨111⟩-axial direction in monocrystalline tungsten was performed at room temperature. For each analyzed area (1.4 mm × 1.4 mm), the ion fluence is estimated to be 1.5 × 10^{15} He^+/cm^2. Quick Kinchin-Peace SRIM-2013 simulations were performed for irradiation of W and He ions in tungsten. The threshold displacement energy of 90 eV and lattice binding energy of 0 eV were adopted based on the recommendations from Stoller, *et al*. [7]. The simulation results are plotted in Figure 1. The self-ion irradiation produces vacancy concentrations located within the depth of 600 nm. The vacancies created by the He ion irradiation are mainly distributed around the depth of 2.7 µm with the maximum vacancy concentration of 2 orders in magnitude smaller than that by the self-ion irradiation. The implanted He atoms are peaked at ~2.8 µm with a value of ~0.06 at.%. Cross-sectional lamellae for TEM from the irradiated single-crystal tungsten were lifted out using a Field Electron and Ion (FEI) Quanta dual-beam focused ion beam (FIB) microscope. Multiple FIB samples were prepared in both the unirradiated and self-ion irradiated areas (1 dpa, 10^{-3} dpa/s and 900 K). A number of flash electrochemical polishing [8] tests under various conditions were performed to remove the FIB damage layer. The lift-outs on Au grids were immersed in a bath of electrolyte as an anode. A pulsed current with a precise time control passed through the anode, where the metal surface was oxidized and dissolved in the electrolyte. For thin foils like FIB lift-outs, a low dissolving rate is critical to remove the damage layer slowly in a well-controlled manner. Optimum parameters are still to be determined. A similar polishing procedure for tungsten FIB samples has also been reported recently [9]. This study focuses on the observation of voids in tungsten. A sample-tilting technique was used to make black-spot defects and dislocation networks less visible or invisible; voids could be clearly imaged using under- and over-focus conditions. Conventional phase contrast TEM and novel diffraction contrast imaging scanning transmission electron microscopy (DCI STEM) [10] were performed using a Japan Electron Optics Laboratory (JEOL) JEM-ARM 200CF microscope operating at 200 kV. More TEM specimens, including irradiated polycrystalline tungsten, are currently being prepared and analyzed.

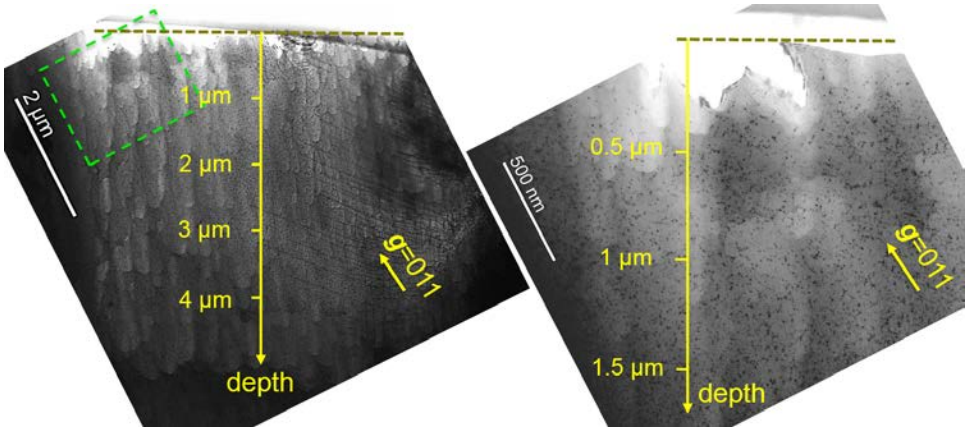

Figure 2. An overview of black-spot defects (dislocation loops) and dislocation lines introduced by mechanical deformation throughout the entire cross-sectional area of a pristine tungsten single crystal after FIB and flash electrochemical polishing.

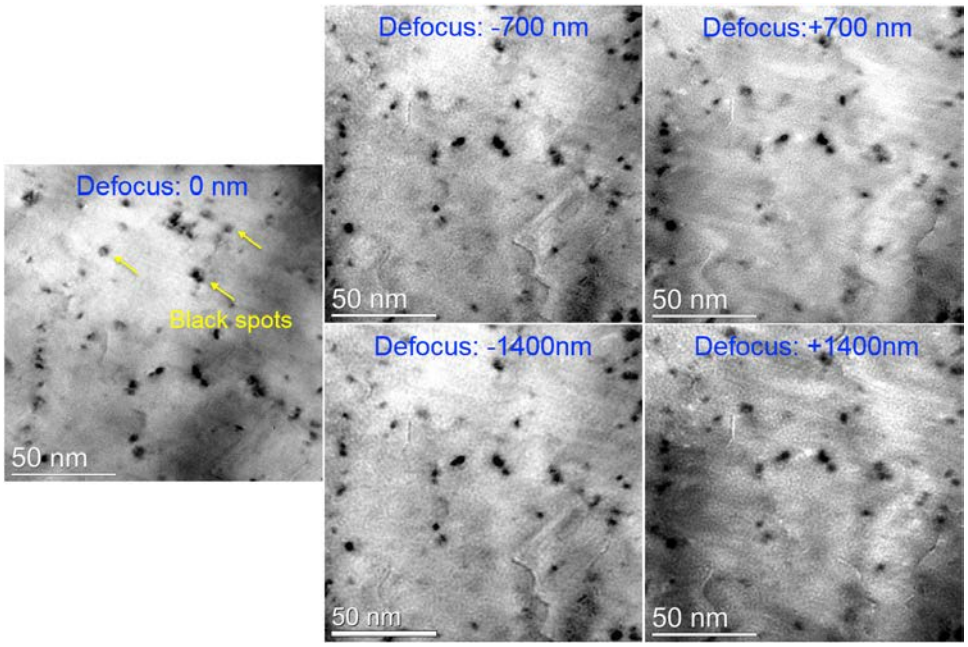

Figure 3. TEM images under various focusing conditions showing no evidence of void formation in the same sample as for Figure 2.

Results

A lamella of unirradiated single-crystal tungsten was lifted out by FIB and examined by TEM. A very high concentration of defects, including black-spot defects and dislocation networks, was observed. The defects originated from the Ga^+ ion irradiation during the FIB process. Flash electrochemical polishing was attempted to remove the radiation damage. Figure 2 shows TEM images of the pristine single-crystal tungsten after the flash polish. Apparently, there is still a high concentration of dislocation loops of ~ 10 nm in size retained at the surface of the lamella. Further polishing is necessary to remove the surface defects with a controlled, low dissolving rate during the FIB process to prevent a complete dissolution.

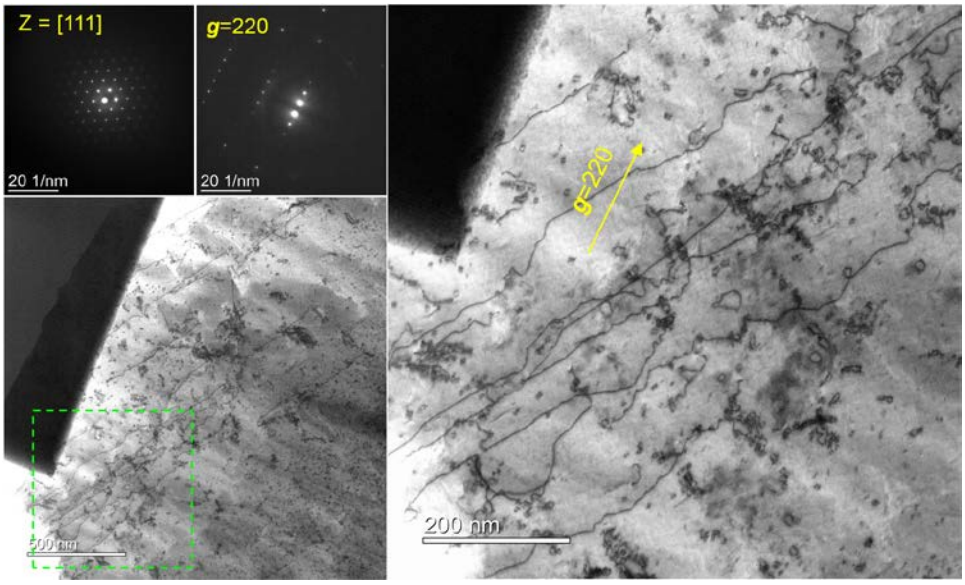

Figure 4. Electron diffraction patterns and DCI STEM images under a systematic row diffraction condition (z=111, ***g***=220) showing distinct dislocation lines and loops in the top 1 μm region of tungsten single crystal irradiated with 4 MeV W^{2+} ions to 1 dpa at 10^{-3} dpa/s and 900 K.

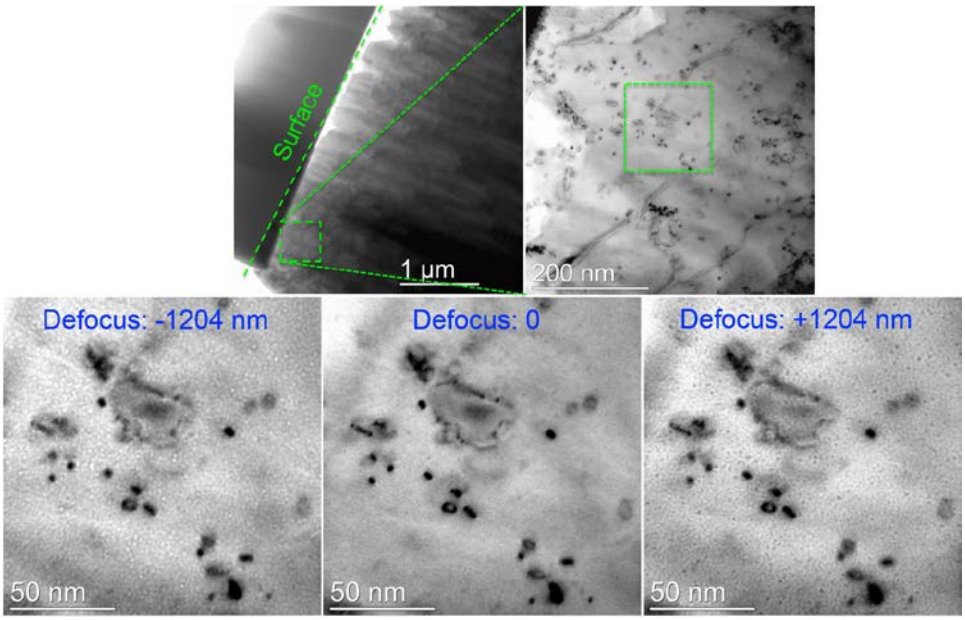

Figure 5. TEM images showing black spots and dislocation loops in the near-surface region and void distribution around the depth of 400 nm in the same sample as for Figure 4.

Figure 3 shows a series of conventional TEM images in focus, under focus and over focus in order to image voids. The data do not provide any evidence for void formation in the FIB lamella of the pristine tungsten. This is an expected result because mono-vacancies in tungsten produced by ion irradiation at room temperature are not mobile and voids with visible size under TEM should not form.

Figure 4 shows DCI STEM images of irradiated tungsten under systematic row diffraction conditions with diffraction vector ***g***=220. This condition is best suited for imaging dislocation lines and loops in bcc tungsten.

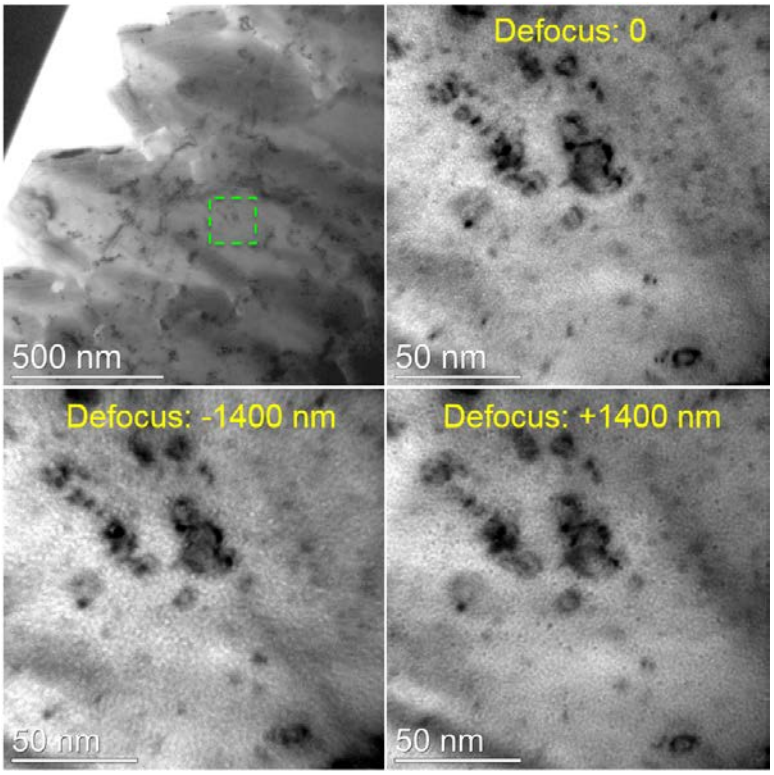

Figure 6. TEM images showing void distribution around the depth of 820 nm in the same sample as for Figure 4.

The irradiation was performed with self-ions to 1 dpa at 10^{-3} dpa/s and 900 K. From Figure 4, the surface region is dominated with dislocation lines, relatively large dislocation loops, and loop-clusters. The dislocation lines could be formed due to mechanical deformation of the TEM foil as it was thinned and slightly bended during TEM sample preparation. Black-spot defects and small dislocation loops are also observed. The defects produced by self-ion irradiation and during FIB processing are virtually indistinguishable. However, self-ion irradiation may make a significant contribution to the formation of the large loops, likely ½⟨111⟩ {111}, in the irradiation affected depth region.

An irradiated area located at the depth of 400 nm with foil thickness of ~100 nm as determined by electron energy loss spectroscopy (EELS) was selected for a close examination. Under-focus and over-focus conditions were applied to image voids in the specimen, as shown in Figure 5. In addition to black spots and dislocation loops, a high concentration of small voids (a few nanometers in size) is observed, which change contrast from bright in under-focus (-1204 nm) to dark in over-focus (+1204 nm). Void formation is attributed to self-ion irradiation at 900 K. However, it still remains to be investigated how voids formed during irradiation interact with mobile SIAs produced during FIB process.

At a depth of 820 nm, where the foil is 120 nm in thickness, a similar void distribution is observed, as shown in Figure 6. This depth is beyond the irradiation range of this study, as suggested by SRIM simulations (Figure 1). The phenomena might be partly due to vacancy inward diffusion and clustering during ion irradiation at 900 K. In addition, the single-crystal tungsten was analyzed by RBS/C with 2 MeV He^+ ions after the self-ion irradiation [5]. Although vacancy contribution to this depth region from the He^+ ion irradiation is insignificant, as shown in Figure 1, it cannot be excluded at this stage that a fraction of the implanted He atoms might diffuse towards the surface at room temperature and interact with vacancies resulting in the formation of large cavities. In the case of α-iron, He atoms can enhance formation of cavities [11,12]. The He^+ ion irradiation effects on the formation of voids near the surface of tungsten are currently being investigated.

Acknowledgements

This research was supported by Office of Fusion Energy Sciences, U.S. Department of Energy (DOE) under Contract DE-AC05-76RL01830. Ion irradiation was performed in collaboration with Texas A&M University. FIB, flash electrochemical polishing and STEM were carried out at Pacific Northwest National Laboratory.

References

[1] W. Jager and H. Trinkaus, J. Nucl. Mater. 205 (1993) 394.
[2] A. J. E. Foreman, Harwell Report AERE-R-7135 (1972).
[3] G. Nandipati, W. Setyawan, H. L. Heinisch, K. J. Roche, R. J. Kurtz, and B. D. Wirth, 2017; available at: https://arxiv.org/abs/1510.02732.
[4] G. Nandipati, W. Setyawan, H. L. Heinisch, K. J. Roche, R. J. Kurtz, and B. D. Wirth, 2017; available at: https://arxiv.org/abs/1606.01308.
[5] W. Jiang, K. Kruska, C. H. Henager, Jr., and R. J. Kurtz, *Fusion Materials Semiannual Progress* Report for Period Ending June 30, 2017, DOE/ER-0313/62, U.S. Department of Energy.
[6] W. Jiang, K. Kruska, C. H. Henager, Jr., and R. J. Kurtz, *Fusion Materials Semiannual Progress* Report for Period Ending December 31, 2016, DOE/ER-0313/61, U.S. Department of Energy, 115.
[7] R. E. Stoller, M. B. Toloczko, G. S. Was, A. G. Certain, S. Dwaraknath, F. A. Garner, Nucl. Instr. Meth. Phys. Res. B 310 (2013) 75.
[8] L. Veleva, R. Schäublin, A.Ramar, Z. Oksiuta, N. Baluc, European Microscopy Congress 2008, Volume 2: Materials Science, Eds. S. Richter and A. Schwedt, Springer-Verlag Publication, Berlin Heidelberg, 2008, p. 503-504.
[9] A. Manhard, U. von Toussaint, M. Balden, S. Elgeti, T. Schwarz-Selinger, L. Gao, S. Kapser, T. Plocinski, J. Grzonka, M. Gloc, L. Ciupinski, Nucl. Mater. Energy 12 (2017) 714.
[10] Y. Zhu, C. Ophus, M. B. Toloczko, D. J. Edwards, Ultramicroscopy 193 (2018) 12.
[11] K. Morishita, R. Sugano, B. D. Wirth, T. D. de la Rubia, Nucl. Instr. Meth. B 202 (2003) 76.
[12] C.-C. Fu, F. Willaime, Phys. Rev. B 72 (2005) 064117.

4.7 MICROSTRUCTURAL ANALYSIS OF NEUTRON-IRRADIATED W-BASED MATERIALS IN THE PHENIX COLLABORATION—L. M. Garrison, E. Lang, C. Parish (Oak Ridge National Laboratory)

OBJECTIVE

The objective of this project is to study the microstructure of various W-based materials after low dose neutron irradiation in High Flux Isotope Reactor (HFIR) as part of the photon electron new heavy ion experiment (PHENIX) campaign.

SUMMARY

A variety of tungsten-based materials were neutron irradiated in HFIR during the PHENIX campaign. These specimens varied from single crystal W, to polycrystalline W, to tungsten-rhenium and tungsten-titanium carbide alloys. Investigation of the microstructure and mechanical properties of these materials is on-going. The first group selected for microstructure analysis include the W-Re and W-TiC alloys. Mechanical and thermal property testing is being performed in parallel with this work to understand how the neutron irradiation affects these complex materials.

PROGRESS AND STATUS

Introduction

Tungsten is proposed as a plasma-facing component material in future fusion reactors due to its high melting temperature, low sputtering yield, and high thermal conductivity. In a D-T burning-plasma fusion reactor plasma-facing components will be exposed to ion and neutron (up to 14.1 MeV) irradiation. Under neutron irradiation, tungsten develops microscopic voids and dislocation loops that alter the microstructure. Additionally, tungsten undergoes transmutation reactions to rhenium (Re) and osmium (Os), altering the material composition. The transmutation reaction cross section is highest for thermal neutrons in tungsten, so the elemental composition of irradiated tungsten depends on the neutron energy spectrum of the reactor. Transmutation reactions result in the formation of Re and Os precipitates within the tungsten matrix at concentrations up to ~5 at.% Re expected after irradiation at fusion conditions. Thus, the analysis of fabricated model W-Re alloys can offer a supplemental understanding of the microstructural and mechanical property effects of Re addition on the W specimen behavior.

In addition to the behavior of W-Re alloys, systematic studies of different varieties of W materials under neutron irradiation are not available. In this work, the behavior of various grades of W (single crystal, polycrystalline, powder-injection molded W) and other W-based alloys (W alloyed with TiC precipitates) will be systematically studied to understand the effects of neutron irradiation on the resulting microstructure, with particular emphasis during this period on the W-Re and W-TiC specimens.

Results

Irradiation

Approximately 20 varieties of tungsten materials were irradiated in the PHENIX United States-Japan collaboration campaign in HFIR. The instrumented capsule, RB*19J, was irradiated in the removable beryllium position of HFIR. The material was irradiated to a fast fluence of approximately 1 to 3.6×10^{25} n/m^2 (E>0.1 MeV), approximately 0.2-0.7 dpa in tungsten, in three different temperature zones, nominally 500°C, 800°C, and 1200°C. A gadolinium shield was utilized to limit the thermal neutron flux to more accurately mimic a fusion spectrum.

Specimens

The specimens of interest for the microscopy campaign are presented in Table 1. The irradiated samples selected for analysis are in Table 2. Sample identifications (ID's) marked TBD (to be determined) will be determined once the full irradiated sample inventory is completed.

Table 1. Matrix of unirradiated tungsten specimens of interest for microscopy campaign in Summer 2018

Material Description	**Material Code**	**Composition (GDMS analysis)**
Thick plate orientation A	AT	99.998% W
Thick plate orientation B	BT	99.998% W
Thick plate orientation C	CT	99.998% W
Alfa Aesar Plate tensile A	GE	99.998% W
Alfa Aesar Plate tensile B	3E	99.998% W
W-PIM	ZE	99.925% W
Single crystal tungsten [110] (GW 104)	GW	99.999% W
W-TiC	8E	99.265% W; 0.735% TI; 0.208% C
Alfa Aesar 2mm foil (P33)	EE	99.999% W
W-0.4%Re ORNL (WRe1-1)	3R	99.584% W; 0.41% Re
W-2.2%Re ORNL (WRe4-1)	5E	97.757% W; 2.24% Re
W-0%Re ORNL (WRe6-2)	KE	99.941% W; 0.043% Re

Table 2. Irradiated samples selected for first round of microscopy investigation

			Nominal irradiation temperature					
Material Type	**Provider**	**Code**	**500°C**		**800°C**		**1200°C**	
			ID	**shape**	**ID**	**shape**	**ID**	**shape**
K-doped W (Rolled, 80%, X-direction)	Japan	60	6001	TEM	6003	TEM	6004	TEM
K-doped W-3%Re (Rolled, 80%, X-direction)	Japan	80	8001	TEM	8003	TEM	8005	TEM
K-doped W-3%Re (Rolled, 80%, X-direction, Heat treated at 1500C)	Japan	70	7001	TEM	7003	TEM	7005	TEM
W-3%Re (Rolled, 80%, X-direction)	Japan	41	4101	TEM	4103	TEM	4104	TEM
Pure W (Rolled, 80%, X-direction)	Japan	P0	P001	TEM	P003	TEM	P004	TEM
Pure W (Rolled, 80%, X-direction, Heat treated at 1500C)	Japan	X0	X001	TEM	X003	TEM	X004	TEM
Alfa Aesar plate	US	FR	FR00	D6T1	FR01	D6T1	FR02	D6T1
Thick plate orientation A	US	AT	AT02	D3TH	AT04	D3TH	AT07	D3TH
Thick plate orientation B	US	BT	BT03	D3TH	BT05	D3TH	BT08	D3TH
Thick plate orientation C	US	CT	CT03	D3TH	CT06	D3TH	CT08	D3TH
Rolled W foil	US	RE	RE02	D6TQ	RE04	D6TQ	RE08	D6TQ
SCW 110 (commercial)	US	UE	UE01	D3TH	UE04	D3TH	UE07	D3TH
W-0%Re (ORNL)	US	KE	KE00	D3TH	KE02	D3TH	KE03	D3TH
W-0.4%Re (ORNL)	US	3R	3R01	D6TH	3R03	D6TH	3R07	D6TH
W-2.2%Re (ORNL)	US	5E	5E00	D6TH	5E01	D6TH	5E02	D6TH
W PIM	US	ZE	TBD	D10T1	TBD	D10T1	TBD	D10T1
W TiC	US	8E	TBD	D10T1	TBD	D10T1	TBD	D10T1
Alfa Aesar 2mm foil	US	EE	EE03	D3TH	TBD	tensile	TBD	tensile
Allied W	Japan*	00	TBD	D6TH	TBD	D6TH	TBD	D6TH
UFG-W	Japan*	Y0	TBD	D6TH	TBD	D6TH	TBD	D6TH
W-5Re	Japan*	71	TBD	D6TH	TBD	D6TH	TBD	D6TH

*These materials are in collaboration with Task 1 and 3 of the PHENIX project and will be used for high heat flux tests and plasma exposures in addition to the Task 2 mechanical and microstructure investigations.

Specimens were machined in various geometries in both the un-irradiated and irradiated state. The “thick plate” W is nominally International Thermonuclear Experimental Reactor (ITER) grade, pure W consisting of elongated grains perpendicular to the surface. The Alfa Aesar and Allied W specimens are polycrystalline W produced commercially. The “W-PIM” specimen is a pure W specimen fabricated via powder injection molding. The “W-TiC” specimen is a tungsten-titanium carbide alloy also fabricated via powder injection molding.

Tungsten-rhenium alloys are of particular interest, as their composition mimics that of a tungsten plasma-facing component after long-term use in a fusion reactor. The W-Re materials from Oak Ridge National Laboratory (ORNL) were fabricated by arc-melting and subsequently hot-rolled at 1200ºC to ~80% reduction. In previous studies, Re was found to be concentrated in areas within specimens, with no formation of second-phase sigma or chi phases. The amount of Re in the model alloys is well below the solid solution solubility limit, so in the unirradiated state, assuming the materials achieved equilibrium in processing, a solid solution of W and Re is expected.

The samples in Tables 1-2 are polished with a colloidal silica suspension to prepare them for microstructural analysis. Additionally, the mechanical and thermal properties of these same materials will be tested as part of the PHENIX campaign. Baseline hardness measurements of the un-irradiated specimens have already been established. Subsequent measurements will analyze the impact of the material composition and irradiation regime on the hardening behavior of these complex materials. It is expected that the complex microstructure of the W-Re alloys will result in altered hardening behavior after neutron irradiation as compared to pure W specimens.

Microscopy

The main thrust of the investigations this summer is the microstructure of these alloys before and after neutron irradiation. Scanning electron microscopy (SEM) and transmission electron microscopy (TEM) will characterize the microstructures. The SEM electron backscatter diffraction (EBSD) will determine the grain boundary and phase character to show potential formation of irradiation-assisted recrystallization and/or second phase formation during neutron irradiation.

Focused ion beam (FIB) methods will be used to prepare specimens for TEM analysis, including energy dispersive spectroscopy (EDS) for compositional analysis and elemental distributions. Comparison of unirradiated and irradiated conditions will determine changes in the W, Re, and Os concentrations and distributions. Additionally, loop, void, and precipitate formation will be studied to understand the neutron-induced alterations of microstructures.

Initial analysis of the material via backscatter electron microscopy in Figure 1 shows a complex microstructure of the unirradiated W-TiC specimen. Large W matrix grains (light grey) are observed with inter-granular TiC precipitates (dark grey/black arrows) and surface cracks and pores (black/red arrows). Cross-sectional micrographs of the W-TiC specimen in Figure 2 confirms the nature of micron-sized dispersed TiC particles within W matrix, but the voids and pores at the surface are not visible.

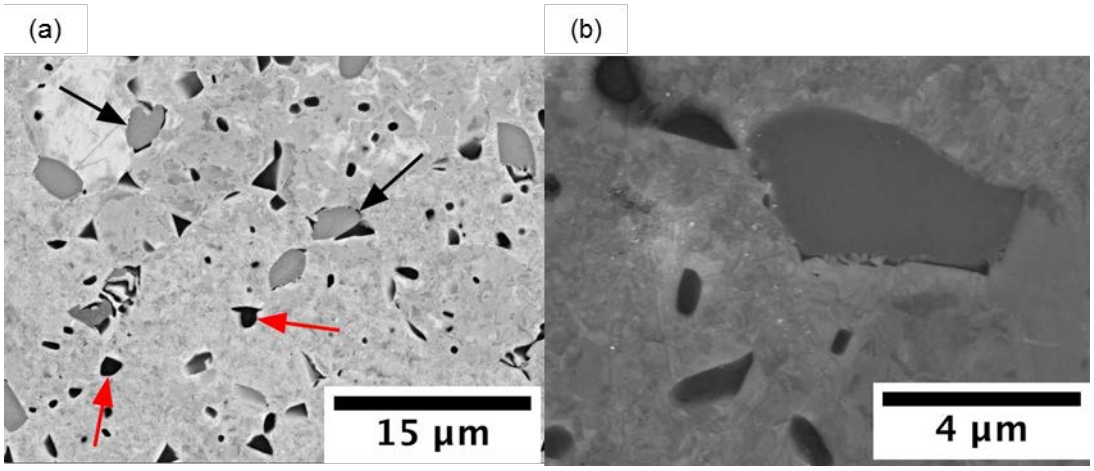

Figure 1. Unirradiated W-TiC specimen imaged in SEM in (a) backscatter (b) and secondary electron modes. TiC precipitates are dark grey within the W matrix. They are indicated with black arrows in (a)**.** The red arrows in (a) indicate surface pores present throughout. **(b)** shows the micron-sized surface pores and ~5 um-sized TiC precipitates in a magnified view.

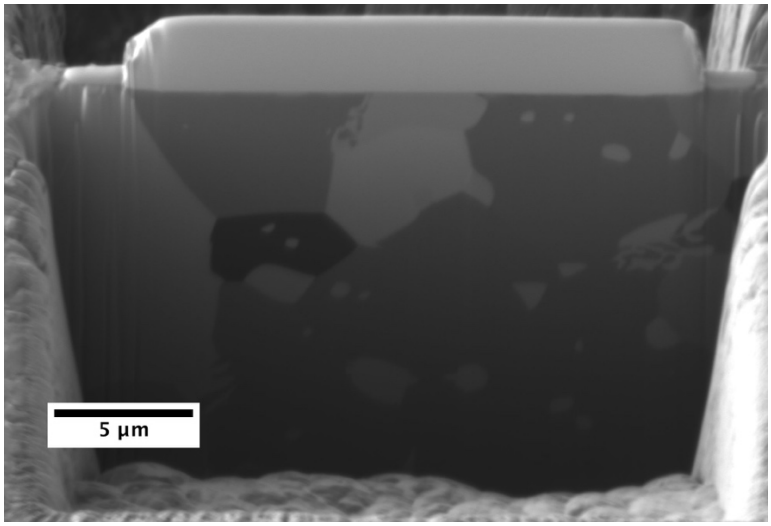

Figure 2. FIB cross-sectional micrograph of unirradiated W-TiC specimen showing dispersed TiC particles in W matrix throughout the material bulk. Image was taken at 30º tilt; in the image, distances in horizontal direction are not distorted, but vertical distances are distorted.

Backscatter electron images of the W-Re specimens shown in Figure 3a indicate no second phase segregation of Re atoms, and show ~1-5 um-size grains. However, the surface polish of these specimens is not good enough to allow EBSD analysis which would offer more accurate and precise analysis of potential second phase formation. Better polishing is necessary for accurate EBSD measurements.

Figure 3b shows a secondary electron micrograph of the W-PIM specimen. Large, 50-100 um-size grains are evident, with smaller sub-grains interspersed at grain boundaries. Further EBSD analysis will elucidate the grain boundary character of these small grains.

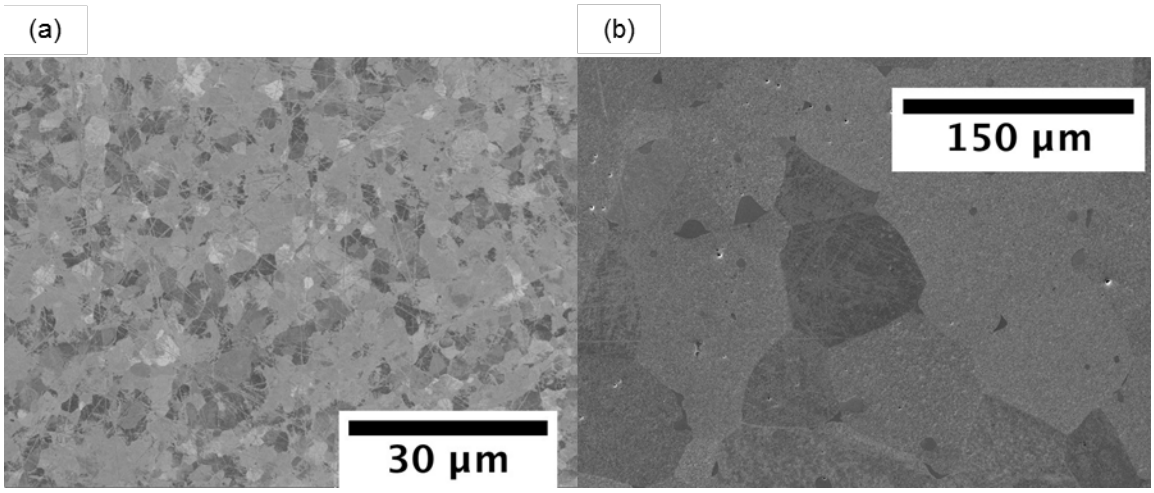

Figure 3. (a) Backscatter electron micrograph of unirradiated WRe4-1 specimen. Micron-sized grains are present, but no information on Re distribution can be determined. Surface scratches need to be eliminated for EBSD analysis. (b) Secondary electron micrograph of W-PIM specimen showing large W grains.

In the preparation of TEM specimens, cross-sectional FIB-SEM micrographs of the subsurface microstructure were obtained. The micrograph in Figure 4 shows the grain structure in the WRe4-1 specimen in the near subsurface region.

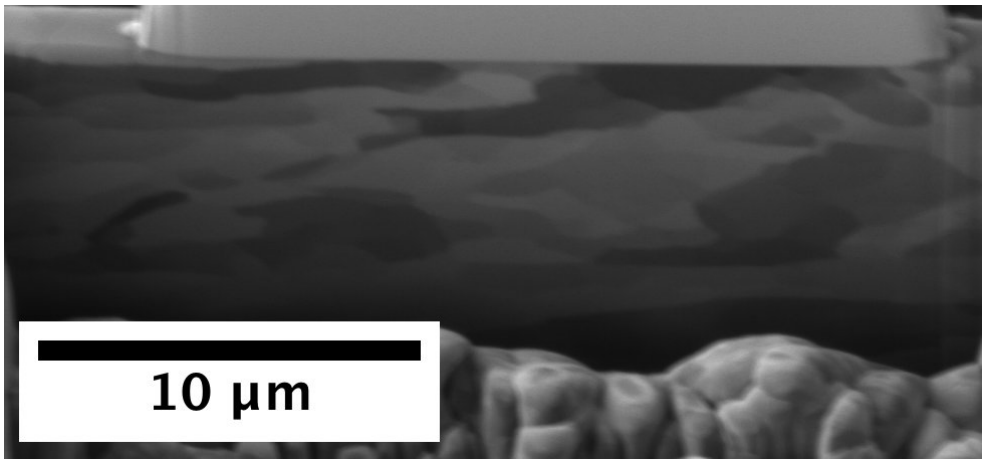

Figure 4. Cross-sectional SEM micrograph of unirradiated WRe specimen showing subsurface grain structure. As with plan view images, micron-sized grains are observed, but no indication of Re distribution is seen. Image was taken at 30º tilt; in the image, distances in horizontal direction are not distorted, but distances in vertical direction are distorted.

Fabrication of TEM specimens of the W-Re and W-TiC alloys is underway via FIB fabrication methods, and TEM/STEM (scanning transmission electron microscopy) analysis will occur on the Field Electron and Ion (FEI) F200X Talos TEM in Low Activation Materials Development and Analysis (LAMDA). The FIB lamella have been fabricated and will be thinned and imaged in the TEM.

4.8 THERMAL PROPERTY EVALUATION OF NEUTRON IRRADIATED TUNGSTEN MATERIALS FROM THE PHENIX COLLABORATION—L. M. Garrison, T. Ray, H. Wang (Oak Ridge National Laboratory)

OBJECTIVE

This project will collect thermal property data on tungsten-based materials to aid in future fusion reactor design.

SUMMARY

Two tungsten thimbles that were used for high heat flux testing at Georgia Tech are being tested for thermal diffusivity and surface elemental composition to determine why their performance degraded over time. The newly acquired LFA467 thermal diffusivity instrument is being prepared for testing by doing several benchmark tests. The irradiated tungsten materials from the photon electron new heavy ion experiment (PHENIX) irradiation capsule ~500°C and ~800°C zones are currently in Low Activation Materials Development and Analysis (LAMDA) and the ~1200°C zone sample holder is being disassembled in the hot cells. The experimental matrix for the irradiated samples has been determined and will proceed after the unirradiated material tests using the LFA467 are completed.

PROGRESS AND STATUS

The PHENIX United States-Japan collaboration is evaluating tungsten for use in Fusion Reactor DEMO (demonstration reactor) divertors and is organized into three interrelated tasks: Task 1 to evaluate high heat flux effects; Task 2 to evaluate irradiation effects on microstructure, thermal, and mechanical properties; and Task 3 to investigate plasma-surface effects. The thermal properties of neutron irradiated tungsten are measured in Task 2 at Oak Ridge National Laboratory (ORNL) and are integrated into the high heat flux tests for Task 1.

Georgia Tech Tungsten High Heat Flux Test

A portion of Task 1 is carried out at Georgia Tech, where a Helium-Cooled Multijet (HEMJ) DEMO divertor geometry is being tested. The HEMJ test facility incorporates one tungsten-based thimble which is exposed to high heat flux with a He coolant loop cooling the thimble. During high heat flux exposure, the tungsten thimbles appeared to degrade over time which reduced its cooling performance. There was a possibility that the thimbles oxidized or had another reaction during high heat flux exposure. Two tested tungsten thimbles were sent to ORNL for thermal and elemental analysis. The two thimbles were fabricated from tungsten alloys WL10 (99% W; 1% La_2O_3) and MT-185 (97%W; 2.1%Ni; 0.9% Fe). The surface degradation from the high heat flux exposure was apparent upon receipt at ORNL, seen as the pieces appearing to be discolored compared to the original dark grey color, and the rough top (exposure) surfaces (Figure 1).

Figure 1. Two tungsten alloy thimbles that were tested under high heat flux conditions with He cooling at Georgia Tech #1) WL10 alloy #2) MT-185 alloys.

To prepare the thimbles for thermal analysis, 12.7 mm diameter, 2 mm thick discs were machined from the thimbles (Figure 2). Because the surface condition was believed to be the cause of the change in thermal performance, no polishing was done on the machined discs to preserve any surface compounds. A reference disc of unexposed WL10 alloy was also machined. Thermal diffusivity measurements were completed on the samples from the WL10 thimble and the reference disc using an LFA457 instrument (Figure 3). During the thermal diffusivity tests the samples were placed on an oxide holder, which caused a concern after the measurement because the W-based samples adhered to the holders. It is also possible that background oxygen in the low vacuum system was enough to cause a reaction on the samples during testing. Thermal diffusivity measurements were made at 50°C, 100°C, and in 100°C increments up to 900°C. To ensure repeatability, measurements were also made on the cooling cycle at 600, 300, and 100°C. It was expected that the reference piece would have a higher thermal diffusivity than the cut samples, but Figure 3 shows that any difference between the samples was unclear. Data on all samples followed a similar trend, but when the machine was cooling down, thermal diffusivity decreased. This is unexpected and believed to be an artifact of the samples adhering to the holders. It appears that the oxidation reaction with the holders started at approximately 800°C. Further tests will be conducted using SiC sample holders, which should not bond to W, to gain a better understanding of the thimbles thermal diffusivity. After different holders are obtained, the MT-185 alloy thimble samples will also be tested. Energy dispersive x-ray spectrometry has been completed on the two thimble surfaces and is being analyzed to determine any elemental changes during high heat flux exposure.

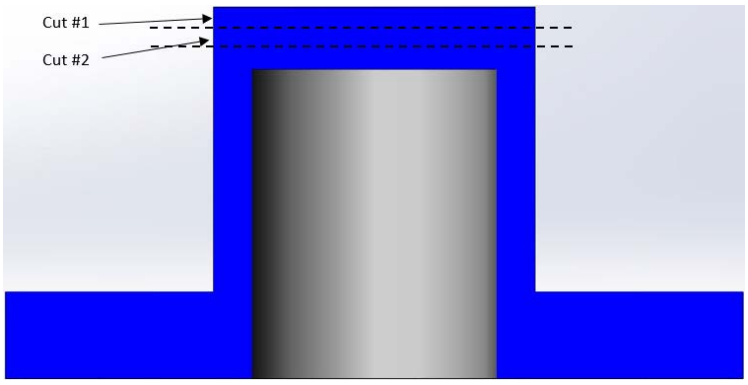

Figure 2. Illustration of Georgia Tech thimble sample geometry and cuts made.

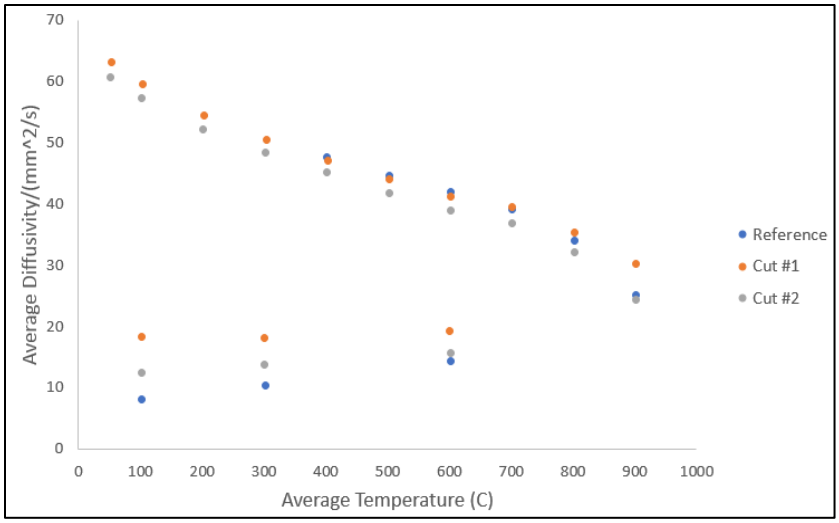

Figure 3. Thermal diffusivity of WL10 alloy thimble sections.

Thermal Properties of PHENIX Irradiated Tungsten

As part of Task 2 of the PHENIX project the thermal diffusivity of the tungsten materials from the High Flux Isotope Reactor (HFIR) RB*19J capsule will be analyzed (Table 1). The LFA467 is planned to be used for these measurements because it has a fast-enough laser pulse that 3 mm diameter 0.5 mm thick samples should be able to be measured. The nominally 500 and 800°C irradiated samples are currently in LAMDA and being inventoried. The 1200°C zone samples will soon be shipped to LAMDA from the hot cells. There are more than twenty types of tungsten-based materials included in the PHENIX irradiation. However, some materials with different codes in the irradiation matrix are in fact the same base material, so the materials in Table 1 should represent the key materials to be tested. Those listed as “TBD” [to be determined] will be selected for testing once the specimen inventory in LAMDA is complete.

Table 1. Experimental plan for thermal diffusivity measurements on the PHENIX irradiated materials

			Nominal Irradiation Temperature (°C)					
Material Type / Condition	**Provider**	**Code**	**500**		**800**		**1200**	
			ID	**shape**	**ID**	**shape**	**ID**	**shape**
Pure W (Rolled, 80%, X-direction)	Japan	P0	P00A	D3TH	P00C	D3TH	P00G	D3TH
K-doped W (Rolled, 80%, X-direction)	Japan	60	6009	D3TH	600E	D3TH	600G	D3TH
K-doped W-3%Re (Rolled, 80%, X-direction, Heat treated at 1500C)	Japan	70	7009	D3TH	700E	D3TH	700G	D3TH
K-doped W-3%Re (Rolled, 80%, X-direction)	Japan	80	8009	D3TH	800E	D3TH	800G	D3TH
W-3%Re (Rolled, 80%, X-direction)	Japan	41	4109	D3TH	410E	D3TH	410G	D3TH
Alfa Aesar 2mm foil	US	EE	EE02	D3TH	TBD	tensile	TBD	tensile
Alfa Aesar plate	US	FR	FR00	D6T1	FR01	D6T1	FR02	D6T1
PCW-0%Re (ORNL)	US	KE	KE00	D6T1	KE01	D6T1	KE02	D6T1
W-0.2%Re (ORNL)	US	3R	3R0L	D6T1	3R0M	D6T1	3R0R	D6T1
W-3.4%Re (ORNL)	US	5E	5E00	D6TH	5E01	D6TH	5E02	D6TH
PCW-ITER (JP) orientation C	US	CT	CT02	D3TH	CT05	D3TH	CT09	D3TH
Single crystal tungsten [110]	US	UE	UE02	D3TH	UE05	D3TH	UE08	D3TH
W PIM	US	ZE	TBD	D10T1	TBD	D10T1	TBD	D10T1
W TiC	US	8E	TBD	D10T1	TBD	D10T1	TBD	D10T1
Allied W	Japan*	00	TBD	D6TH	TBD	D6TH	TBD	D6TH
W-5Re	Japan*	71	TBD	D6TH	TBD	D6TH	TBD	D6TH
UFG-W	Japan*	Y0	TBD	D6TH	TBD	D6TH	TBD	D6TH

*****These materials are in collaboration with Task 1 and 3 of the PHENIX project and will be used for high heat flux tests and plasma exposures in addition to the Task 2 mechanical and microstructure investigations.

Before the irradiated PHENIX materials are tested, some unirradiated material tests are being conducted to fully characterize the new LFA467 instrument and compare it to data on the LFA457 instrument. These tests are ongoing and include the following:

1. Measure 12.7 mm diameter tungsten samples with both LFA457 and LFA467:

    a. Purpose: Confirm that both instruments give the same result for a standard size sample and that there is not any reaction of the tungsten samples with the holders.

2. Size effect study on the new LFA467:

    a. Details: Will test 6 mm diameter x 2 mm, 1 mm, 0.5 mm thicknesses; and then 3 mm diameter x 1 mm, 0.5 mm, 0.25 mm thicknesses.

b. Purpose: confirm results previously obtained by PHENIX colleagues in Japan, that the LFA467 is capable of reliable measurements on such thin samples.

3. Compare results using different graphite sprays:

    a. Purpose: test current graphite spray versus the new Netzsch graphite spray.

4. Test the tensile tab fixture in the LFA467:

    a. Purpose: confirm use of the graphite fixture for measurements on tensile specimen tabs in the new instrument. This capability is essential for testing the thermal properties of samples from the TITAN campaign for comparison with the PHENIX samples.

5. Measure the baseline thermal diffusivity data for all the PHENIX materials included in the RB*19J irradiation:

    a. Purpose: populate the database with the unirradiated materials properties.

4.9 ELEMENTAL CHARACTERIZATION OF NEUTRON IRRADIATED TUNGSTEN USING THE GD-OES TECHNIQUE—L.M. Garrison, N. Reid (Oak Ridge National Laboratory)

OBJECTIVE

The aim of this work is to analyze impurities, alloying elements, and transmutation elements in neutron irradiated tungsten using the glow-discharge optical emission spectroscopy (GDOES) technique to better understand how tungsten will evolve in a fusion environment.

SUMMARY

Tungsten transmutes to Re and Os under neutron irradiation, and these elements are important in determining its microstructure, thermal, and mechanical properties after irradiation. Moreover, tungsten in a fusion reactor will be bombarded by fuel, impurities, elements injected for cooling the plasma, elements eroded from other areas of the device, and more, which comprise a large list of elements that can impact tungsten: D, T, He, Be, Fe, N, C, O, Li, Ne, and more. The GDOES is a technique that can analyze the elemental composition of materials and has depth resolution. To prepare this technique for irradiated tungsten samples, a mounting system was designed and machined. The unirradiated photon electron new heavy ion experiment (PHENIX) United States-Japan collaboration tungsten materials will be analyzed to determine the unirradiated elemental composition. Then, the technique will be used on the irradiated PHENIX materials.

PROGRESS AND STATUS

Tungsten samples that were irradiated in the RB*19J capsule in High Flux Isotope Reactor (HFIR) at temperatures between 450-1200°C to doses of ~0.2-0.7 dpa will be analyzed by the GDOES technique using the glow-discharge (GD) profiler 2 instrument purchased from HORIBA Labs. This irradiation caused W to transmute to Re and Os and these elements form ternary irradiation-induced precipitates. The Re and Os concentration is key to understanding the tungsten properties after irradiation. Additionally, in a fusion application, tungsten will be exposed to numerous other elements from plasma-surface interactions or from bonds with other structural material that may all impact its performance. The GDOES is a useful tool to analyze depth profiles of elements.

The GDOES can measure elemental composition of a sample by eroding the surface of the sample, ionizing the eroded material, and measuring the optical emission of the excited atoms. It has no lateral resolution but erodes an area on the specimen that is dependent on the size of anode (typically 1-8 mm diameter). Not only must the device be capable of detecting trace irradiation-induced transmutant concentrations for neutron-irradiation studies, but it must have a well-characterized standard reference to compare ionization signal intensities to. Radio-frequency GDOES is the only technique which readily and rapidly allows depth profiling analysis of the surface of both conducting and non-conducting specimens, from the first atomic layer to a hundred or more microns. It can do this with nanometer and even sub-nanometer depth resolution, with high sensitivities in the ppm and 100s of ppb ranges for most elements and their isotopes in the periodic table. The GDOES elemental analysis can be correlated with thermo-mechanical testing of W to understand the strengthening and embrittlement mechanisms which occur in a fusion plasma environment.

Compared to industry standard techniques such as glow discharge mass spectrometry (GDMS) or inductively coupled plasma optical emission spectroscopy (ICP-OES), this technique does not require deconvoluting mass peaks in mass spectrometry; analysis is performed under vacuum in a GD plasma regime to allow for higher electron densities, and ergo increased excitation, ionization, and emission rates. It also allows measurement of difficult-to-detect non-metal species such as H, C, N, O, and S; which is virtually impossible for ICP due to low desolvation efficiencies and an atmospheric pressure environment. It does not have as great in-depth resolutions as some other complementary techniques such as secondary ion mass spectrometry (SIMS). However, with any analysis of ion- or neutron-irradiated specimens, it is

often necessary to investigate thicker layers, to which SIMS can be much too time-consuming, expensive, and has a much higher level of complexity.

Current work involves readying the GD Profiler 2 to handle neutron-irradiated W geometries such as 4 mm wide tensile tabs, 6 mm diameter disks, and 10 mm disks. A list of unirradiated materials that are currently being investigated is given in Table 1. Additionally, various W-Re-Os standard references are currently being explored and manufactured. Most of these materials have had their bulk elemental analyses detailed by GDMS and/or ICP-OES, and thus can be compared with the GDOES depth-spectra. To achieve the maximum possible sputtered-material signal from these samples, they will be eroded with a 4 mm diameter anode opening. Differential interferometer profiling (DiP) will aid in achieving the best possible depth resolution by taking real-time depth measurements during erosion of the surface.

Table 1. Unirradiated materials being measured by GD-OES

Material	Geometry
W-Re #1	0.5 in square
W-Re #3	Large rectangle
W-Re #4	6mm disk and small bar
W-ZrC	20 mm disk
W-TiC	10 mm disk
PIM W	10 mm disk
WC	0.75 in square
W-C paint	0.5 in square
Graphite-element furnace heated W	0.5 in square
W-element furnace heated W	0.5 in square
AA 2 mm foil W	Tensile tab

The GD Profiler 2 instrument is typically used for many other commercial or scientific needs where the sample size is relatively large, as compared to typical irradiated material sample sizes. The instrument can easily accommodate material pieces of approximately ~0.5 to 1 in size if they have a flat surface. For irradiation experiments, including the PHENIX irradiation campaign, the samples of interest include 3 mm discs, 6 mm discs, 10 mm discs, and tensile tabs. The GD Profiler 2 is designed such that the sample is placed directly in front of the plasma anode and must make a seal with the O-ring (Figure 1). If the sample is too small, or has an uneven surface, the plasma will not ignite, and it is possible that the cooling block behind the sample could be damaged.

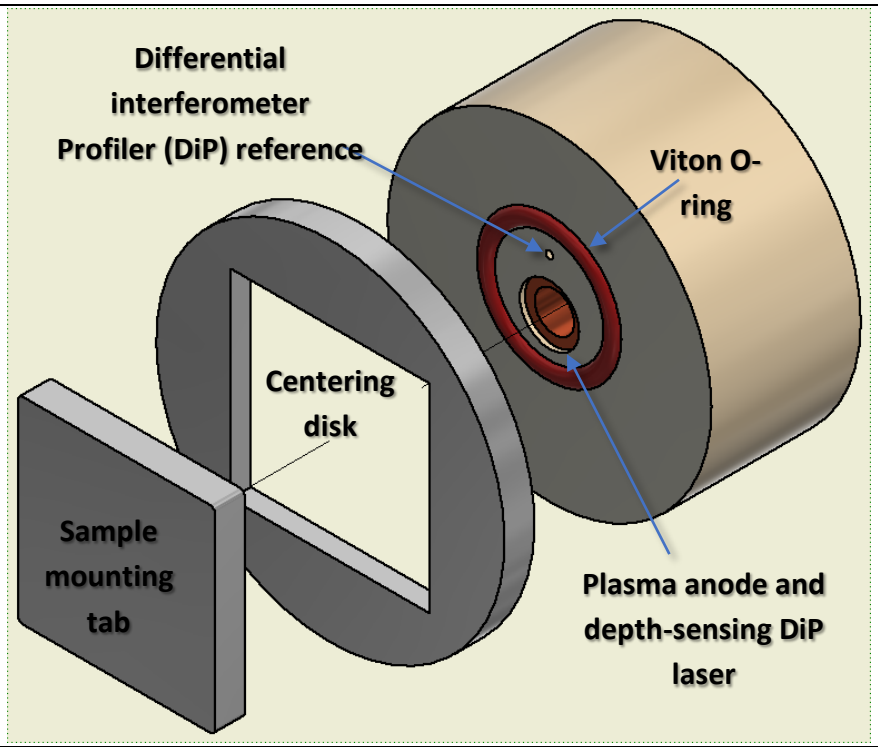

Figure 1. Exploded view of centering ring and sample mount on GD-OES 4 mm anode with DiP.

Samples that are at least 4 mm in diameter can usually be placed right up to the anode and create a seal. However, the irradiated samples are scarce resources, so it is desired to use practices and procedures which are consistent, predictable, and repeatable. To ensure high precision of the sample placement and minimize risk to the equipment, samples will be affixed to an aluminum substrate that can be precisely centered with an outer centering ring, as presented in Figure 1. Samples in this substrate can then be mounted, applied with a conductive passivation layer coating such as C or Ag, and polished to a flush surface. Ensuring that the GDOES analysis crater will form at the center of the sample is key, to minimize any sputtering of the aluminum and maximize signal coming from the sample. The mounting system has been designed and machined. Next, it will be tested with unirradiated materials before using with the irradiated PHENIX samples.

The GD Profiler 2 is a powerful GDOES system and uses state-of-the-art matching network technology which allows stable plasma conditions in about a second. Despite this seemingly fast time to establish a stable plasma, in that amount of time, hundreds of monolayers at the surface may be eroded, which may contain valuable information on fusion samples that have different near surface and bulk elemental composition. Thus, samples that have shallow surface layers will be coated with C or Ag so that the C or Ag can be sacrificially sputtered during the initial turn-on phase of the GD Profiler 2. The interface between C or Ag and W will be visible in the GDOES spectrum to know precisely when the W surface has been reached. After creating the GDOES crater, profilometry will be performed with the Keyence optical microscope in Low Activation Materials Development and Analysis (LAMDA) laboratory. Scanning electron microscopy (SEM) will image the cross-section of the crater.

4.10 INVESTIGATION OF CARBON IN TUNGSTEN FOILS—L.M. Garrison, N. Reid (Oak Ridge National Laboratory)

OBJECTIVE

The aim of this work is to investigate the effects of small carbon quantities on the mechanical properties of tungsten, especially foils and fibers for tungsten composites.

SUMMARY

Tungsten foils were investigated to determine if small carbon quantities could influence their mechanical properties. Tungsten foils were heated in either a graphite- or tungsten-element furnace for 1 h at 300 or 900°C. The as-received and heat-treated foils were tested using microhardness and shear punch. The carbon contend was measured with glow discharge optical emission spectroscopy. The 900°C 1 h heat treatment was enough to cause noticeable changes in the hardness and shear properties of the foils. Any difference between the graphite- and tungsten-element furnace was inconclusive, likely because of the small amount of carbon uptake in the tungsten foils in either furnace.

PROGRESS AND STATUS

The migration of carbon in tungsten at elevated temperatures and during neutron irradiation must be understood , because in High Flux Isotope Reactor (HFIR) irradiation capsules graphite or SiC are often used as spacers with tungsten specimens, and in any fusion plasma with carbon first-wall materials, there will be carbon erosion and mixing with armor materials such as W. Carbon is also being explored as a low-Z vapor shielding material at some facilities. Heat loads on graphite can introduce carbon migration into the tungsten lattice. Upon heating, carbon atoms in contact or in the near-neighborhood react with tungsten. The magnitude of any effect this carbon contact may have on irradiated tungsten mechanical properties is unknown. If it is significant, this creates an issue for both irradiated data and elevated temperature mechanical testing in the presence of graphite. For the photon electron new heavy ion experiment (PHENIX) collaboration the HFIR RB*19J capsule irradiation, graphite spacers were used on both sides of each tungsten sample. The capsule was irradiated for ~4 months at elevated temperatures, nominally 500, 800, and 1200°C. It is important to be able to separate the effects of neutron irradiation, elevated temperatures, and impurities such as C on the measured properties of the tungsten samples after irradiation.

There is scarce data on the diffusion of carbon in W, W_2C, and WC. It proceeds in a carburization sequence where a thin layer of WC is formed first. Diffusion through this layer is insufficient for WC formation, thus resulting in half-interstitial-filled W_2C formation until the W is saturated.

Tungsten foils were selected for this investigation because their particular microstructure makes them ductile at room temperature in the as-received condition. From collaboration with Institute of Plasma Physics (IPP)-Garching on tungsten fibers (similar ductility mechanism as foils), it was postulated that small amounts of carbon in the foil lattice might interfere with the ductility at room temperature.

Three different thicknesses of tungsten foils were heated at two temperatures and held for an hour in either graphite- or W-element furnaces for baseline, unirradiated mechanical and elemental testing. This test was to determine if the presence of carbon from the graphite furnace would be enough to cause a noticeable effect on the tungsten foil properties. Elemental composition was measured using the glow discharge optical emission spectrometer (GDOES) technique. results were compared to changes in mechanical properties of shear tensile strength and hardness. The test matrix for the 1-in. W foils is given in Figure 1.

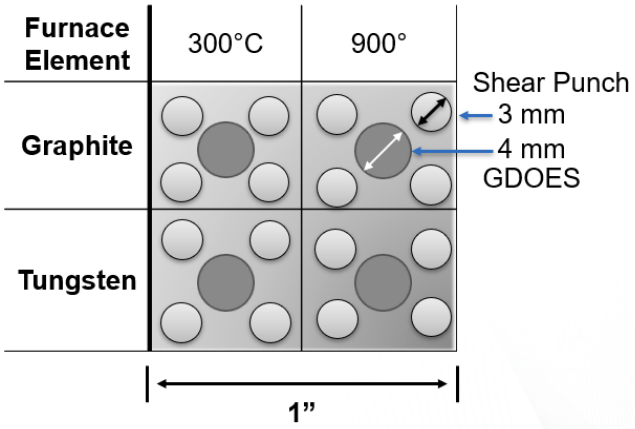

Figure 1. Schematic of testing geometry. Hardness tests were performed in one of the open faces on this side of the foil.

Shear-punch testing is a means of determining mechanical properties of specimens too small for tensile or bend testing. It is useful for thin materials for which tensile testing is difficult to carry out successfully (e.g. W foils). Shear yield and ultimate stress can be linearly related to tensile values. No accurate method of calculating shear strain has been identified in literature. Normalized displacement (δ/t) is analytically useful for comparison of samples of different thickness. Shear-punch tests were performed on the MTS load frame in Low Activation Materials Development and Analysis (LAMDA) laboratory with a 2 kN load cell and a cross-head speed of 0.1 mm/min (2%·min^{-1} strain rate). Stress-strain measurements of yield strength (YS), ultimate tensile strength (UTS), uniform elongation (UE), and total elongation (TE) were determined and test results were interpreted in the program QW, developed by Maxim Gussev at Oak Ridge National Laboratory (ORNL). These results are given in Figures 2-4. This test was used to determine if there was any bulk material property change due to carbon diffusion into the foil. It was found that the greatest effect on the shear stress profile resulted from heating the W foil to 900°C, near but somewhat below the recrystallization temperature of tungsten of 1000-1200°C. There was no significant effect of the type of heating element on the measured shear properties of the foil.

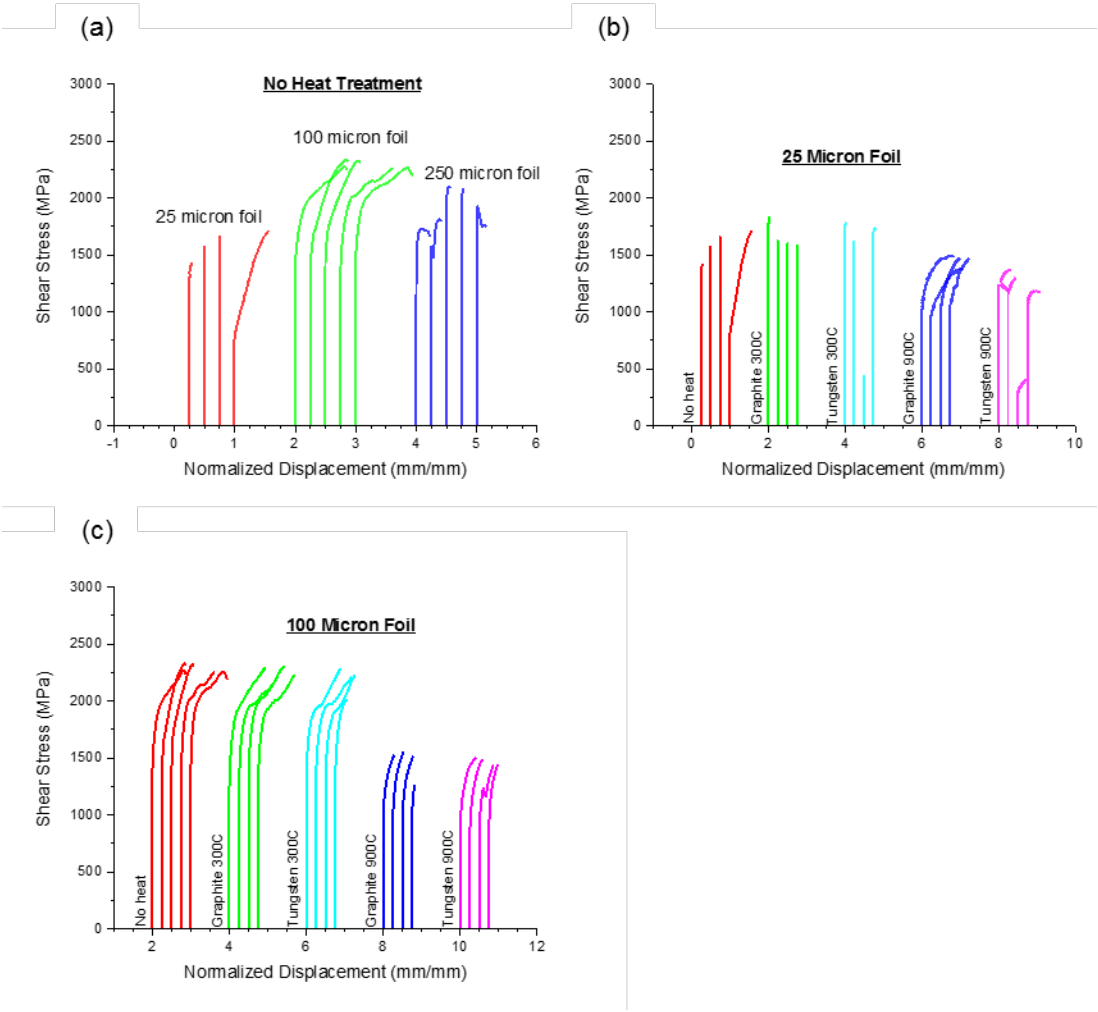

Figure 2. Room temperature shear-punch test results from three thicknesses of tungsten foils (25, 100, and 250 microns) held one hour at two different temperatures (300°C, 900°C) in either a graphite heating element or a tungsten heating element. Only the plastic deformation is shown. (a) as-received, (b) 25 µm thick foil, (c) 100 µm thick foil.

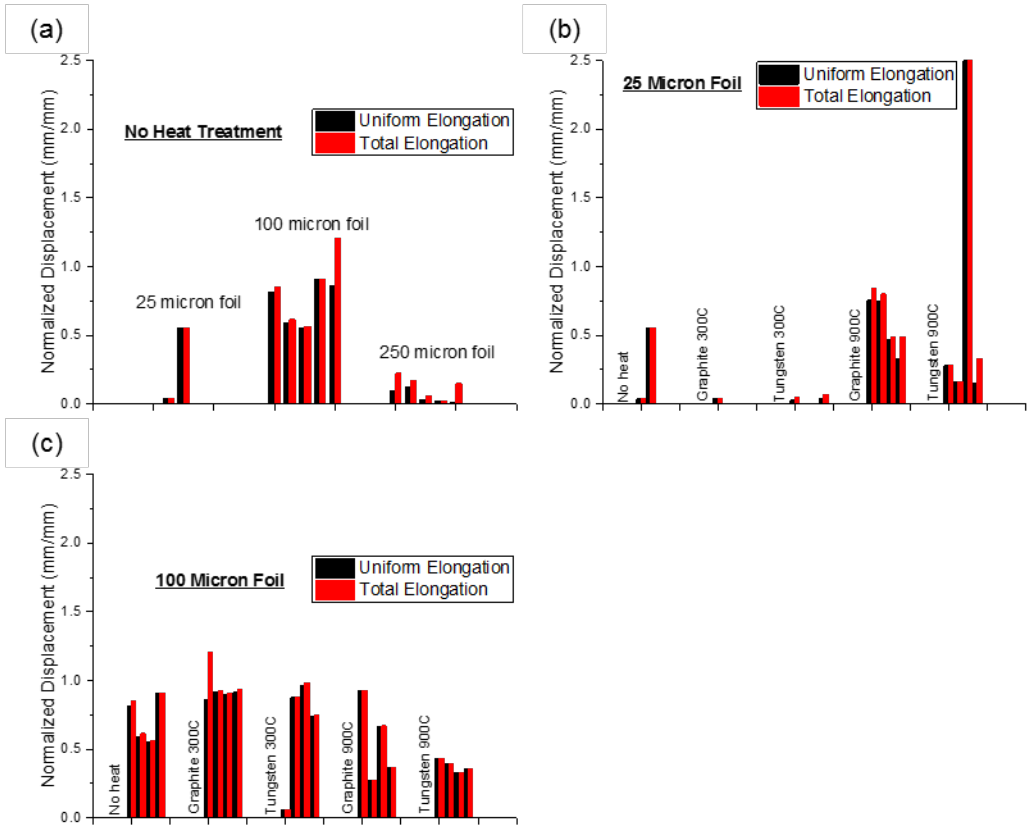

Figure 3. Elongation in shear punch tests of tungsten foils (a) as received, and (b) 25 µm thick foil and (c) 100 µm thick foil after heat treatments.

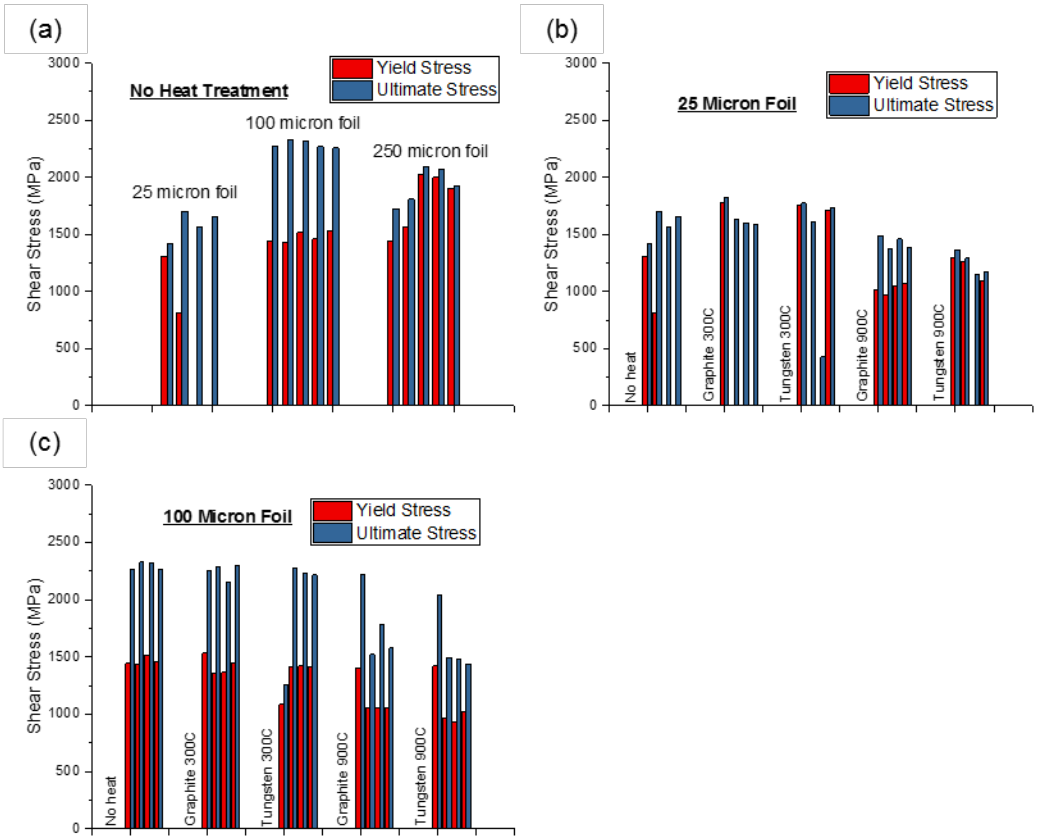

Figure 4. Yield stress and ultimate shear stress from shear punch tests of tungsten foils (a) as received, and (b) 25 µm thick foil and (c) 100 µm thick foil after heat treatments.

Microhardness testing was used to measure any local surface hardening induced by carburization of the tungsten. Vickers hardness indents have a consistent geometry with load and were thus used to observe differences between thicknesses of W foils. The load was determined based on the maximum load that could be used for a valid test, where the depth of the indent does not exceed one-tenth of the thickness of the foil. For the 25 micron-thick foil, an applied load of 50 gf was used. For 100 micron-thick, a load of 500 gf was used. For 250 micron-thick, 1 kgf was used. A dwell time of 10 seconds was used for each indent. Five indents were taken, and the hardness values averaged for each sample, and are given in Figure 5. Because of relieving internal stresses, we would expect the heat treatment to reduce the hardness. However, carburization of the W foil should contribute diffused carbon interstitial atoms that increase the stress state and therefore hardness. We can see from the data that all the foils that were heated in graphite heating elements saw a higher hardness than their tungsten heating-element counterparts. Additionally, the thinner foils also saw a higher hardness value, due to a higher level of carbon saturation at the surface. The higher temperature treatment in the graphite-element furnace also produced an increased level of hardness, which is expected because the diffusivity of carbon is higher at 900°C than at 300°C.It is also worth noting that the foils of all thicknesses had similar hardness values after heating in the tungsten furnace, but the 900°C treated foils had a lower hardness because the elevated temperature relieved internal stresses and lowered the hardness.

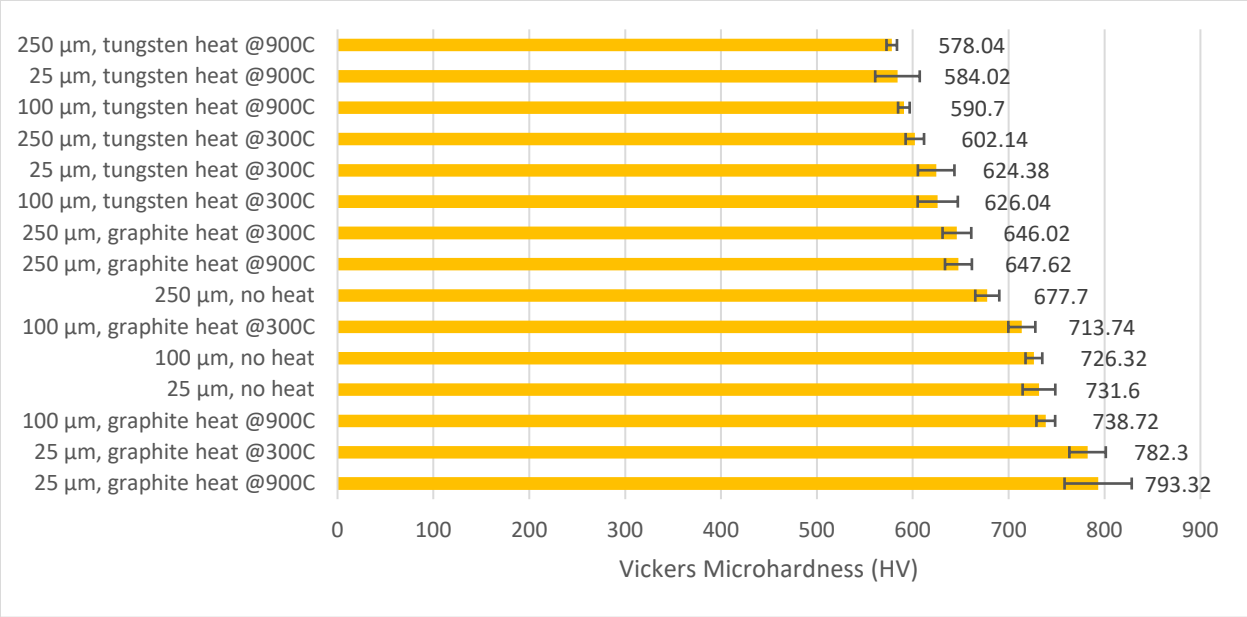

Figure 5. Vickers Microhardness of W foils treated in furnaces with graphite or tungsten heating elements.

The GDOES was performed on each of the foils to get a depth profile of the diffused carbon. The GDOES instrument uses plasma sputter erosion to gather elemental information of the sample with depth. The GDOES analysis was only done for 25 micron and 100 micron-thick foils (Figure 6). The 25-micron foil was experiencing some damage from the plasma after only 30 seconds, so the depth profile does not go deep, only about a tenth of a micron. The 100-micron foil was exposed for 6 minutes and went to a depth between 40-45 microns. We see an increased surface-carbon concentration under each heat treatment, both with the graphite-element and tungsten element furnaces. However, the largest increase in C is seen in the foil that was heated in the graphite-element furnace at 300°C. One of the tungsten-element sample measurements only briefly ignited a plasma and then stopped sputtering, possibly due to a plasma instability, and so the carbon was quickly removed from the surface, but a crater was not properly formed (100 micron-thick W foil heated in the tungsten furnace at 300°C). It was anticipated that the graphite-element furnace at 900°C would show a much larger carbon uptake. However, it is believed that the carbon uptake might depend on which side of the W foil was facing the heating elements versus the graphite substrate below. This was not taken in account when performing the GDOES test and is a likely reason for this discrepancy. Another GDOES test should be performed on the opposite side of the foil to confirm this.

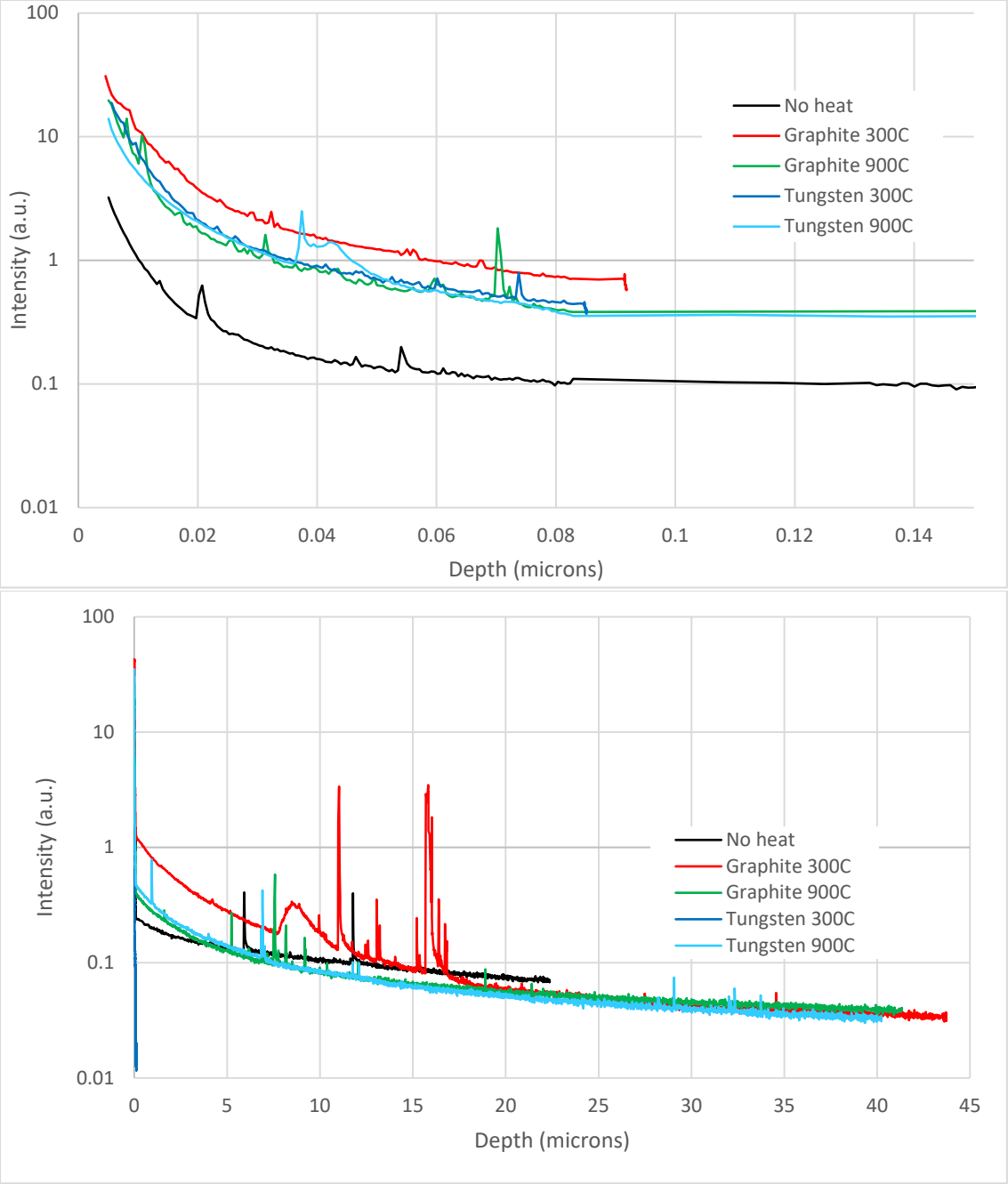

Figure 6. GDOES intensity vs. depth spectrum from 4 mm anode DiP measurement for a) 25 µm thick foil, and b) 100 µm thick foil.

Overall, the shear punch and hardness results showed some differences between the 300°C and 900°C heat treatments, but inconclusive effects of exposure in the graphite versus tungsten element furnaces. The carbon content measured with GDOES was small for all cases, so it was difficult to draw conclusions about differences in C uptake from the different heat treatments. For further investigation, a longer heat treatment with more direct carbon contact with the tungsten may be completed to see the effects of a more significant C uptake. Additionally, the GDOES instrument parameters are being optimized and the data calibrated with standards to reduce the noise level and increase the confidence in the measurements.

4.11 THE INFLUENCE OF LOW ENERGY HELIUM PLASMA ON BUBBLE FORMATION IN MICRO-ENGINEERED TUNGSTEN—Edward X. Gao, Warren Nadvornick, N.M. Ghoniem (University of California, Los Angeles), Russ Doerner (University of California, San Diego)

Extended abstract of a paper published in Journal of Nuclear Materials

Understanding the interaction mechanisms between low-energy helium plasma and solid materials has significant implications in several advanced technologies; primary amongst them are fusion energy and space electric propulsion. Since the penetration of low-energy helium is very shallow, it may be advantageous to manipulate the surface of the solid by micro-engineering techniques to provide a degree of control over the resulting plasma induced damage. Helium plasma exposure of tungsten in fusion devices is known to cause extensive damage due to the creation of nanometer-scale subsurface bubbles [1].

To investigate the effects of surface topology on helium bubble formation in plasma facing materials, four different types of micro-engineered tungsten surfaces were exposed to low energy helium plasma, with a planar surface as control [2]. These samples include two surfaces covered with uniform W-coated rhenium micro-pillars; one with cylindrical pillars 1 μm in diameter and 25 μm in height, the other with dendritic conical pillars 4 - 10 μm in diameter and 20 μm in height. Additionally, two samples with reticulated open-cell foam geometry, one at 45 pores per inch (PPI) and one at 80 PPI were fabricated with Chemical Vapor Deposition (CVD). The samples were exposed to helium plasma at 30 - 100 eV ion energy, 823 - 1123 K temperature, and 5 x 10^{25} m^{-2} - 2 x 10^{26} m^{-2} ion fluence. It is shown that the formation of nanometer-scale tendrils (fuzz) on micro-engineered W surfaces is greatly reduced as compared to planar surfaces. This is attributed to more significant ion backscattering and the increased effective surface area that intercept incident ions in micro-engineered W. A 20% decrease in the average ion angle of incidence via pillar types led to ~30% decrease in average bubble size, down to 30 nm in diameter. W fuzz was found to be absent from pillar sides due to high ion reflection (Figure 1a). In foam samples, 28% increase in PPI is observed to have 24.7% - 36.7% taller fuzz, and 17.0% - 25.0% larger subsurface bubbles. These damages are found to be an order of magnitude smaller than those in planar surface of similar environment. The helium bubble density was found to increase with ion energy in pillars, roughly from 8.2% to 48%, and to increase with increasing PPI, from 36.4% - 116.2%, and with bubble concentrations up to 9.1 x 10^{26} m^{-3}. Geometric shadowing effects in or near surface ligaments of the foam samples were also observed in all foam samples, with near absence of helium bubbles or fuzz in deeper layers of the foam (Figure 1b). The overall size and density of bulk bubbles in micro-engineered tungsten surfaces were found to be significantly smaller than in flat tungsten experiments reported in previous studies, and the associated W fuzz are orders of magnitude shorter as well. This leads to promising areas of research and optimization in utilizing micro-engineered surfaces on plasma facing material to mitigate the potential damages caused by ion irradiation.

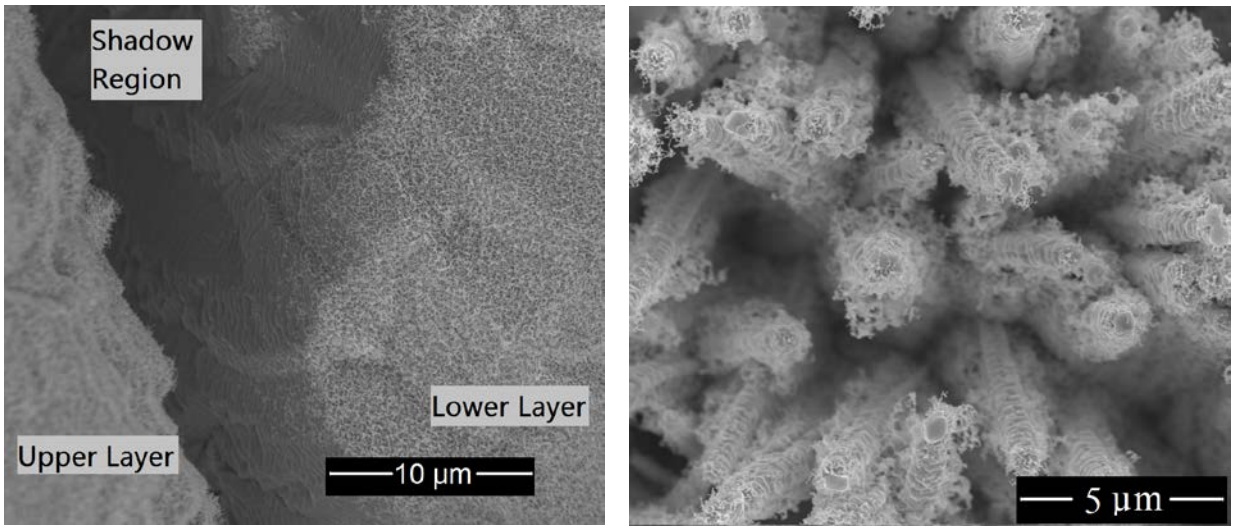

(a) (b)

Figure 1. Scanning electron microscopy (SEM) images of micro-engineered tungsten post low energy helium plasma-exposure for a) micro-pillars depicting fuzz growth near the pillar tips but with pristine pillar side walls; b) reticulated foam depicting the absence of fuzz growth in the "shadow region" where incoming ions are shielded from the lower foam ligament layer by the upper foam layer.

References

[1] N. Yoshida, H. Iwakiri, K. Tokunaga, T. Baba, Impact of low energy helium irradiation on plasma facing metals, *J. Nucl. Mater.* **337** (2005) 946-950.

[2] Edward Gao, Warren Nadvornick, Russ Doerner, Nasr M. Ghoniem, "The influence of low-energy helium plasma on bubble formation in micro-engineered tungsten," *J. Nucl. Mater.* **508** (2018) 319-328.

4.12 DAMAGE MECHANISM INTERACTIONS AT THE PLASMA-MATERIALS INTERFACE (Early Career Award)—C. M. Parish, K. Wang (Oak Ridge National Laboratory)

OBJECTIVE

This work develops the fundamental scientific basis for modeling and predicting the behavior of helium bubbles in refractory materials, to provide support for the science and engineering of the tokamak plasma-facing-material environment. We engaged in collaborations with the University of California – San Diego (UCSD) (Drs. Tynan, Doerner, and Baldwin), and with Dr. Sosuke Konda (Kyoto University). We also hosted two summer students from the University of Illinois Urbana Champaign.

SUMMARY

In this reporting period, we engaged in several parallel efforts to develop the scientific basis of the plasma-materials interaction at the microscopic scale.

First, we collaborated with Dr. Kondo and obtained W-ion irradiated specimens. Irradiation temperature was ~900°C (consistent with our past plasma experiments) and doses around 0.5 dpa. Transmission electron microscopy (TEM) indicated clear dislocation loop formation. We are presently designing experiment to study the plasma interaction with these radiation-induced defects.

Second, we cut and polished (100)-oriented tungsten single crystal obtained from UCSD, and these have been exposed to helium plasma at temperatures below the fuzz-formation threshold (~600°C) in order to produce thick bubble mats underneath the surface. Electron backscatter diffraction (EBSD), nanoindentation, and transmission electron microscopy will be used to study how the helium bubbles modify plasticity and dislocation motion. For instance, a large increase in near-surface nanohardness was observed in ~10^{24} He/m^2 fluence tungsten compared to unexposed material, which we attribute to dislocation blocking by the bubbles. Further analysis is underway.

Third, helium bubbles in nanotendrils have been probed using the monochromated, aberration-corrected scanning transmission electron microscopy (STEM) at Oak Ridge National Laboratory (ORNL). Analysis of the data is underway but preliminary results indicate multi-GPa pressures within the bubbles, as expected from theory. Detailed analysis of bubble pressure vs. size will be valuable to help benchmark theoretical studies and to help rationalize fuzz growth models.

4.13 HIGH HEAT FLUX TESTING OF NEUTRON IRRADIATED TUNSTEN—L.M. Garrison, B. Gregory, A. Sabau (Oak Ridge National Laboratory)

OBJECTIVE

The aim of this work is to understand how neutron irradiation and high heat flux loading change the morphology and properties of tungsten.

SUMMARY

Task 1 of the photon electron new heavy ion experiment (PHENIX) United States-Japan collaboration is to investigate high heat flux (HHF) effects on neutron irradiated tungsten. Tungsten materials with two different orientations were irradiated for Task 1 as part of the High Flux Isotope Reactor (HFIR) RB*19J irradiation capsule. The companion, unirradiated materials have been examined in the scanning electron microscope and will have their height profile measured and will then be exposed in the Oak Ridge National Laboratory (ORNL) Plasma Arc Lamp facility. The same procedure will be used for the irradiated samples.

PROGRESS AND STATUS

A fusion demonstration reactor (DEMO) divertor must be able to withstand extreme conditions including high temperatures, HHF, and neutron irradiation. The ability of irradiated tungsten-based materials to withstand HHF will be evaluated as Task 1 of the PHENIX US-Japan collaboration. Tungsten-based samples irradiated in the HFIR in the RB*19J capsule will be exposed at the Plasma Arc Lamp facility capable of producing HHF of up to 20 MW/m^2. Samples will undergo profilometry and scanning electron microscope (SEM) examination before and after HHF testing to determine the effects of HHF on irradiated tungsten-based materials.

Over twenty types of tungsten-based materials were irradiated in the RB*19J capsule to fast neutron doses of ~0.2-0.7 and at temperatures of 450-1200°C. These tungsten materials will be tested with HHF for Task 1; have their thermal, mechanical, and microstructure properties measured in Task 2; and be exposed to D-T plasma in Task 3 for the PHENIX project. Out of all those in the capsule, there are four types of materials specifically intended for HHF testing. An International Thermonuclear Experimental Reactor (ITER)-grade W with no alloying, and a K-doped W-3Re material were each prepared both parallel and perpendicular to the primary rolling axis to determine the effect of grain elongation orientation on the HHF effects (Table 1).

Prior to testing the irradiated materials, baseline tests will be performed on unirradiated samples. These tests will give insight into the effects of HHF on unirradiated tungsten and allow comparison with the irradiated samples. Table 1 displays the unirradiated material types that will be evaluated. Two or three samples of each material will be tested; all samples are cylindrical disks of 6 mm diameter and 2 mm thickness.

Figures 1-3 display initial SEM images of sample A00C of the K-doped W-3Re material prior to HHF testing. These images are typical of images for all samples in Table 1. All images were taken with a Hitachi S4800 SEM at an accelerating voltage of 5 kV, a beam current around 20 μA, and a working distance around 10 mm. Figure 1 shows the surface of sample A00C at three points across the sample. All materials for the PHENIX irradiation were prepared with approximately an 800-grit surface finish. At this polish level, grains are not visible because of the near surface polishing damage. After neutron irradiation, the samples will not receive additional polishing, so these HHF tests will evaluate the effects on technical rather than pristine surfaces. The upper-left of the sample had more scratches and smaller depressions or pits than the middle and lower-right points on the sample. In general, the amount and size of depressions increased from left to right across the sample. Images taken after HHF testing will be compared to these images to analyze the effect of HHF on general surface structure.

Figure 2 shows areas around laser engraved sample identification (ID) code on each sample. Small crack networks were present near the laser indents, and the effect of HHF on these cracks can be analyzed after HHF exposure. Finally, figure 3 shows a region just outside of the affected area from a laser indent. The laser engraving will be used as a large visual indicator to be able to find the same location on the sample after HHF testing to observe the effect of HHF on specific surface features.

Table 1. Unirradiated tungsten materials to be examined before and after HHF exposure

Material code	Material	Processing
40##	ITER-grade W	Rolled //
50##	ITER-grade W	Rolled ⊥
90##	K-doped W-3Re	Rolled //
A0##	K-doped W-3Re	Rolled ⊥

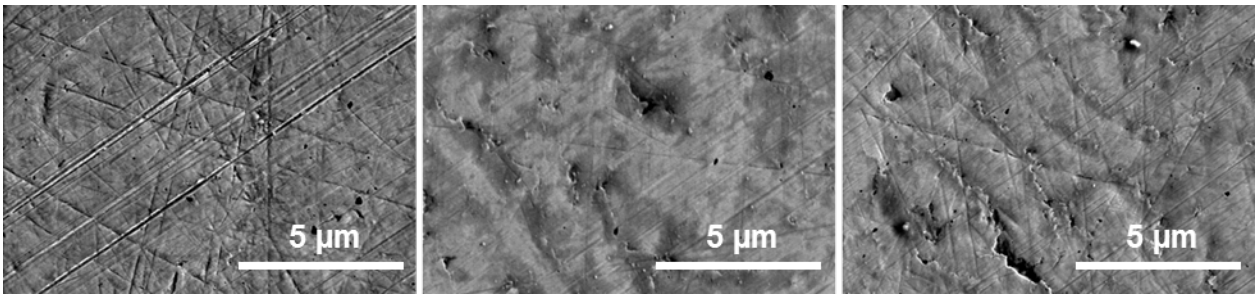

Figure 1. Images of as polished K-doped W-3Re of the upper-left (left), middle (middle), and lower-right (right) of sample A00C.

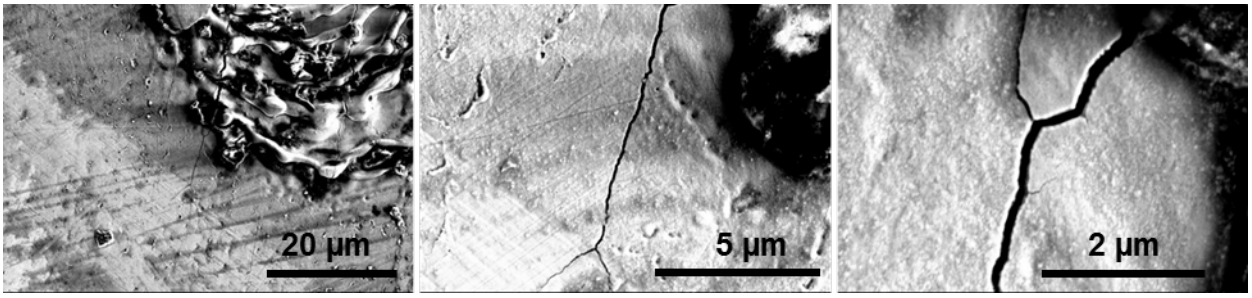

Figure 2. Images of a crack near a laser indent in as polished K-doped W-3Re at increasing magnification from left to right.

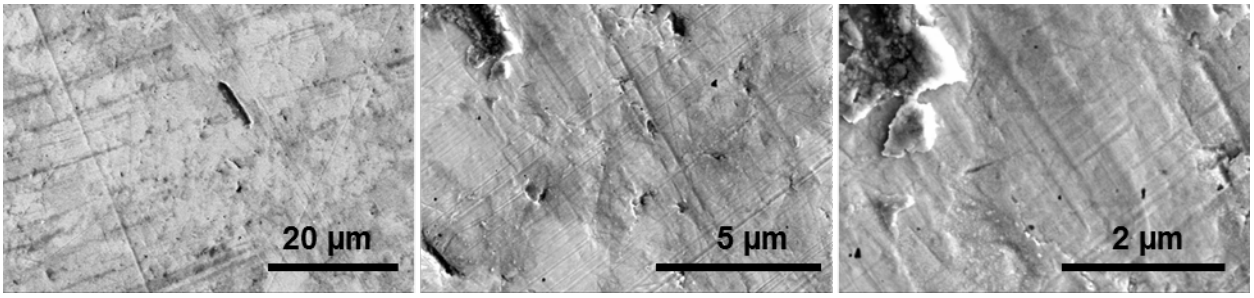

Figure 3. Images of a crevasse about 200 µm from a laser indent in as polished K-doped W-3Re to be used for direct comparison of the same sample after high heat flux testing. The images are taken at increasing magnification from left to right.

5. MAGNETIC AND DIAGNOSTIC SYSTEM MATERIALS

No contributions this reporting period.

6. FUSION CORROSION AND COMPATIBILITY SCIENCE

6.1 LIQUID METAL COMPATIBILITY IN FLOWING SYSTEMS—J. Jun and B. A. Pint (Oak Ridge National Laboratory)

OBJECTIVE

This task is investigating the possibility of increasing the Pb-Li temperature in the dual coolant lead-lithium (DCLL) blanket concept to improve the overall system efficiency. Alloys based on FeCrAl are a potential candidate and monometallic thermal convection loops of a commercial FeCrAl alloy are being built and operated to establish a maximum operating temperature for operation in flowing eutectic Pb-Li.

SUMMARY

Current progress focused on characterizing specimens from the third FeCrAlMo (Kanthal APMT, Fe-21Cr-5Al-3Mo) thermal convection loop (TCL) with a peak temperature of 650°C. Pre-oxidized APMT specimens tended to show lower mass loss than specimens without pre-oxidation but more oxide scale spallation after exposure. Using x-ray diffraction, the surface oxide formed on bare specimens was identified as γ-$LiAlO_2$, while both α-Al_2O_3 and α-$LiAlO_2$ were detected on the pre-oxidized specimens and scanning transmission electron microscopy (STEM) was used to examine the oxide microstructure. Glow discharge optical emission spectroscopy (GDOES) was used to study Pb and Li penetration into the substrate with and without pre-oxidation. Surface W-rich precipitates on specimens from the second TCL (peak 600°C) were identified and attributed to the dissolution of W in the cleaning solution above room temperature.

PROGRESS AND STATUS

Introduction

The DCLL blanket concept (eutectic Pb-17 at.%Li and He coolants) is a leading U.S. design for a DEMOnstration Power Station (DEMO)-type fusion reactor [1]. Typically, reduced activation ferritic martensitic (RAFM) steel is envisioned as a structural material. However, PbLi compatibility will then limit the DCLL to ~475°C metal temperature because Fe and Cr readily dissolve in PbLi above 500°C and reduced activation ferritic martensitic (RAFM) Eurofer 97 plugged a PbLi loop at 550°C [2,3]. Isothermal capsule testing in PbLi and thermodynamic calculations have indicated that Al_2O_3 formed on Al-rich coatings or FeCrAl alloys should be stable in PbLi and inhibit dissolution by forming at the alloy surface [4-9]. However, studies showed that a preformed α-Al_2O_3 surface layer transformed to $LiAlO_2$ during exposures at 600°-800°C [4,10]. The next step in evaluating compatibility is flowing TCL experiments where changes in solubility with temperature can drive mass transfer [2,11]. In 2014, the first monometallic Fe-21Cr-5Al-3Mo alloy (Kanthal APMT) TCL operated with a peak temperature of 550°C and APMT specimens in the hot and cold legs [12]. A second monometallic APMT TCL was operated for 1000 h with a peak temperature of 600°C in 2016 [13-15] and the third TCL with a peak temperature of 650°C operated in 2017 [15]. Only small specimen mass losses were noted after each exposure, especially when the APMT was pre-oxidized to form alumina. For the third TCL, the preoxidation was reduced from 8 h at 1050°C to 2 h at 1000°C [10]. In this report, additional characterization of post-exposure APMT specimens from the third TCL is reported along with analysis of W contamination observed in both the second and third experiments.

Experimental Procedure

The details of the TCL (~1 m tall and 0.5 m wide) and its operation have been previously described [12-15]. The hot and cold leg specimens were SS-3 type tensile (25 x 4 x 0.9 mm) and two rectangular (25 x 18.5 x 1 mm^3) APMT spacer specimens for X-ray diffraction (XRD) and GDOES analyses. All specimens were connected with APMT wire. Most of the specimens, 12 in each leg, were pre-oxidized for 2 h at 1000°C in ambient air to form an α-Al_2O_3 surface layer or scale [10]. Each chain also had four specimens with no pre-oxidation treatment and two specimens pre-oxidized for 8 h at 1050°C, which was the main pre-oxidation condition used in the first two TCL experiments. Rectangular coupons of unalloyed tungsten were attached at the bottom of each specimen chain to act as a "sinker" to keep the relatively low-density specimen chains from floating in the PbLi test fluid, and to act as "spacers" to keep the specimen chain centered within the tubing and liquid metal flow path. The temperature gradient in the TCL was ~120°C from 530-650°C and the velocity was measured at ~0.4 m/min [15]. After operation most of the Pb-Li was poured out of the opened loop while molten, then the entire loop was cooled and filled with a cleaning solution (1:1:1 mixture of ethanol, hydrogen peroxide, and acetic acid) and later specimens were cleaned individually with the same solution. The post-exposure specimens were weighed, then characterized using scanning electron microscopy (SEM) along with energy dispersive spectroscopy (EDS), XRD, X-ray photoelectron spectroscopy (XPS), GDOES and STEM, which was performed on a Field Electron and Ion (FEI) Talos F200X operated at 200 kV and equipped with an extreme field emission gun electron source and Super-X EDS system with 4 silicon drift detectors for chemical analysis. Specimens for STEM analysis were prepared by focused ion beam (Hitachi model NB5000 focused ion beam [FIB]-SEM,) using the *in-situ* lift-out method from exposed surfaces.

Results

The surface and cross-section of pre-oxidized APMT specimens from the cold leg of the third TCL are shown in Figures 1 and 2. The SEM/EDX maps of the region in Figure 1a show the pre-formed alumina scale (enriched in Al and O) and a spalled region, Figure 1b. In cross-section, a pitted area is shown in Figure 1d and the associated maps indicate the Al-rich surface oxide and the Mo-rich phases, Figure 1e. The surface and cross-section of PbLi-exposed APMT specimens without pre-oxidation are shown in Figure 2. The formation of the Al-rich oxide scale was confirmed (Figures 2a-2c). With and without pre-oxidation, dissolution occurred in selected areas apparently followed by oxide formation that inhibited further attack.

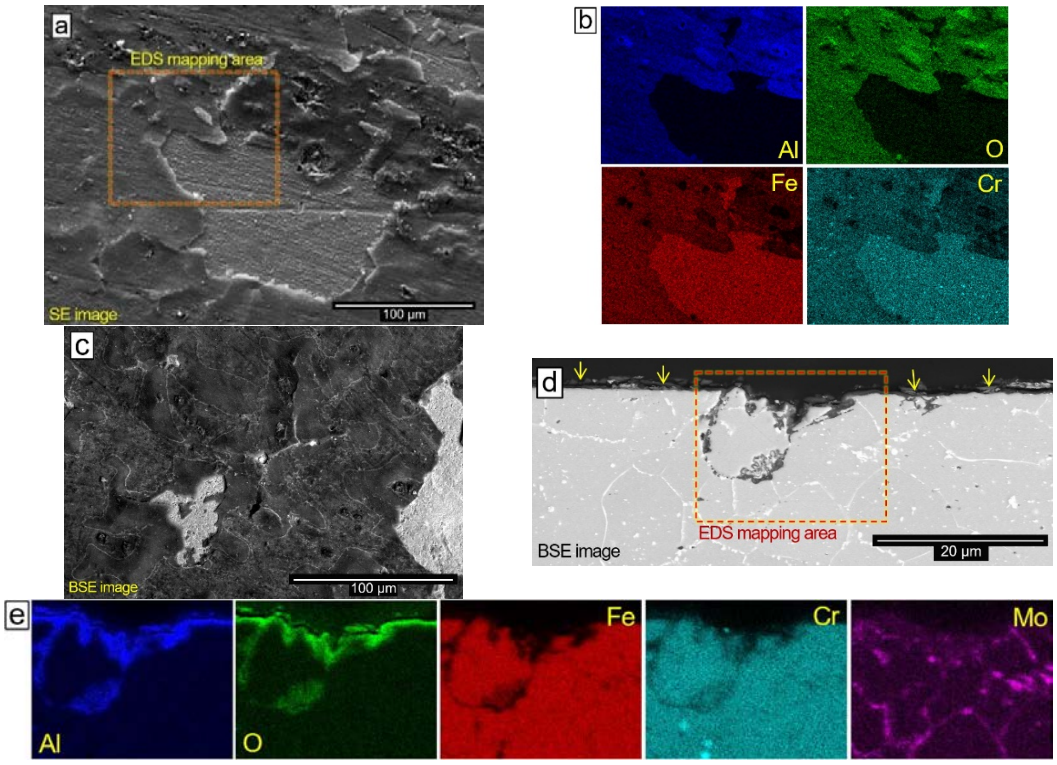

Figure 1. Pre-oxidized APMT specimens exposed to 603 and 611°C Pb-Li in the cold leg of the third TCL: (a) plan view of post-exposure specimen at 603°C, (b) EDS mapping of the selected area in (a), (c) plan and (d) cross-sectioned view of post-exposure at 611°C, and (e) EDS mapping of the selected area in (d). The mass changes were -0.66 and -0.19 mg·cm^{-2} for 603 and 611°C post-exposure specimens.

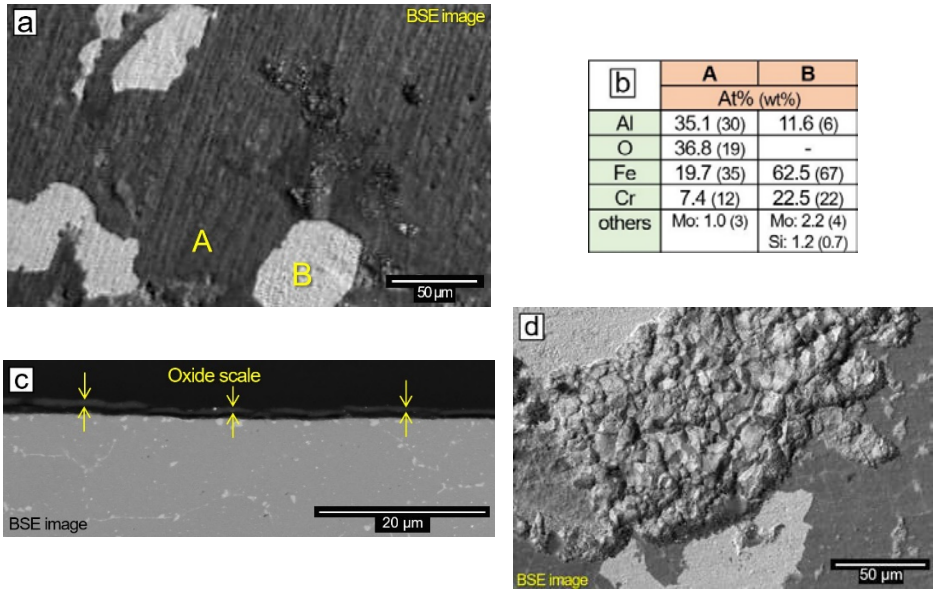

b	A	B
	At% (wt%)	
Al	35.1 (30)	11.6 (6)
O	36.8 (19)	-
Fe	19.7 (35)	62.5 (67)
Cr	7.4 (12)	22.5 (22)
others	Mo: 1.0 (3)	Mo: 2.2 (4) Si: 1.2 (0.7)

Figure 2. Bare APMT specimens exposed to 645 and 626°C Pb-Li in the hot leg of the third TCL: (a) plan view of post-exposure specimen at 645°C, (b) the composition of A and B spots in (a) by EDS analysis, (c) cross-sectional view of the specimen in (a) and (d) plan view of post-exposure at 626°C. The mass changes were -0.44 and -2.2 mg·cm^{-2} for 645 and 626°C post-exposure specimens.

The results of XRD on bare and pre-oxidized APMT coupons after Pb-Li exposure are shown in Figure 3. Two different $LiAlO_2$ phases, α and γ, were detected preferentially on each specimen: γ-$LiAlO_2$ on bare APMT and α-$LiAlO_2$ with α-Al_2O_3 on pre-oxidized APMT. The Pb-Li temperature at which the formation of γ-$LiAlO_2$ occurred on bare APMT was 607°C, which was about 200°C lower than the previous results that confirmed $LiAlO_2$ on a commercial FeCrAl exposed to static Pb-Li at 800°C [10]. Meanwhile, α-$LiAlO_2$ in pre-oxidized APMT is considered to form by a reaction between Al_2O_3 and Pb-Li.

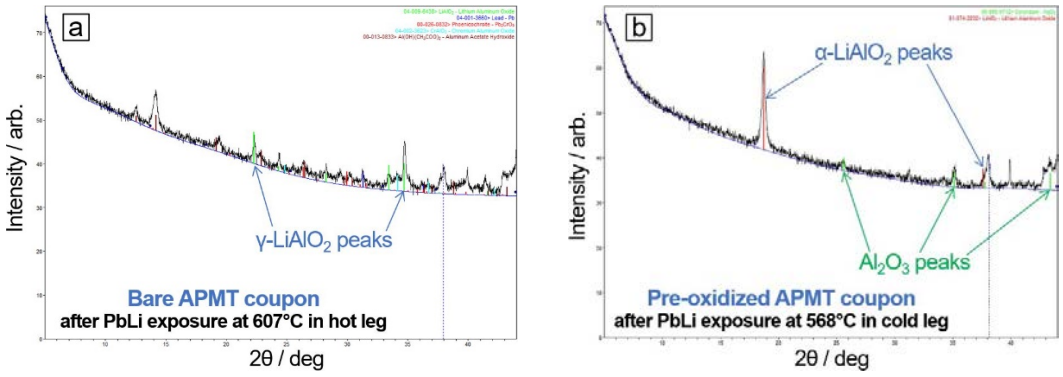

e 3. The XRD results of (a) bare and (b) pre-oxidized APMT coupons from the third TCL.

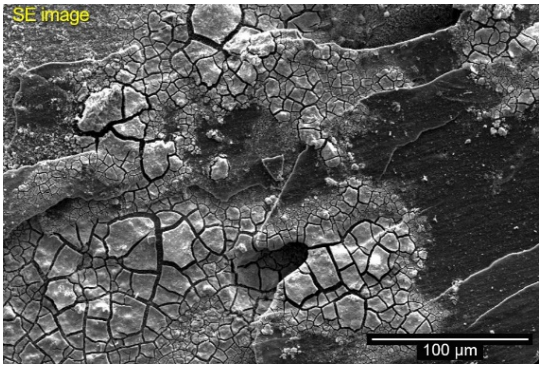

Figure 4. Plan view SEM image of pre-oxidized APMT specimen exposed to Pb-Li at 515°C in the cold leg with mass loss of 3.2 mg·cm^{-2}.

During SEM characterization of specimens from the second TCL, surface precipitates were observed which appeared to be rich in W and C. An example is shown in Figure 4. To confirm this observation, XPS surface mapping was used with an example shown in Figure 5. Figure 5a shows the initial surface and Figure 5b was the same area after 30 s of sputtering. Sputtering was used to remove surface C contamination found on most specimens. A likely source of W was the W "sinkers" used to ensure the specimen chains did not float in the Pb-Li during TCL operation. It is unlikely that W dissolved during the PbLi exposure as it is relatively inert [16-18] and W deposition was not observed in the third loop exposed at higher temperature. A more likely explanation is that W dissolved in the cleaning solution. To verify this, unexposed W coupons were immersed in the cleaning solution at room temperature (*RT*) and 50°C for 2 h. The resulting mass losses of W coupons were 1.5 and 171 mg·cm^{-2} at *RT* and 50°C, respectively, indicating the dissolution of W was possible by the cleaning solution and can be significantly enhanced with increasing temperature. The mass loss of W-sinkers measured from the second TCL lies between the mass loss of W at *RT* and 50°C as shown in Figure. 7, suggesting that W dissolved by the cleaning solution in the temperature range of *RT* to 50°C. This issue will be avoided in the future by ensuring that the cleaning is done at RT.

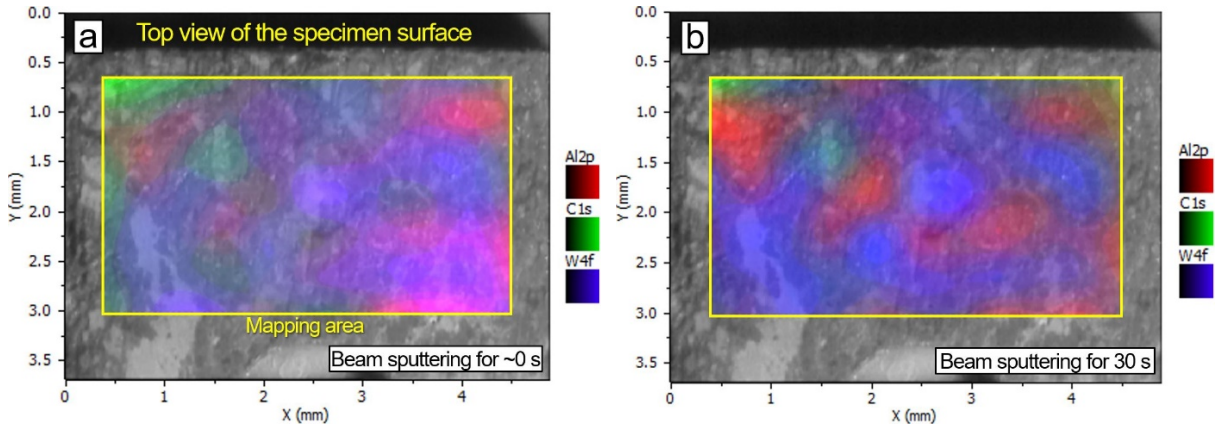

Figure 5. The XPS mapping showing Al, C and W distribution: (a) the initial surface with sputtering time close to 0 s and (b) sub surface exposed after 30 s of sputtering.

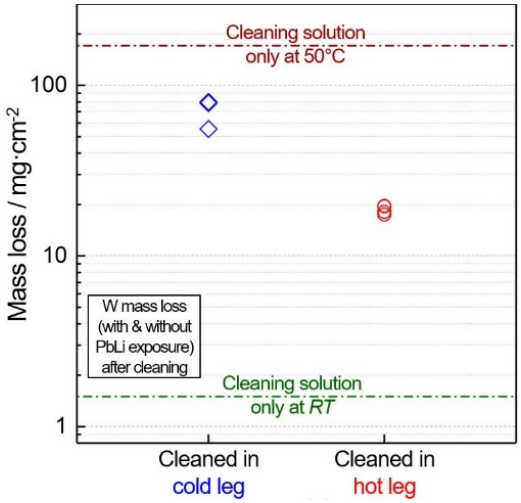

Figure 6. Mass loss of W in the second TCL and the cleaning solution (1:1:1 mixture of ethanol, hydrogen peroxide, and acetic acid) at *RT* and 50°C.

Because the reaction products were relatively thin, STEM was used to characterize the oxide microstructure before and after PbLi exposure, Figure 7. Bare APMT exposed to PbLi at 645°C formed a uniform surface scale with the gaps at the scale–substrate interface likely formed during FIB specimen preparation (Figure 7a). The scale appeared to have a columnar grain structure and contained Al and O together with segregated Fe and Cr as confirmed by EDS (Figure 7b). However, Li cannot be detected by EDS. Pre-oxidized APMT after PbLi exposure showed a bi-layer scale with precipitates in the upper scale layer (Figure 7c). According to the XRD results, this scale should contain both α-Al_2O_3 and α-$LiAlO_2$. The EDS analysis of the upper layer (Figure 7d) identified the precipitates as oxides rich in Fe and Cr. In pre-oxidized APMT prior to exposure, the α-Al_2O_3 scale showed the classic columnar structure with fine grains at the gas interface (Figure 7e), similar to prior observations for an oxide dispersion strengthened FeCrAl alloy oxidized at this condition [10]. The maps shown in Figure 7f indicate that the fine-grained outer layer contained some oxide grains rich in Cr and Fe typical of the first-formed transient oxide on FeCrAl. These precipitates likely lead to the Fe and Cr oxide precipitates observed after PbLi exposure (Figures 7c-7d).

To analyze the possible penetration of Pb and Li into APMT during the third TCL exposure, GDOES was utilized which sputters through a 1-2 mm diameter area [19]. Figure 8 shows sputter profiles through several hot and cold leg specimens compared to a bare APMT specimen without preoxidation. The Al, Cr and O profiles were used to establish the location of the oxide-metal interface, which appeared to occur around 15 s of sputtering time. Profiles for Pb and Li are shown in Figures 8d and 8e, respectively. Compared to the baseline for unexposed bare APMT, higher levels of Pb and Li could be detected. However, only low levels of Pb could be detected and may represent Pb trapped in pits (e.g. Figure 1d) in the sputtered area. In contrast, the diffusion depth of Li was much deeper and the signal in the alloy was much higher. The relative depth of penetration detected did not increase with temperature nor was it significantly affected by pre-oxidation. It is not surprising that the small Li ion was better able to diffuse into the alloy. Currently, the sputter craters are being characterized to convert the sputter time in Figure 8 to depth.

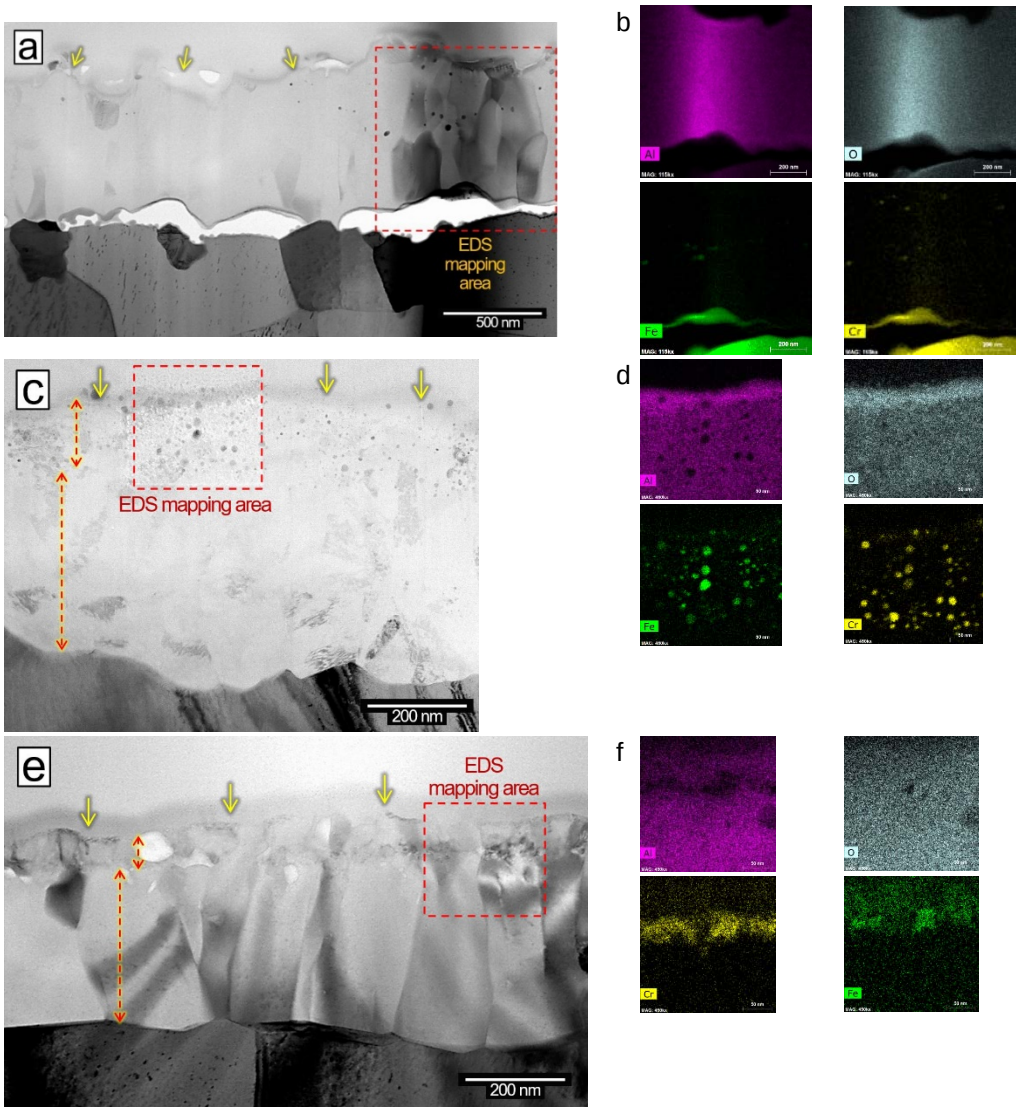

Figure 7. Bright field STEM images and EDS elemental maps of cross-sectioned scale formed on APMT specimens: (a,b) bare and (c,d) pre-oxidized APMT after PbLi exposure in hot leg of 650°C TCL, and (e,f) pre-oxidized APMT with no exposure. The arrows on the top side indicate the interface between scale and C deposition layer, and the two-way arrows designate upper and lower layers of bi-layer scales. The pre-oxidation was conducted at 1000°C for 2 h, and the estimated PbLi temperature and mass change for the APMT specimens were 645°C/-0.44 mg·cm^{-2} in bare condition and 650°C/-0.1 mg·cm^{-2} in pre-oxidized condition.

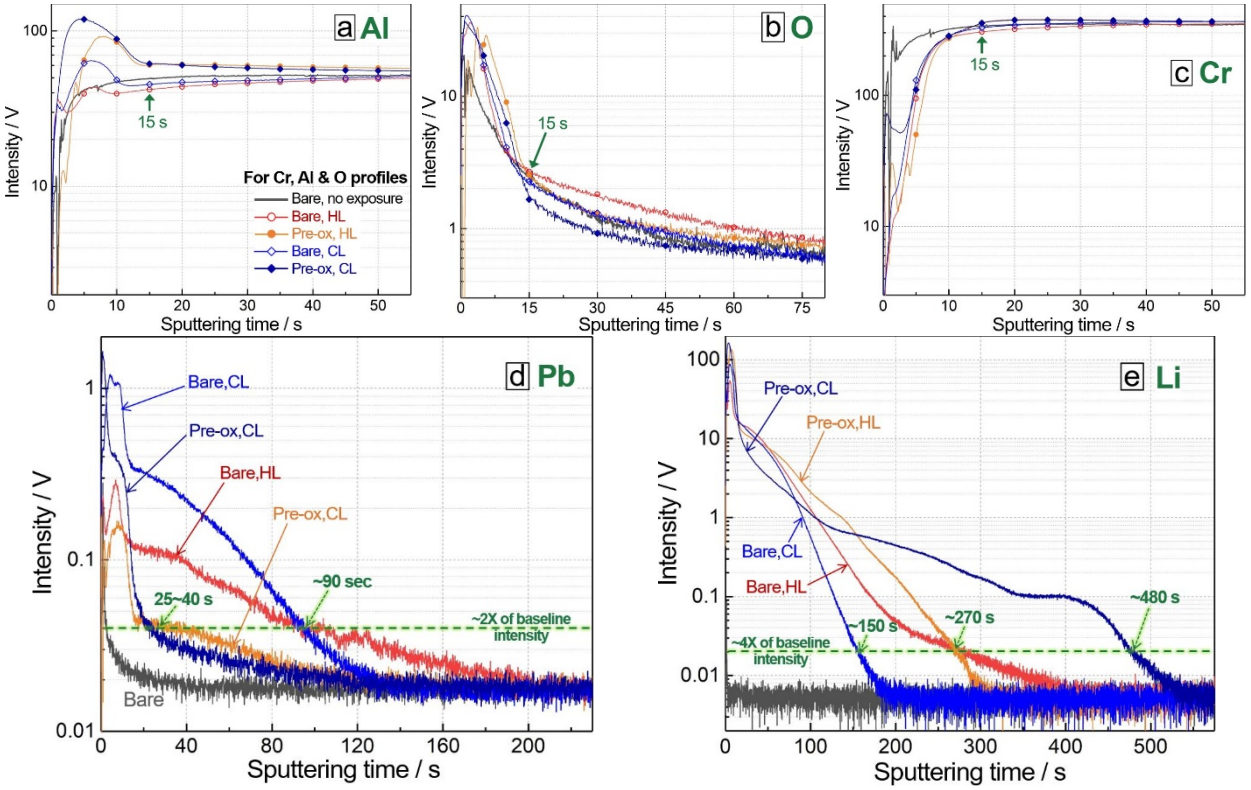

Figure 8. GDOES intensity profiles of (a-c) Al, O and Cr, (d) Pb and (e) Li plotted versus sputtering time. The estimated PbLi temperature and resulted mass change for bare APMT were 607°C/-4.88 mg·cm^{-2} in hot leg (HL), and 573°C/-3.66 mg·cm^{-2} in cold leg (CL). For pre-oxidized (at 1000°C for 2 h, Pre-ox) APMT, the values were 603°C/-0.41 mg·cm^{-2} in HL, and 568°C/-0.43 mg·cm^{-2} in CL.

References

[1] M. Abdou, et al., Fusion Sci. Technol., 47 (2005) 475.
[2] O. K. Chopra, et al., Fusion Technol., 8 (1985) 1956.
[3] J. Konys, et al., J. Nucl. Mater. 386-88 (2009) 678.
[4] B. A. Pint, L. R. Walker and K. A. Unocic, Mater. High Temp. 29 (2012) 129.
[5] K. A. Unocic and B. A. Pint, J. Nucl. Mater. 455 (2014) 330.
[6] B. A. Pint, S. Dryepondt, K. A. Unocic and D. T. Hoelzer, JOM 66 (2014) 2458.
[7] K. A. Unocic, D. T. Hoelzer and B. A. Pint, Mater. High Temp. 32 (2015) 123.
[8] P. Hubberstey, T. Sample and A. Terlain, Fusion Technol., 28 (1995) 1194-9.
[9] P. Hubberstey, J. Nucl. Mater. 247 (1997) 208.
[10] B. A. Pint and K. L. More, J. Nucl. Mater. 376 (2008) 108.
[11] J. H. DeVan, J. Nucl. Mater., 85-86 (1979) 249.
[12] S. J. Pawel and K. A. Unocic, J. Nucl. Mater. 492 (2017) 41.
[13] B. A. Pint and S. J. Pawel, DOE-ER-0313/60 (2016) 137.
[14] B. A. Pint and J. Jun, DOE/ER-0313/61 (2016) 133.
[15] J. Jun and B. A. Pint, DOE/ER-0313/63 (2017) 106-113.
[16] H. Glasbrenner, J. Konys, H.D. Rohrig, K. Stein-Fechner and Z. Voss, J. Nucl. Mater. 283-87 (2000) 1332.
[17] K. Splichal and M. Zmitko, J. Nucl. Mater. 329-33 (2004) 1384.
[18] F. Barbier, Ph. Deloffre and A. Terlain, J. Nucl. Mater. 307-311 (2002) 1351.
[19] M. J. Lance, D. N. Leonard and B. A. Pint, in Proceedings of the 6th International Symposium on Supercritical CO_2 Power Cycles, Pittsburgh, PA, March 2018, Paper #117.

7. MECHANISMS AND ANALYSIS

7.1 FURTHER EVIDENCES ON THE RADIATION TOLERANCE OF Ti-BASED NANOLAYERED MAX PHASES—Matheus A Tunes, Graeme Greaves, Anamul. H. Mir, Stephen E. Donnelly (University of Huddersfield, United Kingdom), Philip D. Edmondson (Oak Ridge National Laboratory)

OBJECTIVE

Stoichiometric $M_{n+1}AX_n$ (MAX) phases are a class of carbides and nitrides that have recently been considered as candidates for the next generation of innovative nuclear reactors where the operation at high-temperatures (1000-1273 K) and extreme doses (200-500 dpa) are major requirements. Prior to their utilisation within the context of nuclear technology, it is important to assess their radiation damage tolerance under energetic particle exposure. To date, only a limited number of neutron irradiation studies have been published that have focused on the microstructural alterations at low doses (~ 3.6 dpa) and at intermediate-to-high-temperatures (from 773 to 973 K) [1]. Ion irradiation has been used as an alternative methodology to investigate whether these materials possess superior radiation tolerance. Recent reports indicate that unlike most ceramic-based materials, MAX phases have not amorphized under irradiation [2], which suggests a self-healing capability for such materials [3].

SUMMARY

The methodology of heavy ion irradiation *in situ* within a Transmission Electron Microscope (TEM) has been used to investigate the microstructural response of two Ti-based MAX phases: Ti_3SiC_2 and Ti_2AlC. The materials have been irradiated with 700 keV Kr^{+2} at 1008 K up to 5 dpa. For a comparison, α-Ti and α-Al (both 99.95% pure) were also irradiated with the same ions and energy up to the same dose levels, but, at temperatures of 1143 and 558 K respectively to match the homologous temperature of the MAX phases. On the latter subject, 1673 K has been used as the reference for the MAX phases "melting point". As it has been previously reported that in the temperature range 1673-1973 K Ti_3SiC_2 decomposes into TiC + liquid [4].

Results

A comparison of the ion irradiations performed is shown in the bright-field TEM (BFTEM) micrographs in Figure 1. Both the pure metals have been observed to develop black-dot damage, dislocation loops and voids in the dose range of 0 to 5 dpa, whereas, the Ti-based MAX phases remained unchanged in this dose range. Nanometre-sized black-rounded particles have been observed in both Ti_3SiC_2 and Ti_2AlC at 1008 K before irradiation and EFTEM characterisation has shown that these particles are intermetallic phases (titanium silicides and aluminides) that have formed upon annealing. They have already been predicted, by means of computer simulations, to form in the Ti–Al–C and Ti–Si–C ternary systems as a result of synergistic competition for nucleation and growth with the major ternary carbide phases [5, 6]. These preliminary results indicate a superior radiation tolerance of the ternary carbides when compared with two of their pure metal counterparts. However, further studies at higher doses (~ 100 dpa) are required to understand whether the MAX phases remain radiation resistant with increased exposure.

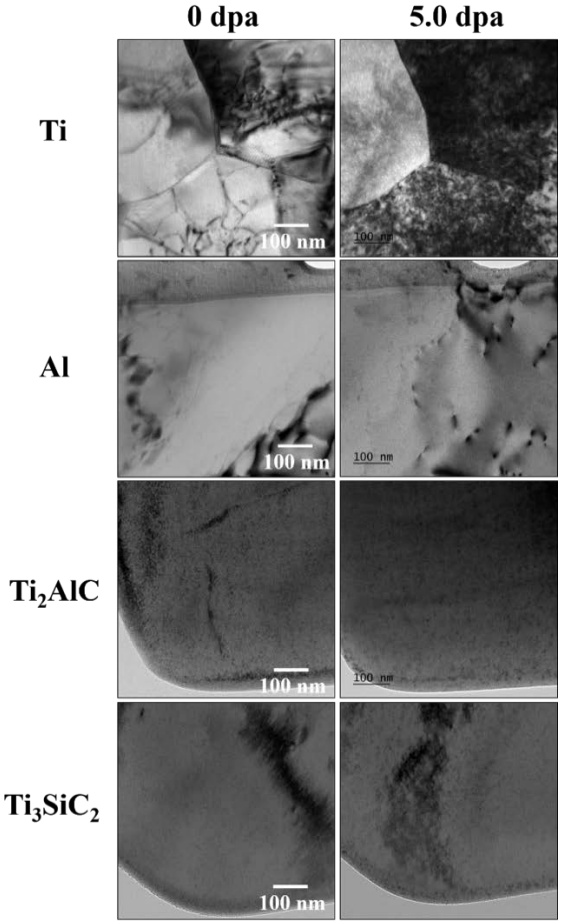

Figure 1: Under focused BFTEM micrographs (1000 nm of defocus) of the four materials; α-Ti, α-Al, Ti_2AlC and the Ti_3SiC_2 at 0 and 5 dpa.

Ongoing work and sponsorship

This work follows a major research effort under the scope of the Oak Ridge National Laboratory (ORNL) fusion materials program which is aimed at establishing a dataset for the behaviour of these Ti-based MAX phases under neutron and ion irradiations. Two manuscripts are currently being prepared to report the complete results at both the Low Activation Materials Development and Analysis (LAMDA) laboratory at ORNL and at the Microscopes and Ion Accelerators for Materials Investigation (MIAMI) facility in the United Kingdom.

Acknowledgements

Mathew A Tunes is grateful to Oak Ridge Associated Universities for provision of an American Society for Therapeutic Radiology and Oncology (ASTRO) fellowship, under the U.S. Department of Energy contract DE-AC05-06OR23100.

References

[1] *Acta Mater.* **85** Acta Materialia Inc. (2015) pp. 132.
[2] *Acta Mater.* **58** (2010) pp. 4362.
[3] *Prog. Solid State Chem.* **28** Pergamon (2000) pp. 201.
[4] *Annu. Rev. Mater. Res.* **41** (2011) pp. 195.
[5] *J. Mater. Res.* **7** (1992) pp. 1473.
[6] *J. Phase Equilibria* **21** (2000) pp. 195.

7.2 A COUPLED DISLOCATION DYNAMICS-CONTINUUM BARRIER FIELD MODEL WITH APPLICATION TO IRRADIATED MATERIALS—Y.N. Cui, G. Po, N.M. Ghoniem (University of California, Los Angeles)

Extended abstract of a paper published in International Journal of Plasticity

Understanding the effects of barriers on dislocation motion is essential in many applications, such as in metal alloys hardened by distributing small precipitates, in structure component that is subjected to irradiation or hydrogen environment. Even though dislocation barriers contribute significantly to hardening, there are more often embrittling effects associated with the presence of barriers. Revealing the collective interactions between dislocations and dispersed barriers is thus a vital prerequisite for designing stronger, yet ductile and more reliable materials and structures.

A persistent challenge in numerical simulations is the tremendous computational cost in direct 3-dimensional (3D) Discrete Dislocation Dynamics (DDD) simulations of dislocations and discrete barriers [1,2], since such barriers are typically small (nano-meter scale) and have very high number density. This work opens up a new route for computational studies of high-density barrier effect by developing a hybrid model through coupling 3D DDD with continuum barrier fields. Taking irradiation defects as an example of general dislocation barriers, the hybrid model is presented in detail, as schematically shown in Figure 1. The continuum irradiation defect field models are critically discussed. Coupled model parameters are obtained from detailed statistical analysis of 3D DDD simulations of single dislocation-barrier interactions (see Figure 2). We develop a crystal lattice-based continuum material point arrangement method to precisely distribute localized plastic strain as a result of dislocation-barrier interactions, enabling the method to be crystal-structure sensitive.

The model is demonstrated by an application to the study of the physics of dislocation channel formation and plastic instability phenomena in irradiated materials. The results are shown to agree with experiments on the magnitude of radiation hardening and the onset of plastic instability (see Figures 3a-b). Plastic flow localization in irradiated materials was shown to be more prevalent at high irradiation dose (see Figures 3c-d). The remarkable high efficiency of the current model compared with previous work demonstrates a new possibility of understanding dislocation channel formation problem in irradiated materials through mechanism-based 3D DDD simulations, complementing the studies by phenomenological crystal plasticity theory and experiments. Another main advantage of the present hybrid model is that it can be readily extended to study flow localization problems in materials with other kinds of dispersed barriers, such as precipitation- hardened alloys, and in materials with hydrogen etc.

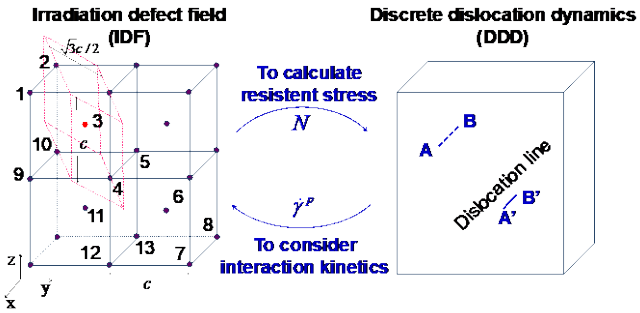

Figure 1. Schematic of variable-transferring procedures in the coupled barrier-field dislocation-dynamics model. The N is the irradiation defect density, $\dot{\gamma}^p$ is plastic shear strain rate. The circle points on the left represent continuum material points. The red dashed hexahedron on the left represents the characteristic volume of the red circle point.

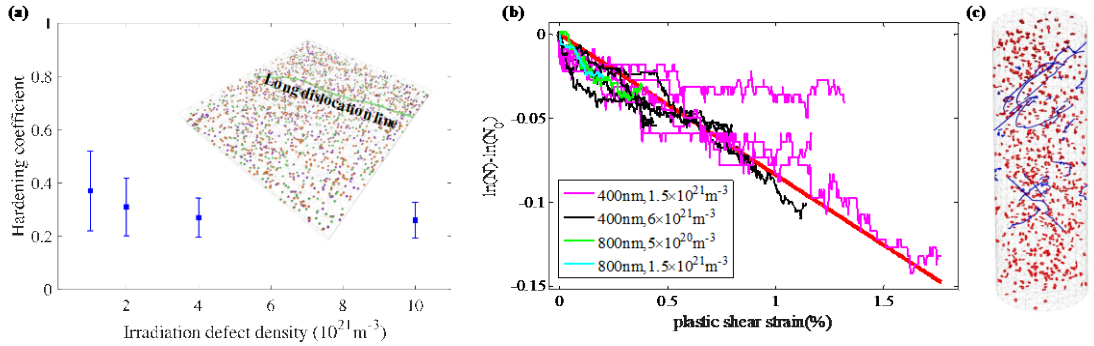

Figure 2. (a) Irradiation hardening parameter caused by interstitial loops. The inset shows an example of DDD simulations with discrete interstitial loops (number density N: 2×10^{21}m^{-3}) to determine the irradiation hardening parameters. (b) Interstitial loop density evolution during the compression test of irradiated Fe micropillar, the thick red line corresponds to $\ln(N)-\ln(N_0)=-8.4\gamma^p$. (c) one typical microstructure configuration of 400 nm irradiated Fe pillar. Blue lines are dislocations networks, while red circles are interstitial loops

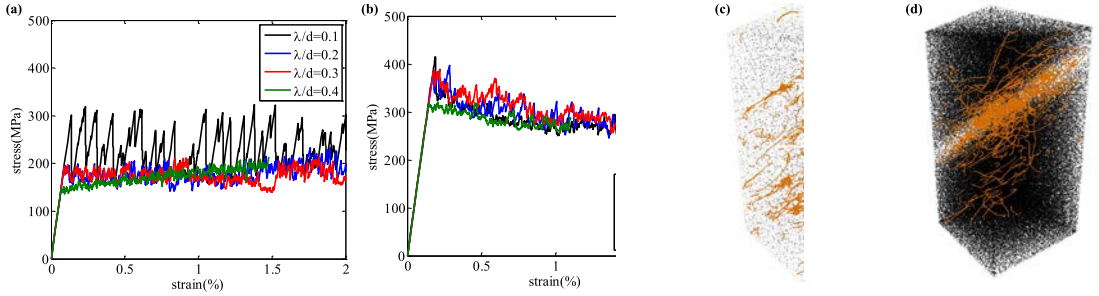

Figure 3. Simulation results for compressed Fe pillar with diameter 1500 nm obtained by coupled Field-DDD simulations. (a-b) stress-strain curves at irradiation dose 7.5×10^{-3} dpa and 3.75×10^{-1} dpa, respectively. λ is the average dislocation source length, and d is the sample diameter. The yield stress values are comparable to the corresponding experimental results [3]. (c-d) Dislocation configurations and irradiation defect distributions after deformation. The homogeneous deformation at low dose condition (7.5×10^{-3} dpa) in (c) and the dislocation channel formation at high dose (3.75×10^{-1} dpa) in (d) are consistent with the corresponding experimental observations in [3].

References

[1] Arsenlis A et al. A dislocation dynamics study of the transition from homogeneous to heterogeneous deformation in irradiated body-centered cubic iron, Acta Materialia, 2012, 60(9), 3748-3757.

[2] de la Rubia TD et al. Multiscale modelling of plastic flow localization in irradiated materials, Nature, 2000, 406(6798), 871-874.

[3] Singh BN et al. Effects of neutron irradiation on microstructure and mechanical properties of pure iron, Journal of nuclear materials,1999, 271, 97-101.

7.3 ADVANCED STEM-BASED DEEP LEARNING FOR SEMANTIC SEGMENTATION OF IRRADIATION DEFECTS—Yuanyuan Zhu, Danny J. Edwards Richland J. Kurtz (Pacific Northwest National Laboratory) Graham Roberts (Western Washington University)

OBJECTIVE

The goal of this work is to develop a (deep) convolutional neural network (CNN) model for recognition of extended irradiation defects, based on optimized diffraction contrast imaging scanning transmission electron microscopy (DCI STEM) data.

SUMMARY

To pave the way for reliable feature recognition, we established an advanced DCI STEM technique capable of recording defect images with high clarity, free of bend contour artifacts. Based on these high-quality DCI STEM images, several CNN sematic segmentation models have been under training to segment three types of typical irradiation defects, dislocations, voids and precipitates, in a neutron-irradiated HT-9 ferritic/martensitic alloy as an example.

PROGRESS AND STATUS

Introduction

Transmission electron microscopy (TEM) is one of the most common characterization tools in the study of irradiation damage in nuclear materials. However, the effort to obtain statistically meaningful quantification of different types of defects and phases produced during irradiation, such as dislocation lines and loops, voids and bubbles, and various types of precipitates, is a labor-intensive and time-consuming task. For most image processing and analysis techniques, the quality of the input images governs the reliability of feature classification. Additionally, for supervised CNN training typically used in image segmentation, the fidelity of the ground truth label determines the best achievable accuracy.

Experimental Procedure

DCI STEM

All TEM images used for CNN models training were acquired using the advanced DCI STEM imaging mode providing bend-contour-free input images[1]. In this work, DCI STEM imaging was performed using a modern Japan Electron Optics Laboratory (JEOL) ARM200CF microscope operated at 200kV, with a convergence semi-angle of 6.2 mrad and bright-field collection angle of 9 mrad. This imaging setting was optimized previously for the irradiated body-centered cubic (BCC) HT-9 ferritic alloy. To balance field-of-view size and pixel resolution, a magnification of 250,000x and a 2048 pixel x 2048 pixel image size along with a dwell time of 16 us were used to acquire all DCI STEM images. Figure 1 presents an example of the DCI STEM image pair obtained under two different diffraction conditions for optimal feature contrast for dislocations, and for voids and precipitates, respectively. For imaging dislocations, the commonly used systematic row diffraction condition was satisfied by tilting the TEM foil away from [001] zone axis to approximately $1\boldsymbol{g}_{011}$ on Bragg. The resulting dark image contrast, as shown in the close-up in Figure 1a, mainly outlines the presence of dislocations (with occasionally interference from Moiré fringes of precipitates[2]). In the same field of view, the TEM foil was then slightly tilted away (about 2^o to 4^o) from the systematic row diffraction condition to produce a kinematical diffraction condition (Figure 1b). As the diffraction contrast of dislocations is suppressed, the mass-thickness contrast becomes dominant, providing an almost exclusive view of the voids and precipitates. Using this divide-and-conquer DCI STEM imaging protocol, the raw images collected are not only free of bend contour artifacts but also clear separation of dislocations from voids and precipitates.

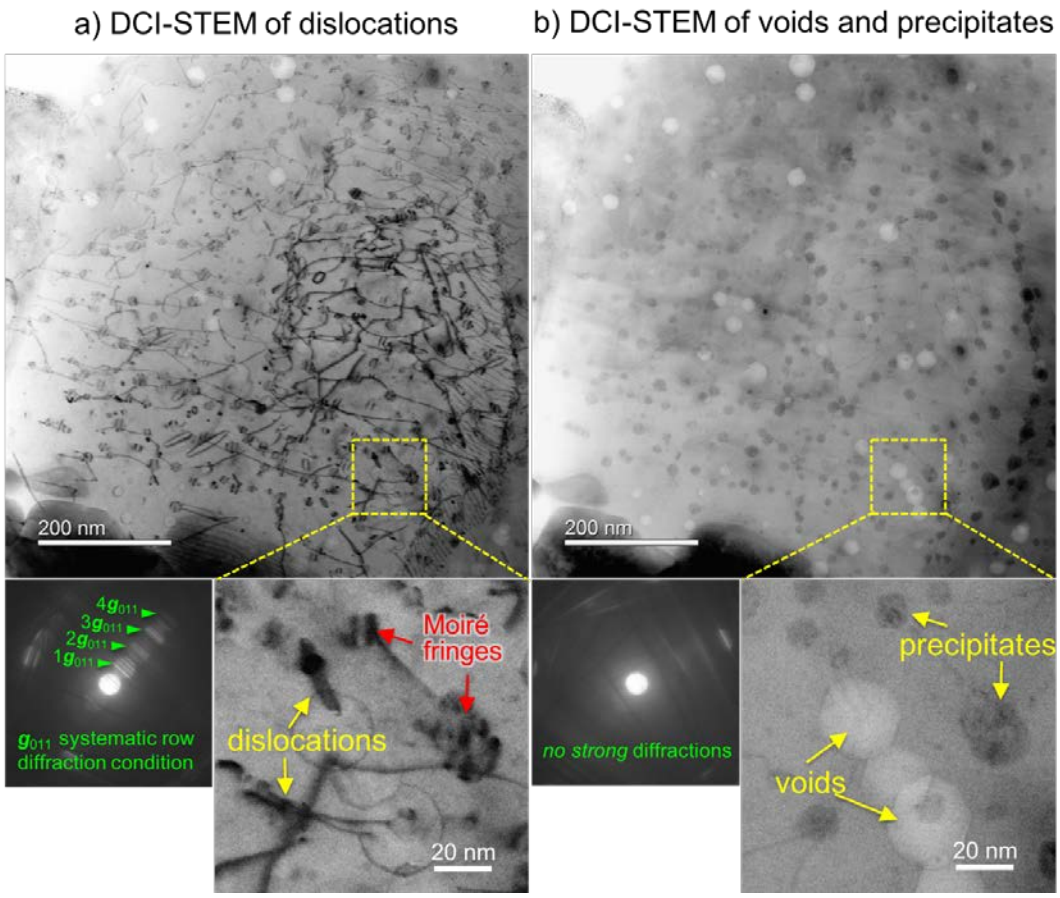

Figure 1. An example of the bend-contour-free DCI-STEM image pair from the same field of view showing a) dislocations and b) voids and precipitates in an HT-9 alloy irradiated with neutrons at 412ºC to 111.8 dpa.

Image pre-processing and labeling

Prior to utilizing the DCI STEM images for deep learning training, the raw micrographs were pre-processed to achieve normalized intensity and pixel alignment. This image pre-processing includes three steps. Firstly, background subtraction and full variance normalization were applied to raw images, effectively enhancing feature contrast even in regions where the diffraction condition is not optimal. For example, in Figure 1a, the relatively weak diffraction contrast of dislocations in the upper left region of the grain is greatly accentuated, as shown in the input dislocation image in Figure 2a. Secondly, an image alignment script developed by Pacific Northwest National Laboratory (PNNL) was used to align the DCI STEM dislocation image with the voids-and-precipitate image pixel by pixel. In this way, for a given image pixel it is spatially equivalent in both images. This was found to be very helpful later in image labeling to facilitate cross referencing when abnormal contrast emerges when different defect classes overlap. Lastly, the enhanced and aligned image pair were plotted into three images, one for each defect class. All have white feature and black background (Figure 2a). The ground truth labelling of the pre-processed micrographs was created by manual annotation. For voids and precipitates, after identifying the feature outline the inner region was filled evenly. Lines with a width of 3 pixels were used to segment the dislocations. As shown in Figure 2b, all labeled features were assigned an intensity of 255, and background intensity is 0. Great care was taken throughout the labelling process to achieve, to a large extent, pixel-level precision.

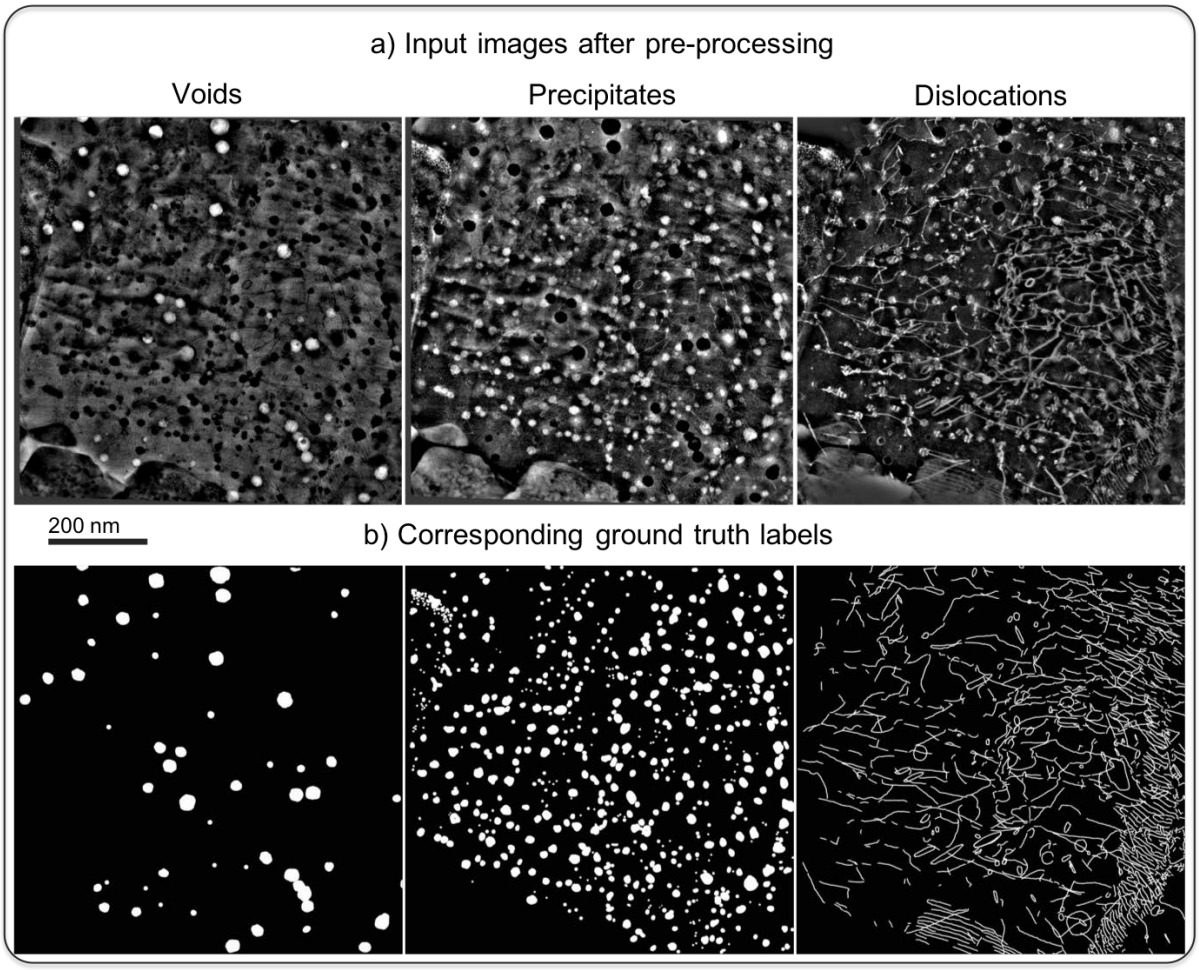

Figure 2. An example overview of pre-processed input images and ground truth labels of the three crystallographic defect classes. All images are 2048 pixel × 2048 pixel.

Image augmentation

To alleviate overfitting[3], a data augmentation strategy was applied to input images and corresponding labels. As demonstrated in Figure 3a, one 2048 pixel × 2048 pixel image was divided into five regions, including three training sets of 1024 pixel × 1024 pixel, and one development set and one test set both of which are 1024 pixel × 512 pixel. Then, each training set was augmented by rotation (i.e. 90°, 180°, and 270° clockwise) and by horizontal flipping each rotated image. This creates eight times more training data sets (both images and labels) that are not identical but maintain the defect features present in the images. The development sets and testing sets were not augmented.

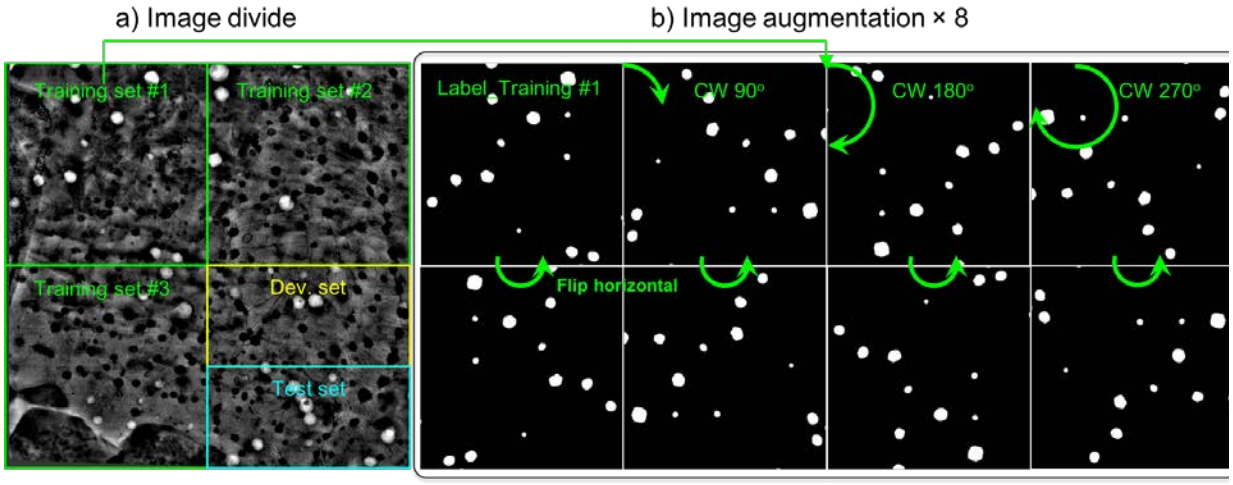

Figure 3. The division and augmentation of one input pre-processed DCI STEM image (2048 pixel × 2048 pixel). For a clear illustration, the label of training set #1 (1024 pixel × 1024 pixel) was employed to show data augmentation.

Deep Learning (CNN) architectures

In this study, we explored a variety of CNN architectures for pixel-wise sematic segmentation of the three defect classes. Starting with a simple encoder CNN with five hidden layers (not showing in this work due to inadequate performance), we mainly focused on model training using three deep learning architectures, including a convolutional/deconvolutional visual geometry group (VGG)19 network, a U-Net model with contracting/expanding paths, a linkage-enhanced VGG and its variations designed in this work. All the deep learning networks were trained with a batch size of 16 patches of 512 pixel × 512 pixel. To further prevent overfitting, beside image augmentation we adopted a combination of batch normalization before each activation, L2 regularization, Dropout and weight decay regularization. A learning rate ranging between 0.00001 and 0.01 was tuned as a hyperparameter. For each experiment, the training was conducted for 100 epochs, with every ten epoch's steps a check was made to see if the learning rate had improved. If after the sixth time the learning rate decayed without improvement, the training stops. An Adam optimizer was used optimizing a weighted cross entropy loss function. For each architecture and each target feature, the network was trained over a collection of random configurations of hyperparameters and then evaluated for performance. All network trainings were carried out at PNNL Institutional Computing Cluster on NVIDIA P100 graphics processing units (GPUs). Training results and comparison will be reported in the next semiannual report.

Acknowledgements

This research is jointly funded by the U.S. Department of Energy Office of Nuclear Energy's Nuclear Energy Enabling Technologies program project CFA 16-10570, and the Office of Fusion Energy Sciences under contract DE-AC05-76RL01830.

References

[1] Zhu, Y., Ophus, C., Toloczko, M. B. & Edwards, D. J. Towards bend-contour-free dislocation imaging via diffraction contrast STEM. *Ultramicroscopy* **193**, 12-23, (2018).

[2] Bassett, G. A., Menter, J. W. & Pashley, D. W. MOIRE PATTERNS ON ELECTRON MICROGRAPHS, AND THEIR APPLICATION TO THE STUDY OF DISLOCATIONS IN METALS. *Proceedings of the Royal Society of London Series a-Mathematical and Physical Sciences* **246**, 345-&, doi:10.1098/rspa.1958.0144 (1958).

[3] Simard, P. Y., Steinkraus, D. & Platt, J. C. in *Seventh International Conference on Document Analysis and Recognition, 2003. Proceedings.* 958-963.

8. MODELING PROCESSES IN FUSION SYSTEM MATERIALS

8.1 REVERSE MACHINE LEARNING FOR IMPROVING CLASSICAL INTERATOMIC POTENTIALS—W. Setyawan and R. J. Kurtz (Pacific Northwest National Laboratory)

OBJECTIVE

Fitting a classical interatomic potential often involves a large number of trial sets, from which the "best" set is selected. The objective of this research is to develop a computational framework to explore the feasibility of using machine learning to improve the current "best" set by utilizing the available trial sets.

SUMMARY

The first version of the framework (named *rfitml*) has been developed. *rfitml* consists of a unix daemon (named *rfitmld*) and a set of unix, batch, and python scripts. The scripts run *potfit*, Large-scale Atomic/Molecular Massively Parallel Simulator (LAMMPS), and machine learning (ML) codes, while *rfitmld* manages the overall framework. *potfit* is used to convert potential parameters in a trial set to a LAMMPS-formatted potential file. The LAMMPS is used to calculate the properties of a trial set via molecular dynamics (MD) simulations. Currently, Keras with TensorFlow backend is used to build, train, and evaluate a neural network ML model. The *rftml* was tested using training data from previously generated trial sets of Re embedded-atom method (EAM) potential. The training data were found to be unsuitable for this purpose because the knots position of functions used in the EAM parametrization vary among trial sets, resulting in non-monotonic knots in the predicted set of parameters obtained by evaluating the trained ML model. Force-matching fits are currently being performed to generate new training data.

PROGRESS AND STATUS

In previous reports, we developed an EAM potential for point defect studies in tungsten-rhenium (W-Re) systems. The potential was recently published in Ref [1]. The potential reproduces Re defect formation energies in W, binding energies of Re to self-interstitial clusters in W, and the convex-hull of formation energies of structures in ♦ and ♍ Re-W phases reasonably well. The potential also predicts a Re melting temperature (3130 K) much closer to the experimental value (3459 K) than a previously published Re potential [2] (4836 K). Nevertheless, the predicted elastic constants of hcp Re need improving [1]. Note that the potential was not directly fit to target properties, but rather through a force-matching method. The force-matching method is selected over a conventional property-fit method because the former uses only first-principles forces, energies, and stresses, making it suitable for automated/high-throughput approaches of potential development. In addition, disordered and liquid structures are readily incorporated in a force-matching method to fit the potential far beyond the ground state configuration. Consequently, force-matched potentials typically exhibit better transferability than property-fit potentials.

A large number of trial sets (1000 sets of Re potential and 500 sets of Re-W potential) was generated during the potential development. In this report, we explore the idea of using ML on the existing trial sets to improve the "best" potential among these trial sets. The ML is typically used to model parameter-property relationships. We employ a reverse ML to obtain a property-parameter relationship, i.e. the properties of the trial sets are used as inputs while the potential parameters of the trial sets are used as outputs. Once a ML model has been trained using the trial sets, it is used to predict a "target" set of parameters given a set of target properties. The "worst" set in the trial sets is subsequently replaced by the "target" set, and the process is repeated until a new "best" set is obtained or until the needed improvement is achieved. In this research, a computational framework is developed to automate the iteration process.

The *rfitml* consists of an *rfitmld* and a set of unix, batch, and python scripts. The scripts are responsible for running *potfit*, LAMMPS, and ML codes, while *rfitmld* manages the overall framework. The force-matching fit of the potentials was previously performed using the *potfit* code. In this framework, it is employed to convert potential parameters in a trial set to a LAMMPS-formatted potential file. The LAMMPS is used to calculate the properties of a trial set via MD simulations. Currently, TensorFlow is used as the ML code.

The first version of *rfitmld* has been completed. It is designed to manage the framework by monitoring the presence of certain files called state files. The main state files are *state_run_ml*, *state_run_potfit,* and *state_run_lmp.* These state files signal *rfitmld* to invoke unix scripts *run_ml.sh*, *run_potfit.sh*, and *run_lmp.sh*, respectively. In turn, these scripts submit the batch scripts *qml*, *qpotfit*, and *qlmp* to perform ML, *potfit*, and LAMMPS tasks, respectively. The cycle of the framework is *state_run_ml* → *state_run_potfit* → *state_run_lmp* and loops back. Once *rfitmld* is launched, a user typically creates *state_run_ml* file to start performing a ML task. However, a user can choose to start whichever task by creating the appropriate state file. Subsequently, *rfitmld* proceeds to the next task by creating the appropriate state file automatically. An iteration counter is incremented every time *run_ml.sh* is invoked.

Once *rfitmld* is launched, a user can manually interrupt, cancel, or resume iterations by creating corresponding state files without exiting the daemon. A user can also exit the daemon by creating a *state_stop* file. A user specifies a walltime, number of iterations, convergence criterion, and how the error is calculated, i.e. as a mean-absolute-error (mae) or as a root-mean-squared-error (rmse), in an input file named *rfitml.in*. A walltime is the maximum runtime allowed for *rfitmld*. Specifying a walltime prevents the daemon from running indefinitely. For convenience, *rfitml.in* is re-read at every iteration, allowing the user to adjust those variables during runtime.

A python script named *ml.py* has been developed to perform the ML tasks. It uses Keras with the TensorFlow backend to build, train, and evaluate a neural network ML model. Note that *rfitmld* and *ml.py* do not depend on the type (e.g. EAM or other potential types), the parameters, and the properties of the potential. On the other hand, the scripts associated with *potfit* and LAMMPS need to be modified by the users based on their needs. For convenience, the framework comes with an example directory containing all the necessary files and scripts.

The trial sets of the Re potential are used as training data to test *rfitml*. The list of 19 properties with their target values and weights is presented in Table 1. A user specifies target properties and weights in *prop.target* file. The weights are used to calculate the error of a set with respect to the target properties as follows

$$f[i] = prop[i]/target\_prop[i] - 1$$

$$mae = \frac{\sum_i w[i]*abs(f[i])}{\sum_i w[i]}$$

$$rmse = \sqrt{\frac{\sum_i w[i]*f[i]*f[i]}{\sum_i w[i]}}$$

where *w[i]* is the weight of property *i*. The 19 properties are used as input nodes in the neural network, forming an input layer. Three neural network layers are constructed with each layer consisting of 64 nodes with an *relu* activation function employed in each node. All potential parameters, except the cutoff distance, for a total of 42 parameters, are used as output nodes forming an output layer. The ML model is successfully trained, and subsequently used to predict parameters based on the target properties. It was found that because the knot positions of the cubic polynomials used in the pair interaction and the electron density function vary among the training data, the predicted parameters contain non-monotonic knots. Therefore, new training data are needed.

Table 1. List of properties for the Re EAM potential. The weights are used to calculate the error of a trial set with respect to the target values. Data labelled with (Exp.) are from experiments, while the rest are *ab initio* data from our calculations. E_c is cohesive energy, E_f is point defect formation energy. Interstitial positions C to BC are depicted in [1]. Units are Å, eV, and GPa.

Property	Target	Weight	Property	Target	Weight
a	2.761 (Exp.)	1	E_f {vac}	3.08	1
c/a	1.614 (Exp.)	1	E_f {C}	6.52	1
E_c	8.03 (Exp.)	10	E_f {O}	8.13	1
ΔE_c {hcp-fcc}	0.06	10	E_f {S}	6.53	1
ΔE_c {hcp-bcc}	0.31	10	E_f {T}	6.52	1
C_{11}	613 (Exp.)	1	E_f {BO}	7.41	1
C_{33}	683 (Exp.)	1	E_f {BS}	8.09	1
C_{12}	270 (Exp.)	1	E_f {BT}	Relaxed to BO	1
C_{13}	206 (Exp.)	1	E_f {BC}	Relaxed to BO	1
C_{44}	163 (Exp.)	1			

Efforts are then shifted to performing the force-matching fit again. The “best” set from previous results is taken as a starting point with the pair interaction and embedding function are set close to zero by scaling their strength by a factor of 100 to minimize a bias towards converging to the same local minimum. The knot positions are fixed. In this fit, we also experiment with using only the liquid structures to fit the potential. Six liquid structures under various strain tensors are used. Each structure contains 64 atoms, therefore a total of 6*64*3 forces, 6 energies, and 6*6 stresses is used to fit the potential. A weight ratio between force:energy:stress of 1:10:10 is used. In a force-matching fit, simulated annealing is employed to explore the parametric space. For each parameter, a new value is randomly sampled from within the allowed range. In *potfit*, we found that even though random sampling is used, the parameters are iterated sequentially, i.e. a random sampling is performed for parameter 1, followed by parameter 2, and so on. This procedure introduces a bias which favors parameters located earlier in the parameter array. To eliminate this, we modified *potfit* so that the parameters are also selected randomly.

For each trial set, the properties are evaluated and the error is calculated using the property weight previously presented in Table 1. This error is referred to as property error to distinguish it from the force-matching (FM) fit error. Figure 1 shows a plot of property rmse versus FM rmse from 635 sets completed so far. The FM rmse consists of errors from forces, energies, and stresses with their weights given in the previous paragraph. No correlations are observed. However, the set with the smallest FM error has a property error that is close to the minimum value of property error. This indicates that it is possible to get a good potential set with the force-matching method using only liquid structures. More trial sets are being generated and *rfitml* will be tested with these training data.

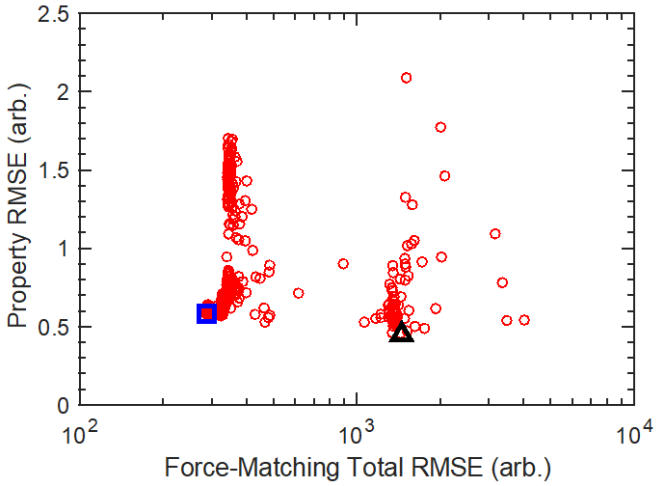

Figure 1. Scatter plot of root-mean-squared-error (rmse) of properties of trial sets with respect to target properties as a function of rmse of force-matching (FM) fit. The plot is gathered from 635 trial sets. The data point marked with a rectangle denotes the set with the minimum FM rmse, while the one marked with a triangle denotes the set with the minimum property rmse.

Acknowledgement

This research has been supported by the U.S. Department of Energy, Office of Science, Office of Fusion Energy Sciences (DE-AC05-76RL0-1830).

References

[1] W. Setyawan, N. Gao, R. J. Kurtz, *Journal of Applied Physics* 123 (2018) 205102.
[2] G. Bonny, et al., *Journal of Applied Physics* 121 (2017) 165107.

8.2 STRUCTURES AND TRANSITIONS IN BCC TUNGSTEN GRAIN BOUNDARIES AND THEIR ROLE IN THE ABSORPTION OF POINT DEFECTS—Timofey Frolov, T. Oppelstrup, R. E. Rudd (Lawrence Livermore National Laboratory), Q. Zhu (University of Nevada Las Vegas), J. Marian (University of California Los Angeles)

OBJECTIVE

The objective of this study is to apply a new computational methodology to predict structure and energies of many tungsten grain boundaries, to inform the search for the high-temperature grain boundary phases. Grain boundary properties are needed for thermomechanical model of recrystallization of tungsten for magnetic fusion applications being developed by the Marian Group at University of California Los Angeles (UCLA).

SUMMARY

We have continued to apply evolutionary search techniques to discover *in silico* new grain boundary structures in tungsten relevant to plasma facing components in tokamaks [1]. This investigation extends our initial work which employed grain boundary searches based on classical interatomic potentials and then verified the results with first principles calculations [2]. This work was motivated by an earlier study of grain boundary (GB) phases in copper. The new tungsten study is a systematic investigation of [100] and [110] symmetric tilt high-angle and low-angle boundaries. The key to the technical approach is to avoid the use of the gamma-surface technique which is overly restrictive and instead to apply evolutionary search techniques [3]. We have used a recently developed computational tool based on the Universal Structure Predictor: Evolutionary Xtallography (USPEX) structure prediction code to perform an evolutionary grand canonical search of GB structure at 0K. For [110] tilt boundaries, the search predicts novel high-density low-energy grain boundary structures and multiple grain boundary phases across the entire misorientation range. We have used molecular dynamics simulations to show that the new structures are more stable at high temperature. We have investigated point defect absorption in GBs, showing the effect of structural multiplicity on the process. The absorption occurs through a two-step nucleation process. Initially point defects are absorbed through a formation of a metastable GB structure increasing the atomic density. Later this structure transforms into a GB interstitial loop or a different GB phase. This work was performed under the auspices of the U.S. Department of Energy by Lawrence Livermore National Laboratory under Contract No. DE-AC52-07NA27344.

References

[1] T. Frolov, Q. Zhu, T. Oppelstrup, J. Marian, and R. E. Rudd, “Structures and transitions in bcc tungsten grain boundaries and their role in the absorption of point defects,” to appear Acta Mater (2018) arXiv:1804.05140.
[2] T. Frolov et al., “Grain boundary phases in bcc metals,” Nanoscale 10, 8253 (2018).
[3] Q. Zhu et al., “Predicting phase behavior of grain boundaries with evolutionary search and machine learning,” Nature Comm. 9, 467 (2018).

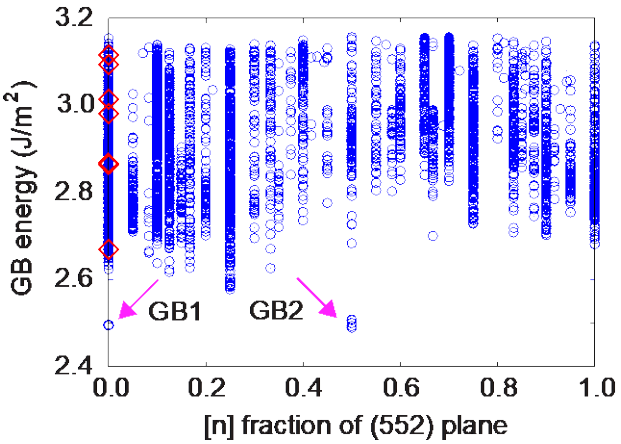

Figure: An evolutionary algorithm was used to generate a large collection of grain boundaries, allowing for point defect diffusion such as due to radiation damage. The scatter plot shows the grain boundary energies vs. excess atomic density. New low-energy grain boundary structures were found, as indicated by the arrows. Red diamonds indicate standard structures. [2]

8.3 OKMC SIMULATION STUDY COMPARING ROOM TEMPERATURE IRRADIATION OF TUNGSTEN WITH AND WITHOUT INTRAGRANULAR TRAPS—G. Nandipati, W. Setyawan, K. J. Roche, R. J. Kurtz (Pacific Northwest National Laboratory) and B. D. Wirth (University of Tennessee)

OBJECTIVE

The objective of this work is to understand differences in damage accumulation with and without the presence of intragranular traps in pure tungsten (W) at room temperature due to neutron irradiation with a primary knock-on atom (PKA) spectrum corresponding to a 14 MeV-Neutron source using the object kinetic Monte Carlo (OKMC) method.

SUMMARY

Using *KSOME* [1,2], OKMC simulations of room temperature (300 K) irradiation damage in polycrystalline W with a grain size of 2.0 μm with and without intragranular traps were carried out. Preliminary simulation results are presented for damage accumulation in W when subjected to neutron bombardment with a 14 MeV-neutron PKA spectrum for dose rates of $2.3 \times (10^{-4} - 10^{-8})$ displacements per atom (dpa/s), and with intragranular trap concentrations of 0, 100 and 150 appm. The overall damage accumulation behavior with and without traps is similar. However, the damage accumulation is significantly larger, while the average void size is considerably smaller, in the presence of intragranular traps.

PROGRESS AND STATUS

Simulation Details

Simulations were performed using a non-cubic box with dimensions 95.10 x 96.37 x 97.00 nm^3 ($300a_0$ x $304a_0$ x $306a_0$, where a_0 is the lattice constant of tungsten), with each axis parallel to an $a_0\langle 100\rangle$ type direction. Each defect can hop to one of eight possible body-centered cubic nearest neighbor lattice sites at a distance of $a_0/2\langle 111\rangle$. Finite periodic boundary conditions were adopted in all three directions i.e. periodic boundary conditions are applied, but whenever a mobile object moves a distance larger than the average grain size, it is removed from the simulation, and it is no longer tracked. In the present simulations, an average grain size was taken to be 2.0 μm and assumed to be dislocation free. Simulations were performed with intragranular trap concentrations of 0 (corresponds to a pure tungsten), 100 and 150 appm, in order to understand the effect of trap concentration on damage accumulation. Trap concentrations of 100 and 150 appm correspond to volumetric concentrations of 6.3×10^{24} and 9.45×10^{24} $/m^{-3}$, respectively. The term 'trap' in this work always means 'intragranular trap'.

The values of the binding energies of defects used in the present annealing simulations were taken from *ab initio* calculations of Becquart *et al*. [3] while the migration barriers were taken from molecular dynamics (MD) simulations [4] using an embedded-atom method (EAM) potential for W [5]. In the present simulations, SIA clusters larger than size five were constrained to diffuse in 1D along one of four ⟨111⟩ directions. The SIA clusters up to size five can change their direction of 1D motion via rotation and thereby perform a mixed 1D/3D migration. The activation barrier for changing direction from one ⟨111⟩ direction to another is 0.38 eV [6]. The direction of 1D motion was assigned randomly to the SIAs at the start of a simulation, and interstitial clusters of all sizes are assumed to be glissile. Their migration/diffusion rates decrease with increasing cluster size (n) according to $\nu_o n^{-1}$ ($\nu_o = 6 \times 10^{12}$ s^{-1}) while the migration barrier is taken to be independent of cluster size. For a single vacancy, the activation barrier for diffusion is taken as 1.30 eV [7], and vacancy clusters larger than five are assumed to be immobile. However, at room temperature vacancy clusters of all sizes are immobile, but can emit mono-vacancies. The vacancy (SIA) dissociation rate is given by $\Gamma_d = \nu_d \exp((E_m + E_d)/k_B T)$, where E_d is the binding energy of a vacancy (SIA) to a vacancy (SIA) cluster, and E_m is the migration energy of a single vacancy (SIA). We have assumed that defect clusters of all sizes and types are spherical objects, and their capture radii are obtained from Ref. [3].

An extensive database of cascades with PKA energies ranging from 10 keV to 200 keV, generated at 300 K using molecular dynamics simulations [7, 8] was used to carry out the present simulations. Individual cascades were randomly selected from the cascade database based on the PKA spectrum being considered and were inserted into the simulation box at random positions based on the cascade production rate. The production rate of cascades, which is the number of cascades produced in the simulation cell per second, dose rates and the accumulated dpa are calculated based on the NRT displacements per cascade (ν_{NRT}) [9]. Also note that unless explicitly specified, the term 'PKA energy' represents the damage energy (E_{MD}) and not the recoil energy (E_{PKA}) of a PKA.

In the present simulations, all intragranular traps are distributed randomly within the simulation box, assumed to be stable under irradiation, and immobile with a capture radius of 6.32 Å (i.e. two lattice constants) (arbitrary). Furthermore, intragranular traps are considered to be unsaturable for both vacancies and interstitials. In addition, trap-vacancy and trap-SIA complexes, are distinguished from each other as different types of defects. Trap-vacancy(SIA) complexes may grow or shrink by capturing vacancies (SIAs) or SIAs (vacancies), respectively. Accordingly, there are five different defect types, namely vacancies, SIAs, traps, trap-vacancy complexes and trap-SIA complexes.

Results

Figure 1 shows the densities of individual vacancies and vacancy clusters, and the average vacancy cluster size (diameter) without intragranular traps as a function of dose for various dose rates for 14 MeV neutron irradiation. While Figures 2 (a, c, e), and Figures 2 (b, d, f) show the same information for trap concentrations of 100 and 150 appm, respectively. However, as mentioned earlier, trapped vacancies (trap-vacancy complex) and un-trapped vacancies are considered to be different defect types. Therefore, it should be noted that in Figure 2, the density of vacancies and vacancy clusters corresponds to the total (or the sum of) of the vacancy and vacancy cluster densities. Also, for simplicity, only the order of magnitude of the dose rate is shown in the figure legend.

The general behavior of damage accumulation, with and without the traps, as a function of dose is similar. Regardless of trap concentration, it is apparent from Figures 1 and 2 that the dose rate does not affect vacancy density. While both the dose rate and dose seem to have no effect on the average vacancy cluster size. In tungsten, SIA clusters are the only diffusing defect species at 300 K. During irradiation, SIAs either recombine with vacancies or are captured by grain boundaries or traps. Therefore, as expected, no effect of dose rate on the damage accumulation was found, regardless of trap concentration. This is the general behavior of the damage accumulation when vacancies are immobile. Nevertheless, the vacancy and vacancy cluster densities are significantly higher (more than an order-of-magnitude) when traps are present. Correspondingly, in the presence of traps, the average vacancy cluster size is considerably smaller (see Figures 1(c) and 2(e, f)). Furthermore, without traps, vacancy and vacancy cluster densities start to approach saturation at smaller doses (< 0.02 dpa). On the contrary, with traps, they did not seem approach the beginning of saturation at the dose of 0.1 dpa. In short, the data in Figures 1 and 2 indicate that at room temperature damage accumulation in tungsten in the presence of intragranular traps is much higher than without them. On the other hand, the density of vacancies and vacancy clusters seems to decrease when the trap concentration increased from 100 to 150 appm, but the average vacancy cluster size remains unchanged (see Figures 2 (a, b, c, d))

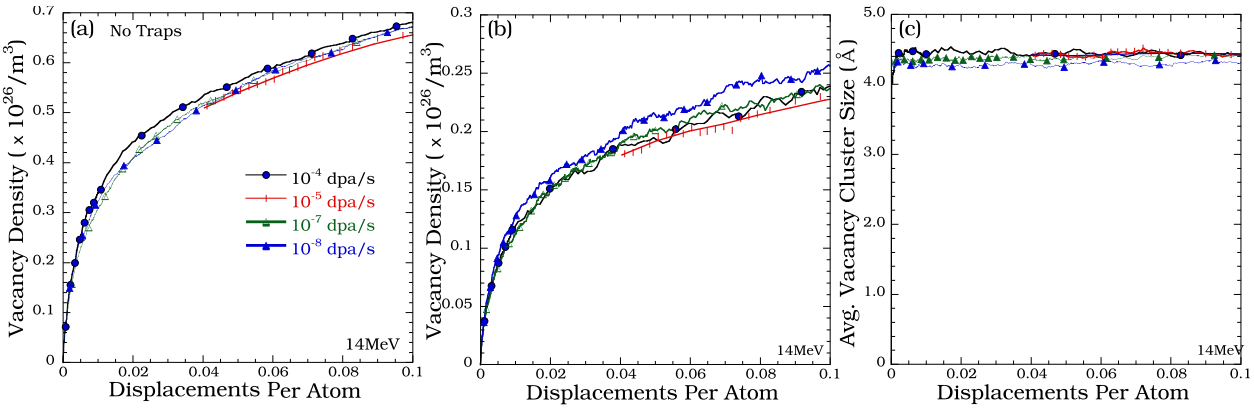

Figure 1. Comparison of (a) vacancy density, (b) vacancy cluster density and (c) average vacancy cluster radius as a function of dose at various dose rates for a 14 MeV-Neutron PKA spectrum.

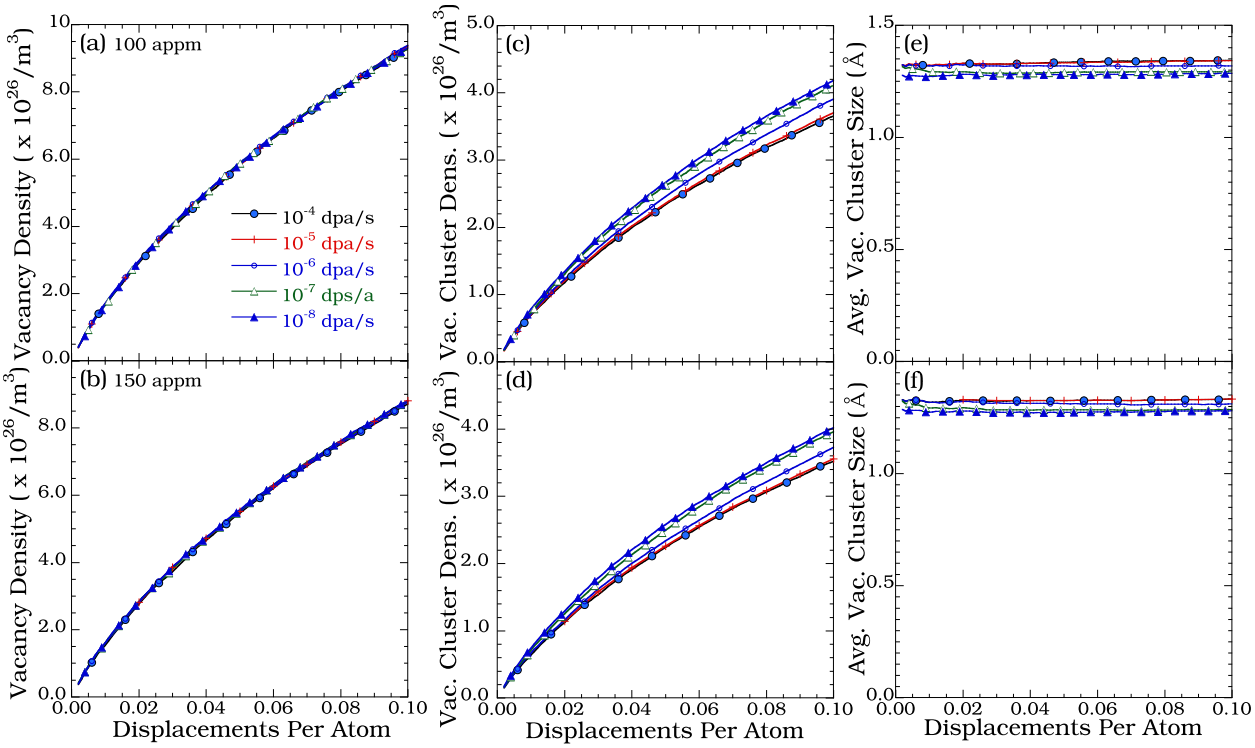

Figure 2. Comparison of (a, b) vacancy density, (c, d) vacancy cluster density and (e, f) average vacancy cluster size for 100 and 150 appm of traps, respectively, as a function of dose at various dose rates for the 14 MeV-neutron PKA spectrum.

As mentioned earlier, SIA clusters are the only diffusing species at 300 K. However, differences in damage accumulation in the cases considered here are due to where the SIA clusters are trapped/or absorbed. Without the traps, SIAs are absorbed at grain boundaries, whereas they are trapped intragranularly when traps are present. This results in a significant difference in the average diffusion length of SIA clusters at low doses and how it varies during irradiation (or with increasing dose). Without the traps, the average diffusion length of SIA clusters during the initial stages of irradiation (at very low doses) is determined by the grain size. As a result, during the initial stages, a large fraction of SIA clusters reaches grain boundaries resulting in the vacancy accumulation. However, as the vacancy density increases the frequency of SIA clusters encountering immobile vacancy clusters also increases. Accordingly, with increasing dose, the

average diffusion length of SIA clusters is increasingly determined by the average spacing between the vacancy-rich regions of cascade cores (inter-cascade-core spacing). In contrast, in the presence of traps, the average diffusion length of SIA clusters is determined by the average inter-trap distance, which is considerably shorter than the inter-cascade-core spacing. As a result, at low doses, SIA clusters are more likely to be captured by traps than encountering vacancy clusters, resulting vacancy-type defect accumulation. In both cases of with and without the traps, the accumulation of vacancy-type defects is evident in Figures 1(a, b) and 2(a, b, c, d). Regardless of the trap concentration, as the dose increase, the frequency of SIA-Vacancy cluster encounters is expected to increase. However, the key difference in the defect accumulation with and without the traps would be at what dose does the frequency of SIA - vacancy cluster collisions result in a significant reduction in the vacancy accumulation rate and eventually to saturation of the vacancy density. In the absence of traps, because the average diffusion length corresponds to the average inter-cascade-core spacing, the frequency of SIA - vacancy cluster collisions begins to increase at very low doses. In contrast, in the presence of traps, vacancy-type defect accumulation dominates until the average inter-cascade-core spacing is smaller than the average inter-trap spacing. In other words, the transition of the average diffusion length of SIA clusters from being inter-trap spacing to inter-cascade-core spacing dependent occurs at a much higher dose. Accordingly, in the absence of traps, the density of vacancies and vacancy clusters are significantly lower, and their concentrations appear to approach saturation at a lower dose.

Using the above reasoning, one would predict that the accumulation of vacancy-type defects should increase with increasing trap concentration. However, it is evident from Figures 2 (a, b, c, d) that the density of vacancies and vacancy clusters decreases when the trap concentration increases from 100 to 150 appm, suggesting an increase in recombination caused by activation of a different mechanism. With increasing trap concentration, the density of trapped SIA clusters increases with a corresponding decrease of their average size and, more importantly, SIA clusters would be more densely distributed in space. Therefore, we hypothesize that the increase in the recombination is because of the increased probability of formation of vacancy-rich cascade cores in the proximity of trapped SIA clusters (overlap of cascade damage onto a trapped SIA cluster). Additional simulations with trap concentrations above and below the values examined here are to test this hypothesis.

Acknowledgements

These simulations were performed using the CONSTANCE cluster at Pacific Northwest National Laboratory (PNNL).

References

[1] G. Nandipati *et al* Semiannual Progress Report DOE/ER-0313/54, June 2013, 179-183.
[2] G. Nandipati, *et al* J. Nucl. Mater. (2015) 462 338–334.
[3] C. S. Becquart *et al.* J. Nucl. Mater. 403 (2010) 75.
[4] T. Faney, N. Juslin, B. D. Wirth, (*private communication)*.
[5] N. Juslin, B. D. Wirth, J. Nucl. Mater. 432(2013)61.
[6] D. A. Trentyev, L. Malerba, M. Hou, Phys. Rev. B 75 (2007) 104108.
[7] W. Setyawan, *et al* J. Nucl. Mater. (2015) 462 329–337.
[8] W. Setyawan *et al* Semi-annual Progress Report DOE/ER-0313/58 June2015 272-277.
[9] M. J. Norgett, M. T. Robinson, I. M. Torrens, Nucl. Eng. Des. 33 (1975) 50.
[10] G. Nandipati *et al* Semiannual Progress Report DOE/ER-0313/59, June 2016, 178-182.

8.4 THREE-DIMENSIONAL MODELING OF THE EFFECTS OF HELIUM BUBBLES ON THE STRESS-STRAIN BEHAVIOR OF POLYCRISTALLINE IRON BY A MECHANISTIC FINITE ELEMENT APPROACH INFORMED BY MOLECULAR DYNAMICS DATA—B.N. Nguyen, R.J. Kurtz (Pacific Northwest National Laboratory)

OBJECTIVE

The objective of this study is to investigate the effects of helium (He) bubbles on the stress-strain behavior of polycrystalline iron (α-Fe) by a mechanistic finite element (FE) approach using a continuum damage mechanics (CDM) description of the material behavior informed by molecular dynamics (MD) data. The approach models an α-Fe bicrystal system in which the elastic-plastic crystals finely discretized in three-dimensional (3D) FE are connected one to another by cohesive elements. The He bubbles at the GB are explicitly modeled through an equivalent hollow sphere under internal pressure and located in the middle of the modeling domain. The MD and FE analyses of this bicrystal system subjected to uniaxial tensile loading and internal He pressure at 5 K and room temperature (RT) were performed using the Large-scale Atomic/Molecular Massively Parallel Simulator (LAMMPS) software and ABAQUS FE package, respectively. The modeling results reveal a very significant effect of high-pressure He bubble on the stress-strain response of the bicrystal system.

SUMMARY

First, MD analyses of the single crystal and bicrystal lattice configurations ({332} orientation) were performed to compute the uniaxial responses of the α-Fe single crystal and GB. The MD results were then used in FE analyses of the same systems to identify parameters for the CDM constitutive relations for the crystal and the traction-separation law for the GB depicted by cohesive elements. Next, a 3D FE model of the α-Fe bicrystal system with an imperfect GB subjected to uniaxial tensile loading was developed. This model includes an equivalent hollow sphere under internal pressure in the middle of the GB to model the effects of pressurized He bubbles at 5K and RT on stress, strain and damage distributions. The radius of the equivalent sphere was determined assuming the presence of two vacancies in the system. Finally, MD stress/strain data of the same bicrystal system with He bubbles were compared to the corresponding FE results to validate this approach that appears to be very efficient in terms of computational time.

PROGRESS AND STATUS

Background

Ferritic/martensitic steels are prime candidate materials for structural applications in future fusion reactors [1]. In such applications, these materials are exposed to high-energy neutrons leading to He generation due to transmutation reactions. Formation of He is of concern because it can cause hardening and increases in the ductile-to-brittle transition temperature (DBTT) [2-3] and swelling because of nucleation and growth of He bubbles [4]. The He also weakens GBs by lowering the GB cohesive stress or by promoting nucleation, growth and coalescence of GB cavities, which can lead to intergranular fracture at high temperature [5]. As it is very difficult to experimentally quantify the effects of nano-scale He bubbles on material integrity, computational methods such MD simulations have been very helpful to elucidate the degradation mechanisms associated with He bubble formation. Although there are a significant number of atomistic studies of He in bulk α-Fe e.g., [6-27], work on He at α-Fe GBs is less extensive [28-38]. Our previous report [39] has shown that a promising and efficient approach to model the effects of He on the material integrity is by FE modeling of an α-Fe bicrystal system in which CDM is used to describe the constitutive behavior of α-Fe and cohesive elements are used to model the GB behavior. In [39], MD data for the bicrystal lattice configuration Σ11 <110> {332} specified in [40-41] were used in plane-strain FE analyses to determine the He bubble effects on the response of this system to tensile loading under periodic boundary conditions. During this reporting period, to directly quantify the material stress-strain response

and strength affected by He bubbles at the GB, full 3D MD and FE analyses of a similar system with perfect and imperfect GB subjected to *uniaxial tensile loading* were performed.

Model Development

First, an MD model of the α-Fe single crystal was developed to compute the crystal response to uniaxial tensile loading. The MD results for the single crystal were then used in a FE analysis using a homologue 3D FE model to identify the parameters of the elastic-plastic damage model for the α-Fe crystal. Next, the 3D FE models to study the effects of He bubbles were developed based on the bicrystal system configuration for MD analysis like the one given in [39-40]. Figures 1a and 1b show the FE models developed for analyses of the α-Fe bicrystal systems containing the clean GB (without He bubbles) and the GB involving two vacancies depicted by an equivalent hollow sphere occupied by He at a given pressure. In these models the two crystals were connected one to another by cohesive elements. The dimensions of the modeling domains are 8 nm x 25 nm. In these models, the vertical displacements of the bottom boundaries were fixed while uniform vertical displacement loadings were incrementally applied on the top surfaces. The loading for the model with He bubbles (Figure 1b) also involved the prescribed internal pressure ramping up to a maximum value at the first loading step before application of the vertical displacement at the next loading step. Figure 1b illustrates a vertical section through the model with imperfect GB showing the location of the equivalent hollow sphere that is further illustrated in Figure 1c. The model with the clean GB (Figure 1a) was used to identify the material parameters for the traction-separation law describing the GB. Subsequently, the same set of model parameters for the crystal and GB was used in all the analyses to determine the He bubbles effect on the stress-strain response of the *as-formed* bicrystal system at 5K and RT.

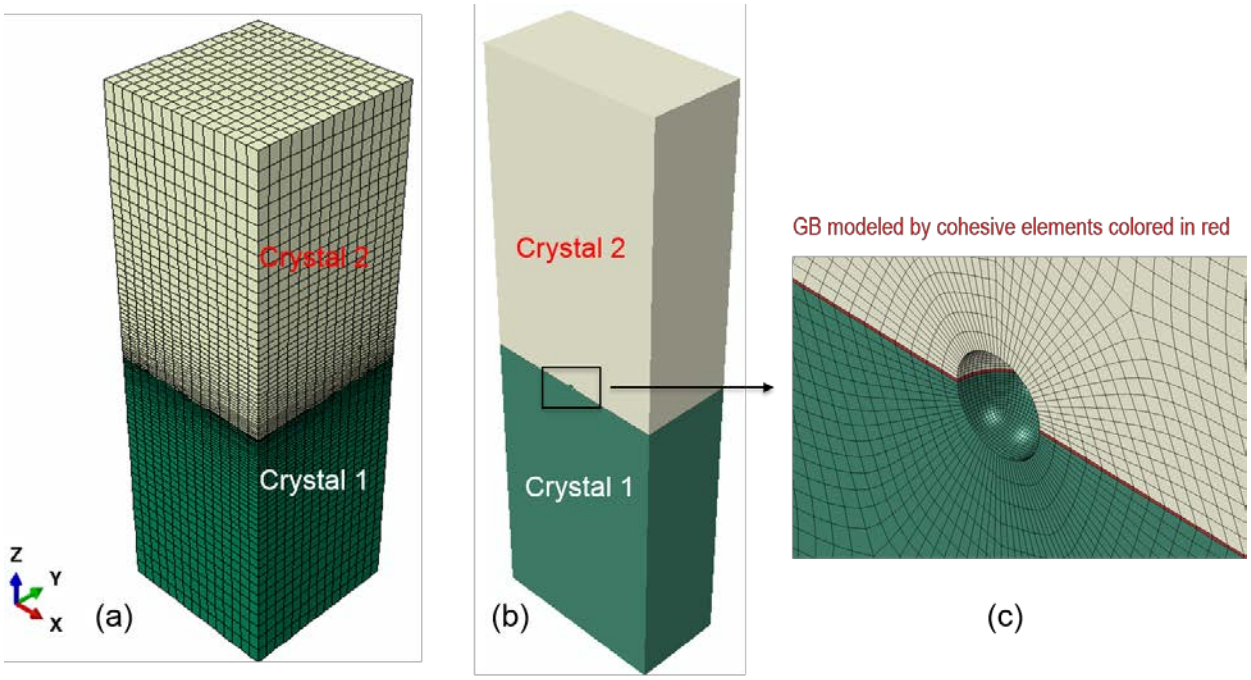

Figure 1. 3D FE models for the α-Fe bicrystal system subjected to uniaxial tensile loading in the vertical direction (z-direction) – (a) model with clean GB, (b) a vertical cross section of the model with two vacancies depicted by an equivalent hollow sphere occupied by He, and (c) a magnified view showing the hollow sphere region.

Results

A series of ABAQUS FE analyses had first been conducted for the single crystal model and the bicrystal model with clean GB to identify the material parameters for the constitutive laws at 5 K and RT, which were subsequently used for the analyses of the bicrystal system with imperfect GB. In this work, the elastic-plastic model with isotropic hardening and isotropic damage available in the ABAQUS material model options was used for the crystals while cohesive elements were used to describe the behavior of the GB. Figures 2a and 2b, respectively report the longitudinal stress-strain (in the z-direction) results at 5 K and RT predicted by continuum damage mechanics modeling (labelled as CDM) compared to the corresponding MD data. Very good correlations between CDM and MD results allowed identification of the material parameters at these temperatures for use in subsequent analyses of the bicrystal model with He bubbles.

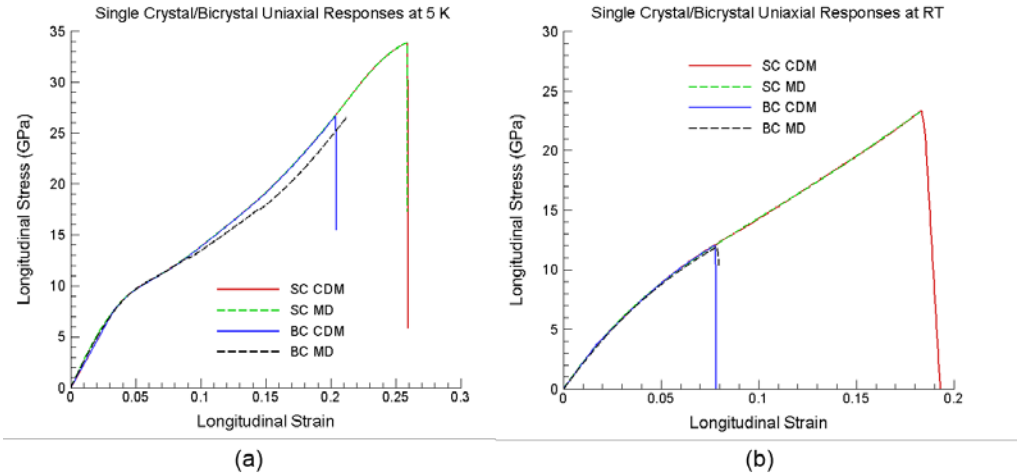

Figure 2. Longitudinal stress-strain responses at 5 K (a) and RT (b) predicted by FE analysis using CDM compared to the corresponding MD data.

Next, MD and CDM FE analyses were conducted at 5 K to study the effects of He bubbles on the stress-strain response of the bicrystal system with imperfect GB. The FE mesh resolution shown in Figure 1c was carefully designed to capture damage and fracture initiated and propagated from the pressurized sphere as expected due to stress concentrations in this area. As mentioned earlier, the He pressure was applied inside the hollow sphere incrementally to a prescribed level during the first loading step. At the next loading step, while maintaining the He pressure at the maximum prescribed level, uniform vertical displacements were applied on the top model boundary incrementally until the system completely failed. Figures 3a and 3b illustrate the contours of damage and fracture in the bicrystal system at total failure for 0 and 25 GPa He pressure, respectively. The 0-pressure case represents the bicrystal with imperfect GB without He. Damage is described by a failure indicator (damage variable) of the CDM model. A FE totally fails if the failure indicator is equal to 1. Figure 3 shows a significant effect of He pressure on the fracture stress (σ_r), damage and fracture pattern in the system.

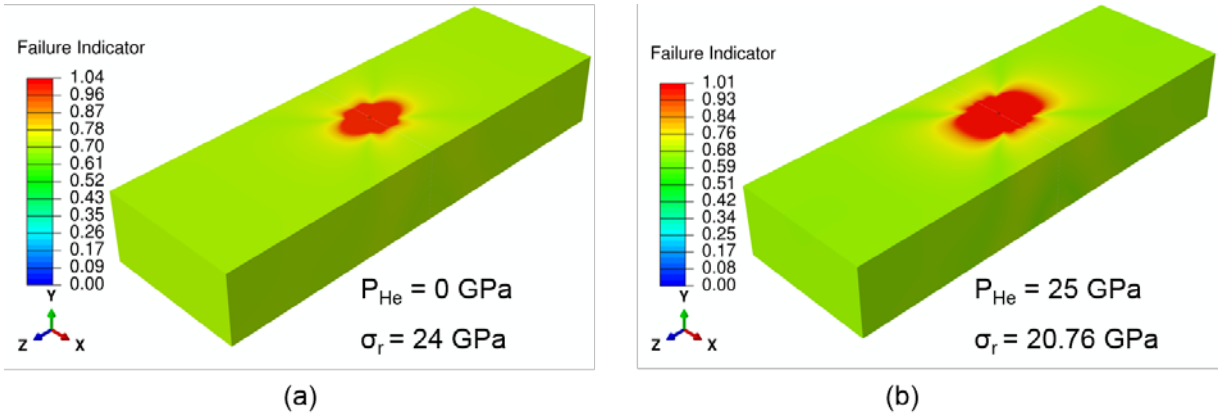

Figure 3. Damage distributions (viewed through a cross section along the z-direction) depicted by the failure indicator (1: failed, 0: undamaged) for (a) 0 and (b) 25 GPa He pressure in the bicrystal system with 2 vacancies.

The most important results from these analyses are the determination of the effects of He bubbles on the fracture stress (strength) and strain of the bicrystal system as shown in Figures 4a and 4b. These figures show the strength and failure strain for increasing levels of He pressure predicted by CDM analyses compared to the corresponding MD results. First, even without He, the presence of vacancies at the GB reduces the material strength and ductility significantly. With increasing He pressure, there is a gradual reduction of both failure strain and strength. For small to moderate He pressures, the effects of He bubbles on the material strength is rather small, but this effect becomes more and more pronounced at higher He pressures. Beyond 40 GPa pressure, both strength and failure strain drop significantly.

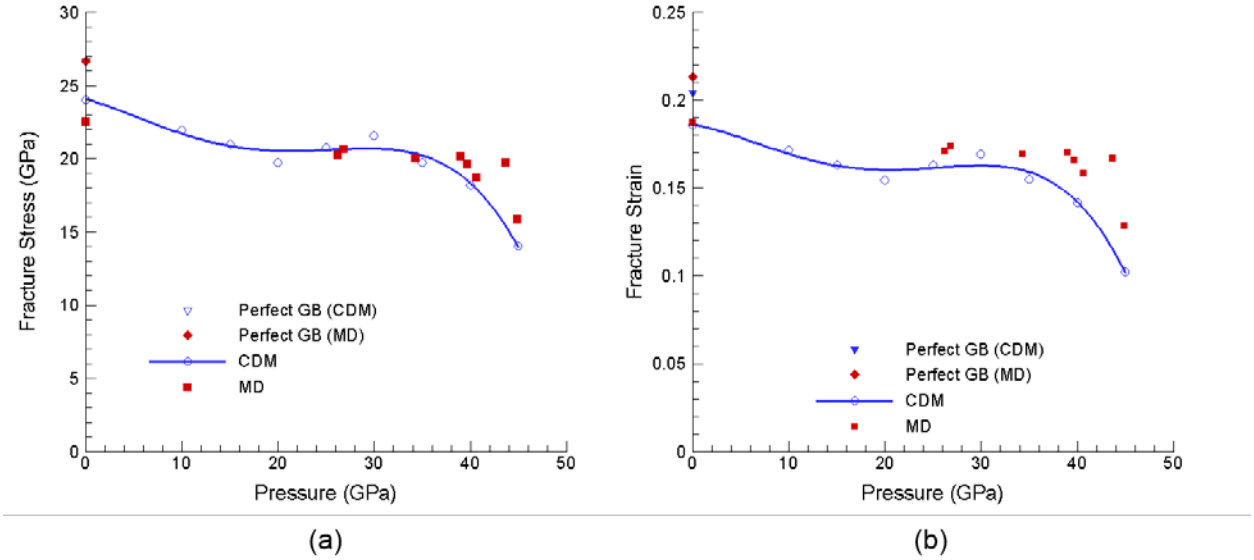

Figure 4. (a) Strength and (b) failure strain as a function of the He bubble pressure for the α-Fe bicrystal system at 5 K predicted by CDM FE and MD analyses.

We also conducted similar MD and CDM analyses for a bicrystal system with two vacancies at RT (300 K). The CDM FE results for strength and failure strain versus He pressure are given in Figures 5a and 5b, respectively. Comparing Figures 5 to 4 reveals similar trends of strength and fracture strain with He

pressure at RT and 5 K. First, the presence of vacancies even without He pressure causes a significant reduction in strength and failure strain. With increasing He pressure, strength and failure strain gradually decrease, but more pronounced reductions were found once the He pressure exceeds ~ 22.5 GPa. The MD results for strength and failure strain at RT as function of the ratio n_{He}/n_V where n_{He} is number of He atoms and n_V the number of vacancies (=2 in this work) are presented in Figures 6a and 6b. At the time of this report, we are working on relating the ratio n_{He}/n_V to the He bubble pressure for direct comparison between CDM and MD results.

Conclusions

During this report period, the mechanistic FE approach informed by MD data was further developed and validated to investigate the effects of He bubbles on the stress-strain behavior of an α-Fe bicrystal system. The analysis results show an important effect of He pressure at high levels that reduces material ductility and strength substantially. Current model predictions show good agreement with MD results at 5 K while only qualitative comparison between CDM and MD results can be made by the time of this report. As observed previously, the developed approach appears to be very efficient in terms of computation time compared to MD simulations. Thus, it can serve as a very good complimentary approach to MD simulations to study He bubbles or other radiation-induced effects on material integrity.

Future Work

There is a need to further assess the material stress-strain response at RT to correlate CDM FE results with the corresponding MD data.

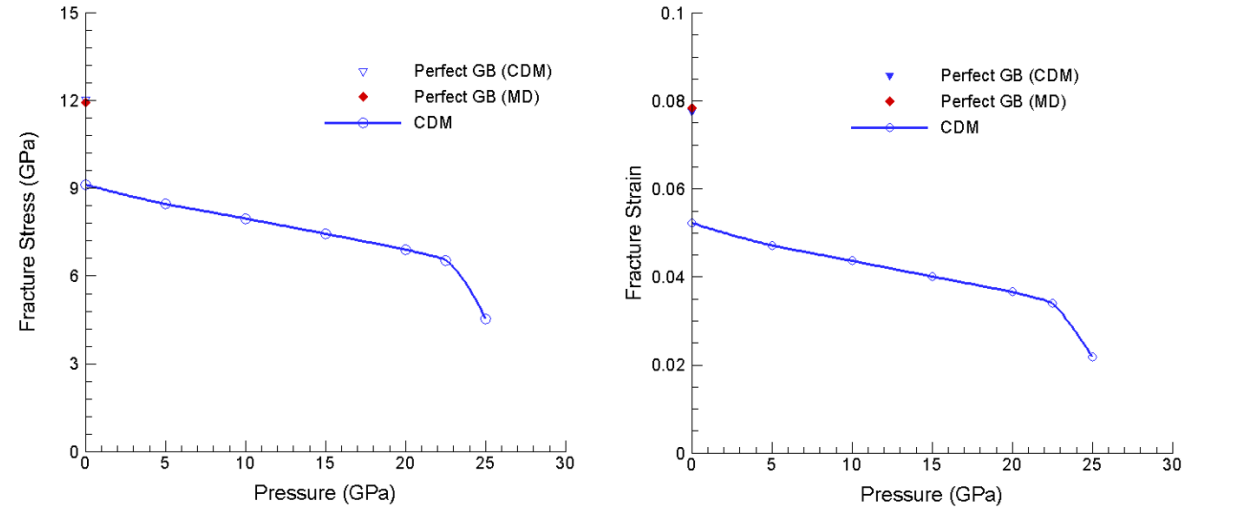

Figure 5. (a) Strength and (b) failure strain as a function of the He bubble pressure for the α-Fe bicrystal system at RT predicted by CDM FE analyses.

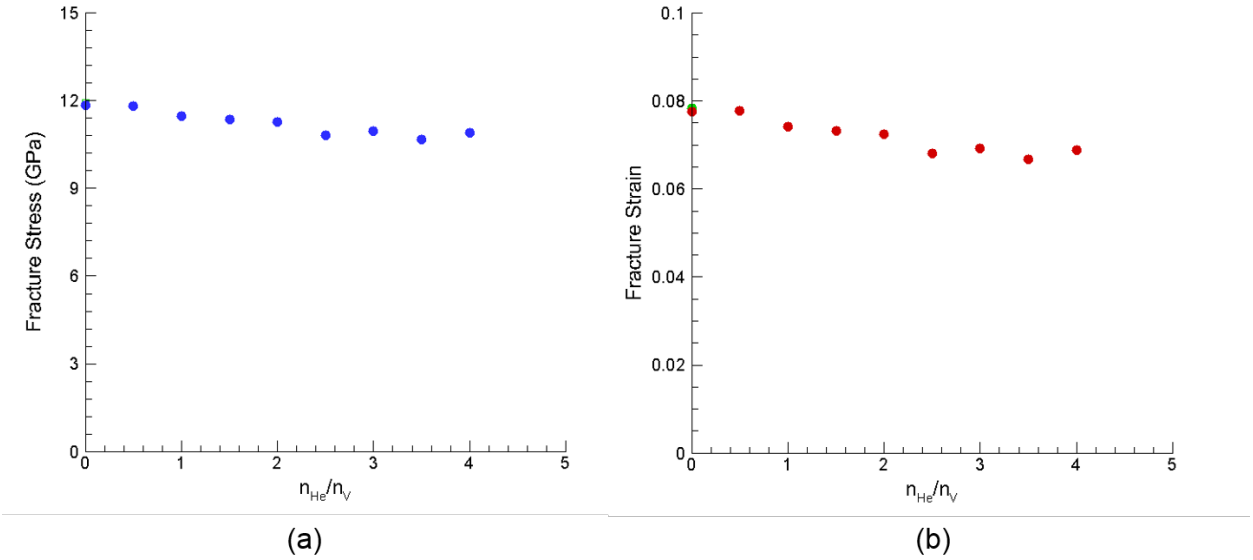

Figure 6. (a) Strength and (b) failure strain as a function of the ratio n_{He}/n_V for the α-Fe bicrystal system at RT predicted by MD analyses.

References

[1] A. Kohyama, A. Hishinuma, D.S. Gelles, R.L. Klueh, W. Dietz, K. Ehrlich, J. Nucl. Mater. 233–237 (1996) 138–147.
[2] N. Baluc, R. Schaublin, C. Bailat, F. Paschoud, M. Victoria, J. Nucl. Mater. 283–287 (2000) 731–735.
[3] X. Jia, Y. Dai, J. Nucl. Mater. 323 (2003) 360–367.
[4] F.A. Garner, Materials Science and Technology, Vol. 10A, VCH, Germany, 1994 (Chapter 6).
[5] H. Trinkaus, J. Nucl. Mater. 133–134 (1985) 105–112; C.C. Fu, F. Willaime, Phys. Rev. Lett. 92 (17) (2004) 175503.
[6] Yang, L., F. Gao, Z.Q. Zhu, S.M. Peng, X.G. Long, X.S. Zhou, H.L. Heinisch, R.J. Kurtz, X.T. Zu, J. Nuc. Mater. 441 (2013) 6.
[7] Yang, L., H.Q. Deng, F. Gao, H.L. Heinisch, R.J. Kurtz, S.Y. Hu, Y.L. Li, X.T. Zu, Nucl. Inst. Meth. Phys. Res. B 303 (2013) 68.
[8] Heinisch, H.L., Gao, F., Kurtz, R.J., Phil. Mag. 90 (2010) 885.
[9] Yang L., Zu, X.T., Gao, F., Peng, S.M., Heinisch, H.L., Kurtz, R.J., Physica B 405 (2010) 1754.
[10] Yang L, XT Zu, F Gao, HL Heinisch, RJ Kurtz, Nucl. Inst. Meth. Phys. Res. B 267 (2009) 3046.
[11] Zu XT, L Yang, F Gao, SM Peng, XG Long, HL Heinisch, RJ Kurtz, Phys. Rev. B 80 (2009) 0541041.
[12] Yang, L., Zu, X.T., Wang, Z.G., Gao, F., Wang, XY, Heinisch, H.L., Kurtz, R.J., Nucl. Inst. Meth. Phys. Res. B 265 (2008) 541.
[13] Pu, J., Yang, L., Gao, F., Heinisch, H.L., Kurtz, R.J., and Zu., X.T., Nucl. Inst. Meth. Phys. Res. B 266 (2008) 3993.
[14] Yang, L., Zu, X.T., Wang, Z.G., Gao, F., Heinisch, H.L., Kurtz, R.J., Wang, X.Y., Liu, K.Z., J. Nuc. Mater. 374 (2008) 437.
[15] Yang, L., Zu, X.T., Wang, Z.G., Yang, H.T., Gao, F., Heinisch, H.L., Kurtz, R.J., J. of App. Phys. 103 (2008) 063528.
[16] Yang, L., Zu, X.T., Xiao, H.Y., Gao, F., Heinisch, H.L., Kurtz, R.J., Wang, Z.G., and Liu, K.Z., Nucl. Inst. Meth. Phys. Res. B 255 (2007) 63.
[17] Yang, L., Zu, X.T., Xiao, H.Y., Gao, F., Heinisch, H.L., and Kurtz, R.J., Physica B 391 (2007) 179.
[18] Heinisch, H.L., Gao, F., and Kurtz, R.J., J. Nuc. Mater., 367 (2007) 311.
[19] Heinisch, H.L., Gao, F., Kurtz, R.J, Le, E.A., J. Nuc. Mater. 351 (2006) 141.

[20] Yang, L., Zu, X.T., Xiao, H.Y., Gao, F., Heinisch, H.L., Kurtz, R.J., Liu, K., App. Phys. Lett. 88 (9) (2006) 091915.
[21] Yang, L., Zu, X.T., Xiao, H.Y., Gao, F., Liu, K., Heinisch, H.L., Kurtz, R.J., Yang, S.Z., Mater. Sci. Eng. A 427 (2006) 343.
[22] T. Seletskaia, Yu.N. Osetsky, R.E. Stoller, G.M. Stocks, J. Nucl. Mater. 351 (2006) 109–118.
[23] K. Morishita, R. Sugano, B.D. Wirth, J. Nucl. Mater. 323 (2003) 243–250.
[24] L. Ventelon, B. Wirth, C. Domain, J. Nucl. Mater. 351 (2006) 119–132.
[25] G. Lucas, R. Shäublin, J. Phys.: Condens. Matter 20 (2008) 415206.
[26] N. Juslin, K. Nordlund, J. Nucl. Mater. 382 (2008) 143–146.
[27] G. Lucas, R. Schäublin, J. Nucl. Mater. 386–388 (2009) 360–362.
[28] Deng, H.Q., W.Y. Hu, F. Gao, H.L. Heinisch, S.Y. Hu, Y.L. Li, R.J. Kurtz, J. Nuc. Mater. 442 (2013) S667.
[29] Heinisch HL, F Gao, RJ Kurtz, in proceedings ASTM 23rd Symposium on Effects of Radiation on Materials, (2009) 190.
[30] Gao F, HL Heinisch, RJ Kurtz, J. Nuc. Mater. 386 (2009) 390.
[31] Kurtz RJ, HL Heinisch, F Gao, J. Nuc. Mater. 382 (2008) 134.
[32] Gao, F., Heinisch, H.L., and Kurtz, R.J., J. Nuc. Mater. 367 (2007) 446.
[33] Heinisch, H.L., F. Gao, R.J. Kurtz, J. ASTM Inter. 4 2007).
[34] Gao, F., Heinisch, H.L., Kurtz, R.J., J. Nuc. Mater. 351 (2006) 133.
[35] Kurtz R.J., Heinisch H.L.,, J. Nuc. Mater. 329-333 (2004) 1199.
[36] T. Suzudo, H. Kaburaki, M. Yamaguchi, J. Nucl. Mater. 417 (2011) 1102–1105.
[37] T. Suzudo, T. Tsuru, M. Yamaguchi, H. Kaburaki, J. Nucl. Mater. 442 (2013) S655–S659.
[38] D. Terentyev, X. Hea, A. Serra, J. Kuriplach, Comp. Mater. Sci. 49 (2010) 419–429.
[39] Nguyen B.N., R.J. Kurtz, F. Gao, "Modeling the Effects of Helium Bubbles On The Stress-Strain Behavior of Iron Grain Boundaries by A Mechanistic Finite Element Approach Using Molecular Dynamics Data," in Fusion Materials Semiannual Progress Report For the Period Ending December 31, 2017, ed. FW Wiffen and S Melton, Oak Ridge National Laboratory, Oak Ridge, TN.
[40] J. Shi, L. Peng, M. Ye, F. Gao, IEEE Trans. Plasma Sci. 45(2) (2017) 289-293.
[41] F. Gao, *Personal communication*.

8.5 MODELING DUCTILE-PHASE TOUGHENED TUNGSTEN FOR PLASMA-FACING MATERIALS BY A MULTISCALE MICROSTRUCTURAL APPROACH: APPLICATIONS TO NICKEL-IRON-TUNGSTEN COMPOSITE—B.N. Nguyen, C.H. Henager, Jr., R.J. Kurtz (Pacific Northwest National Laboratory)

OBJECTIVE

The objective of this study is to investigate the deformation behavior of ductile phase toughened W-composites such as tungsten-copper (W-Cu) and tungsten-nickel-iron (W-Ni-Fe) using a multiscale microstructural approach that involves a dual-phase model where the constituent phases (i.e., W, Cu, Ni-Fe) are finely discretized in finite elements and are described by a continuum damage mechanics (CDM) model. Such an approach is suitable for modeling deformation, cracking, and crack bridging for W-Cu, W-Ni-Fe, and other ductile phase toughened W-composites, or more generally, any multi-phase composite structure where two or more phases undergo cooperative deformation in a composite system. During the current report period, we applied this approach, which was previously developed and validated for W-Cu composites [1], to three-dimensional (3D) analyses of a W-Ni-Fe notched specimen subjected to four-point bending. Model predictions are compared to corresponding experimental results. In addition, this modeling capability was used as a tool to investigate hypothetical W-Ni-Fe microstructures to increase strength and ductility of these composites.

SUMMARY

A promising approach to increasing fracture toughness and decreasing the ductile-brittle transition temperature (DBTT) of a W-alloy is by ductile-phase toughening (DPT) [2-4]. In this approach, a ductile phase is included in a brittle matrix to increase the overall work of fracture for the composite material. Previously, Pacific Northwest National Laboratory (PNNL) had developed a multiscale microstructural approach to study DPT of W and validated it through analyses of W-Cu bend bar tests [1]. Reference [1] shows that such an approach is very robust and is able to capture the bridging mechanism responsible for increased strength, toughness, and ductility. This report describes recent applications of this approach to simulate four-point bending of W-Ni-Fe specimens and investigate microstructural features that impact the mechanical properties of W-Ni-Fe composites (i.e., stress-strain response, strength, and failure strain) as it is desirable to optimize these composites with regard to high-temperature strength and fracture toughness for fusion applications.

PROGRESS AND STATUS

Introduction

The W and W-alloys are the solid materials of choice for plasma-facing components (PFCs) of future fusion reactors, such as the International Thermonuclear Experimental Reactor (ITER) and Demonstration Power Plant (DEMO), due to their high melting point, strength at high temperatures, high thermal conductivity, low coefficient of thermal expansion, and low sputtering yield [5-7]. However, W and most W-alloys exhibit low fracture toughness and a high DBTT that would render them as brittle materials during reactor operations [5,7,8]. The DBTT for unirradiated W-alloys typically ranges from 573K to 1273K (300˚C to 1000˚C), and in a reactor environment radiation hardening would further elevate this range [7,9,10]. W-alloys toughened by engineered reinforcement architectures, such as DPT are strong candidates for PFCs. The principle of DPT is illustrated in Figure 1, which shows an actual and schematic illustration of ductile bridging ligaments stretching across an open crack in a brittle W matrix material [1]. The W-Cu was a DPT composite for model development purposes only, and there is an important need to develop other W-alloys employing DPT mechanisms to achieve high-strength and high-toughness W-composites meeting fusion energy application requirements. Our efforts have moved in this direction and have focused on applying the developed approach to simulate four-point bending of W-Ni-Fe specimens and to tailor the microstructure of W-Ni-Fe composites.

Model Development

The W-Ni-Fe material (90-wt% W, 7-wt% Ni, 3-wt% Fe) studied in this work has a lamellar-like microstructure as presented in Figure 2 that shows the Ni-Fe phase embedded in nearly parallel W-phase regions. This microstructure is repeated in the thickness direction (out-of-plane direction). During this report period, our efforts first focused on building 3D FE models containing a 3D meshed dual-phase (W-Fe-Ni) microstructure for a four-point bend specimen from a 2D microstructural FE model of this specimen. The 2D FE model (Figure 3a) containing the dual-phase microstructural domain was created using the method reported in [1]. This method generates homogenized, meshed regions adjacent to the dual-phase meshed region shown in Figure 3a to create a fully meshed model of a bend bar that corresponds to the physical dimensions of an actual W-Fe-Ni SENB specimen (25 mm x 4 mm x 1.85 mm). The dimensions of the silicon carbide (SiC) supports and loading pins are the same as those for the SENB specimens studied in [1]. The loading and support spans are 10 mm and 20 mm, respectively. Next, 3D FE models with different mesh refinements in the specimen thickness direction were built by extrusion in that direction (Figure 3b). The as-created FE meshes shown in Figures 3a and 3b for the bend specimens possess three regions: the dual phase W-Ni-Fe microstructural domain where damage, fracture and large deformation occur, and two adjacent continuum homogenized W-Ni-Fe linear elastic-plastic regions that deform but do not fracture. All contacts between different entities of the models (Figure 3) are assumed to be frictionless.

The constitutive behaviors of W and of the Ni-Fe alloy in the microstructural domain were described by an elastic-plastic damage model [1] implemented in the ABAQUS FE package via user subroutines. This model treats the different behaviors in tension and compression by not allowing damage evolution for a compressive stress state. The details of the damage model formulation and identification of material parameters are given in [1].

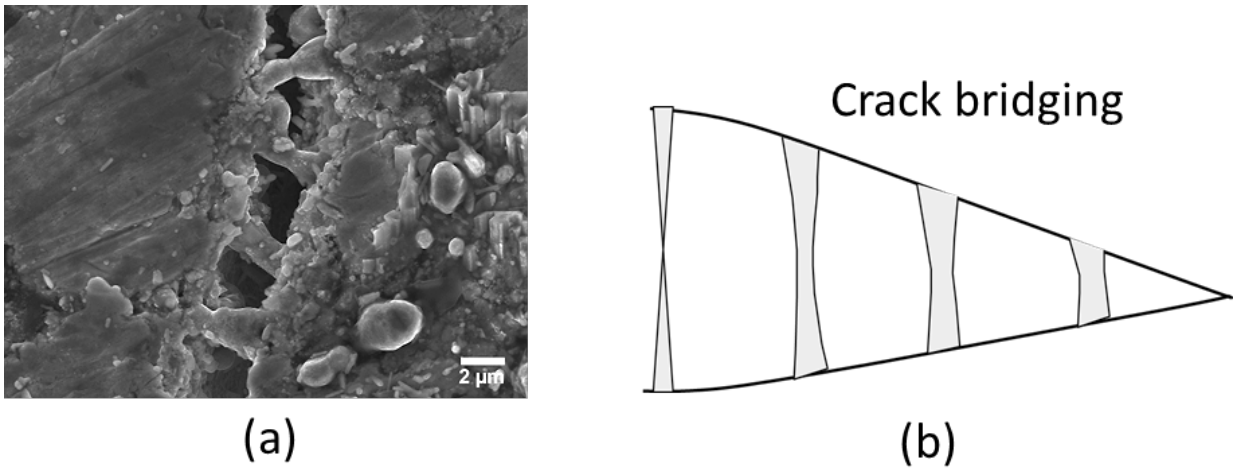

Figure 1. a) Scanning Electron Microscopy (SEM) images of a crack in W-Cu tested at 632˚C in argon showing Cu ligaments bridging a crack. b) A steady-state bridging zone shown schematically in 2D [1].

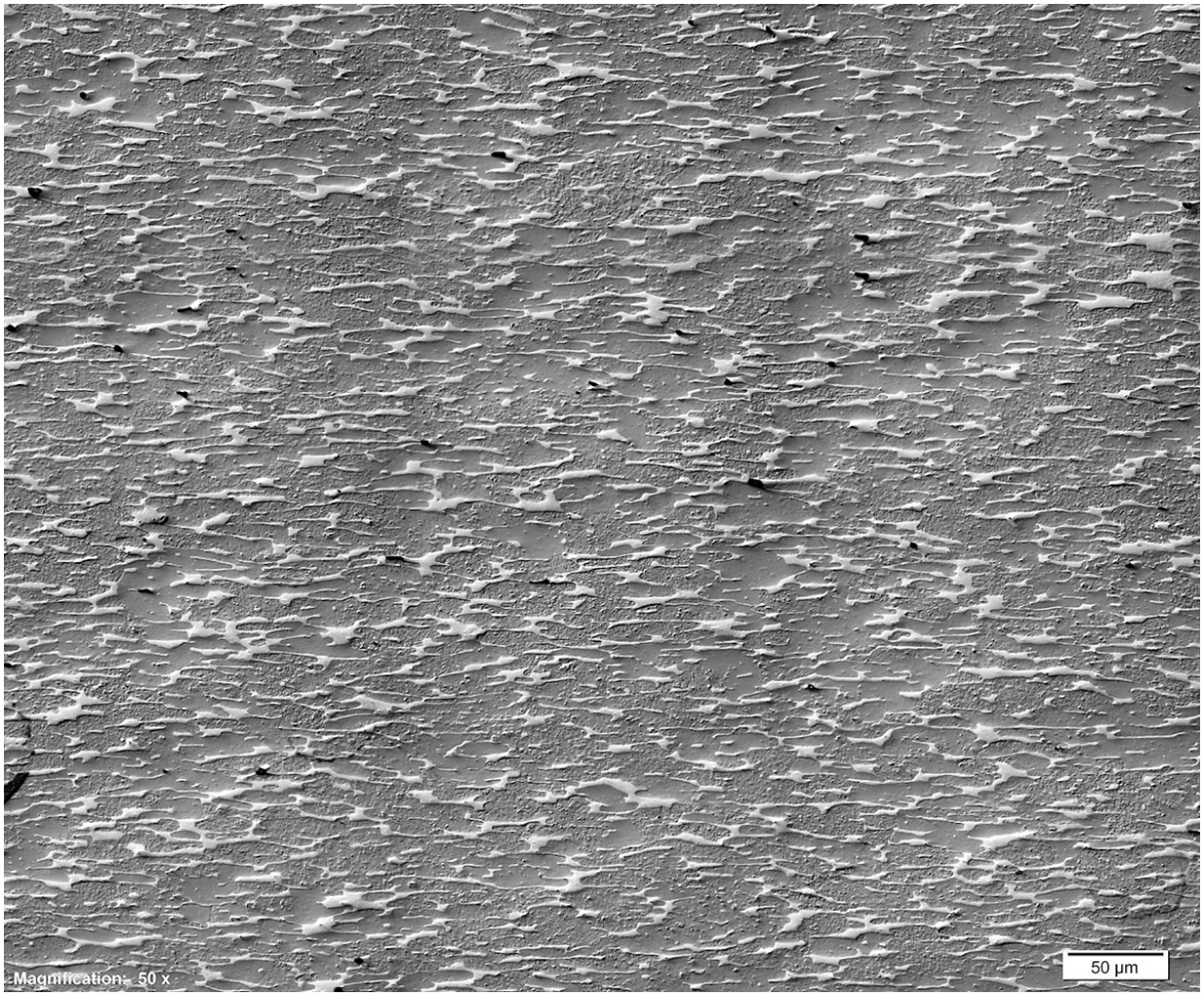

Figure 2. The microstructure of the W-Ni-Fe composite studied in this work (dark gray: W; light gray: Ni-Fe; black: microvoids).

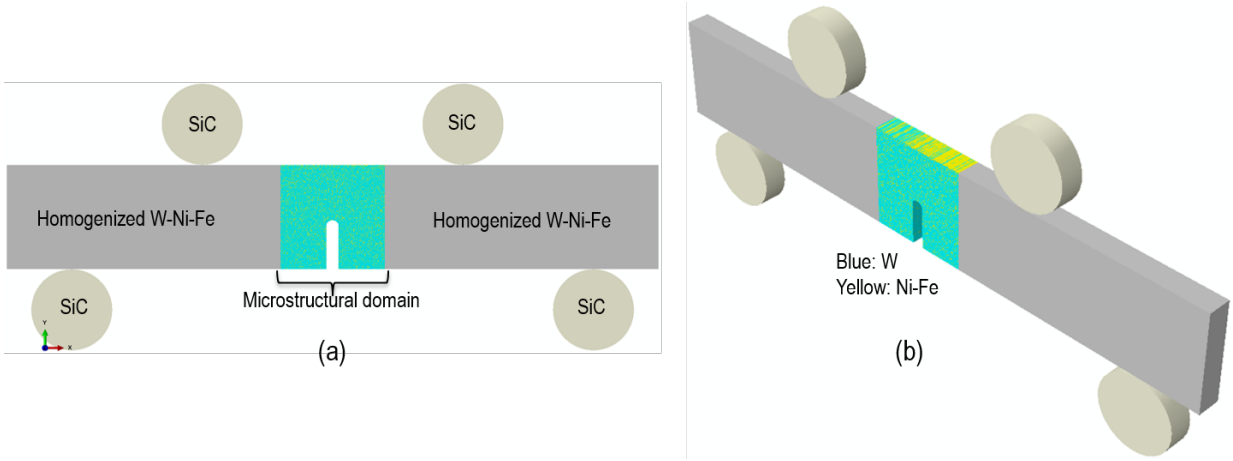

Figure 3. (a) The plane-strain FE mesh of the W-Ni-Fe SENB specimen. (b) A 3D FE mesh of the same specimen. The dual-phase microstructural domain contains the constituent phases identified by color.

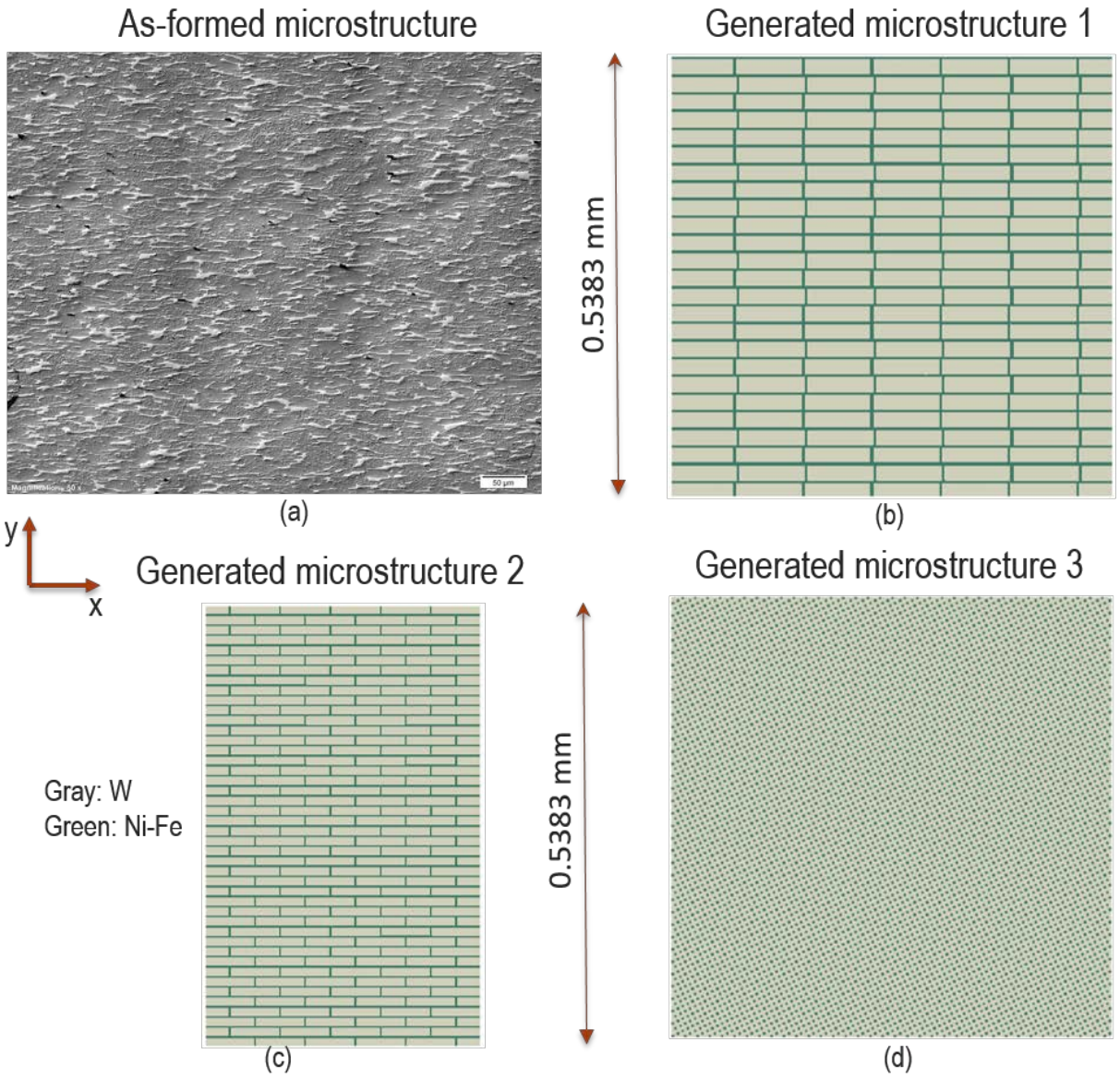

Figure 4. (a) The as-formed microstructure from a tensile specimen, (b) Generated microstructure 1 with l/d=4.4 (l=80 µm) and spacing between W "bricks" producing nearly straight connected Fe-Ni regions, (c) Generated microstructure 2 with l/d = 6 (l=60 µm) and a brick-type lattice, and (d) Generated microstructure 3 with l/d= 1 and (l=3 µm). The volume fraction of W is 0.8 in all cases.

From a micrograph of the W-Ni-Fe microstructure taken from a tensile specimen (Figure 4a), a high-resolution FE mesh of the microstructure was created using the OOF2[1] software and a 2D plane-stress FE model using this mesh was built to study the W-Ni-Fe composite response to tensile loading. Subsequently, a series of W-Ni-Fe microstructures was created, meshed, and modeled in a similar manner (Figures 4b to 4d) to investigate the effects of microstructural features and morphologies on the composite stress-strain response, damage, and fracture patterns. All the microstructure models presented in Figure 4 have the same thickness (0.254 mm) and volume fractions of W (0.8), but they are different in microstructural

[1] Software developed at the National Institute of Standards and Technology.

features and topology. Figure 4a presents the as-formed W-Ni-Fe material, which has a lamellar-like microstructure as discussed above. Figure 4b shows the generated microstructure 1 which exhibits the W-phase regions in the form of regular "bricks". The W "brick" aspect ratio l/h is 4.4 (with l denoting the length = 80 μm, and h, the height). This microstructure has the spacing between W "bricks" that produces nearly straight Fe-Ni connected regions. The generated microstructure 2 shown in Figure 4c with l/d = 6 (l = 60 μm) exhibits a brick-type lattice structure that prevents vertical connections of the Fe-Ni phases regions. Generated microstructure 3 has a uniform distribution of Fe-Ni elements with l/d=1 (l = 3 μm) in the W matrix. All the ABAQUS FE analyses of these microstructures subjected to tensile loading in the x-direction (Figure 4) used the same elastic-plastic damage model [1] as the analysis for the four-point SENB specimen.

Results

The 2D plane-strain and 3D FE models for the W-Ni-Fe SENB specimen subjected to four-point bending were analyzed by ABAQUS using the elastic-plastic damage model reported in [1] to describe the constitutive behaviors of W and Ni-Fe phases in the microstructural domain. Damage is quantified by a damage indicator that varies from 0 to 1. If the failure indicator is equal to 1, total failure (or fracture) causing crack propagation occurs and is captured by a vanishing element method [11,1]. Figures 5(a-c) respectively show the crack propagation patterns in the dual-phase domain for the W-Ni-Fe SENB specimen using the plane-strain FE model and two 3D FE models with different mesh refinements in the specimen thickness direction at an advanced stage of fracture. The 3D Mesh 1 has about 1.5M elements and 3D Mesh 2 about ~2M elements. All the analyses predicted cracks meandering and linking up to form a main crack that propagates into the material close to the vertical centerline of the dual-phase domain. These predictions agree with the experimental observations reported in Figures 5d.

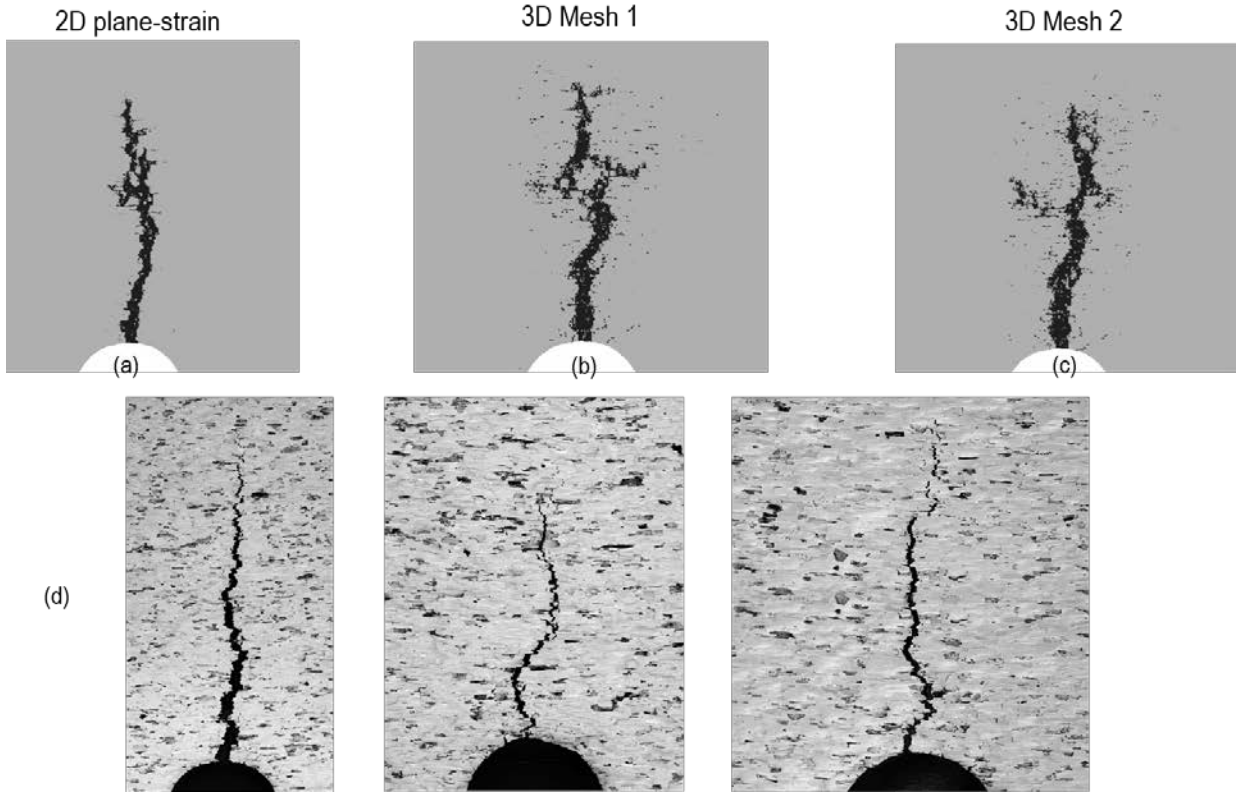

Figure 5. Predicted crack patterns (black areas) in the W-Ni-Fe microstructural domain from (a) a plane-strain model, (b) 3D Mesh 1 model, and (c) 3D Mesh 2 model compared to (d) experimental observations after bend tests at room temperature (RT).

To investigate in a preliminary manner what microstructural features govern composite material response, plane-stress FE simulations were performed using this damage model to analyze the W-Ni-Fe microstructures presented in Figure 4 subjected to tensile loading. The corresponding crack development patterns at final failure and stress-strain responses are presented in Figures 6(a-d) and 7, respectively.

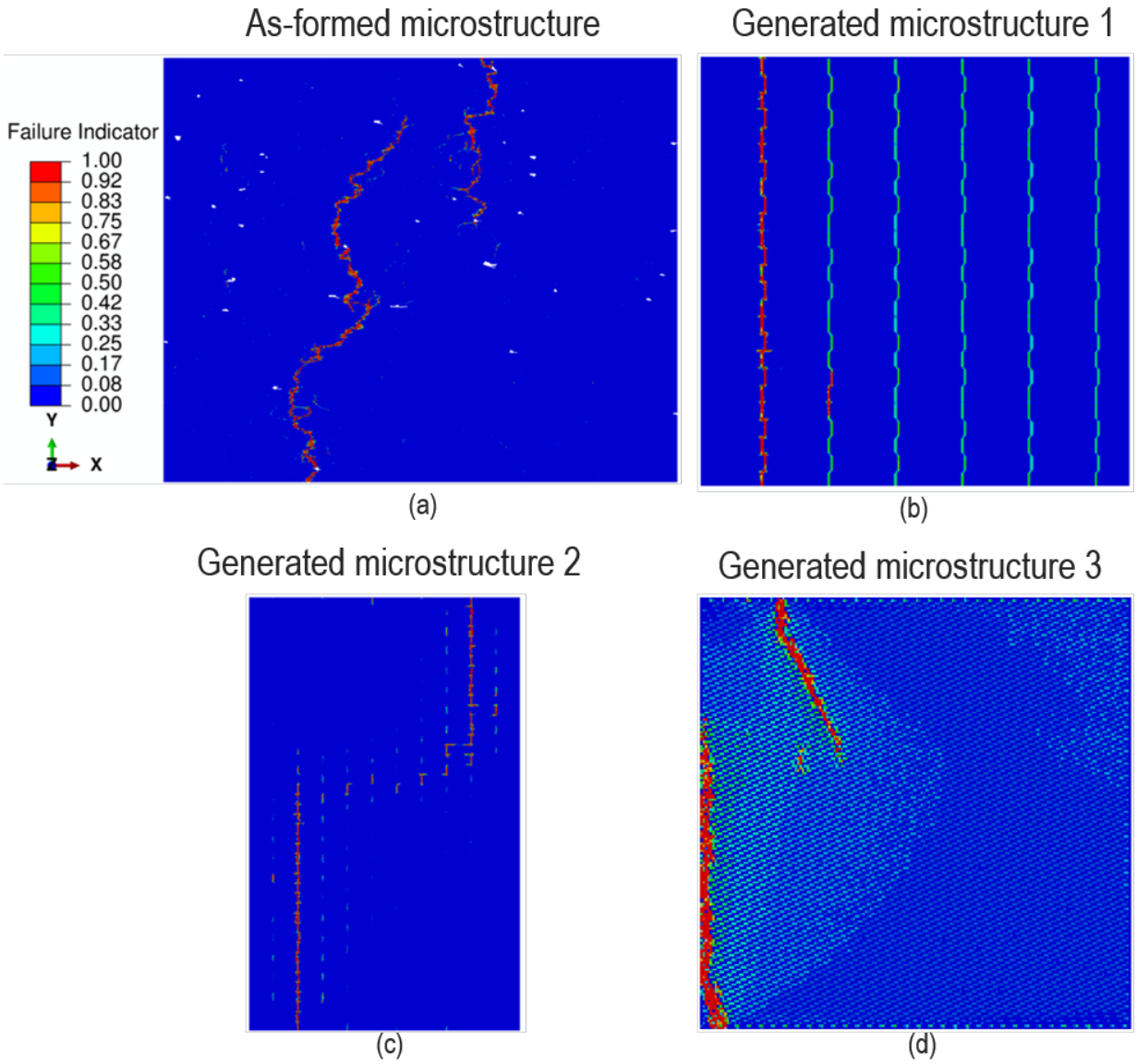

Figure 6. Crack development patterns at final failure predicted for the microstructures shown in Figures 4(a-d) subjected to tensile loading in the x-direction.

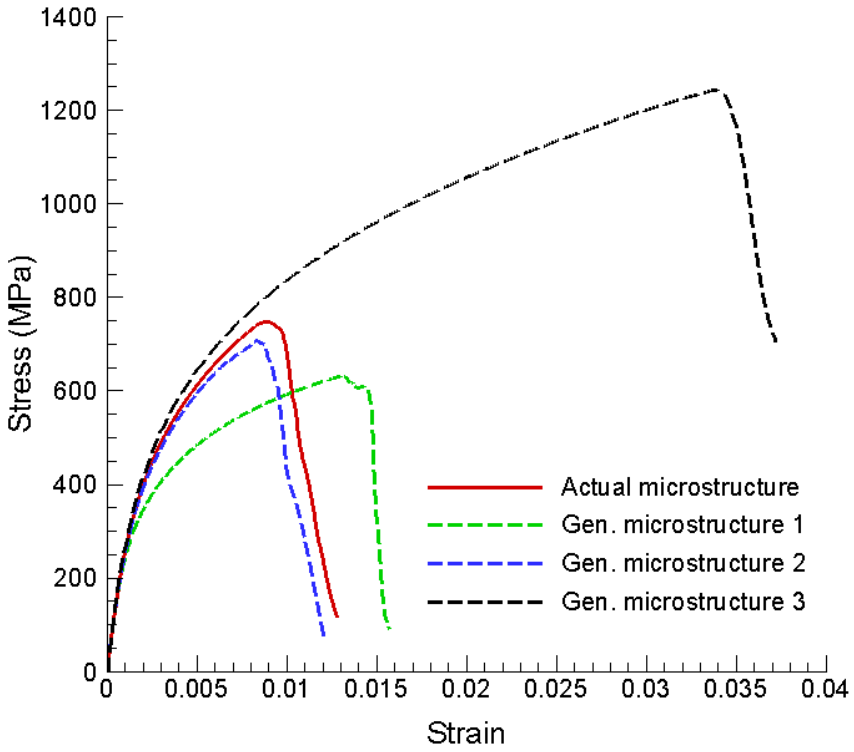

Figure 7. Predicted tensile stress-strain responses in the x-direction for the microstructures presented in Figures 4(a-d).

Under tensile loading, the actual microstructure (Figure 4a) experienced the most crack bridging and meandering leading to greater work of fracture than generated microstructures 1 and 2. This resulted in higher strength for the actual material than the generated microstructures 1 and 2. Microstructure 1 contains paths formed by connected Ni-Fe regions that are perpendicular to the loading direction and no W regions fracture. In this microstructure, cracks developed and linked up quickly along one of these paths leading to material failure at a lower strength but greater failure strain than the corresponding values exhibited by the actual and microstructure 2 materials. The brick-type lattice structure in generated microstructure 2 mitigates the weak paths present in microstructure 1. In this microstructure, a microcrack that develops in a Ni-Fe region must cause fracture of a high-strength W “brick” to propagate into adjacent Ni-Fe regions with lower fracture energy. Finally, generated microstructure 3 produces the highest strength and failure strain due to a well-dispersed and uniform particle distribution. Such a microstructure appears to represent an extreme case, which will be helpful for understanding how to optimize a DPT microstructure, but manufacturing this microstructure might not be achievable.

Conclusions

During this report period, important progress has been made on developing our capability for modeling ductile phase-toughened tungsten for plasma-facing applications by implementing 3D modeling and variable microstructure investigation. We applied the dual-phase microstructural approach previously developed to simulate W-Ni-Fe SENB specimen tests using 2D and 3D modeling. Current model predictions show good agreement with our recent experimental data with respect to fracture loads and crack patterns as well as propagation directions in W-Ni-Fe composites. The microstructure study revealed important

effects of crack bridging and crack meandering mechanisms for retarding crack propagation leading to increased material strength and toughness. The developed approach, while preliminary and narrow in scope, appears to be robust and will be used to tailor the mechanical properties of DPT composites.

Future Work

We will complete our work on W-Ni-Fe composites. Tensile tests and additional bend tests will be conducted for W-Ni-Fe composite specimens. The FE analyses using the developed approach will be performed to simulate these tests and compare predictions to experimental results. The large literature describing the mechanics of "brick and mortar" microstructures will also be assessed.

References

[1] Nguyen, B.N., C.H. Henager, Jr, N.R. Overman, and R.J. Kurtz. 2018. A Multiscale Microstructural Approach to Ductile-Phase Toughened Tungsten for Plasma-Facing Materials. J. Nucl. Mater., 2018. 508: p. 371-384 .
[2] Deve, H.E., A.G. Evans, G.R. Odette, R. Mehrabian, M.L. Emiliani, and R.J. Hecht, Acta metallurgica et materialia, 1990. 38(8): p. 1491-502.
[3] Erdogan, F. and P.F. Joseph, J. Am. Ceram. Soc., 1989. 72(2): p. 262-270.
[4] Sigl, L.S., P.A. Mataga, B.J. Dalgleish, R.M. McMeeking, and A.G. Evans, Acta Metall., 1988. 36(4): p. 945-953.
[5] Rieth, M., J.L. Boutard, S.L. Dudarev, T. Ahlgren, S. Antusch, N. Baluc, M.F. Barthe, C.S. Becquart, L. Ciupinski, J.B. Correia, C. Domain, J. Fikar, E. Fortuna, C.C. Fu, E. Gaganidze, T.L. Galan, C. Garcia-Rosales, B. Gludovatz, H. Greuner, K. Heinola, N. Holstein, N. Juslin, F. Koch, W. Krauss, K.J. Kurzydlowski, J. Linke, C. Linsmeier, N. Luzginova, H. Maier, M.S. Martinez, J.M. Missiaen, M. Muhammed, A. Munoz, M. Muzyk, K. Nordlund, D. Nguyen-Manh, P. Norajitra, J. Opschoor, G. Pintsuk, R. Pippan, G. Ritz, L. Romaner, D. Rupp, R. Schaublin, J. Schlosser, I. Uytdenhouwen, J.G. Van Der Laan, L. Veleva, L. Ventelon, S. Wahlberg, F. Willaime, S. Wurster, and M.A. Yar, J. Nucl. Mater., 2011. 417: p. 463-467.
[6] Pitts, R.A., A. Kukushkin, A. Loarte, A. Martin, M. Merola, C.E. Kessel, V. Komarov, and M. Shimada, Physica Scripta Volume T, 2009. 2009(T138): p. 014001 (10 pp.).
[7] Mertens, P., T. Hirai, M. Knaup, O. Neubauer, V. Philipps, J. Rapp, V. Riccardo, S. Sadakov, B. Schweer, A. Terra, I. Uytdenhouwen, and U. Samm, Fusion Eng. Des., 2009. 84(7-11): p. 1289-93.
[8] Mertens, P., V. Philipps, G. Pintsuk, V. Riccardo, U. Samm, V. Thompson, and I. Uytdenhouwen, Physica Scripta Volume T, 2009. 2009(T138): p. 014032 (5 pp.).
[9] Gludovatz, B., S. Wurster, A. Hoffmann, and R. Pippan, Int. J. Refract. Met. Hard Mater., 2010. 28(6): p. 674-8.
[10] Zinkle, S.J. and N.M. Ghoniem, Fusion Eng. Des., 2000. 51-52: p. 55-71.
[11] V. Tvergaard, J. Mech. Phys. Solids, 1982. 30(6): p. 399-425.

9. FUSION SYSTEM DESIGN

No contributions this reporting period.

10. IRRADIATION METHODS, EXPERIMENTS AND SCHEDULES

10.1 HFIR IRRADIATION EXPERIMENTS—Y. Katoh, J.L. McDuffee, C. Bryan, J.P. Robertson (Oak Ridge National Laboratory)

SUMMARY

Neutron irradiation experiments were performed in support of the research and development of fusion reactor materials using various materials irradiation facilities in the High Flux Isotope Reactor (HFIR).

The HFIR operated for 3.75 cycles between January 1 and June 30, 2018. Cycle 477 was completed on February 4 (2026.49 MWD), Cycle 478 on March 16 (2036.33 MWD), and Cycle 479 on May 24 (2033.77 MWD). Cycle 480 began on June 12 and is expected to complete on July 6.

During this time up to 22 target zone rabbit capsules were in HFIR in a given cycle. The capsules are listed in Table 1 along with condensed information on material, specimen type, temperature, fluence, and period of irradiation. Eight rabbit capsules completed the scheduled irradiations.

Table 1. HFIR fusion materials program rabbit capsules under irradiation in the first half of 2018

Experiment Designation	Primary Materials	Specimen Types	Irradiation Temperature (°C)	Max Exposure (dpa)	Number of Reactor Cycles
F13A5	FeCrAlY Steel	Bend bar	300	28	16
F13A6*	FeCrAlY Steel	Bend bar	300	50	29
F13B4	FeCrAlY Steel	tensile	300	50	29
JCR11-05	SiC/SiC	bend bars	950	200	115
JCR11-07	SiC/SiC	Mini bend bars	950	100	47
JCR11-08	SiC/SiC	Mini bend bars	950	200	115
SCF8	SiC/SiC	Bend bars	600	100	45
SCF9	SiC/SiC	Bend bars	600	200	90
SCF11	SiC/SiC	Bend bars	950	100	57
ES21*	EUROFER alloy variants	Tensile/MPC**	300	2.5	2
ES22*	EUROFER alloy variants	Tensile/MPC	300	2.5	2
ES31*	EUROFER alloy variants	Bend Bar	300	2.5	2
ES32*	EUROFER alloy variants	Bend Bar	300	2.5	2
ES33*	EUROFER alloy variants	Bend Bar	300	2.5	2
ES34*	EUROFER alloy variants	Bend Bar	300	2.5	2
ES35*	EUROFER alloy variants	Bend Bar	300	2.5	2
ES01	EUROFER reference alloy	Tensile/MPC**	220	20	12
ES02	EUROFER reference alloy	Tensile/MPC	240	20	12
ES03	EUROFER reference alloy	Tensile/MPC	275	20	12
ES04	EUROFER reference alloy	Tensile/MPC	300	20	12

Experiment Designation	Primary Materials	Specimen Types	Irradiation Temperature (°C)	Max Exposure (dpa)	Number of Reactor Cycles
ES05	EUROFER reference alloy	Tensile/MPC	325	20	12
ES06	EUROFER reference alloy	Tensile/MPC	350	20	12
ES07	EUROFER reference alloy	Tensile/MPC	375	20	12
ES11	EUROFER reference alloy	Bend Bar	220	20	12
ES12	EUROFER reference alloy	Bend Bar	240	20	12
ES13	EUROFER reference alloy	Bend Bar	275	20	12
ES14	EUROFER reference alloy	Bend Bar	300	20	12
ES15	EUROFER reference alloy	Bend Bar	325	20	12
ES16	EUROFER reference alloy	Bend Bar	350	20	12
ES17	EUROFER reference alloy	Bend Bar	375	20	12

*completed irradiation this reporting period
**MPC = Multi-Purpose Coupon